



UNIVERSITY OF MESSINA

DEPARTMENT OF MATHEMATICAL AND COMPUTER SCIENCES,
PHYSICAL SCIENCES AND EARTH SCIENCES (MIFT)

Ph.D. Programme in Physics, Cycle XXXIV

SSD FIS/07

DOCTORAL THESIS

Natural radioactivity due to radon in northeastern Sicily (Italy): application, measurement and radiological hazard

Author:
Davide Romano

Supervisor:
Prof. Salvatore Magazù
Salvatore Magazù
Co-Supervisors:
Dott. Francesco Italiano
Dott. Giuseppe Sabatino

Coordinator:
Prof. Vincenza Crupi

ACADEMIC YEAR 2020/2021

Contents

| | |
|--|---------|
| <i>Abstract</i> | page 1 |
| <i>Chapter I - Introduction and purposes</i> | page 4 |
| <i>Chapter II - Natural radioactivity</i> | page 9 |
| 2.1 History and types of radioactivity | page 9 |
| 2.2 Isotopes and decay types | page 10 |
| 2.3 Decay energy | page 13 |
| 2.4 Sources of natural radioactivity | page 13 |
| 2.4.1 Cosmogenic radionuclides | page 13 |
| 2.4.2 Primordial radionuclides | page 14 |
| 2.5 Radioactive decay law | page 16 |
| 2.6 Activity and specific activity | page 18 |
| 2.7 Secular Equilibrium | page 19 |
| 2.8 Radon | page 20 |
| <i>Chapter III - The study area</i> | page 23 |
| 3.1. Physiographic and geological features | page 23 |
| 3.2. The Calabria-Peloritani Orogen (CPO) | page 24 |
| 3.3. Active deformation along the southern portion of the CPO | page 31 |
| <i>Chapter IV - Radiological features of the Peloritani crystalline rocks: gamma radiation and radon release</i> | page 45 |
| 4.1 Introduction | page 45 |
| 4.2 Exposure and dosimetry | page 46 |
| 4.3 Radon releasing from solid materials | page 48 |
| 4.4 Materials | page 51 |
| 4.4.1 Samples | page 51 |
| 4.4.2 Sample preparation | page 53 |
| 4.5 Method | page 53 |
| 4.5.1 Gamma spectroscopy | page 53 |
| 4.5.2 Outdoor radiological hazard due to gamma radiation: the absorbed dose and the annual effective dose | page 54 |
| 4.5.3 Exposure to gamma radiation originating from building materials: radiological indexes | page 55 |
| 4.5.4 Radon emanation measurements | page 56 |

| | |
|---|----------|
| 4.5.5 Calculation of indoor radon concentrations and indoor effective doses | page 61 |
| 4.6 Results and discussion | page 63 |
| 4.6.1 Activity concentration of ^{226}Ra , ^{232}Th and ^{40}K | page 63 |
| 4.6.2 Outdoor gamma radiation | page 65 |
| 4.6.3 Hazard indexes | page 67 |
| 4.6.4 Natural radioactivity due to radon | page 68 |
| 4.6.5 Indoor radon | page 75 |
| 4.7 Concluding remarks | page 78 |
| <i>Chapter V - Soil gas radon and hazard assessment</i> | page 84 |
| 5.1 Introduction | page 84 |
| 5.2 Radon migration through the Earth's crust | page 86 |
| 5.3 Measurement locations | page 89 |
| 5.4 Method | page 91 |
| 5.4.1 Soil-radon measurements | page 91 |
| 5.4.1.1 Techniques | page 91 |
| 5.4.1.2 Uncertainties | page 93 |
| 5.4.1.3 Spatial and environmental parameters affecting the soil radon concentration | page 93 |
| 5.4.2 Statistical properties: Exploratory Data Analysis | page 94 |
| 5.4.3 Geostatistics: data interpolation | page 96 |
| 5.4.4 Soil permeability | page 97 |
| 5.4.5 Radon hazard | page 97 |
| 5.4.6 CO ₂ measurements in soil gas | page 99 |
| 5.5 Results and Discussion | page 100 |
| 5.5.1 Soil-gas radon concentration and statistical analysis | page 100 |
| 5.5.2 Interpolation and radon maps | page 112 |
| 5.5.3 Hazard assessment | page 116 |
| 5.5.3.1 Radon Index | page 116 |
| 5.5.3.2 RI maps used in the field of indoor hazard mitigation | page 122 |
| 5.5.4 Geophysical and tectonic implications | page 123 |
| 5.5.4.1 Radon vs thoron: deep degassing vs shallow circulation | page 123 |
| 5.5.4.2 CO ₂ percentage in soil: preliminary data | page 125 |

| | |
|--|----------|
| 5.5.4.3 Type and location of radon anomalies | page 127 |
| 5.5.4.4 The meaning of Radon anomalies within the regional geodynamic framework | page 131 |
| 5.6 Concluding remarks | page 144 |
| Chapter VI - Radon in groundwater | page 160 |
| 6.1 Introduction | page 160 |
| 6.2 Method | page 161 |
| 6.2.1 Sampling locations | page 161 |
| 6.2.2 Temperature, pH, and conductivity measurements | page 164 |
| 6.2.3 Radon concentration measurement in water samples | page 166 |
| 6.2.4 Dosimetry | page 167 |
| 6.3 Results and Discussion | page 168 |
| 6.3.1 Distribution of ^{222}Rn dissolved in groundwater | page 168 |
| 6.3.2 Comparison of radon levels measured in the Peloritani groundwater with other areas | page 174 |
| 6.3.3 Radiological Hazard | page 175 |
| 6.4 Concluding remarks | page 178 |
| Chapter VII- Summary and conclusions | page 182 |
| Acknowledgements | page 187 |
| Appendix 1 - Soil-Rn spectra | page 188 |
| Appendix 2 - Groundwater-Rn spectra | page 206 |

This work is licensed under a Creative Commons License CC BY-NC.

Abstract

A radiological study was carried out over the Tyrrhenian margin of the Peloritani Mountains (northeastern Sicily, southern Italy) to investigate the natural radioactivity with the aim of defining if radiation levels, particularly those produced by radon, are higher than the global averages exposing inhabitants to dangerous radiation doses.

The collected results demonstrate that groundwater radon levels and gamma radiation derived from soils and rocks do not constitute a health threat. On the other hand, anomalous radon concentrations in soil gases were detected along a ~NW-SE oriented zone located in the Barcellona-Milazzo alluvial plain.

The diffuse degassing appears to be generated by the uprising of deep-originated fluids along faults and fractures, and it is favoured by the high permeability of the clastic Quaternary sediments outcropping in the area. Structural and geophysical indications allow considering the tectonic lineament promoting the radon degassing as a potential “silent” on-land prolongation of the Vulcano-Milazzo fault zone (VMFZ), a transtensional tectonic element located in the Gulf of Patti and belonging to the Aeolian-Tindari-Letojanni System.

In this framework, as already suggested by other authors, a regional degassing of CO₂-dominated fluids is triggered by the activity of lithospheric faults. Mantle volatiles are produced by the depressurization of the upper mantle and they are driven toward the surface due to the enhanced vertical permeability occurring along tectonic structures. During their ascent, mantle volatiles mix with radon-rich crustal-derived fluids likely produced by thermo-mechanical processes. Therefore, radon atoms, carried by CO₂, migrate from the crust to the atmosphere generating local radiological hazards for inhabitants.

In detail, radiological measurements were carried out by means of gamma and alpha spectroscopy on different types of natural samples including crystalline rocks, soil gases and groundwaters.

Crystalline rocks show ²²⁶Ra, ²³²Th and ⁴⁰K activity ranging from (17 ± 4) to (56 ± 8) Bq kg⁻¹, from (14 ± 3) to (77 ± 14) Bq kg⁻¹ and from (167 ± 84) to (1760 ± 242) Bq kg⁻¹, respectively. The effective dose outdoor derived from gamma radiation is slightly above the global average. Despite this evidence, it does not constitute a menace to human health.

Since some of the crystalline rocks are extensively used as building materials, the potential hazard for population derived from the radon released from the rock matrix was assessed. The results show that the ^{222}Rn emanation coefficient and the ^{222}Rn surface exhalation rate range from (0.63 ± 0.3) to $(8.27 \pm 1.6)\%$ and from (0.12 ± 0.03) to (2.75 ± 0.17) $\text{Bq m}^{-2} \text{ h}^{-1}$, respectively. These values do not generate dangerous indoor radon levels, and therefore the crystalline rocks can be used in construction without restrictions.

Concerning soil gases, a total of 172 samples were analysed for the ^{222}Rn and ^{220}Rn activity concentrations. Analyses were carried out by using a hollow probe to pump out soil gas from depths of 0.5-0.6 m and the RAD7 Durrige to determine the radon concentration. ^{222}Rn and ^{220}Rn concentrations range from (0.69 ± 0.2) to (81.3 ± 2.5) kBq m^{-3} and from (2.63 ± 0.6) to (123.48 ± 5) kBq m^{-3} , respectively. Radon index (RI) estimations point out that the radiological hazard for the population living in the studied area is low to moderate, except along the ~NW-SE oriented zone already described, where widespread radon degassing from soils takes place.

Moreover, 70 groundwater samples were collected from wells and natural springs, and the activity of dissolved ^{222}Rn was measured by using the alpha counter RAD7 Durrige coupled with the RAD H₂O setup.

Analyses show that the ^{222}Rn activity concentration ranges between (1.6 ± 1.1) and (57.5 ± 5.3) Bq L^{-1} . Groundwater coming from natural springs and wells is generally used as tap water for human consumption and other domestic purposes. All the measured radon activities are lower than the reference limit set by the Italian legislation, and the annual effective dose received by the population due to ingestion is in the range of 4-146.8 $\mu\text{Sv y}^{-1}$, then below the worldwide average value. As a result, groundwaters extracted in northeastern Sicily can be used for domestic purposes and human consumption without taking remedial actions.

It is important to understand that all the data were collected within a restricted amount of time, providing only an instantaneous photograph that is valid only for a very short time span. Future events, such as increased seismicity or powerful earthquakes, may strongly increase the degassing rate by further enhancing the vertical permeability along the crust.

Therefore, the concept of “temporal variation” of radiological parameters becomes a key factor in the field of human health protection, since harmful injections of deep-originated radioactive fluids into the atmosphere could suddenly occur in those areas affected by intense tectonic and seismic activity.

Moreover, performing physical-radiological analyses in other areas of northeastern Sicily together with the deployment of monitoring stations with continuous recording of radiological data should be the future goal in order to improve the health hazard assessment due to natural sources.

Chapter I - Introduction and purposes

This Ph.D. Thesis deals with the study of natural radioactivity in the Peloritani Mountains (northeastern Sicily, southern Apennines of Italy).

The world population and all living organisms on the Earth are constantly exposed to ionizing radiation emitted from natural sources. Radionuclides are atoms characterized by an excess of nuclear energy, which makes them unstable giving rise to decay by emitting dangerous energy and particles.

Natural radiation originates from two distinct sources: terrestrial radionuclides (e.g. ^{235}U , ^{238}U , ^{232}Th , ^{40}K and ^{87}Rb) occurring in the Earth's crust and mantle, and cosmogenic radionuclides generated by the interaction of cosmic rays with the Earth's atmosphere and crust. Interactions between natural radiation with organs and tissues can produce serious health consequences such as cancer, anaemia, necrosis and DNA and RNA modifications. Two components contribute to human exposure from natural radiation: external and internal exposures. External exposure is caused by natural sources located outside the human body whereas internal exposure is provoked by ingestion or inhalation of radionuclides occurring in food, water and air. Exposure from natural sources can occur in both indoor and outdoor environments. Indoor exposure is essentially connected to radiation emitted from building materials, while outdoor exposure is mainly derived from naturally occurring radionuclides of terrestrial origin.

Radon is considered one of the most dangerous sources of ionizing radiation. Radon is a colourless and odourless noble gas occurring as an intermediate product in the ^{238}U , ^{235}U and ^{232}Th decay series. The main isotopes are ^{222}Rn and ^{220}Rn (also known as thoron), generated by the α decay of ^{226}Ra and ^{224}Ra respectively.

Radon inhalation is responsible for around 50% of the annual effective dose received by humans (UNSCEAR, 2000), and in the last 40 years the study of natural radioactivity originated from radon has gained much interest around the scientific community and people in general.

This is due to the fact that several epidemiological studies evidenced the strong relationship between indoor radon exposure and the increase of the risk of lung cancer. For instance, radon was indicated as the primary cause of lung cancer in underground miners in central Europe since the 1950s, and for this reason, it was

classified as a human carcinogen by the IARC (International Agency for Research on Cancer) in 1988 (IARC 1988). Moreover, studies regarding radon-exposed workers in uranium, tin, iron and fluorspar mines in Europe, Asia, Australia and North and South America were conducted in the 1990s and the 2000s (e.g. BEIR VI 1999; Veiga et al., 2004; Grosche et al., 2006; Tomasek et al., 2008) demonstrating that lung cancer rates increased with the increase of the cumulative radon exposure. On the other hand, the studies concerning indoor radon in residential buildings and the incidence of lung cancer in the general population started during the 1980s. Lubin et al. (2004), Darby et al. (2005, 2006) and Krewski et al. (2005, 2006), evidenced that the increase of the risk of lung cancer for general people ranges from 8 to 16% per 100 Bq m⁻³.

According to WHO (2009), radon is the second cause of lung cancer after smoking, provoking between 3 and 14% of all lung cancers. Health risks due to the natural radioactivity from radon are substantially connected to the ingestion of drinking water and to the inhalation of radon deriving from soils and building materials.

Environmental radon levels usually depend on the content of U and Th in soils and rocks as well as on the occurrence or not of ascending gases able to transport radon from the Earth's crust to the Earth's surface (Etiope and Martinelli, 2002). As a result, the presence of high levels of radon is characteristic of active geological areas such as volcanic and seismic ones, where the upward migration of radon-rich gases take places along permeable fault planes and fractures.

In this main framework, I want to highlight that the Peloritani Mountains are characterized by the presence of a poly-metamorphic crystalline basement composed of granitoids, meta-sediments, meta-volcanites and meta-granitic rocks. Those kinds of rocks usually show high concentrations of U, Th and K. Consequently, they could represent a dangerous radiation source. In addition, the Peloritani Mountains constitute the northeastern edge of Sicily, an area affected by a continuous and intense seismic activity certificated by the occurrence, during the last centuries, of a series of destructive historical earthquakes (see Orecchio et al., 2014 and references therein). For those reasons, the Peloritani Mountains could represent a radon-prone area (i.e. a zone where the probability of occurrence of dangerous radon levels is very high).

With those important points in mind, a study regarding the natural radioactivity in northeastern Sicily was conducted by means of a series of radiological measurements including gamma and alpha spectroscopic analyses performed on different types of samples (i.e. crystalline rocks, soil-gases and groundwaters).

It is noteworthy to mention that there are no studies focused on natural radioactivity available in literature for northeastern Sicily. Hence, this research should be considered as a milestone as it reports for the first time radiological data collected in this area.

The main objectives of this Thesis are:

- determining the activity concentration of ^{238}U , ^{232}Th and ^{40}K in crystalline rocks and evaluating the radiological hazards for inhabitants due to the gamma radiation crossing the soil-air interface;
- assessing the potential health hazard originating from the building use of the Peloritani crystalline rocks in terms of indoor radon. This outcome was achieved through the estimation of the ^{222}Rn emanation factor and the ^{222}Rn exhalation rate;
- measuring the ^{222}Rn and ^{220}Rn activity concentration in soils in order to assess the radiological hazard deriving from radon degassing as well as detecting the radon anomalies generated by the active migration of deep-originated fluids along pre-existing geological lineaments;
- calculating the ^{222}Rn activity concentration in groundwaters and evaluating the radiological hazard due to ingestion.

Accordingly, all those indications will ascertain whether northeastern Sicily is an “enhanced natural radiation area” or if radioactivity levels are similar to those of the global averages.

References

BEIR VI: National Research Council. Committee on Health Risks of Exposure to Radon. Health Effects of Exposure to Radon. National Academy Press, Washington D.C.,1999.

S. Darby, D. Hill, A. Auvinen, J.M. Barros-Dios, H. Baysson, F. Bochicchio, H. Deo, R. Falk, F. Forastiere, M. Hakama, I. Heid, L. Kreienbrock, M. Kreuzer, F. Lagarde, I. Makelainen, C. Muirhead, W. Oberaigner, G. Pershagen, A. Ruano-Ravina, E. Ruosteenoja, A.S. Rosario, M.

Tirmache, L. Tomasek, E. Whitley, H.E. Wichmann and R. Doll. Radon in homes and risk of lung cancer: collaborative analysis of individual data from 13 European case-control studies. *British Medical Journal*, **330**(7485), 223-227, 2005.

S. Darby, D. Hill, H. Deo, A. Auvinen, J.M. Barros-Dios, H. Baysson, F. Bochicchio, R. Falk, S. Farchi, A. Figueiras, M. Hakama, I. Heid, I. Hunter, L. Kreienbrock, M. Kreuzer, F. Lagarde, I. Makelainen, C. Muirhead, W. Oberaigner, G. Pershagen, E. Ruosteenoja, A.S. Rosario, M. Tirmache, L. Tomasek, E. Whitley, H.E. Wichmann and R. Doll. Residential radon and lung cancer--detailed results of a collaborative analysis of individual data on 7148 persons with lung cancer and 14,208 persons without lung cancer from 13 epidemiologic studies in Europe. *Scandinavian Journal of Work, Environment and Health*, **32**(Sup 1):1-83, 2006.

G. Etiope and G. Martinelli. Migration of carrier and trace gases in the geosphere: an overview. *Physics of the Earth and Planetary Interiors*, **129**(3-4):185-204, 2002.

B. Grosche, M. Kreuzer, M. Kreishemer, M. Schnelzer and A. Tschense. Lung cancer risk among German male uranium miners: a cohort study, 1946-1998. *British Journal of Cancer*, **95**(9):1280-1287, 2006.

IARC (International Agency for Research on Cancer). Man-made mineral fibres and radon. IARC Monographs on the evaluation of carcinogenic risks to humans, Vol. 43. IARC, Lyon, 1988.

D. Krewski, J.H. Lubin, J.M. Zielinski, M. Alavanja, V.S. Catalan, R.W. Field, J.B. Klotz, E.G. Letourneau, C.F. Lynch, J.L. Lyon, D.P. Sandler, J.B. Schoenberg, D.J. Steck, J.A. Stolwijk, C. Weinber and H.B. Wilcox. Residential radon and risk of lung cancer: a combined analysis of 7 North American case-control studies. *Epidemiology*, **16**(2):137-145, 2005.

D. Krewski, J.H. Lubin, J.M. Zielinski, M. Alavanja, V.S. Catalan, R.W. Field, J.B. Klotz, E.G. Letourneau, C.F. Lynch, J.L. Lyon, D.P. Sandler, J.B. Schoenberg, D.J. Steck, J.A. Stolwijk, C. Weinber and H.B. Wilcox. A combined analysis of North American case-control studies of residential radon and lung cancer. *Journal of Toxicology and Environmental Health*, **69**(7):533-597, 2006.

J.H. Lubin, Z.Y. Wang, J.D. Jr Boice, Z.Y. Xu, W.J. Blot, L. De Wang and R.A. Kleinerman. Risk of lung cancer and residential radon in China: pooled results of two studies. *International Journal of Cancer*, **109**(1):132-137, 2004.

B. Orecchio, D. Presti, C. Totaro and G. Neri. What earthquakes say concerning residual subduction and STEP dynamics in the Calabrian Arc region, south Italy. *Geophysical Journal International*, **199**(3): 1929–1942, 2014.

L. Tomasek, A. Rogel, M. Tirmache, N. Mitton and D. Laurier. Lung cancer in French and Czech uranium miners: radon associated risk at low exposure rates and modifying effects of time since exposure and age at exposure.

Radiation Research, **169**(2):125-137, 2008.

UNSCEAR (United Nations Scientific Committee on the Effects of Atomic Radiations). *Source and Effects of Ionizing Radiation*. United Nations, New York, 2000.

L. H. Veiga, V. Melo, F. Koifman and E.C.S. Amaral. High radon exposure in a Brazilian underground coal mine. *Journal of Radiological Protection*, **24**:295-305, 2004.

WHO (World Health Organization). *Handbook on indoor Radon: a public health perspective*. WHO, Geneva, 2009.

Chapter II - Natural radioactivity

2.1 History and types of radioactivity

Radioactivity was discovered by Henry Becquerel in 1896 during a series of physical experiments focused on the study of phosphorescence. He detected the radioactive particles emitted from uranium-bearing salts observing that those materials were able to cause the blackening of a photographic plate in absence of a source of light. Becquerel concluded that an undiscovered type of radiation had to be responsible for that phenomenon.

Later, Pierre and Marie Curie identified the radioactive elements thorium, polonium and radium. A large quantity of pitchblende (currently known as uraninite), a radioactive uranium-rich mineral extracted at Jachimov (Czechoslovakia), was necessary to isolate radium in pure form. Radioactive materials became popular for their curative effect against tumours at that time, whereas the dangerous effect of radiation on the human body were not known.

Actually, the term “radioactivity” was coined by Pierre and Maria Curie, who received the 1903 Nobel Prize in Physics along with Henry Becquerel. In 1911, Maria Curie won also the Nobel Prize in Chemistry.

Radioactivity is a complex process characterizing the Earth planet since its formation, which occurred around 4.6 Ga. Approximately half of the current Earth’s internal heat budget originates from the radioactive decay of radioisotopes.

There are two types of radioactivity, natural and artificial:

- natural radioactivity develops from solid, liquid and gaseous sources such as rocks, soils, oceans and volcanic gases. It takes place spontaneously, and generally, it cannot be controlled.
- artificial radioactivity is determined by human activities involving radioactive materials. For instance, it occurs during nuclear energy production and for medical purposes (e.g. radiotherapy). It is induced by “man-made” methods, often bombarding atoms with fast-moving particles.

During the last forty years, the term radioactivity has tragically become famous among people because of the Chernobyl and Fukushima nuclear accidents.

The Chernobyl disaster occurred in 1986 at one of the four reactors in the Chernobyl nuclear power plant (Ukraine). Some imperfection in the reactor design, along with a

series of human mistakes caused a steam explosion that dismantled the core and the roof of the no. 4 reactor. A great amount of radioactive material was released in the atmosphere. Those substances were transported by winds across all European countries, especially in Belarus, Russia, Estonia, Finland, Sweden and Austria. In 2001, a dreadful nuclear accident occurred at the Fukushima-Daiichi nuclear power plant (Japan). It was provoked by a tsunami generated by an earthquake that occurred along the eastern coast of Japan. The tsunami wave swept over the energy production site damaging the reactors cooling systems. A huge amount of radioactive substances was released into the atmosphere and into the Pacific Ocean.

2.2 Isotopes and decay types

Atoms are formed by a nucleus and by one or more negative electric charge particles called electrons, bound to the nucleus by electromagnetic forces. The nucleus is composed of a number of positive electric charge particles known as protons, and zero or more particles with no electric charge called neutrons. As regards atoms, we can define the “atomic number” (Z) as the number of protons, and the “mass number” (A) as the sum of the number of protons and neutrons.

Moreover, a species of atom characterized by a series of well-defined nuclear properties, such as a specific energy state or a certain number of protons and neutrons, can be defined as a nuclide.

Isotopes are atoms of the same chemical elements having equal Z and different A , and then they differ only for the number of neutrons (N).

Isotopes can be stable or unstable. Unstable isotopes are generally called radionuclides or radioisotopes. Within the nucleus, protons and neutrons are bound by nuclear forces. The total number of neutrons (N), with respect to the number of protons (Z), is fundamental to keep stable the nucleus. Accordingly, three different scenarios take place: i) isotopes with Z ranging from 1 to 20 are stable with $Z=N$; ii) isotopes with Z values between 20 and 82 are stable with $Z<N$; iii) all isotopes with $Z>82$ are unstable (Fig. 1).

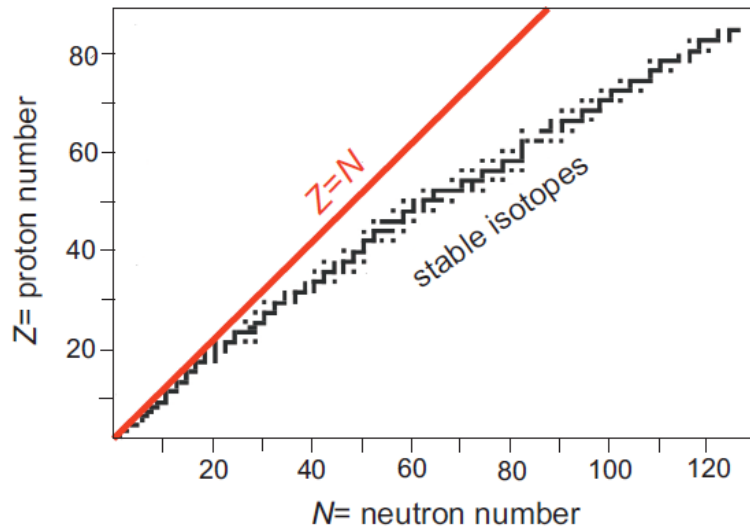


Figure 1. Stable isotopes having $Z= 1-20$ are characterized by an equal number of protons and neutrons ($Z=N$); stable isotopes with a number of protons between 20 and 82 have more neutrons than protons ($Z < N$); all elements with $Z > 82$ are unstable (from Romano et al., 2021).

Radioactive decay is the process in which unstable isotopes emit particles and energy with the aim of reaching a stable nuclear configuration. Concerning this process, characterized by the emission of particles and energy, a radionuclide (called “parent”) transform into a new nuclide (called “daughter”).

The three main modes of decay are alpha, beta and gamma decay (Fig. 2):

- alpha decay (α decay): a parent radionuclide emits an α particle composed of two protons and two neutrons; then, Z and A values of the daughter nuclide will be reduced by 2 and 4 respectively (Fig. 2A).
- beta decay: there are two different types of beta decay, beta- (β^-) and beta+ (β^+), depending on the nature of the beta particle emitted from the decaying radioisotope. A β^- particle is a fast energetic electron, emitted from a nucleus when a neutron transforms into a proton (Fig. 2B), whereas a β^+ particle is a positron emitted because of the conversion of a proton into a neutron (Fig. 2C). The Z value of the daughter nuclides increases by 1 in β^- decay, and decreases by 1 in β^+ decay.
- gamma decay: an excited state radionuclide is converted into a lower energy state through the emission of gamma rays (Fig. 2D).

In the alpha and beta decays, a parent radionuclide transforms into a daughter nuclide with a different number of protons and thereby into a different chemical element, whereas in the gamma decay the chemical element does not change after the gamma rays emission.

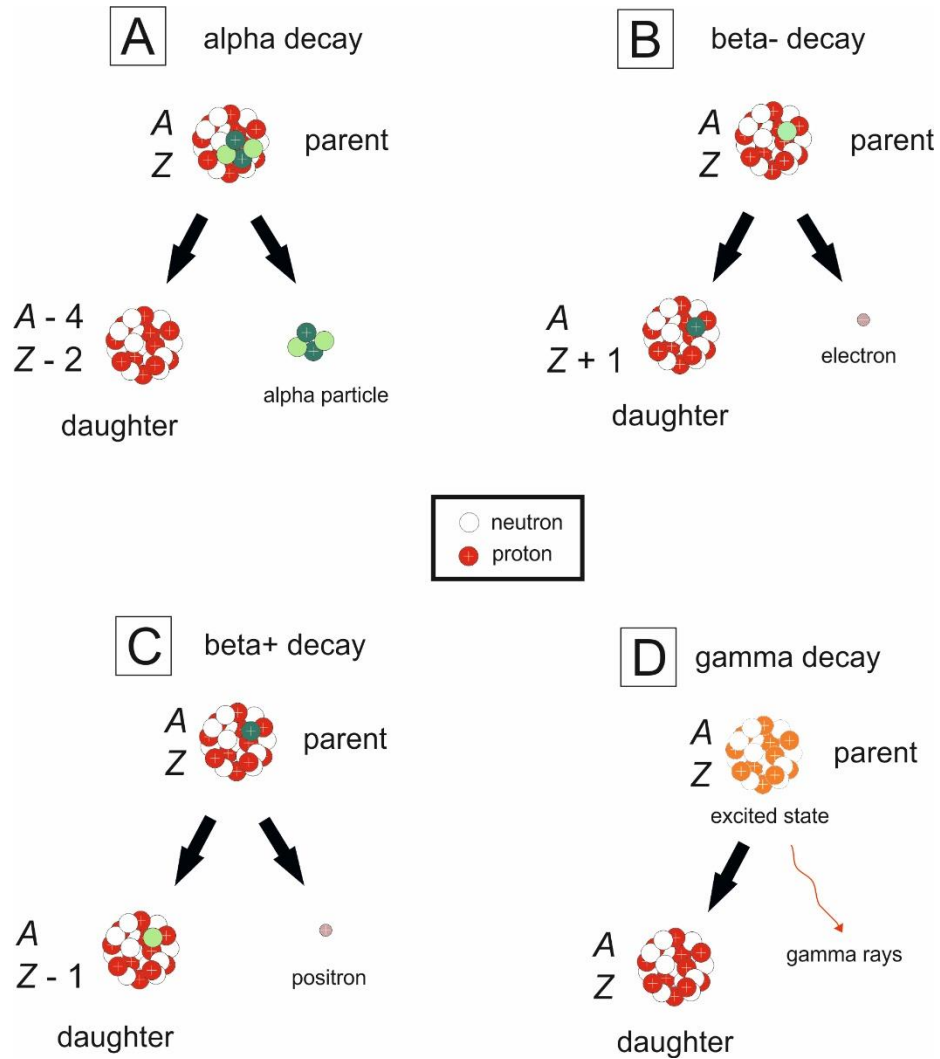


Figure 2. A “parent” radionuclide transform into a “daughter” nuclide by emitting particles and energy. Here, the main types of radioactive decay are illustrated: A) alpha decay: a radionuclide loses an alpha particle composed of two neutrons (pale green) and two protons (dark green) transforming into a daughter nuclide reduced by four nucleons; B) beta- decay (β^-): a neutron (pale green) transforms into a proton (dark green) and, during the transmutation, a high-energy electron is emitted; C) beta+ decay (β^+): a proton (dark green) transforms into a neutron (pale green) with the emission of a positron; D) gamma decay: an excited state radionuclide reaches a lower energy state by emitting gamma rays (from Romano et al., 2021).

2.3 Decay energy

The total energy released by radioactive decay, considering the conservation of energy between the initial and final energy of the process, can be generally expressed as the Q value, which represents the amount of energy absorbed or released by a reaction.

For a given radioactive decay, the Q value is:

$$Q = T_f - T_i = (m_i - m_f)c^2 \quad [1]$$

where T_f and T_i are the final and initial kinetic energies of the final (m_f) and initial (m_i) rest mass, respectively.

The decay will occur spontaneously only if $Q > 0$.

2.4 Sources of natural radioactivity

The main sources of natural radioactivity are: i) radionuclides produced by cosmic rays (the so-called cosmogenic radionuclides); ii) primordial radionuclides incorporated into the Earth at the time of its formation.

Primordial and cosmogenic radionuclides occur in all natural media, thereby in rocks soils, oceans, groundwaters and air. Moreover, radionuclides can be physically transported by winds, water and other natural forces. For this reason, we can affirm that the population is constantly exposed to natural radioactivity.

2.4.1 Cosmogenic radionuclides

Primary cosmic rays come from the outer space and from the sun. This kind of radiation is mainly composed of protons and α particles with minor photons, neutrinos, positrons, light nuclei and electrons.

Primary radiation has high energy ($\sim 10^9$ - 10^{20} eV); it enters the Earth's atmosphere generating a cascade of secondary cosmic rays that are able to reach the Earth's surface. Secondary cosmic rays consist of electrons, photons, protons, mesons, neutrons, gamma rays and muons.

Cosmic ray-produced isotopes are continuously generated in the atmosphere and in the Earth's crust because of the interactions of cosmic radiation with Earth's constituents. Cosmogenic radionuclides generated in the atmosphere are brought to the Earth's surface by rainfall. A list of atmospheric cosmic ray-produced isotopes

is reported in Table 1. Only ^{14}C , ^3H , ^{22}Na and ^{24}Na produce a non-negligible contribution to the natural background radiation dose.

Table 1. Half-lives of atmospheric cosmic-rays produced radionuclides (Eisenbud, 1997).

| Radionuclide | Half-life |
|--------------------------|-----------------------|
| ^{10}Be | $1.6 \cdot 10^6$ y |
| ^{26}Al | $7.2 \cdot 10^{-5}$ y |
| ^{36}Cl | $3 \cdot 10^{-5}$ y |
| ^{81}Kr | $2.3 \cdot 10^{-5}$ y |
| ^{14}C | 5730 y |
| ^{32}Si | 650 y |
| ^{39}Ar | 269 y |
| ^3H | 12.33 y |
| ^{22}Na | 2.62 y |
| ^{35}S | 87.4 d |
| ^7Be | 53.3 d |
| ^{37}Ar | 35 d |
| ^{33}P | 25.3 d |
| ^{32}P | 14.28 d |
| ^{38}Mg | 21 h |
| ^{24}Na | 15 h |
| ^{38}S | 2.83 h |
| ^{31}S | 2.62 h |
| ^{18}F | 109.8 m |
| ^{39}Cl | 56.2 m |
| ^{38}Cl | 37.29 m |
| $^{34\text{m}}\text{Cl}$ | 31.99 m |

2.4.2 Primordial radionuclides

Primordial radionuclides (also called terrestrial radionuclides) have existed since before the Earth was formed. They show half-lives comparable to the age of the Earth (4.58×10^9 years), and for this reason, they have not completely decayed yet.

These radionuclides are very abundant within the Earth's crust. Recently, the occurrence of a great amount of terrestrial radioisotopes was identified also within the Earth's mantle (Borexino Collaboration, 2020). Around half of the Earth's internal heat budget is due to the radiogenic heat released from radioactive decay, particularly from ^{238}U , ^{232}Th , ^{235}U and ^{40}K decay (Korenaga, 2011)

Primordial radionuclides are classified as non-series and series radionuclides, depending on the decay pathway (see Ojovan and Lee, 2014).

Non-series primordial radionuclides do not belong to any decay series, and some of them are listed in Table 2. Among these nuclides, ^{40}K and ^{87}Rb are the most abundant, and their average concentration in crustal rocks is 0.6 and 0.07 Bq g^{-1} respectively (Ojovan and Lee, 2014). One of the most used methods to determine the

age of rocks is the so-called K-Ar method. It relies on the radiological characteristic of ^{40}K , which decays to ^{40}Ar . The decay product is able to escape the system as long as the rock is molten, but starts to accumulate when the rock solidifies or recrystallizes. Time since crystallization or recrystallization is obtained by measuring the ratio of the ^{40}Ar accumulated against the ^{40}K remaining.

Table 2. List of the most abundant non-series primordial radionuclides lighter than Lead (Eisenbud, 1997).

| Radionuclide | Half-life |
|---------------------|------------------------|
| ^{40}K | $1.26 \cdot 10^9$ y |
| ^{50}V | $6 \cdot 10^{15}$ y |
| ^{87}Rb | $4.8 \cdot 10^{10}$ y |
| ^{113}Cd | $>1.3 \cdot 10^{15}$ y |
| ^{115}In | $6 \cdot 10^{14}$ y |
| ^{123}Te | $1.2 \cdot 10^{13}$ y |
| ^{138}La | $1.12 \cdot 10^{11}$ y |
| ^{142}Ce | $>5 \cdot 10^{16}$ y |
| ^{144}Nd | $2.4 \cdot 10^{15}$ y |
| ^{147}Sm | $1.05 \cdot 10^{11}$ y |
| ^{152}Gd | $1.1 \cdot 10^{14}$ y |
| ^{147}Hf | $2.0 \cdot 10^{15}$ y |
| ^{176}Lu | $2.2 \cdot 10^{10}$ y |
| ^{187}Re | $4.3 \cdot 10^{10}$ y |
| ^{190}Pt | $6.9 \cdot 10^{11}$ y |
| ^{192}Pt | $1 \cdot 10^{15}$ y |
| ^{209}Bi | $>2 \cdot 10^{18}$ y |

Series primordial radionuclides, thereby ^{238}U , ^{232}Th and ^{235}U , are the parent radionuclides for the three decay series (or decay chains), occurring in nature (Fig. 3). Within a decay series, radioisotopes decay into unstable nuclides, which in turn decay aiming for reaching a stable state. These processes generate a sequential series of decays. The series ends when a stable progeny forms. All three series end with the generation of a lead isotope. Examples of radionuclides occurring in the decay chains are isotopes of radium, radon and polonium.

The ^{238}U , ^{235}U and ^{232}Th decay series are commonly called the uranium (or radium), actinium and thorium series, respectively (Fig. 3). However, their abundances in nature are extremely different. Since the natural abundance of ^{238}U is 99.3% and that of ^{235}U is 0.7%, the actinium series is very rare in nature.

The ^{238}U , ^{235}U and ^{232}Th decay series are commonly called the $4n + 2$, $4n + 3$ and $4n$ series, respectively. This is due to the fact that when the mass numbers of isotopes is

divided by 4, the ^{238}U and ^{235}U series isotopes leaves a remainder of 2 and 3, respectively, whereas the ^{232}Th series isotopes are evenly divisible.

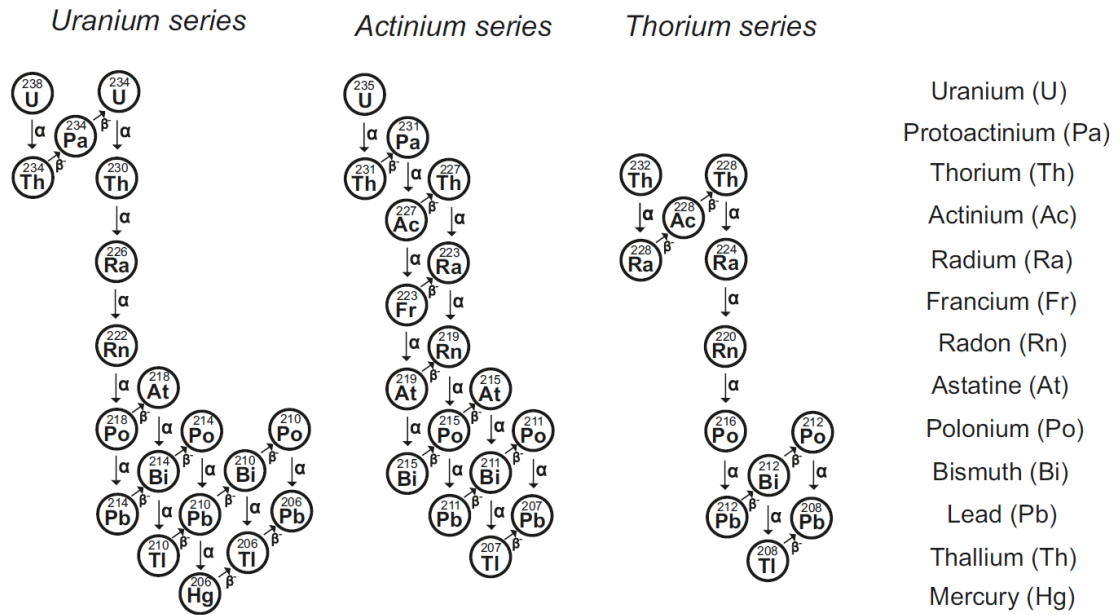


Figure 3. Decay chains of ^{238}U (Uranium series), ^{235}U (Actinium series) and ^{232}Th (Thorium series). The decay chains are characterized by a subsequential series of α and β^- decays. All three series end with the generation of a stable Pb isotope. Full names of elements are on the right side of the figure. The image is modified from the decay chains at https://en.wikipedia.org/wiki/Decay_chain.

2.5 Radioactive decay law

To express the statistical behaviour of a large number of nuclides, we use the law of radioactive decay. The decrease of a certain number of atoms due to the radioactive decay is proportional to the number of atoms, and occurs at a rate. This process is exponential in time and is generally described by the following differential equation:

$$dN/dt = -\lambda N \quad [2]$$

where N is the quantity, t is time and λ is the exponential decay constant. The equation indicates that the probability per unit of time, that a certain nucleus will decay, is constant. Its solution is:

$$N(t) = N_0 e^{-\lambda t} \quad [3]$$

where $N(t)$ is the quantity at time t and N_0 is the initial quantity (at time $t = 0$).

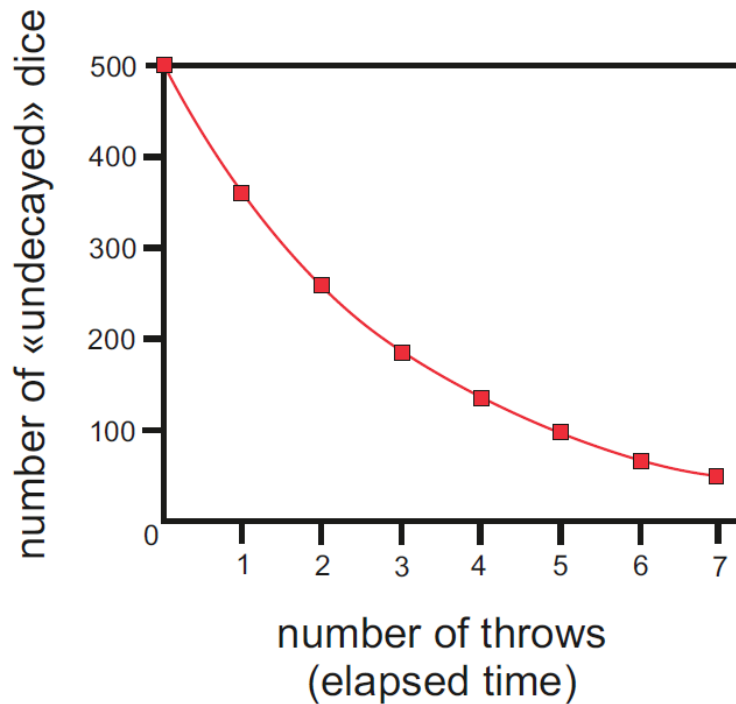


Figure 4. The “radioactive dice” experiment. A number of dice are thrown simultaneously; all dice showing the same number are deemed to have decayed as radioactive nuclei, and then they are removed and put aside. The remaining “undecayed” dice are counted and thrown again. This process is repeated for a number of throws, and results in a reduction in the number of “undecayed” dice as the number of throws increases. The curve of the undecayed dice, against the total number of throws, shows an exponential trend (from Romano et al., 2021)

This concept can be easily described with a simple experiment; the so-called “radioactive dice”, where a number of dice, symbolizing a number of radionuclides, are thrown simultaneously. All dice showing the same number, for instance, the number 4, are supposed to have “decayed”, and then, they are removed from the group of “undecayed” dice. The remaining “undecayed” dice are counted and thrown again. Those showing the number 4 are removed, whereas the “undecayed” dice are counted and thrown again. Continuing with the experiment, after a number of throws we can observe that the curve of the undecayed dice against the number of throws displays an exponential trend (Fig. 4), which is represented by equation 3.

The decay constant, and then the decay rate, varies among different radionuclides. Therefore, to express the decay rate of a certain radionuclide two parameters are

commonly used, the mean lifetime and the half-life, both depending on the decay constant. The mean lifetime (τ) represents the average length of time that an atom can live until decay:

$$\tau = 1/\lambda \quad [4]$$

The half-life ($t_{1/2}$) is the time required for a certain number of radionuclides to reach one half of the initial quantity:

$$t_{1/2} = \ln 2 / \lambda = \tau \ln 2 \quad [5]$$

A decay chain is characterized by a subsequential series of decays. Radioisotopes decay into unstable nuclides, which in turn decay themselves until a stable progeny forms. The number of atoms of each nuclide in the chain can be calculated through Bateman's equations.

In order to simplify the approach, we can consider one nuclide A decaying into another B , and then B decays into C , which is stable. The number of atoms of A , B , C can be calculated by solving three differential equations:

$$dN_A/dt = -\lambda_A N_A \quad [6]$$

$$dN_B/dt = \lambda_A N_A - \lambda_B N_B \quad [7]$$

$$dN_C/dt = \lambda_B N_B \quad [8]$$

the solution of equation 6 is the equation 3, whereas the solution of equations 7 and 8, if the initial number of atoms of B and C is 0, are:

$$N_B(t) = \lambda_A / (\lambda_B - \lambda_A) * N_{A0} (e^{-\lambda_A t} - e^{-\lambda_B t}) \quad [9]$$

and

$$N_C(t) = N_{A0} (1 - \lambda_A / (\lambda_B - \lambda_A) * e^{-\lambda_B t} - \lambda_B / (\lambda_B - \lambda_A) * e^{-\lambda_A t}) \quad [10]$$

, respectively.

2.6 Activity and specific activity

The radioactivity is measured in terms of activity (A), which represents the number of disintegration per unit of time. As following expressed, activity depends on the constant decay of the radionuclide:

$$-dN/dt = \lambda N = A \quad [11]$$

The unit of measure for A used in the I.S. since 1975 is the Becquerel (Bq), which corresponds to 1 disintegration per second.

The former units of the measure were the Curie (Ci) and the Rutherford (Rd), defined in 1910 and 1948, respectively. Their quantities with respect to the Becquerel are:

$$1 \text{ Rd} = 10^6 \text{ Bq}$$

$$1 \text{ Ci} = 3.7 \cdot 10^{10} \text{ Bq}$$

The radioactivity of materials is defined in terms of specific activity, also known as activity concentration. The specific activity indicates the activity of a certain radionuclide considering the total amount of matter.

For solids materials, the specific activity is usually expressed in Bq kg⁻¹, whereas for gases and liquids is generally given in Bq L⁻¹ or Bq m⁻³.

2.7 Secular Equilibrium

We already reported that the decay constant varies among different radionuclides. Then, considering a portion of decay chain in which a parent radionuclide *A* decays into a daughter radionuclide *B*, three different situations can take place depending on the decay constant of *A* and *B* (Fig. 5):

- if $\lambda_A \ll \lambda_B$ radionuclides approach the secular equilibrium: the daughter activity becomes equal to the parent activity within ~6 half-lives of the decay product (Fig. 5A). It can be demonstrated by using equation 9 and considering $\lambda_B - \lambda_A \approx \lambda_B$ and $e^{-\lambda_A t} \gg e^{-\lambda_B t}$. Therefore we have:

$$N_B(t) = \lambda_A / (\lambda_B) * N_{A0}(e^{-\lambda_A t}) \quad [12]$$

comparing equations 12 and 3 one gets:

$$N_B(t) = \lambda_A / (\lambda_B) * N_A(t)$$

$$N_B(t)\lambda_B = N_A(t)\lambda_A$$

and according to equation 11 we obtain:

$$A_B(t) = A_A(t) \quad [13]$$

- if $\lambda_A < \lambda_B$ the transient equilibrium occurs: the parent activity decays slowly so the daughter activity will increase reaching a maximum and after that starts to decrease; the long-time behaviour of the daughter follows that of the parent (Fig. 5B);
- if $\lambda_A > \lambda_B$ the situation is known as non-equilibrium (Fig. 5C);

The ²²⁶Ra decaying into ²²²Rn represent an example of secular equilibrium, which is achieved in ~21 days (~6 times of the *t*_{1/2} of ²²²Rn).

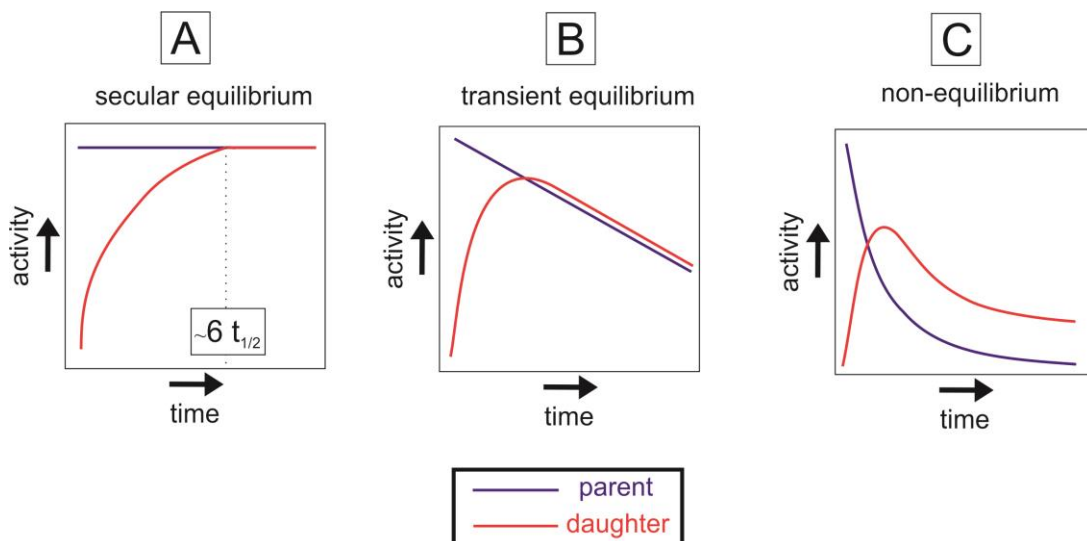


Figure 5. Representation of secular equilibrium (A), transient equilibrium (B) and non-equilibrium (C).

2.8 Radon

Radon is a colourless and odourless radioactive noble gas ($Z=86$). Moreover, is considered the greatest contributor to indoor radioactivity. In nature, the two main radon isotopes are the ^{222}Rn and the ^{220}Rn (also known as thoron).

^{222}Rn , having a half-life of 3.8 days, belongs to the ^{238}U decay chain, and derives from the ^{226}Ra alpha decay (Fig. 4 and 6). On the other hand, ^{220}Rn occurs as a product of the alpha decay of ^{224}Ra in the ^{232}Th decay series (Fig. 4 and 5), and is characterized by a half-life of 55 seconds.

The radon progeny is composed of radioactive isotopes of bismuth, polonium and lead (Fig. 6). Their radioactive decay produces alpha, beta and gamma radiation, which can be very dangerous since these heavy metals can be easily fixed to aerosol particles in the atmosphere.

Radon is released in the atmosphere from solid materials (i.e. soils, rocks and building materials), which are responsible for a permanent flux of radon into the air because of the continuous generation of radon from radium decay. In certain conditions, radon can be transported far away from its source by carrier gases and groundwaters. Radon is a carcinogenic gas, and this concept is currently accepted around the scientific community. Nevertheless, in certain thermal localities is still

allowed, in the name of unknown healing properties, to inhale radon during sessions of the so-called radon therapy.

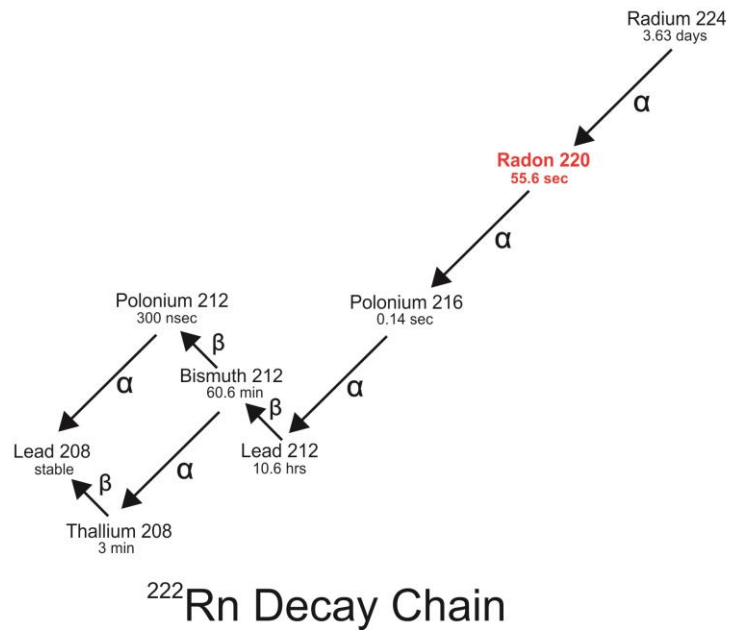
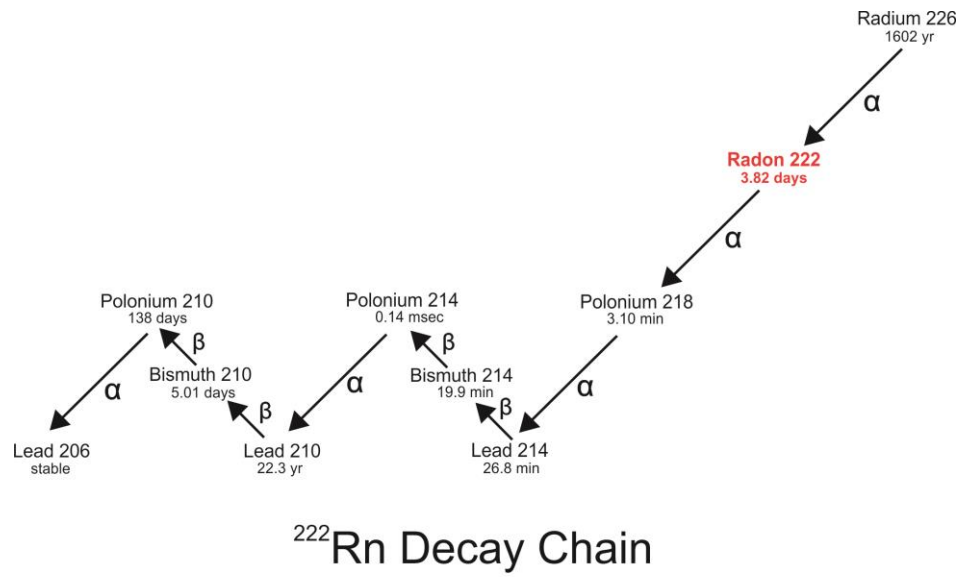


Figure 6. ^{222}Rn and ^{220}Rn (thoron) are generated by the radioactive decay of ^{226}Ra and ^{224}Ra respectively (modified from RAD7 Durrige Manual).

References

Borexino Collaboration. Comprehensive geoneutrino analysis with Borexino. *Physical Review D*, **101**, Article Number 012009, 2020

Durridge Company. RAD 7, electronic radon detector user manual. 2018.

M. Eisenbud and T. Gesell. *Environmental Radioactivity*. Academic Press, London, 656, 1997.

J. Korenaga. Earth's heat budget: Clairvoyant geoneutrinos. *Nature Geoscience* **4**(9):581-582, 2011.

M.I. Ojovan and W.E. Lee. *An Introduction to Nuclear Waste Immobilisation (Second Edition)*. Elsevier, Amsterdam, 376, 2014.

D. Romano, G. Sabatino, M. Di Bella, F. Italiano, M. T. Caccamo, A. Tripodo and S. Magazu. Natural radioactivity and radiological hazard for humans: A simple introduction for newbies and students. New perspectives and innovative teaching methods. *Atti Accademia Peloritana dei Pericolanti, Cl. Sci. Fis. Mat. Nat.*, **99**: No. S1, A39, 2021.

Chapter III - The study area

3.1. Physiographic and geological features

The study area is represented by the northeastern edge of Sicily, dominated by the NE-SW trending Peloritani Mountains (Fig. 7). This area, having a surface of around 1100 km², is bordered on the north and on the south by the Tyrrhenian and Ionian Seas, respectively. The Peloritani Mountains ridge runs along northeastern Sicily; it extends for around 60 km from Capo Peloro to the Nebrodi Mountains and the Alcantara Valley (Fig. 7). The highest peaks are the “Montagna” Grande (1374 m.b.s.l.) and the “Rocca” of Novara (1340 m.b.s.l.).

The Tyrrhenian flank of the Peloritani Mountains shows the presence of a large alluvial plain (i.e. the Barcellona-Milazzo plain), dominated by a series of streams that during the Quaternary age have transported a great amount of sediments from

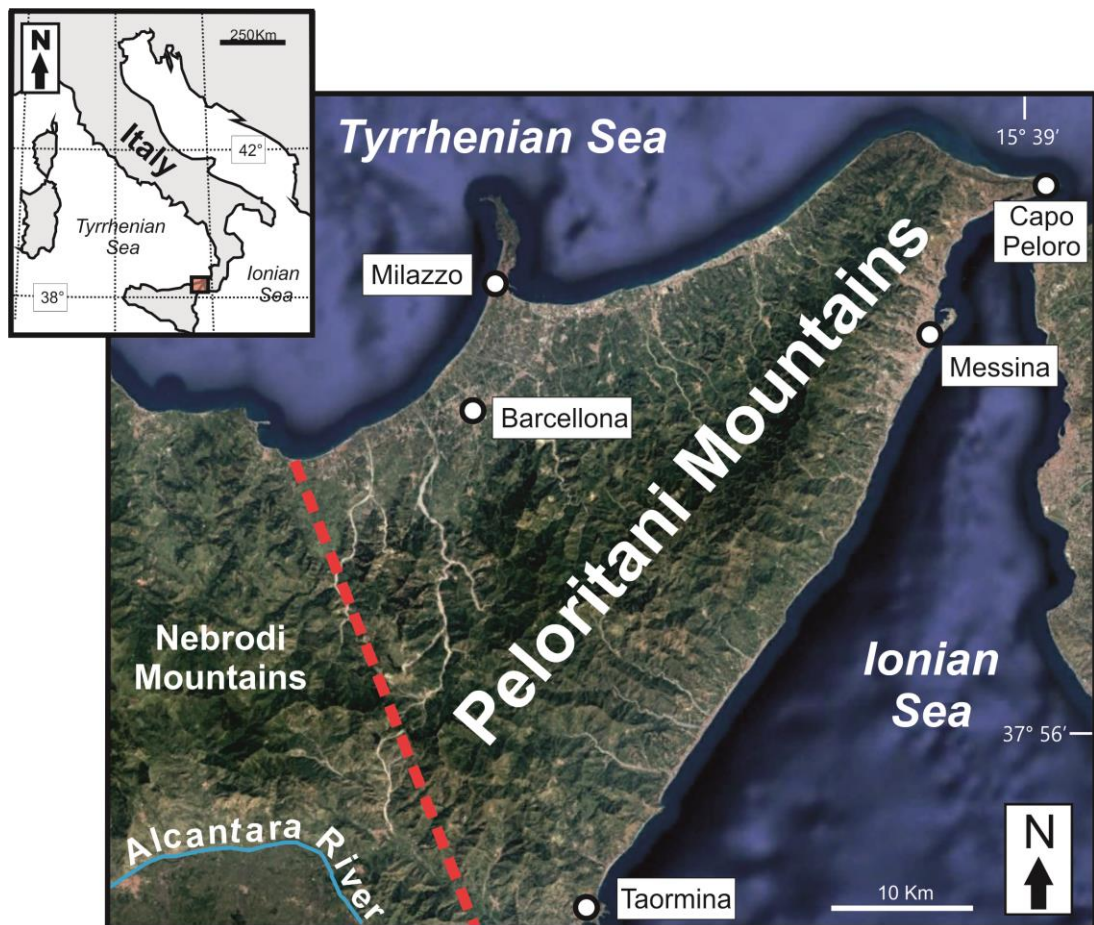


Figure 7. The study area is represented by the Peloritani Mountains, constituting the northeastern termination of Sicily. Satellite images are modified from Google Earth.

the Peloritani ridge to the coastline. On the other hand, the Ionian side does not display any alluvial plain and it is characterized by high and steep escarpments.

Geomorphic features depend on the mechanical and physical properties of outcropping rocks. Therefore, steep slopes, which are dominated by mass wasting processes, occur when high-grade metamorphites and limestones crop out, whereas low-relief landscapes are present in correspondence with terrigenous sediments and low-grade metamorphic rocks. The drainage network shows that streams of both Tyrrhenian and Ionian margins of northeastern Sicily are arranged in subparallel elongate watersheds.

The Peloritani Mountains are framed in the main context of the still ongoing Eurasia-Africa convergence, culminated with the continental collision between the Eurasian and African plates after the closure of the Alpine Tethys (i.e. the oceanic branch separating the two tectonic plates). This process is called Alpine Orogeny and generated the Alps, the Apennines and the Mountain Belts of Sicily.

Sicily is geologically described as a multilayer pile of four distinct structural domains (*e.g.* Lentini et al., 1990, 1996, 2000, 2006; Lentini and Carbone, 2014).

From the top the bottom, the multiplayer pile includes:

- the Peloritani Mountains, which constitute the southernmost portion of the Calabria-Peloritani Orogen (CPO). They are composed of a series of continental units including a metamorphic basement sometimes overlaid by a Meso-Cenozoic sedimentary cover;
- the Maghrebian Chain, consisting of “basinal” and “shallow water” sedimentary tectonic Units belonging to the African paleomargin;
- the External Thrust System, representing the deformed foreland area ;
- the Hyblean Plateau, which is the undeformed foreland of the Sicilian Alpine chain.

3.2. The Calabria-Peloritani Orogen (CPO)

From a physiographic point of view, the CPO is divided into a northern sector (including the Sila Massif and the Catena Costiera) and a southern sector (represented by the Serre and the Aspromonte Massifs in Calabria and the Peloritani Mountains in northeastern Sicily).

Peloritani Mountains

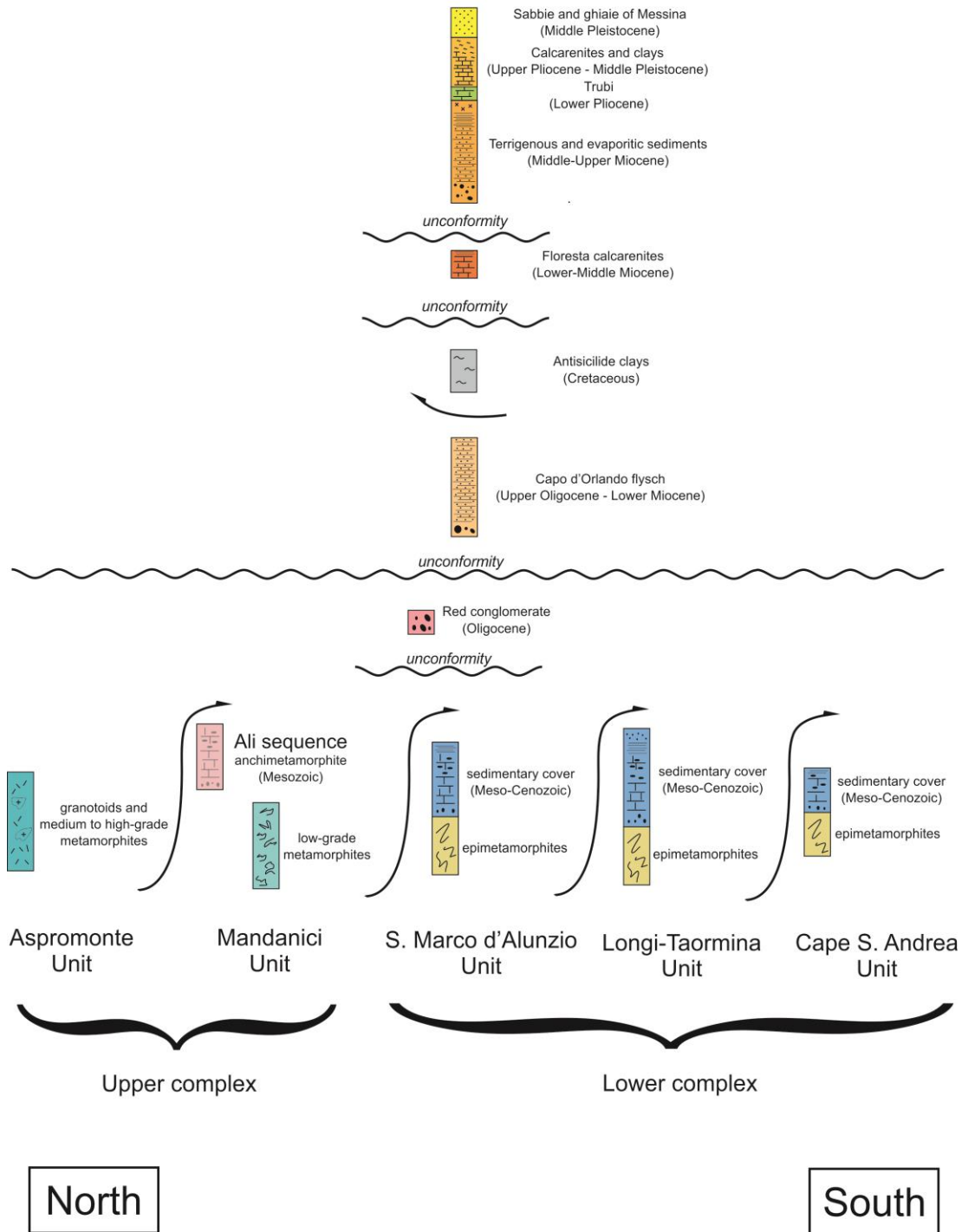


Figure 8. Schematic representation of the relationships occurring among the various tectonic Units of the Peloritani Mountains.

Concerning the geological evolution of the CPO, uncertainty still persists around scientists after decades of studies. Currently, three different hypotheses can explain the geometry of the different geological units outcropping in Calabria and Sicily. The CPO was alternatively considered as: i) entirely deriving from the Eurasian margin of the Mesozoic Alpine Tethys (Ogniben, 1973; Bouillin, 1984; Knott, 1987; Dietrich, 1988; Dewey et al., 1989; Thomson, 1998); ii) the northernmost portion of the African plate (Haccard et al., 1972; Alvarez et al., 1974; Amodio-Morelli et al., 1976; Scandone, 1979; Bonardi et al., 1982; 1993); iii) deriving from a micro-plate (i.e. Meso-Mediterranean plate) interposed between the Eurasian and the African plates (Guerrera et al., 1993; Cello et al., 1996; Perrone, 1996; Critelli and Le Pera, 1998).

The Peloritani Mountains are composed of different continental units forming a south-verging nappe system. These units are characterized by distinct tectono-metamorphic features, and they are divided into an upper and a lower complex (see Cirrincione et al., 2015 and references therein). The continental units are overlaid by syn and post-orogenic sedimentary sequences (Lentini and Carbone, 2014 and references therein).

The stratigraphic and geometrical scheme of the relationships among the Peloritani Units is depicted in Figure 8, whereas the geological-structural map of the Peloritani Mountains is instead represented in Figure 9.

The upper complex, outcropping in the northern sector of the Peloritani Mountains, (Fig. 8 and 9) is composed of the Aspromonte and the Mandanici metamorphic Units, which are separated by a regional thrust surface (Aspromonte basal thrust; Catalano et al., 2017).

The Aspromonte Unit is the highest tectono-metamorphic unit of the Peloritani Belt. This unit is composed of fine-grained paragneiss, orthogneiss and migmatitic paragneisses with minor amphibolite gneisses and marbles. All rocks show a Variscan (300-340 Ma; De Gregorio et al., 2003; Bonardi et al., 2008) amphibolite facies metamorphism with P-T estimations in the range of ~ 0.5 GPa at ~ 550-680 °C (Ioppolo and Puglisi, 1988; Rotolo and De Fazio, 2001).

SHRIMP U-Pb age determinations performed by Williams et al. (2012) and Fiannacca et al. (2013), indicated that a large portion of the Aspromonte Unit formed during the latest stages of the Pan-African Orogeny (~ 550 Ma).

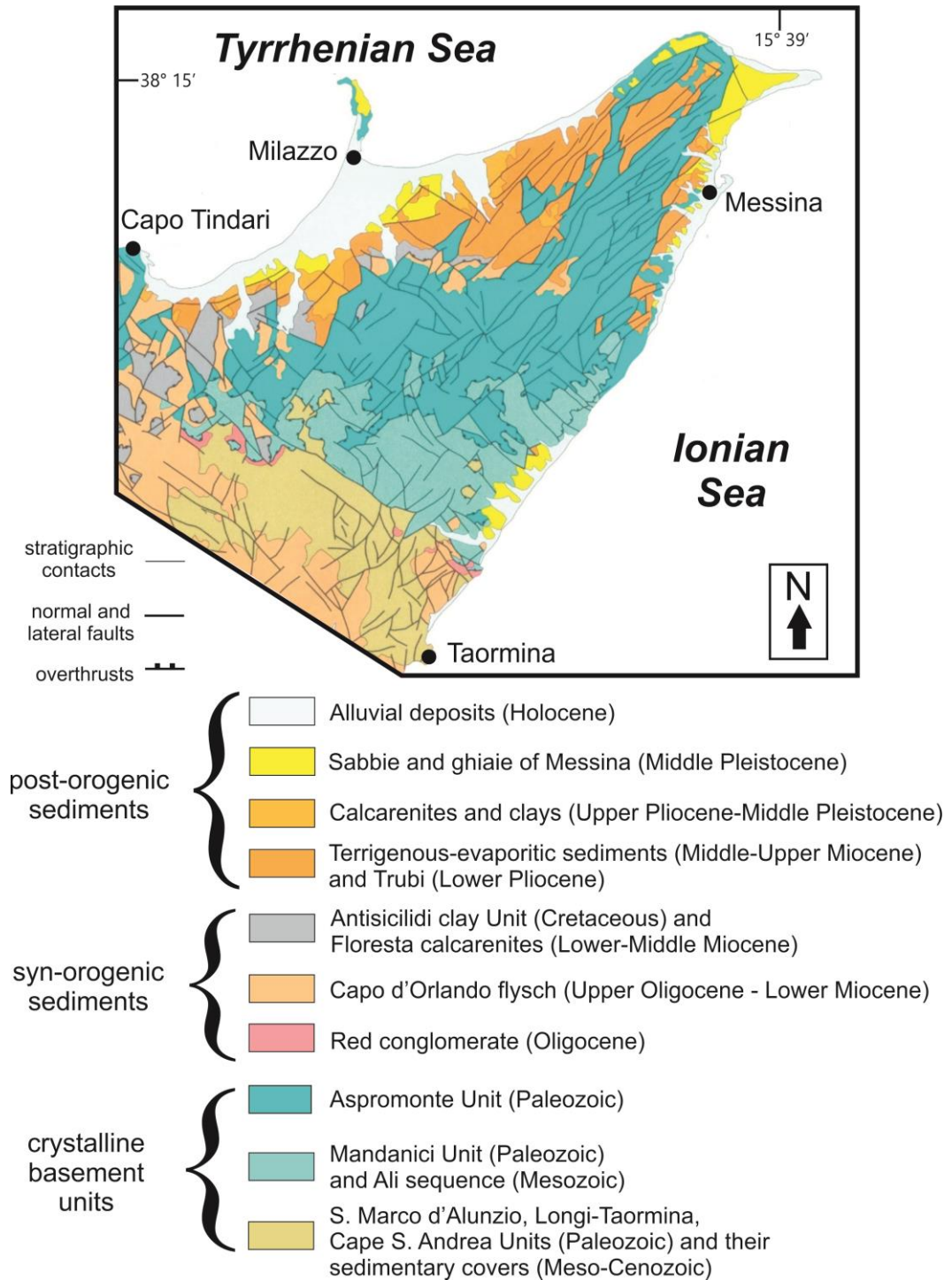


Figure 9. Geological structure map of the easternmost part of Sicily (modified from Lentini et al. 2000).

Late Variscan igneous rocks, dated from 315 Ma (Fiannacca et al., 2008) to 290 Ma (Rottura et al., 1990), intruded the high-grade metamorphic rocks of the Aspromonte Unit, generating dykes and small plutons (D'Amico, 1979; D'Amico et al., 1982; Rottura et al., 1993; Fiannacca et al., 2005; 2008).

The Mandanici Unit is composed of medium to low-grade metamorphites; phyllites with minor meta-volcanics and meta-carbonates are the most common rocks within this tectonic unit. The Mandanici metamorphic rocks are characterized by a greenschist to lower amphibolite Variscan metamorphism. Interposed between the Aspromonte and the Mandanici Units, an extremely tectonized Mesozoic sedimentary sequence (i.e. the Ali Sequence) occurs (Fig. 8). These Mesozoic rocks exhibit a weak Alpine metamorphism (anchizone facies conditions). The Alpine metamorphic event, locally involving also the Mandanici and the Aspromonte Units, is dated ~ 26 Ma (Atzori et al., 1994). The Ali sequence was interpreted as the Mesozoic sedimentary cover of the Mandanici Unit by Pezzino et al. (2008) and Cirrincione et al. (2012).

The lower complex, entirely outcropping in the southern sector of the Peloritani Mountains (Fig. 9), is made up of three similar tectonic Units (Lentini and Vezzani, 1978): the St. Marco d'Alunzio, Longi-Taormina and Capo St. Andrea Units. All three tectonic Units include a metamorphic basement affected exclusively by a Variscan sub-greenschist facies metamorphism ($T \leq 350$ °C, $P \geq 0.2$ GPa; Atzori, 1970; Atzori and Ferla, 1992), composed of metamorphosed fine-grained sedimentary rocks. Sometimes, the epimetamorphites of the Longi-Taormina Unit are interbedded by felsic porphyroids and meta-volcanic rocks with mafic to intermediate compositions (Pezzino, 1982; Acquafredda et al., 1994; Ferla et al., 2000; Trombetta et al., 2004).

The metamorphic basement rocks of the lower complex are covered by Mesozoic-Cenozoic sediments connected with the Triassic rifting processes responsible for the Lower-middle Jurassic opening of the Alpine Tethys Ocean. The sequence is composed of fluvial to deltaic conglomerates and sandstones of Hettangian age, followed by limestones and dolostones dated to Sinemurian, representing the remnants of an ancient carbonate platform and its margin. The partial drowning of the platform is testified by the presence of marls and marly limestones of

Pleinsbachian age, followed by Middle Jurassic to Early Cretaceous nodular limestones, radiolarites, cherty limestones and calcilutites. The Upper Cretaceous-Eocene interval is represented by marls and marly limestones, whereas the top of the sedimentary cover consists of Upper Eocene to Lower Oligocene terrigenous deposits indicating the onset of the orogenic compressional deformation.

In northeastern Sicily, this orogenic phase is symbolized by two main events: the juxtaposition of the tectono-metamorphic units of the Peloritani Mountains and the overthrusts of the whole Peloritani block onto the Alpine Tethys units, (i.e. Sicilide Units of Ogniben, 1960). The latter is expressed through a NW-SE oriented, NE-dipping regional thrust, (i.e. the Peloritani sole-thrust of Catalano et al., 2017).

The tectono-metamorphic units of the Peloritani Mountains are unconformably overlaid by syn- to post-orogenic sedimentary sequences (Fig. 8 and 9). The first syn-orogenic sequence is composed of Oligocene conglomerates and sandstones known as “red conglomerate”, which are entirely involved in the orogenic cycle and include large olistoliths of Mesozoic carbonates. The Upper Oligocene to Lower Miocene deposits of the Capo d’Orlando Flysch represents the second syn-orogenic cycle. These sediments consist of conglomerates followed by sandstones and an alternation of sandstones, marls and marly clays. They extensively outcrop in the southern sector of the Peloritani Mountains (Fig. 9), and they can be considered as thrust-top deposit sealing the overthrusts among the Peloritani tectonic units.

During the Lower Miocene, the backthrust of the Antisicilidi Unit (composed of Cretaceous clays deriving from the Alpine Tethys basin), interrupted the syn-orogenic sedimentation. The Floresta calcarenites, unconformably deposited over the Cretaceous clays, are the last syn-orogenic sequence. This formation shows three different sedimentary facies including calcarenites, biolithites, and sandstones.

Since the Middle Miocene, an important event changed the tectonic regime of the Mediterranean area: the Tyrrhenian Sea opening, which in the Peloritani Mountains triggered a post-orogenic extensive tectonic pulse.

The Middle-Upper Miocene sediments were deposited in shallow water and in transitional environments, which characterized the extensive basin opened at the top of the Peloritani Belt. The original geometry of this formation is that of a fan-delta system. These deposits extensively crop out along the Tyrrhenian margin, whereas

only a few outcrops occur along the Ionian side (Fig. 9). They consist of conglomeratic horizons followed by an arenaceous-pelitic alternation of sandstones. In the Late Miocene, the Messinian salinity crisis (see Roveri et al., 2014 for further information) lead to the genesis of evaporitic rocks (i.e. evaporitic limestones and gypsum) linked to the partial desiccation of the Mediterranean Sea.

Evaporites are rarely preserved, and they sporadically crop out only within tectonic grabens. The shallow to deep water environment was restored during the Lower Pliocene, driving to the deposition of the marly limestones of the Trubi formation (Fig. 8).

The upper Pliocene to Middle Pleistocene sedimentation mostly occurred along the Tyrrhenian and Ionian margins (Fig. 9), since the summit of the Peloritani Mountains became a permanent emerged sector. The Upper Pliocene to Middle Pleistocene cycles filled structural basins (e.g. the Barcellona Pozzo di Gotto and the Rodi-Falcone basins) originated from the extensional tectonic phase. This formation consists of shallow water calcarenites and sands, which eteropically evolve to clays and sandy clays.



Figure 10. The Sabbie and ghiaie of Messina outcropping in the northern area of Messina.

The top of the post-orogenic sequence consists of Middle Pleistocene terrigenous deposits (the so-called “Sabbie and ghiaie of Messina” formation) representing the remnant of fluvial and deltaic systems generated in response to the regional uplift that occurred in northeastern Sicily during the Quaternary (Catalano and Cinque, 1995; Catalano and Di Stefano, 1997; Lentini et al., 2000).

As like the Pliocene-Pleistocene sediments, also the Sabbie and ghiaie of Messina outcrop along the Tyrrhenian and Ionian margin of the Peloritani Mountains (Fig. 9). They are composed of sands and gravels (Fig. 10) mainly deriving from erosion and dismantling of three different types of metamorphic rocks belonging to the Aspromonte Unit: Late Variscan plutonites, orthogneisses and paragneisses.

3.3. Active deformation along the southern portion of the CPO

The CPO is considered as a segment of continental crust migrated away from the Sardinian block in response to the opening and spreading of the Tyrrhenian Sea, which occurred during Neogene (Fig. 11A; see Malinverno and Ryan, 1986; Ben Avraham et al., 1990; Faccenna et al., 2004 and Carminati and Doglioni, 2005 for further information).

The Tyrrhenian Sea, including transitional and oceanic crust, was considered as a back-arc basin created by the subduction and rollback of the Ionian plate beneath the CPO (Boccaletti and Guazzone, 1972; Dewey et al., 1973; Malinverno and Ryan, 1986; Rehault et al., 1987) or as result of delamination process (Wezel, 1985; Locardi, 1986; Channell, 1986), or as a passive rift generated by lateral extrusion of continental blocks (Tapponnier, 1977; Boccaletti et al., 1984, 1990; Ben Avraham et al., 1990; Faccenna et al., 1996; Catalano et al., 2004).

The northwestwards subduction of the Ionian plate dominates the geodynamic setting of the Central Mediterranean Sea. Earthquakes down to a depth of 600 km (Frepoli et al., 1996) and tomographic data (Neri et al., 2012) evidence the presence of a NW-SE trending Wadati-Benioff zone beneath the CPO (e.g. Chiarabba et al., 2005). Although in the last 5-6 Ma the subduction rate was around 5-6 cm per year (Faccenna et al., 2004), during the Late Pleistocene this process became slower or stopped (e.g. Faccenna et al., 2001; Goes et al., 2004).

Recently, Neri et al. (2012) performed tomographic investigations in the CPO region, and according to their data, the Ionian subducting slab is continuous in depth only beneath the central part of the CPO (Fig. 11B). Conversely, beneath the northern and southern portions of the CPO, the slab is detached at depth. Transitional areas from continuous to detached subduction mode, were identified beneath the Messina Straits and the Sila Massif.

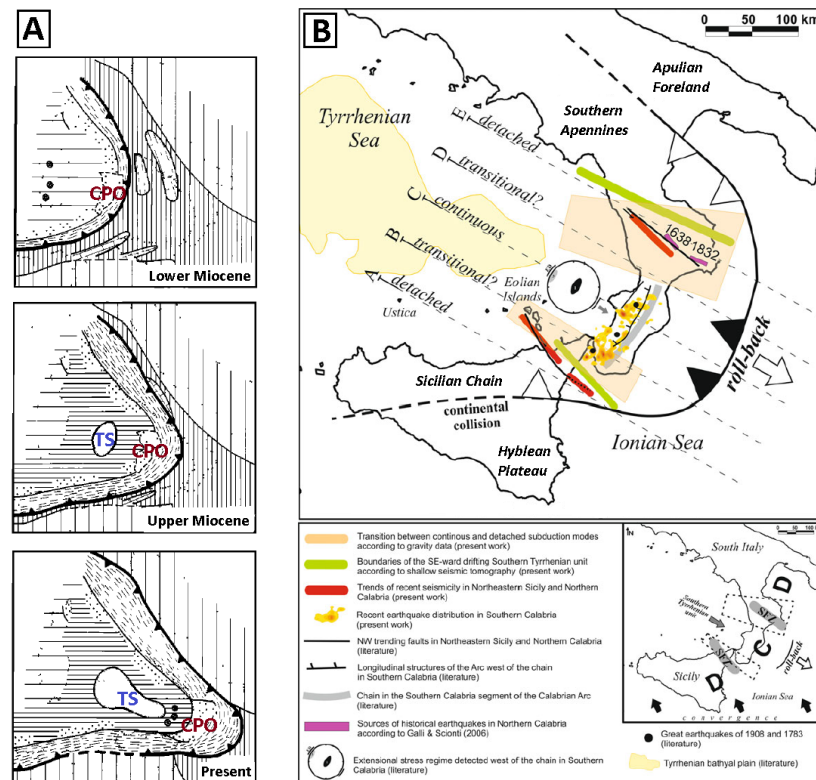


Figure 11. A) paleogeographic reconstruction of the Tyrrhenian Sea (TS) opening and the CPO migration since the last 20 Ma to present (modified from Malinverno and Ryan, 1986); B) scheme representing the continuous to detached subduction mode of the Ionian plate slab beneath the CPO along the seismic profiles analysed by Neri et al., 2012 (modified from Neri et al., 2012).

According to Goes et al. (2004), the decrease of the Ionian subduction rate caused a plate reorganization in the south-central Mediterranean Area. Currently, the geodynamic setting of this area evidences the coexistence of extension, compression and transcurrent (Fig. 12). These features make the Central Mediterranean Sea one

of the most studied areas of the Earth, where volcanism, earthquakes and landslides strongly affect the life of the resident population.

The ongoing convergence between Africa and Eurasia plates is expressed along a W-E oriented compressional zone located in the southern Tyrrhenian, from the Ustica Island to the Aeolian Islands. Geodetic data show shortening rates of around 1-1.5 mm/yr (D'Agostino and Selvaggi, 2004; Palano et al., 2012): Moreover, seismicity (up to M5-6) is characterized by reverse (thrust) focal mechanisms with P-axis oriented NNO-SSE e NO-SE (Pondrelli et al., 2004, 2006; Neri et al., 2005).

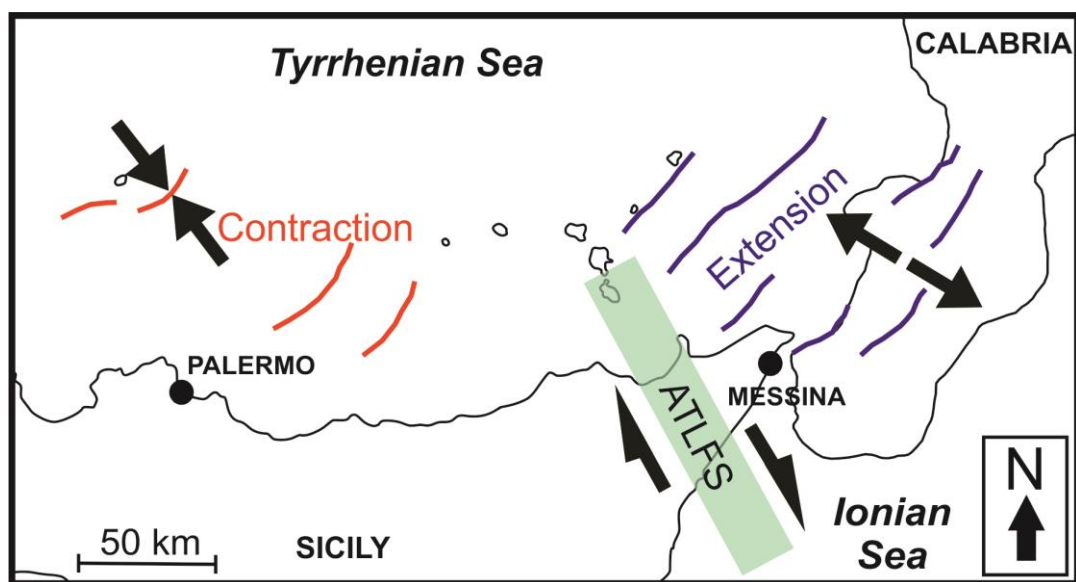


Figure 12. Active deformation in the southern CPO and along the Tyrrhenian margin of Sicily. GPS and seismological data suggest the coexistence of contraction (thrust faults in red) and extension (normal faults in purple). The deformation is accommodated along NW-SE trending dextral faults belonging to the Aeolian-Tindari-Letojanni fault system (ATLFS) indicated with the green rectangle (modified after Cultrera et al., 2017).

Northeastern Sicily and southern Calabria are affected by an active ESE-ONO oriented extension (Tortorici et al., 1995; Monaco and Tortorici, 2000; Catalano et al., 2008). Deformation occurs at rates of 1.5-3 mm/yr (Hollenstein et al., 2003; D'Agostino and Selvaggi, 2004; Goes et al., 2004; Serpelloni et al., 2005; Mattia et al., 2009; ; D'Agostino et al., 2011). The engine which causes the extension is still debated. Some authors suggested the presence of an active rifting zone (Tortorici et al., 1995; Monaco and Tortorici, 2000; Jacques et al., 2001; Catalano et al., 2008),

others related the extension to the back-arc stretching in the Tyrrhenian Sea (Neri et al., 2005), D'Agostino and Selvaggi, (2004). In addition, Goes et al. (2004) proposed the contribution of the counterclockwise rotation of the Ionian block, whereas Westaway (1993) invoked the isostatic response to the Ionian slab detachment.

Normal faults in southern Calabria and northeastern Sicily are responsible for intense crustal seismicity. Historical $M > 6$ earthquakes struck this area many times during the last centuries. For instance, the famous earthquakes of 6 Feb 1783 ($M \sim 6$) and 28 Dec 1908 ($M = 7.2$) that destroyed the cities of Messina and Reggio Calabria were probably generated by coseismic extensional deformation that occurred along a normal fault located in the Calabrian side of the Messina Straits (see Ghisetti, 1982; 1992; Valensise and Pantosti 1992; Tortorici et al., 1995; Jacques et al., 2001; Amoruso et al., 2002; Ferranti et al., 2007).

The deformation between compressional and extensional crustal domains is accommodated along a NNW-SSE trending, right-lateral transtensional zone: the so-called Aeolian-Tindari-Letojanni Fault System (ATLFS), which today controls both volcanism and seismicity (Goes et al., 2004; Palano et al., 2012, 2015; Barreca et al., 2014; Cultrera et al., 2017). The ATLFS has been alternatively interpreted as: i) the result of a plate reorganization (Goes et al., 2004; Billi et al., 2006); ii) the surface expression of a STEP (Subduction Transform Edge Propagator) fault (Govers and Wortel, 2005; Argnani et al., 2007; Polonia et al., 2011, 2016); iii) as a discontinuity bounding a region of incipient rifting (Dellong et al., 2018).

It is accepted that the northern tip of the ATLFS is located in the central sector of the Aeolian Island (Barreca et al., 2014). A highly deformed extensional zone with associated en-echelon-arranged structures is clearly detectable in the Sicilian mainland up to the Rocca Novara locality. The most intriguing enigma about the ATLFS is the propagation of the active deformation to the south. According to Billi et al. (2016), there is no evidence of a prosecution of the ATLFS southwards. Contrastingly, recent studies (Barreca et al., 2019) recognized an oblique faulting zone, with a general NW-SE tectonic trend, extending from Rocca Novara to Capo St. Alessio, connecting the northern side of the ATLFS with a transtensional sector located offshore in the Ionian Sea (i.e. Ionian Fault System; Polonia et al., 2011, 2016, 2017).

References

- P. Acquafredda, S. Lorenzoni and E. Zanettin Lorenzoni. Palaeozoic sequences and evolution of the Calabrian-Peloritan Arc (Southern Italy). *Terra Nova*, **6**(6):582-594, 1994.
- W. Alvarez, T. Coccozza and F.C. Wezel. Fragmentation of the alpine orogenic belt by microplate dispersal. *Nature*, **248**(5446):309-314, 1974.
- L. Amodio-Morelli, G. Bonardi, V. Colonna, D. Dietrich, G. Giunta, F. Ippolito, V. Liguri, S. Lorenzoni, A. Paglionico, V. Perrone, G. Piccarreta, M. Russo, P. Scandone, E. Zanettin Lorenzoni and A. Zuppetta. L'Arco Calabro-peloritano nell'orogene appenninico-maghrebide. *Memorie della Società Geologica Italiana*, **17**:1-60, 1976.
- A. Amoruso, L. Crescentini and R. Scarpa. Source parameters of the 1908 Messina Straits, Italy, earthquake from geodetic and seismic data. *Journal of Geophysical Research*, **107**(B4):ESE 4-1-ESE 4-11, 2002.
- A. Argnani, E. Serpelloni and C. Bonazzi. Pattern of deformation around the central Aeolian Islands: Evidence from multichannel seismics and GPS data, *Terra Nova*, **19**(5):317–323, 2007.
- P. Atzori. Contributo alla conoscenza degli Scisti epizonali dei Monti Peloritani (Sicilia). *Rivista mineraria siciliana*, **21**:124-126, 1970.
- P. Atzori and P. Ferla. The pre-Alpine crystalline basement of the Peloritani Mountains (Sicily): acquired knowledge and open questions. *IGCP Project n. 276 Newsletter*, **5**:331-320, 1992.
- P. Atzori, R. Cirrincione, A. Del Moro and A. Pezzino. Structural, metamorphic and geochronologic features of the Alpine event in south-eastern sector of the Peloritani Mountains (Sicily). *Periodico di Mineralogia*, **63**(1-3):113-125, 1994.
- G. Barreca, V. Bruno, F. Cultrera, M. Mattia, C. Monaco and L. Scarfi L. New insights in the geodynamics of the Lipari–Vulcano area (Aeolian Archipelago, southern Italy) from geological, geodetic and seismological data. *Journal of Geodynamics*, **82**:150–167, 2014.
- G. Barreca, L. Scarfi, F. Gross, C. Monaco and G. De Guidi. Fault pattern and seismotectonic potential at the south-western edge of the Ionian Subduction System (southern Italy): New field and geophysical constraints. *Tectonophysics*, **761**:31.45, 2019.

Z. Ben-Avraham, M. Boccaletti, G. Cello, M. Grasso, F. Lentini, L. Torelli and L. Tortorici. Principali domini strutturali originatisi dalla collisione continentale neogenico-quadernaria nel Mediterraneo centrale. *Memorie della Società Geologica Italiana*, **45**:453-462, 1990.

A. Billi, G. Barberi, C. Faccenna, G. Neri, F. Pepe, and A. Sulli. Tectonics and seismicity of the Tindari Fault System, southern Italy: crustal deformations at the transition between ongoing contractional and extensional domains located above the edge of a subducting slab. *Tectonics*, **25**(2), Article Number 2006, 2006.

M. Boccaletti and G. Guazzone. Gli archi appenninici, il Mar Ligure e il Tirreno nel quadro della tettonica dei bacini marginali retro-arco. *Memorie della Società Geologica Italiana*, **11**:201-216, 1972.

M. Boccaletti, R. Nicolich and L. Tortorici. The Calabrian Arc and the Ionian Sea in the dynamic evolution of the central Mediterranean. *Marine Geology*, **55**(3-4): 219-245, 1984.

M. Boccaletti, R. Nicolich and L. Tortorici. New data and hypothesis on the development of the Tyrrhenian basin. *Palaeogeography, Palaeoclimatology, Palaeoecology*, **77**(1):15-40, 1990.

G. Bonardi, G. Cello, V. Perrone, L. Tortorici, E. Turco and A. Zuppetta. The evolution of the northern sector of Calabria Peloritani Arc in a semiquantitative palinspastic restoration. *Bollettino della Società Geologica Italiana*, **101**:259-274, 1982.

G. Bonardi, G. Giunta, A. Messina, V. Perrone and S. Russo .The Calabria-Peloritani Arc and its correlation with northern Africa and southern Europe. *Field Trip Guidebook, IGCP Project*, **276**:1-87, 1993.

G. Bonardi, R. Compagnoni, A. Del Moro, E. Macaione, A. Messina and V. Perrone. Rb–Sr age constraints on the Alpine metamorphic overprint in the Aspromonte Nappe (Calabria–Peloritani Composite Terrane, southern Italy). *Bollettino della Società Geologica Italiana*, **127**(2):173-190, 2008.

J.P. Bouillin. Nouvelle interprétation de la liason Apennin-Maghrebides en Calabre: consequences sur la palaeogéographie téthysienne entre Gibraltar et les Alpes. *Revue de géologie dynamique et de géographie physique*, **25**:321-338, 1984.

S. Catalano and A. Cinque. L'evoluzione neotettonica dei Peloritani settentrionali (Sicilia nord-orientale): il contributo di una analisi geomorfologica preliminare. *Studi Geologici Camerti, Special Issue (1995/2)*: 113-123, 1995.

S. Catalano and A. Di Stefano. Sollevamento e tetto-genesi Pleistocenica lungo il margine tirrenico dei Monti Peloritani: integrazione dei dati geomorfologici, strutturali e biostratigrafici. *Il Quaternario*, **10**(2):337-342, 1997.

S. Catalano, C. Monaco, L. Tortorici, W. Paltrinieri and N. Steel. Neogene-Quaternary tectonic evolution of the Southern Apennines. *Tectonics*, **23**, Article Number TC2003, 2004.

S. Catalano, G. De Guidi, C. Monaco, G. Tortorici and L. Tortorici. Active faulting and seismicity along the Siculo–Calabrian Rift Zone (Southern Italy). *Tectonophysics*, **453**(1-4):177–192, 2008.

S. Catalano, R. Cirrincione, P. Mazzoleni, F. Pavano, A. Pezzino, G. Romagnoli and G. Tortorici. The effects of a Meso-Alpine collision event on the tectono-metamorphic evolution of the Peloritani mountain belt (eastern Sicily, southern Italy). *Geological Magazine*, **155**(2):422–437, 2017.

E. Carminati and C. Doglioni. Mediterranean tectonics. In: R.C. Shelley, R.M. Cocks and I.R. Plimer, *Encyclopedia of Geology*, Elsevier, Oxford, 135-146, 2005.

G. Cello, C. Invernizzi and S. Mazzoli. Structural signature of tectonic processes in the Calabrian Arc, southern Italy: Evidence from the oceanic-derived Diamante-Terranova Unit. *Tectonics*, **15**(1):187-200, 1996.

J.E.T. Channell. Paleomagnetism and continental collision in the Alpine Belt and the formation of late-tectonic extensional basins. In: M.P. Coward and A.C. Ries, *Collision tectonics*, Geological Society London Special Publication, **19**:261-284, 1986.

C. Chiarabba, L. Jovane, and R. Di Stefano. A new view of Italian seismicity using 20 years of instrumental recordings. *Tectonophysics*, **395**(34):251-268, 2005.

R. Cirrincione, E. Fazio, G. Ortolano, A. Pezzino and R. Punturo. Fault-related rocks: Deciphering the structural-metamorphic evolution of an accretionary wedge in a collisional belt, NE Sicily. *International Geology Review*, **54**(8), 940-956, 2012.

R. Cirrincione, E. Fazio, P. Fiannacca, G. Ortolano, A. Pezzino and R. Punturo. The Calabria-Peloritani Orogen, a composite terrane in Central Mediterranean; its overall architecture and geodynamic significance for a pre-Alpine scenario around the Tethyan basin. *Periodico di Mineralogia*, **84**(3B):701-749, 2015.

S. Critelli and E. Le Pera (1998) - Post-Oligocene sediment-dispersal systems and unroofing history of the Calabrian microplate, Italy. *International Geology Review*, **40**(7), 609-637, 1998.

F. Cultrera, G. Barreca, P. Burrato, L. Ferranti, C. Monaco, S. Passaro, F. Pepe and L. Scarfi. Active faulting and continental slope instability in the Gulf of Patti (Tyrrhenian side of NE Sicily, Italy): a field, marine and seismological joint analysis. *Natural Hazards*, **86**:253–272, 2017.

N. D'Agostino and G. Selvaggi. Crustal motion along the Eurasia-Nubia plate boundary In the Calabrian Arc and Sicily and active extension in the Messina Straits from GPS measurements. *Journal of Geophysical Research*, **109**, Article Number B11402, 2004.

N. D'Agostino, E. D'Anastasio, A. Gersavi, I. Guerra, M.R. Nedimović, L. Seeber and M.S. Steckler. Forearc extension and slow rollback of the Calabrian Arc from GPS measurements. *Geophysical Research Letters*, **38**, Article Number L17304, 2011.

C. D'Amico. General picture of Hercynian magmatism in the Alps, Calabria-Peloritani and Sardinia-Corsica. *International Geoscience Program*, **5**:50-68, 1979.

C. D'Amico, A. Rottura, E. Maccarrone and G. Puglisi. Peraluminous granitic suite of Calabria-Peloritani arc (Southern Italy). *Rendiconti della Societa Italiana di Mineralogia e Petrologia*, **38**(1):35-52, 1982.

S. De Gregorio, S.G. Rotolo and I.M. Villa. Geochronology of the medium to high grade metamorphic units of the Peloritani Mts., Sicily. *International Journal of Earth Sciences*, **92**: 852-872, 2003.

D. Dellong, F. Klingelhoefer, H. Kopp, D. Graindorge, L. Margheriti, M. Moretti, S. Murphy and M.A. Gutscher. Crustal Structure of the Ionian Basin and Eastern Sicily Margin: Results From a Wide-Angle Seismic Survey. *Journal of Geophysical Research Solid Earth* **123**(3): 2090–2114, 2018.

J.F. Dewey, W.C. Pitman, W.B.F. Ryan and J. Bonnin. Plate tectonics and the evolution of the alpine system. *Geological Society of America Bulletin*, **84**(10):3137-3180, 1973.

J.F. Dewey, M.L. Helman, E. Turco, D.H.W. Hutton and S.D. Knott. Kinematics of the western Mediterranean. In: M.P. Coward, D. Dietrich and R.G. Park , *Alpine Tectonics*, Geological Society London Special publication, **45**:265-283, 1988.

F. Dietrich. Sense of overthrust shear in the Alpine nappes of Calabria (Southern Italy). *Journal of Structural Geology*, **10**(4): 373-381, 1988.

- C. Faccenna, P. Davy, J.P. Brun, R. Funicello, D. Giardini, M. Mattei and T. Nalpas. The dynamics of back-arc extension: an experimental approach to the opening of the Tyrrhenian Sea. *Geophysical Journal International*, **126**(3):781-795, 1996.
- C. Faccenna, T.W. Becker, F.P. Lucente, L. Jolivet and F. Rossetti. History of subduction and back-arc extension in the central Mediterranean. *Geophysical Journal International*, **145**(3): 809–820, 2001.
- C. Faccenna, C. Piromallo, A. Crespo-Blanc, L. Jolivet and F. Rossetti. Lateral slab deformation and the origin of western Mediterranean arcs. *Tectonics*, **23**, Article Number TC1012, 2004.
- P. Ferla. A model of continental crust evolution in the geological history of the Peloritani Mountains (Sicily). *Memorie della Società Geologica Italiana*, **55**:87-93, 2000.
- L. Ferranti, C. Monaco, F. Antonioli, L. Maschio, S. Kershaw and V. Verrubbi. The contribution of regional uplift and coseismic slip to the vertical crustal motion in the Messina Straits, Southern Italy: evidence from raised Late Holocene shorelines. *Journal of Geophysical Research*, **112**, Article Number B06401, 2007.
- P. Fiannacca, P. Brotzu, R. Cirrincione, P. Mazzoleni and A. Pezzino. Alkali metasomatism as a process for trondhjemite genesis: evidence from Aspromonte Unit, north-eastern Peloritani, Sicily. *Mineralogy and Petrology*, **84**:19-45, 2005.
- P. Fiannacca, I.S. Williams, R. Cirrincione and A. Pezzino. Crustal Contributions to Late Hercynian Peraluminous Magmatism in the Southern Calabria Peloritani Orogen, Southern Italy: Petrogenetic Inferences and the Gondwana Connection. *Journal of Petrology*, **49**(8):1897-1514, 2008.
- P. Fiannacca, I.S. Williams, R. Cirrincione and A. Pezzino. The augen gneisses of the Peloritani Mountains (NE Sicily): granitoid magma production during rapid evolution of the northern Gondwana margin at the end of the Precambrian. *Gondwana Research*, **23**(2):782-796, 2013.
- A. Frepoli, G. Selvaggi, C. Chiarabba and A. Amato. State of stress in the Southern Tyrrhenian Subduction Zone from fault-plane solutions. *Geophysical Journal International*, **125**(3):879-891, 1996.
- F. Ghisetti and L. Vezzani. Different styles of deformation in the Calabrian Arc (southern Italy): Implications for a seismotectonic zoning. *Tectonophysics* **85**(3-4), 149-165, 1982.
- F. Ghisetti. Fault parameters in the Messina Straits (southern Italy) and relations with the seismogenic source. *Tectonophysics*, **210**(1-2): 117-133, 1992.

- S. Goes, D. Giardini, S. Jenny, C. Hollenstein, H.G. Kahle and A. Geiger. A recent tectonic reorganization in the south-central Mediterranean. *Earth and Planetary Science Letters*, **226**(3-4):335-345, 2004.
- R. Govers and M.J.R. Wortel. Lithosphere tearing at STEP faults: response to edges of subduction zones. *Earth and Planetary Science Letters*, **236**(1-2):505-523, 2005.
- F. Guerrera, A. Martín-Algarra and V. Perrone. Late Oligocene-Miocene syn-late-orogenic successions in Western and Central Mediterranean Chains from the Betic Cordillera to the Southern Apennines. *Terra Nova*, **5**(6):525-544, 1993.
- D. Haccard, C. Lorenz and C. Grandjacquet. Essai sur l'évolution tectogénétique de la liaison Alpes-Apennines (de la Ligurie à la Calabre). *Memorie della Società Geologica Italiana*, **11**: 309-381, 1972.
- C. Hollenstein, H.G. Kahle, A. Geiger, S. Jenny, S. Goes and D. Giardini. New GPS constraints on the Africa-Eurasia plate boundary zone in southern Italy. *Geophysical Research Letters*, **30**(18), Article Number 1935, 2003.
- S. Ioppolo and G. Puglisi G. Petrological study of some Hercynian metamorphics from the NE peloritani mountains, Sicily. *Rendiconti della Società Italiana di Mineralogia e Petrologia*, **43**(3):643-656, 1988.
- E. Jacques, C. Monaco, P. Tapponnier, L. Tortorici and T. Winter. Faulting and earthquake triggering during the 1783 Calabria seismic sequence. *Geophysical Journal International*, **147**(3), 499-516, 2001.
- S.D. Knott. The Liguride Complex of Southern Italy- a Cretaceous to Paleogene accretionary wedge. *Tectonophysics*, **142**(2-4):217-226, 1987.
- F. Lentini and L. Vezzani. Tentativo di elaborazione di uno schema strutturale della Sicilia orientale. *Memorie della Società Geologica Italiana*, **19**:495-500, 1978.
- F. Lentini, S. Carbone, S. Catalano and C. Monaco. Tettonica a thrust neogenica nella Catena appenninica maghrebide: esempi dalla Lucania e dalla Sicilia. *Studi Geologici Camerti, Special Issue*:19-26, 1990.
- F. Lentini, S. Catalano and S. Carbone. The External Thrust System in Southern Italy: A target for petroleum exploration. *Petroleum Geoscience*, **2**(4):333-342, 1996.

- F. Lentini, S. Carbone, M. Grasso, A. Di Stefano, M. Romeo and A. Messina. Carta Geologica della Provincia di Messina 1:50,000, S.EL.CA. Firenze, Italy, 2000.
- F. Lentini, S. Carbone and P. Guarnieri. Collisional and postcollisional tectonics of the Apenninic-Maghrebien orogen (southern Italy). Geological Society of America Special Paper, **409**:57-81, 2006.
- F. Lentini and S. Carbone. Geologia della Sicilia-ISPRA. Memorie Descrittive della Carta Geologica d'Italia **95**:7-414, 2014.
- E. Locardi. Tyrrhenian volcanic arcs: volcanotectonics, petrogenesis and economic aspects. In: F.C. Wezel, The origin of the arcs, Elsevier, Amsterdam, 351-373, 1986.
- A. Malinverno and W.B.F. Ryan. Extension in the Tyrrhenian Sea and shortening in the Apennines as result of arc migration driven by sinking of the lithosphere, *Tectonics*, **5**(2):227–245, 1986.
- M. Mattia, M. Palano, V. Bruno and F. Cannavò. Crustal motion along the Calabro-Peloritan Arc as imaged by twelve years of measurements on a dense GPS network. *Tectonophysics*, **476**(3-4):528-537, 2009.
- C. Monaco and L. Tortorici. Active faulting in the Calabrian arc and eastern Sicily. *Journal of Geodynamics*, **29**(3-5):407–424, 2000.
- G. Neri, G. Barberi, G. Oliva and B. Orecchio. Spatial variations of seismogenic stress orientations in Sicily, South Italy. *Physic of the Earth and Planetary Interiors*, **148**(2-4):175-191, 2005.
- G. Neri, A. M. Marotta, B. Orecchio, D. Presti, C. Totaro, R. Barzaghi and A. Borghi. How lithospheric subduction changes along the Calabrian Arc in southern Italy: Geophysical evidences. *International Journal of Earth Sciences*, **101**:1949-1969, 2012.
- L. Ogniben. Nota illustrativa dello schema geologico della Sicilia nord-orientale. *Riserva Mineraria Siciliana*, **11**:183- 222, 1960.
- L. Ogniben. Schema geologico della Calabria in base ai dati odierni. *Geologica Romana*, **12**:243-585, 1973.
- M. Palano, L. Ferranti, C. Monaco, M. Mattia, M. Aloisi, V. Bruno, F. Cannavò and G. Siligato. GPS velocity and strain fields in Sicily and southern Calabria, Italy: Updated geodetic constraints on tectonic block interaction in the central Mediterranean. *Journal of Geophysical Research*, **117**, Article Number B0740, 2012.

- M. Palano, D. Schiavone, M. Loddo, M. Neri, D. Presti, R. Quarto, C. Totaro and G. Neri. Active upper crust deformation pattern along the southern edge of the Tyrrhenian subduction zone (NE Sicily): Insights from a multidisciplinary approach. *Tectonophysics*, **657**:205–218, 2015.
- V. Perrone. Une nouvelle hypothèse sur la position paléogéographique et l'évolution tectonique des Unités de Verbicaro et de San Donato (region Calabro-Lucanienne; Italie): implications sur le limite Alpes-Apennines en Calabre. *Comptes Rendus de l'Académie des Sciences, Paris*, **322**:877-884, 1996.
- A. Pezzino. Confronti petrografici e strutturali tra i basamenti metamorfici delle unità inferiori dei Monti Peloritani (Sicilia). *Periodico di Mineralogia*, **1**:35-50, 1982.
- A. Pezzino, G. Angi, R. Cirrincione, E. De Vuono, E. Fazio, P. Fiannacca, A. Lo Giudice, G. Ortolano and R. Punturo. Alpine metamorphism in the Aspromonte Massif: implications for a new framework for the southern sector of the Calabria-Peloritani Orogen (Italy). *International Geology Review*, **50**(5):423-441, 2008.
- A. Polonia, L. Torelli, P. Mussoni, L. Gasperini, A. Artoni and D. Klaeschen. The Calabrian arc subduction complex in the Ionian Sea: regional architecture, active deformation and seismic hazard. *Tectonics*, **30**, Article Number TC5018, 2011.
- A. Polonia, L. Torelli, A. Artoni, M. Carlini, C. Faccenna, L. Ferranti, L. Gasperini, D. Klaeschen, C. Monaco, G. Neri, N. Nijholt, B. Orecchio, R. Wortel and R. Govers. The Ionian and Alfeo-Etna fault zones: new segments of an evolving plate boundary in the central Mediterranean Sea? *Tectonophysics* **675**:69–90, 2016.
- A. Polonia, L. Torelli, L. Gasperini, L. Cocchi, F. Muccini, E. Bonatti, C. Hensen, M. Schmidt and S. Romano. Lower plate serpentinite diapirism in the Calabrian Arc subduction complex. *Nature Communication*, **8**(1), Article Number 2172, 2017.
- S. Pondrelli, C. Piromallo and E. Serpelloni. Convergence vs. retreat in Southern Tyrrhenian Sea: insights from kinematics. *Geophysical Research Letters*, **31**, Article Number L06611, 2004.
- S. Pondrelli, S. Salimbeni, G. Ekström, A. Morelli, P. Gasperini and G. Vannucci. The Italian CMT dataset from 1977 to the present. *Physics of the Earth and Planetary Interiors*, **159**(3-4):286-303, 2006.
- J.P. Rehault, E. Moussat and A. Fabbri. Structural evolution of the Tyrrhenian back-arc basin. *Marine Geology*, **74**(1-2):123-150, 1987.

S. Rotolo and P. De Fazio. Clinopiroxene bearing garnet amphibolites from the Ferrà Valley (northern Peloritani Mts., Sicily). *Bollettino della Società Geologica Italiana*, **120**(1):31-35, 2001.

A. Rottura, G.M. Bargossi, V. Caironi, A. Del Moro, E. Maccarrone, P. Macera, A. Paglionico, R. Petrini, G. Piccareta and G. and Poli. Petrogenesis of contrasting Hercynian granitoids from the Calabrian Arc, Southern Italy. *Lithos*, **24**(2):97-119, 1990.

A. Rottura, A. Caggianelli, R. Campana and A. Del Moro. Petrogenesis of Hercynian peraluminous granites from the Calabrian Arc, Italy. *European Journal of Mineralogy*, **5**(4):737-754, 1993.

M. Roveri, R. Flecker, W. Krijgsman, J. Lofi, S. Lugli, V. Manzi, F.J. Sierro, A. Bertini, A. Camerlenghi, G.J. de Lange, R. Govers, F.J. Hilgen, C. Hubscher, P.T. Meijer and M. Stoica. The Messinian Salinity Crisis: past and future of a great challenge for marine sciences. *Marine Geology* **349**:113–125, 2014.

P. Scandone. Origin of the Tyrrhenian Sea and Calabrian Arc. *Bollettino della Società Geologica Italiana*, **98**:27-34, 1979.

E. Serpelloni, M. Anzidei, P. Baldi, G. Casula and A. Galvani. Crustal velocity and strain rate fields in Italy and surrounding regions: new results from the analysis of permanent and non-permanent GPS networks. *Geophysical Journal International*, **161**(3):861–880, 2005.

P. Tapponnier. Evolution du système Alpin en Méditerranée: poinçonnement et écrasement rigide-plastique. *Bulletin de la Société Géologique de France*, **7**(3):437-460, 1977.

S.N. Thomson. Assessing the nature of tectonics contacts using fission-tracks thermochronology: an example from the Calabrian arc, southern Italy. *Terra Nova*, **10**(6): 32-36, 1998.

L. Tortorici, C. Monaco, C. Tansi and O. Cocina. Recent and active tectonics in the Calabrian Arc (Southern Italy). *Tectonophysics*, **243**(1-2):37-49, 1995.

A. Trombetta, R. Cirrincione, F. Corfu, P. Mazzoleni and A. Pezzino. Mid-Ordovician U-Pb ages of porphyroids in the Peloritan Mountains (NE Sicily): palaeogeographical implications for the evolution of the Alboran microplate. *Journal of the Geological Society*, **161**(2):265-276, 2004.

G. Valensise and D. Pantosti. A 125 Kyr-long geological record of seismic source repeatability: the Messina Straits (southern Italy) and the 1908 earthquake (Ms 7.1/2). *Terra Nova*, **4**(4):472-483, 1992.

R. Westaway. Quaternary uplift of Southern Italy. *Journal of Geophysical Research*, **98**(B12): 21741-21772, 1993.

F.C. Wezel. Structural features and basin tectonics of the Tyrrhenian Sea. In: D.J. Stanley and F.C. Wezel, *Geological evolution of the Mediterranean Basin*, Springer-Verlag, New York: 153-194, 1985.

I.S. Williams, P. Fiannacca, R. Cirrincione and A. Pezzino. Peri-Gondwanan origin and early geodynamic history of NE Sicily: A zircon tale from the basement of the Peloritani Mountains. *Gondwana Research*, **22**(3-4):855-865, 2012.

Chapter IV - Radiological features of the Peloritani crystalline rocks: gamma radiation and radon release

4.1 Introduction

The Peloritani Mountain Ridge constitutes the northeastern portion of Sicily, and it is characterized by the presence of crystalline rocks (i.e. granites and low to high-grade metamorphites).

Generally, the highest abundance of U and Th is associated with acid and intermediate igneous rocks. This is due to the fact that during magmatic processes, U and Th behave as highly incompatible elements (as LILE, LREE and other HFSE) tending to accumulate in residual Si-rich melts generating uranium and thorium-bearing minerals.

Conversely, in sedimentary rocks such as carbonates, U, Th, and K abundances are very low. Among sediments, clays and shales usually show a higher level of natural radioactivity. Moreover, high K contents are related to feldspars (e.g. orthoclase and microcline), micas (e.g. biotite and muscovite) and clay minerals.

Concerning metamorphic rocks, U, Th and K concentrations depend on the original content of the protolith. In addition, metamorphites can easily display high levels of natural radiation if metasomatic and/or hydrothermal fluids interact with rocks during metamorphic processes, as fluids are able to leak and redistribute mobile and incompatible elements.

In this framework, it seems clear that acid magmatic rocks and metamorphites might represent dangerous radiation sources. Therefore, in all the areas, such as the Peloritani Mountains, where those kind of rocks outcrop, the annual effective dose from natural radiation can be very high.

Taking into account all those considerations, the main aim of this Chapter is to assess the environmental impact and the radiological hazards for inhabitants living in northeastern Sicily, caused by the occurrence of crystalline rocks. Moreover, some of these crystalline rocks are mined and used as building materials. For this reason, the potential hazards due to their use in construction were also evaluated. In order to constrain the radiological properties of the Peloritani crystalline basement, rock samples were collected, and gamma and alpha spectroscopies were used to evaluate

the gamma radiation and the amount of radon (^{222}Rn) released from the solid media, respectively.

The results of this Chapter were already published in Romano et al. (2020).

4.2 Exposure and dosimetry

Decaying radionuclides release gamma rays and alpha and beta particles (see Chapter 2). Alpha and beta radiation show a low to medium penetrating power, and they can be stopped by a sheet of paper and aluminium, respectively. On the contrary, gamma rays are constituted by photons having no mass and no charge, and for this reason, they are able to penetrate dense materials. Gamma rays show a less ionizing power than alpha and beta particles, and they can be halted by lead or concrete barriers

Even though they behave differently when they interact with matter, all types of radiation are harmful to humans. The more common health effects induced by natural radioactivity are living cell damages and DNA and RNA modifications. Exposure to radioactive materials can provoke several diseases (e.g. cancer, anaemia necrosis, hereditary effects and death).

There are two types of exposure: external and internal. Radioactive sources located outside the human body produce external exposure, and the main contributor is the gamma radiation originating from the decay of terrestrial radionuclides. Conversely, internal exposure is related to the intake of radioisotopes into the human body. Inhalation of air and dust together with ingestion of food and water are the two main processes concurring to the internal exposure. In this context, radon is considered the main contributor to the effective dose induced by inhalation.

Several radiation quantities are used to assess the biological hazard for humans caused by radioactivity. The most common are the absorbed dose (D), the equivalent dose (H) and the effective dose (E).

The absorbed dose is measured in Gray (Gy), and represents the amount of energy collected in tissue or organs per unit mass ($1\text{Gy}= 1\text{ J/kg}$). The equivalent dose (H) was introduced because different types of radiation show a different interaction with the human body. Various types of radiation are weighted in order to correctly describe the effect induced on tissues and organs. E is measured in Sieverts (Sv) and the general formula is:

$$H = \sum w_R D_{T,R} \quad [14]$$

where $D_{T,R}$ is the mean absorbed dose in tissue or organ T due to radiation R , and w_R is the weighting factor depending on the type and energy of the radiation. For example, the weighting factor of alpha particles is 20 whereas that of gamma and beta radiation is 1. Finally, the effective dose (E) represents the equivalent dose weighted for all organs and tissue. The effective dose is calculated by the following formula:

$$E = \sum w_T H \quad [15]$$

where w_T is the weighting factor for tissue T . The effective dose is measured in Sievert.

Table 3. Average radiation dose from natural sources (data from UNSCEAR, 2000).

| Source | Average effective dose (mSv) | |
|------------------------------|------------------------------|------------|
| <i>External exposure</i> | | |
| Terrestrial gamma rays: | | |
| - Outdoor | 0.07 | |
| - Indoor | 0.41 | |
| Total terrestrial gamma rays | | 0.48 |
| Cosmic rays | | 0.39 |
| <i>Internal exposure</i> | | |
| Inhalation | | 1.26 |
| Ingestion | | 0.29 |
| Total | | 2.4 |

Every year, all people in the world receive an average effective dose of 2.4 mSv due to ionizing radiation from natural sources (UNSCEAR, 2000). This value is also known as natural background radiation. In comparison, a computed tomography of the abdomen and pelvis induces around 6 mSv whereas a chest X-ray analysis accounts only for 0.1 mSv.

The worldwide average annual effective dose is the sum of different contributions including 0.48 mSv due to gamma rays originating from the decay of terrestrial radionuclides, 0.39 mSv due to cosmic rays and 1.26 and 0.29 mSv from inhalation and ingestion of radionuclides, respectively (Table 3). Unfortunately, several factors (e.g. living in seismic areas or where soils show high contents of U and Th) can be

responsible for an increase of the natural background radiation well above the worldwide average of 2.4 mSv/y, resulting in a significant enhancement of the radiological hazard.

4.3 Radon releasing from solid materials

The release of radon from solid materials is a complicated phenomenon. Solids, such as soils and rocks, are constituted by interstitial spaces and grains, and three different processes regulate the release of radon:

- emanation: radon atoms escape from solid grains reaching the interstitial space.
- transport: once radon is free to migrate, it can move toward the surface of the solid by diffusion and/or advection.
- exhalation: finally radon atoms cross the surface-atmosphere interface.

Among those processes, emanation has a key role, and for this reason, during the last decades, it became a hot topic (see the Sakoda & Ishimori, 2017 for a complete review about emanation). Actually, two concurring processes rule radon emanation: alpha recoil and diffusion. The “recoil” is the distance travelled by the “newly formed” radon atom in consequence of the alpha decay of the parent radionuclide (i.e. radium), whereas diffusion is the movement of radon atoms due to concentration gradients. Therefore, we can define the emanation (Em) through the equation:

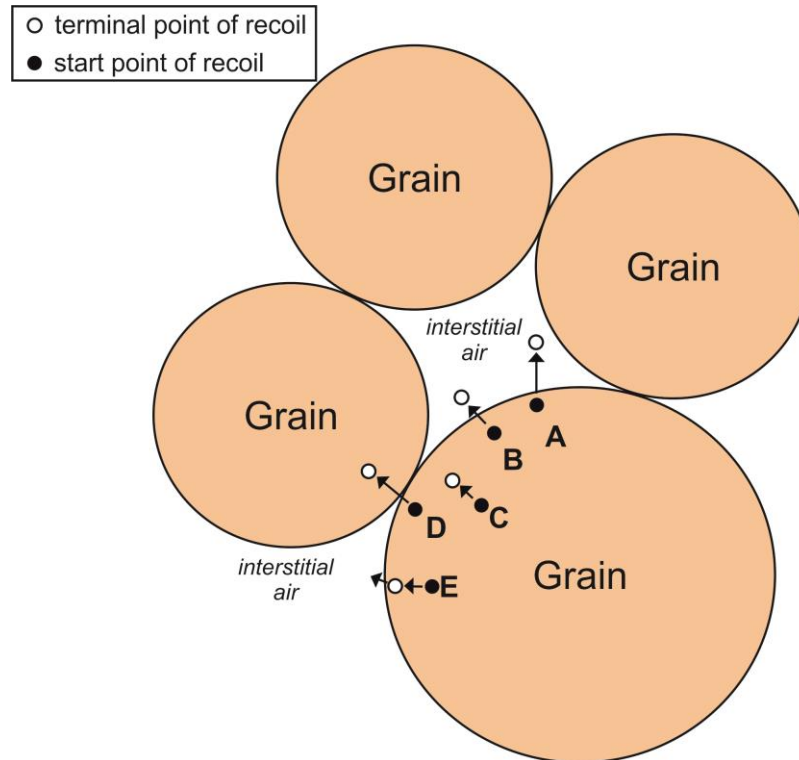
$$Em_{total} = Em_{recoil} + Em_{diffusion} \quad [16]$$

where Em_{recoil} and $Em_{diffusion}$ are the alpha recoil and diffusion components, respectively.

The radon diffusion coefficient in solid materials is very low (10^{-25} - 10^{-69} m² s⁻¹ in minerals; Leach et al., 1982). Therefore, alpha recoil is considered to be the main contributor to radon emanation (see Sakoda et al., 2011 and references therein).

Figure 13 highlights that only a part of radon generated by radium decay actually escapes from the solid grains. For instance, alpha recoil allowed radon atoms in points A, B and E to reach the interstitial air becoming free to migrate by entering the porous system of the sample, whereas atoms in points C and D are not emanated.

All those considerations forced the scientific community to introduce two parameters to evaluate the attitude of solid materials to release radon: the emanation coefficient and the exhalation rate.



Figur13. Scheme of radon emanation (modified from Sakoda et al., 2011). See the text for details.

The emanation coefficient (also known as emanation factor, emanation fraction or emanation power) is the ratio between the number of radon atoms escaping the solid grains and the number of atoms generated by the radioactive decay of radium.

This ratio ranges from around 0.1% to around 40% in soils and rocks (Sakoda et al., 2011). The emanation coefficient is controlled by several parameters such as temperature, moisture, specific surface, radium distribution, grain size, grain shape, pore size, inner network, interstitial material, density, pressure and mineralogy (e.g. Sakoda et al., 2011; Bikit et al., 2011; Krupp et al., 2017; Zhang et al., 2019).

The exhalation rate is defined as the radon activity discharged into the atmosphere per unit of time. It can be referred as the total mass of the solid media (mass exhalation rate) or as the active surface able to release radon (surface exhalation rate).

The techniques employed to assess the release of radon from solid materials are divided into active and passive (see Petropoulos et al., 1999). Active methods measure the radon concentrations by using commercially available integrated instruments (e.g. portable α -counting system), scintillation cells, SSNTDs and photo-

multipliers. Conversely, passive methods rely on activated charcoal to absorb and count the released radon.

Generally, active methods are the most used. Samples are enclosed in airtight containers or vessels where the radon concentration grows in the air volume. Then, two different procedures can be followed, taking into account that usually only ^{222}Rn is considered because of the short half-life of ^{220}Rn :

1. continuous (or quasi-continuous) measurements: the radon concentration is continuously (or quasi-continuously) measured by integrated instrumentations, which can be placed either inside the container or be connected to it through a piping system forming a closed circuit in which air continuously circulates. The growing radon concentration in the container increases exponentially and tends to an equilibrium value that, if back diffusion (the emanated radon coming back into the solid by diffusion) and leakage (i.e. radon escaped from a not completely airtight measurement system) are absent, is reached in about 30 days. Otherwise, if back diffusion and/or leakage occur, the time needed to reach the equilibrium concentration results shorter (De Martino et al., 1998).
2. measurements after the establishment of the secular equilibrium between radium and radon: the sample is closed in a container for around 4 weeks, in order to ensure the establishment of the secular equilibrium between radium and radon. Then, the radon value at equilibrium is measured by one of the aforementioned analytic techniques (i.e. α -counting system, scintillation cells, SSNTDs and photo-multipliers).

It is noteworthy to mention, that in order to determine the radon emanation coefficient it is required to know the value of the activity concentration of radium, which is usually measured by spectroscopic techniques (e.g. γ spectrometry).

Moreover, it should be underlined that a unique protocol to investigate the amount of radon release solids does not exist. For instance, in several works, samples have been crushed and sieved before measurements. Alternatively, other works reported the execution of experiments on natural rock blocks or slabs realized by cutting and shaping samples. Thus, different conditions have to be chosen on the basis of the aim of the study (Sakoda et al., 2011).

4.4 Materials

4.4.1 Samples

In order to investigate the amount of radioactivity released from the crystalline basement of the CPO in northeastern Sicily, ten samples of crystalline rocks were collected. Locations and coordinates of the sampled rocks are listed and plotted in Table 4 and Figure 14, respectively.

Table 4. Location and coordinates of the collected samples.

| Sample ID | Type of rock | Tectonic Unit | Locality | North | East |
|------------------|-----------------------------|----------------------|-----------------|--------------|-------------|
| ASP1 | Late Variscan monzogranite | Aspromonte | Tono | 4237468 | 549973 |
| ASP2 | Orthogneiss | Aspromonte | Marmara | 4235290 | 541451 |
| ASP3 | Paragneiss | Aspromonte | Dinnammare | 4223617 | 540613 |
| ASP4 | Amphibolite gneiss | Aspromonte | Dinnammare | 4223594 | 540971 |
| ASP5 | Marble | Aspromonte | Capo Tindari | 4220994 | 504626 |
| MAN1 | Phyllite | Mandanici | Percia Rovetti | 4211439 | 516590 |
| SMU1 | Metapelite | St. Marco d'Alunzio | Fracianida | 4207313 | 516633 |
| LTU1 | Metapelite | Longi-Taormina | P.lla Pandolfo | 4191929 | 524118 |
| LTU2 | Felsic porphyroid | Longi-Taormina | Castelmola | 4190603 | 524346 |
| LTU3 | Intermediate meta-volcanite | Longi-Taormina | Castelmola | 4190149 | 524643 |

The collected samples include the most common rocks outcropping along the “Sicilian” CPO:

1. from the Aspromonte Unit: Late Variscan monzogranite (ASP1 sample), orthogneiss (ASP2 sample), paragneiss (ASP3 sample), amphibolite gneiss (ASP4 sample) and marble (ASP5 sample);
2. from the Mandanici Unit: phyllite (MAN1 sample);
3. from the St. Marco d'Alunzio Unit: metapelite (SMU1 sample);
4. from the Longi-Taormina Unit: metapelite (LTU1 sample), felsic porphyroid (LTU2 sample) and intermediate meta-volcanite (LT3 sample).

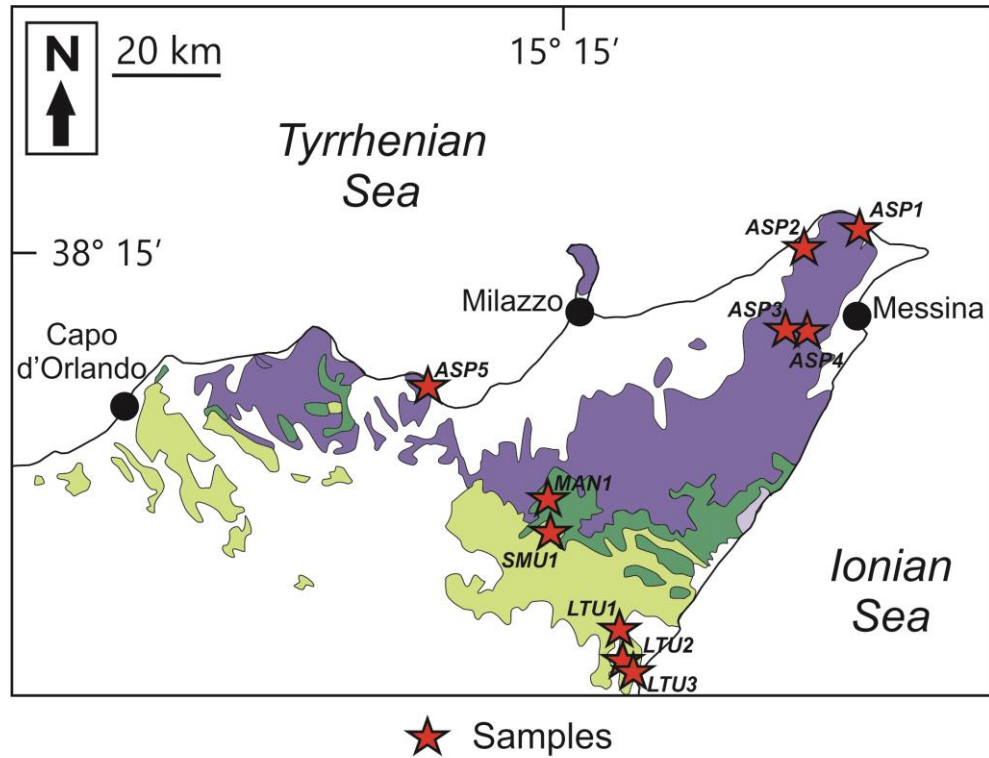


Figure 14. Geological sketch map of the Peloritani Mountains (modified from Cirrincione et al., 2015) with the location of the collected samples (red stars).

Concerning the use of these rocks in construction, the ASP2, ASP3 and ASP5 samples are currently mined and used as building materials. Conversely, the ASP4, MAN1, SMU1, LTU1, LTU2 and LTU3 samples are not used in construction, and therefore we examine only the possible effects deriving from their potential use. Moreover, ASP1, ASP2 and ASP3 compositions are representative of the “Sabbie and ghiaie of Messina” formation, which is extensively extracted around the city of Messina and used as inert material in bulk amounts (e.g. concrete).

4.4.2 Sample preparation

Before analyses, all collected samples were carefully cleaned and the macroscopic altered portions were removed. After that, each sample was crushed in an agate mill and sieved in order to obtain a particle size less than 2 mm. Then, samples were dried in an oven for 24 h at a temperature of 105°C and then cooled in a desiccator to constant weight. This procedure has already been adopted in Lee et al. (2018) and Sabatino et al. (2019).

Samples were sealed in airtight containers for more than four weeks, in order to secure the attainment of the secular equilibrium between ^{226}Ra and their daughters. Then samples were analysed for gamma ray spectroscopy at the laboratories of the ARPACal Reggio Calabria Department and for the radon release at the laboratories of the MIFT Department of the Messina University.

4.5 Method

4.5.1 Gamma spectroscopy

Samples were packed in polyethylene plastic vials of 20 mL of volume and analysed for gamma spectrometry. Thus, a homogeneous geometry around the detector is obtained. Obviously, the net weights of all samples had been measured before the analysis. Analyses were performed under the supervision of Dr. Francesco Caridi.

Samples were counted for 70000 s and analysed to determine the ^{226}Ra , ^{232}Th and ^{40}K activity concentrations. The ^{226}Ra activity concentration was determined through the 295.21 keV and 351.92 keV ^{214}Pb and 1120.29 keV ^{214}Bi γ -lines. The ^{232}Th activity concentration was calculated by the 911.21 keV and 968.97 keV ^{228}Ac γ -lines whereas, for ^{40}K , the evaluation was performed from its γ -lines at 1460.8 keV. The measurement setup was composed of two Ortec HPGe detectors and integrated digital electronics. The first detector is a negative biased detector (GMX) with FWHM of 1.94 keV, peak to Compton ratio of 65:1 and relative efficiency of 37.5% at 1.33 MeV (^{60}Co). The second one is a positive biased detector (GEM) with FWHM of 1.85 keV, peak to Compton ratio of 64:1 and relative efficiency of 40% at 1.33 MeV (^{60}Co). The detectors were shielded from the environmental background by using lead shields with copper and tin lining. Efficiency and energy calibrations were carried out by suitable standards, such as the Eckert and Ziegler Nuclitec GmgH traceable multinuclide

radioactive standards (number AK 5901). They cover the energy range 59.54-836 keV, and they were customized to clone the identical geometries of samples in a water-equivalent epoxy resin matrix. Moreover, for the efficiency transfer factors calculations with respect to the vial sample geometry, the ANGLE 4 code was employed.

Data acquisition was performed by the Gamma Vision (Ortec) software was used (see Caridi et al., 2016). Energy, half-life and other key information about the investigated radionuclides are contained in a library that was used to identify the spectrum and to perform activity concentration calculations and corrections (e.g. self-absorption).

The activity concentrations of the radioisotopes were calculated using the following equation:

$$C = \frac{N_E}{\varepsilon_E \gamma_d M t} \quad [17]$$

where N_E is the net area of the radioisotope photopeak, ε_E and γ_d indicate the efficiency and yield of the photopeak, M represents the mass of the sample (g) and t indicates the live time (s).

The total uncertainty, coverage factor $k=2$, was calculated considering the single uncertainty of the counting estimation, calibration source, efficiency calibration, background subtraction and γ -branching ratio (Caridi et al., 2016).

4.5.2 Outdoor radiological hazard due to gamma radiation: the absorbed dose and the annual effective dose

As stated above, the main contribution to the outdoor effective doses is the gamma radiation coming from the decay of terrestrial radionuclides in rocks and soils. Gamma rays are able to cross the soil-air interface producing external exposure to people. The activity of ^{226}Ra , ^{232}Th and ^{40}K is adopted to calculate the absorbed and the effective dose received by a person who stays over an area formed of the studied rocks.

The absorbed dose in the air (D) is expressed in nGy h^{-1} , and it is determined by using conversion coefficients (UNSCEAR, 2000; Rafique et al., 2014; Srinivasa et al., 2019) as follows:

$$D = 0.462C_{Ra} + 0.604C_{Th} + 0.0417C_K \quad [18]$$

where C_{Ra} , C_{Th} and C_K are the activity concentrations in Bq kg⁻¹ of ²²⁶Ra, ²³²Th and ⁴⁰K in the analysed samples, respectively.

D is used to estimate the annual effective dose equivalent outdoor ($AEDE_{outdoor}$) by the following equation (UNSCEAR, 2000):

$$AEDE_{outdoor} = D \cdot 8760 h \cdot F \cdot 0.7 \cdot 10^{-6} \quad [19]$$

where 0.7 (Sv Gy⁻¹) is the conversion coefficient from absorbed dose to effective dose whereas F is the outdoor occupancy factor (20%). The annual effective dose equivalent is expressed in mSv y⁻¹.

4.5.3 Exposure to gamma radiation originating from building materials: radiological indexes

Building materials used in the field of construction derive from soil and rocks, which usually contain natural radioisotopes. Generally, rocks are used as ornamental and pavement stones, while soils and crushed rocks are used as inert materials in concrete. Building materials might induce harmful effective doses to humans due to the radiation emitted from radioisotopes inherited from their natural raw materials.

In order to evaluate the health hazard derived from the Peloritani rocks, if they are used as building materials, a number of radiological indexes were calculated: the gamma index, the alpha index, the radium equivalent index, the external hazard index and the internal hazard index.

The gamma index, also known as activity concentration index (I_γ : EC, 1999; 2013/59 Euratom directive), was calculated to assess the exposure to the gamma radiation with the following formula:

$$I_\gamma = \frac{C_{Ra}}{300 \text{ Bq kg}^{-1}} + \frac{C_{Th}}{200 \text{ Bq kg}^{-1}} + \frac{C_K}{3000 \text{ Bq kg}^{-1}} \quad [20]$$

where C_{Ra} , C_{Th} and C_K are the activity concentrations (in Bq kg⁻¹) of ²²⁶Ra, ²³²Th and ⁴⁰K, respectively.

The alpha index (I_α : Nordic, 2000) can be used as a screening tool to preliminarily estimate the hazard connected to the indoor radon. It depends on the activity concentration of ²²⁶Ra (in Bq kg⁻¹) as follows:

$$I_\alpha = \frac{C_{Ra}}{200 \text{ Bq kg}^{-1}} \quad [21]$$

The radium equivalent index (Ra_{eq}) is based on the assumption that 1 Bq kg⁻¹ of ²²⁶Ra, 0.7 Bq kg⁻¹ of ²³²Th, and 13 Bq kg⁻¹ of ⁴⁰K induce the same gamma radiation dose (Hewanamma et al., 2001). According to Beretka & Matthew (1985), it is determined with the given equation:

$$Ra_{eq} = C_{Ra} + 1.43 C_{Th} + 0.077 C_K \quad [22]$$

where C_{Ra} , C_{Th} and C_K are the activity concentrations (obviously expressed in Bq kg⁻¹) of ²²⁶Ra, ²³²Th and ⁴⁰K, respectively.

Moreover, Beretka & Matthew (1985) defined the external (H_{ex}) and internal (H_{in}) hazard indexes. They are calculated by using the following equations:

$$H_{ex} = \frac{C_{Ra}}{370 \text{ Bq kg}^{-1}} + \frac{C_{Th}}{259 \text{ Bq kg}^{-1}} + \frac{C_K}{4810 \text{ Bq kg}^{-1}} \quad [23]$$

$$H_{in} = \frac{C_{Ra}}{185 \text{ Bq kg}^{-1}} + \frac{C_{Th}}{259 \text{ Bq kg}^{-1}} + \frac{C_K}{4810 \text{ Bq kg}^{-1}} \quad [24]$$

where, as for other indexes, C_{Ra} , C_{Th} and C_K are the mean activity concentrations of ²²⁶Ra, ²³²Th and ⁴⁰K, respectively. The external index evaluates the gamma radiation hazard, whereas the internal index gives information about the internal exposure to carcinogenic radon.

4.5.4 Radon emanation measurements

The release of ²²²Rn was evaluated by enclosing 0.8 L of each sample in an airtight container whose volume is equal to 8 L (Fig. 15).

After that, the container was connected to a dryer unit filled with drierite (calcium sulphate; CaSO₄) and to an electronic α spectrometer (RAD7, Durridge Co.) through a piping system forming a closed loop in which air circulates (Fig. 16). The experimental setup is rather similar to that reported in IAEA (2013) and in Arabi et al. (2015, 2016). Moreover, a silicon sealing was installed along the piping system and the valves in order to reduce the air leakage from the setup.

The RAD7 α spectrometer (Durridge Co.) was used to measure the radon concentration in the air volume of the container. The RAD7 (see the RAD7 manual at the site www.durridge.com) relies on a solid-state ion-implanted planar silicon alpha detector, which is located inside an internal cell of 0.7 L (Fig. 17A). The air is transferred into the internal cell by an internal pump.

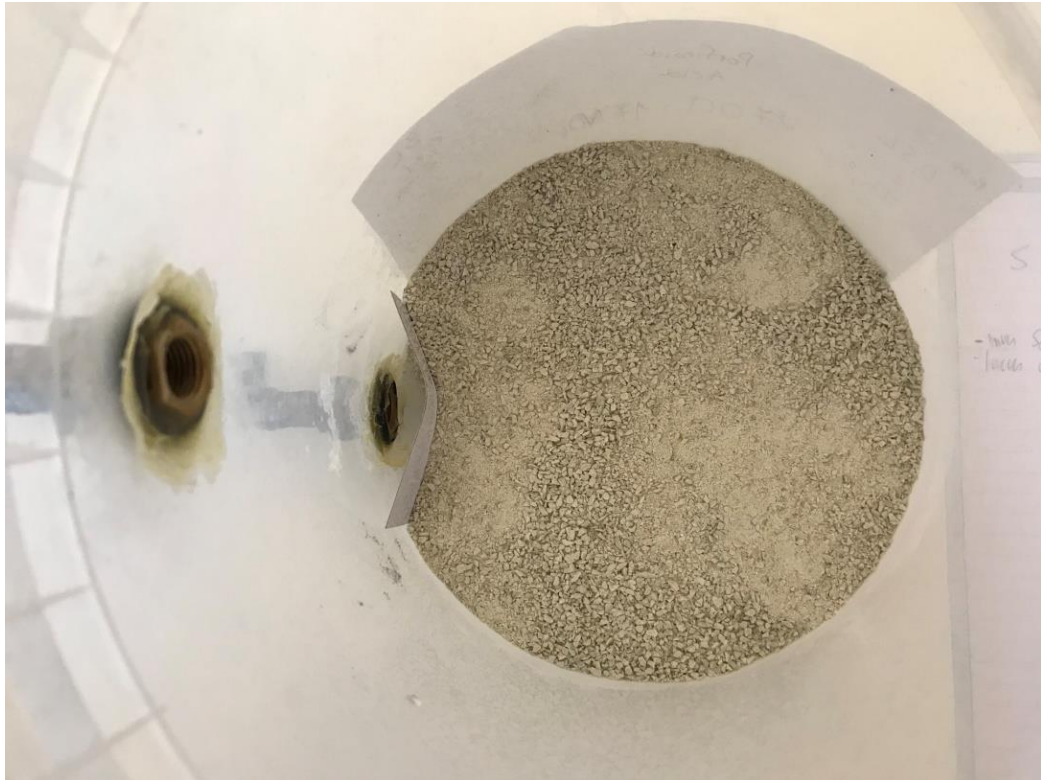


Figure 15. 0.8 L of sample material is enclosed in a container of a capacity of 8 L. The top surface of the sample is flat (i.e. horizontal) and has an area of 0.0254 m^2 .

The ^{222}Rn activity concentration is measured through the activity of relative daughters (i.e. ^{218}Po and ^{214}Po isotopes) at secular equilibrium with the parent.

In Chapter II is explained that at equilibrium, the parent and daughter activity concentrations are the same. Concerning radon, the equilibrium between ^{222}Rn and ^{218}Po is attained after around 10 minutes, whereas between ^{222}Rn and ^{214}Po after around 3 hours.

The alpha detector is located at the centre of the internal cell, which has a hemispherical shape. The internal cell is coated on the inside with an electrical conductor charged by a high voltage power circuit, which is able to develop a potential of 2000/2500 V with respect to the alpha detector.

Radon nuclei that decay within the internal cell produce transformed nuclei (i.e. polonium atoms) as positively charged ions. The electric field inside the cell drives the positively charged ions straight onto the alpha detector. The short-lived polonium nuclei that decay upon the alpha detector's active surface, emitted alpha particles having a 50% probability of entering the detector. The beta particles are not detected.

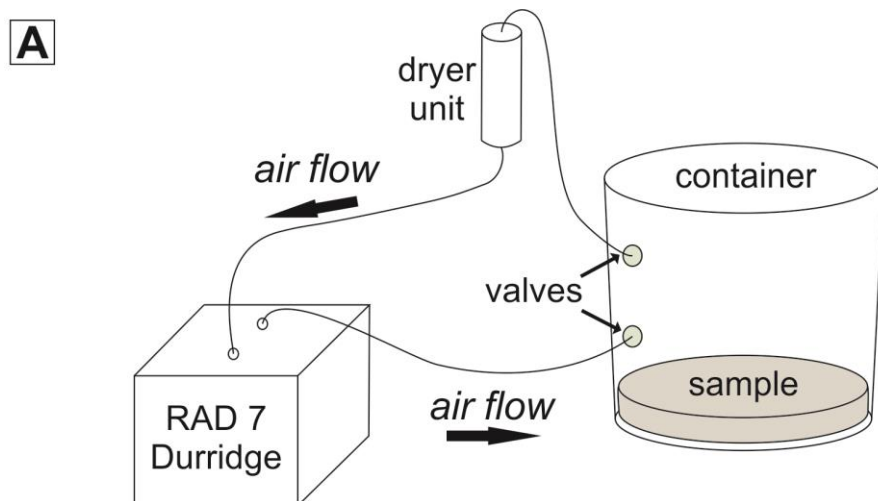


Figure 16. (A) Schematic diagram and (B) view of the setup used for radon emanation measurement. The air from the container moves into the dryer unit, and then into the RAD7 monitor for the ^{222}Rn measurement; after that, the air returns to the container forming a closed loop.

An alpha particle entering the detector produces an electrical signal proportional in strength to the energy of the alpha particle. Obviously, different isotopes have different alpha energies (i.e. every alpha emitter releases alpha particles of characteristic energy), and therefore they produce different strength signals. The RAD7 produces

spectra on a scale of alpha energies from 0 to 10 MeV (Fig. 17B). Spectra are divided into 4 main window energy ranges. Particularly, the ^{222}Rn daughters produce alpha particles in the range of 6 to 8 MeV. For instance, window A covers the energy range of 5.40 to 6.40 MeV and includes the 6.00 MeV alpha particles from ^{218}Po . Contrastingly, the ^{214}Po peak is at 7.69 MeV and fall within windows C. The RAD7 microprocessor converts all the alpha particle counts into the radon concentration. In the experiment, the “Sniff” mode was adopted. By using this mode, the ^{222}Rn activity concentration is determined only from the ^{218}Po alpha peak.

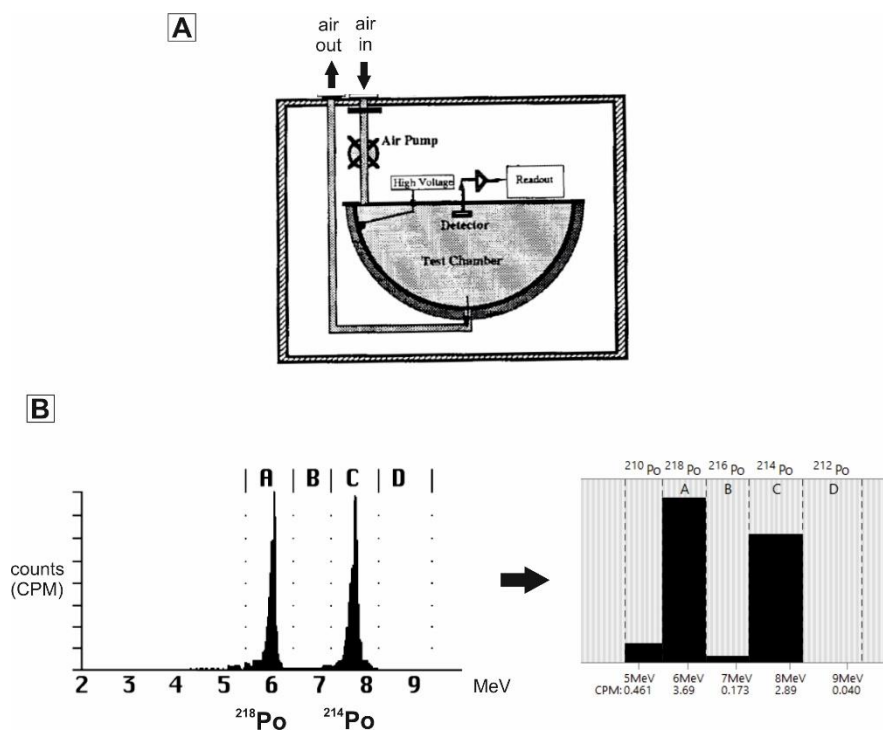


Figure 17. (A) Schematic sketch of the RAD7 internal cell and (B) example of spectrum released by the RAD7; ^{218}Po and ^{214}Po peaks are at 6.00 and 7.69 MeV, respectively. Modified from the RAD7 manual (site www.durridge.com).

Samples were sealed in the container causing the exponential growth of the radon activity concentration in the air volume. After four weeks, the establishment of the secular equilibrium between ^{226}Ra and ^{222}Rn was attained, and the ^{222}Rn activity concentration, released from rock samples into the air volume of the container, reached an equilibrium value, which was measured by the RAD7. It was used a cycle of four hours composed of sub-cycles of 20 minutes. After that, the ^{222}Rn emanation

coefficient (ε) was determined by the following equation (IAEA, 2013; Arabi et al., 2015, 2016):

$$\varepsilon = \frac{VC_{Rn}}{MC_{Ra}} \quad [25]$$

where C_{Rn} (Bq m⁻³) is the measured radon activity concentration at equilibrium, C_{Ra} (Bq kg⁻¹) is the radium activity concentration determined through gamma spectroscopy, M (kg; see Table 7) is the mass of the sample and V (8.3 × 10⁻³ m³) is the effective volume of the system, calculated by taking into account the volume of the container, of the sample, of the loop system and of the RAD7 internal cell. Moreover, the pore volume of the samples is <10% with respect to the effective volume of the system to prevent back diffusion effects (Petropoulos et al., 2001; Tuccimei et al., 2006).

The homemade measurement system is not completely airtight, so a fraction of radon is able to escape the container. This fraction can be expressed as a value called “leakage from container” (λl), having the same unit of the decay constant (i.e. h⁻¹). It was determined by continuously measuring the ²²²Rn activity released in the container from one of the samples (i.e. the Mandanici phyllite), at intervals of 2 hours for 5 days. The series of the measured ²²²Rn concentrations were fitted to the following equation, expressing the radon activity growth as a function of time (Dentoni et al., 2020):

$$C_t = C_0 e^{-t(\lambda + \lambda l)} + C_m (1 - e^{-t(\lambda + \lambda l)}) \quad [26]$$

where C_t is the ²²²Rn concentration at time t , C_0 and C_m are the ²²²Rn concentration at $t=0$ and at maximum, respectively, and λ (7.56 × 10⁻³ h⁻¹) is the radon decay constant. The experimental data fitted very well with the model described by equation 26, and the leakage of the experimental setup (λl) was determined to be 6.96 × 10⁻³ h⁻¹ (Fig. 18).

By knowing C_{Rn} and λl , it was possible to determine the ²²²Rn exhalation rate (E) as follows (IAEA, 2013; Dentoni et al., 2020):

$$E = \frac{C_{Rn}(\lambda + \lambda l)V}{X} \quad [27]$$

where X is the surface area of the sample (0.0254 m²) if the exhalation rate is expressed as surface exhalation rate (E_S , Bq m⁻² h⁻¹), or the mass of the sample (kg; see Table 7) if E is expressed as mass exhalation rate (E_M , Bq kg⁻¹ h⁻¹).

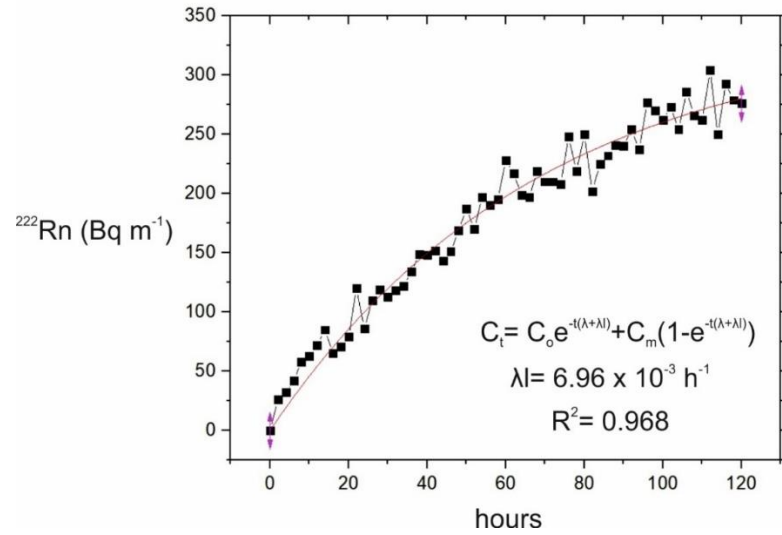


Figure 18. The exponential growth of the ^{222}Rn activity concentration for the Mandanici phyllite sample. The ^{222}Rn activity concentration was measured at intervals of 2 hours for 5 days. Results were fitted to equation 26 in order to determine the leakage from container (λ).

Radon values measured by the RAD7 are associated to uncertainty expressed as 2σ (confidence interval of 95%) which is based on counting statistics. Moreover, regarding the emanation coefficient, since ^{226}Ra e ^{222}Rn are both affected by uncertainties, and the coefficient was derived from the quotient of these two values, the uncertainty associated to the emanation coefficient is determined by considering the relative errors:

$$\frac{\Delta\varepsilon}{|\varepsilon|} = \frac{\Delta C_{Ra}}{|C_{Ra}|} + \frac{\Delta C_{Rn}}{|C_{Rn}|} \quad [28]$$

4.5.5 Calculation of indoor radon concentrations and indoor effective doses

Figure 19 shows that indoor radon concentration accounts for three main contributors:

1. radon atoms that are continuously released in soil and rocks can enter buildings from cracks and discontinuities in floor and walls. They represent the major source of indoor radon, and underground spaces and ground floor rooms are the most exposed places;
2. the second major source of indoor radon derive from radon exhaled from building materials;

- radon dissolved in domestic waters is released into the air every time water is used.

By knowing the surface exhalation rate of building materials, it is possible to estimate the amount of radon released in a room from walls, floor and ceiling ($Ci_{Rn(bm)}$, Bq m⁻³) by the following equation (Stoulos et al., 2003; Ujic et al, 2010; Dentoni et al., 2020):

$$Ci_{Rn(bm)} = \left[\sum_{i=1}^n w_{si} \cdot E_{Si} \right] \frac{S}{V\lambda_v} \quad [29]$$

where E_{Si} (Bqm⁻²h⁻¹) is the surface exhalation rate of the building material, w_{si} is the fractional usage of the building material, S/V (m⁻¹) is the surface to volume ratio of the room and λ_v (h⁻¹) is the annual average ventilation rate.

The annual effective dose induced by indoor radon originated from building materials ($Hi_{Rn(bm)}$, μSv y⁻¹) is determined considering an indoor occupancy factor of 0.8, a ²²²Rn equilibrium factor of 0.4, and a dose conversion factor for ²²²Rn of 9 nSv (Bq h m⁻³)⁻¹ as reported in UNSCEAR (2000):

$$Hi_{Rn(bm)} = Ci_{Rn(bm)} \cdot 8760 h \cdot 0.8 \cdot 0.4 \cdot 9 \cdot 10^{-3} \quad [30]$$

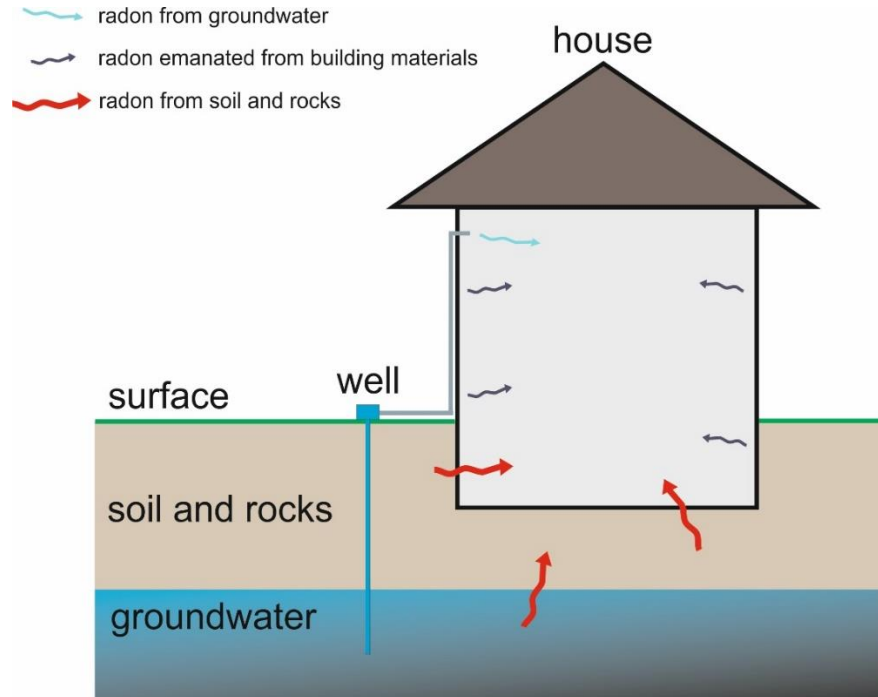


Figure 19. Indoor radon pollution depends on radon coming from groundwater (pale blue arrow), on radon exhaled from building materials (dark blue arrows) and on radon from soil and rocks entering buildings due to cracks in walls and floor (red arrows).

4.6 Results and discussion

4.6.1 Activity concentration of ^{226}Ra , ^{232}Th and ^{40}K

Table 5 reports the activity concentrations values of ^{226}Ra , ^{232}Th and ^{40}K in the investigated samples (unfortunately, I did not receive permission from ARPACal Reggio Calabria Department to publish the γ spectra).

^{226}Ra , ^{232}Th and ^{40}K activity concentrations range from (17 ± 4) to (56 ± 8) Bq kg⁻¹, from (14 ± 3) to (77 ± 14) Bq kg⁻¹ and from (167 ± 84) to (1760 ± 242) Bq kg⁻¹, respectively.

LTU2 (felsic porphyroid) and LTU3 (meta-volcanite) samples exhibit the highest activity of ^{226}Ra (56 ± 8 Bq kg⁻¹) and ^{40}K (1760 ± 242 Bq kg⁻¹), respectively. Regarding the ^{232}Th , ASP2, ASP3, MAN1 and LTU3 samples display the highest values (> 60 Bq kg⁻¹).

Contrastingly, the ASP5 sample shows the lowest concentration values for both ^{226}Ra (17 ± 4 Bq kg⁻¹) and ^{232}Th (14 ± 3 Bq kg⁻¹), whereas the ASP4 sample is characterized by the lowest ^{40}K value (167 ± 84 Bq kg⁻¹).

Table 5. Activity concentrations of ^{226}Ra , ^{232}Th and ^{40}K detected in the samples coming from the metamorphic basement of the Peloritani Belt, along with the calculated values of absorbed dose rate (D) and annual effective dose outdoor ($AEDE_{outdoor}$).

| Sample ID | ^{226}Ra (Bq kg ⁻¹) | ^{232}Th (Bq kg ⁻¹) | ^{40}K (Bq kg ⁻¹) | D (nGy h ⁻¹) | $AEDE_{outdoor}$ (mSv y ⁻¹) |
|-----------|---|---|---|-------------------------------|--|
| ASP1 | 18 ± 4 | 31 ± 9 | 1220 ± 176 | 78 | 0.096 |
| ASP2 | 45 ± 6 | 77 ± 14 | 1345 ± 190 | 123 | 0.152 |
| ASP3 | 40 ± 7 | 68 ± 17 | 1009 ± 163 | 102 | 0.125 |
| ASP4 | 27 ± 5 | 15 ± 2 | 167 ± 84 | 28 | 0.035 |
| ASP5 | 17 ± 4 | 14 ± 3 | 1060 ± 165 | 61 | 0.074 |
| MAN1 | 40 ± 6 | 64 ± 15 | 1063 ± 168 | 101 | 0.124 |
| SMU1 | 25 ± 4 | 36 ± 9 | 595 ± 100 | 58 | 0.071 |
| LTU1 | 34 ± 6 | 39 ± 11 | 674 ± 127 | 67 | 0.083 |
| LTU2 | 48 ± 7 | 47 ± 12 | 1760 ± 242 | 123 | 0.152 |
| LTU3 | 56 ± 8 | 62 ± 14 | 785 ± 135 | 96 | 0.118 |

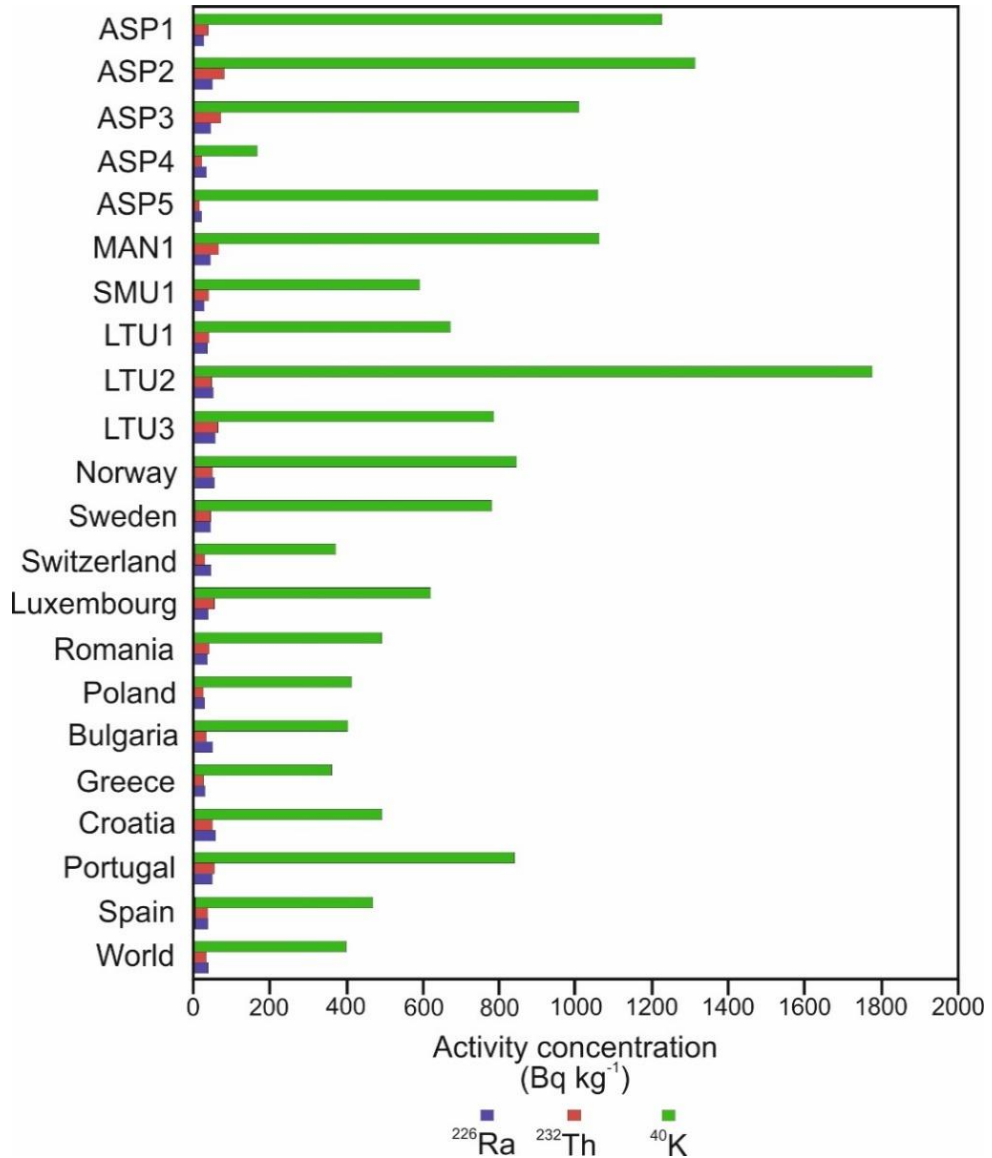


Figure 20. ^{226}Ra , ^{232}Th and ^{40}K activity concentrations in the Peloritani rock samples compared with those of European Countries and with the worldwide average (UNSCEAR, 2020 and references therein).

If we compare the activity concentrations of ^{226}Ra , ^{232}Th and ^{40}K in the crystalline rocks of the Peloritani Mountains with the average worldwide value and with data of other European Countries (UNSCEAR, 2000 and references therein), we can observe that the total amount of specific activity in the studied samples is higher than the reference level for other Countries (Fig. 20). In particular, six analysed rocks (ASP1, ASP2, ASP3, ASP5, MAN1 and LTU2) show ^{40}K activity concentration values higher

than that of both the worldwide average and other European Countries. Conversely, ^{226}Ra and ^{232}Th specific activities result to be rather similar.

Concerning Italy, a dataset including Ra, Th and K activity concentrations determined for the most common building materials was provided by Risica et al. (1999). It can be observed that Peloritani granites and gneisses (ASP1, ASP2 and ASP3 samples) display ^{226}Ra , ^{232}Th , and ^{40}K contents that are similar or lower with respect to the average values for those kinds of rocks, whereas the ASP5 sample is characterized by a higher concentration of terrestrial radionuclides than that detected in other Italian marbles.

4.6.2 Outdoor gamma radiation

The potential hazard effect due to the terrestrial gamma radiation coming from the analysed rocks was estimated by calculating the absorbed dose rate (D) and the annual effective dose equivalent outdoor ($AEDE_{outdoor}$).

The results are reported in Table 5. I want to stress on the fact that both D and $AEDE_{outdoor}$ have to be referred to an outdoor exposure over an area formed of the studied rocks, thereby to the gamma radiation received by people when they are not in houses.

Moreover, if soil is present above the bedrock, the received doses are lower than those for rocks having the same natural activity concentration of ^{226}Ra , ^{232}Th and ^{40}K . This is due to the fact that soils are usually less dense than rocks, and contain a higher percentage of moisture.

The absorbed dose rate induced by the Peloritani basement rocks ranges from 28 to 123 nGy h⁻¹. In Figure 21 is shown a comparison with doses from other Countries obtained by direct measurements (UNSCEAR, 2000 and references therein). Although some samples induce absorbed doses higher than 100 nGy h⁻¹, the average value for the studied rocks results to be 84 nGy h⁻¹, which is comparable with values measured in Spain, Thailand, Malaysia, Portugal and Hong Kong SAR.

The highest $AEDE_{outdoor}$ value (0.152 mSv y⁻¹) was calculated for the ASP2 (orthogneiss) and LTU2 (felsic porphyroid) samples, whereas the lowest values are those calculated for the ASP4 and ASP5 samples: 0.035 mSv y⁻¹ and 0.074 mSv y⁻¹, respectively. Values higher than 0.1 mSv y⁻¹ were determined for the ASP3, MAN1

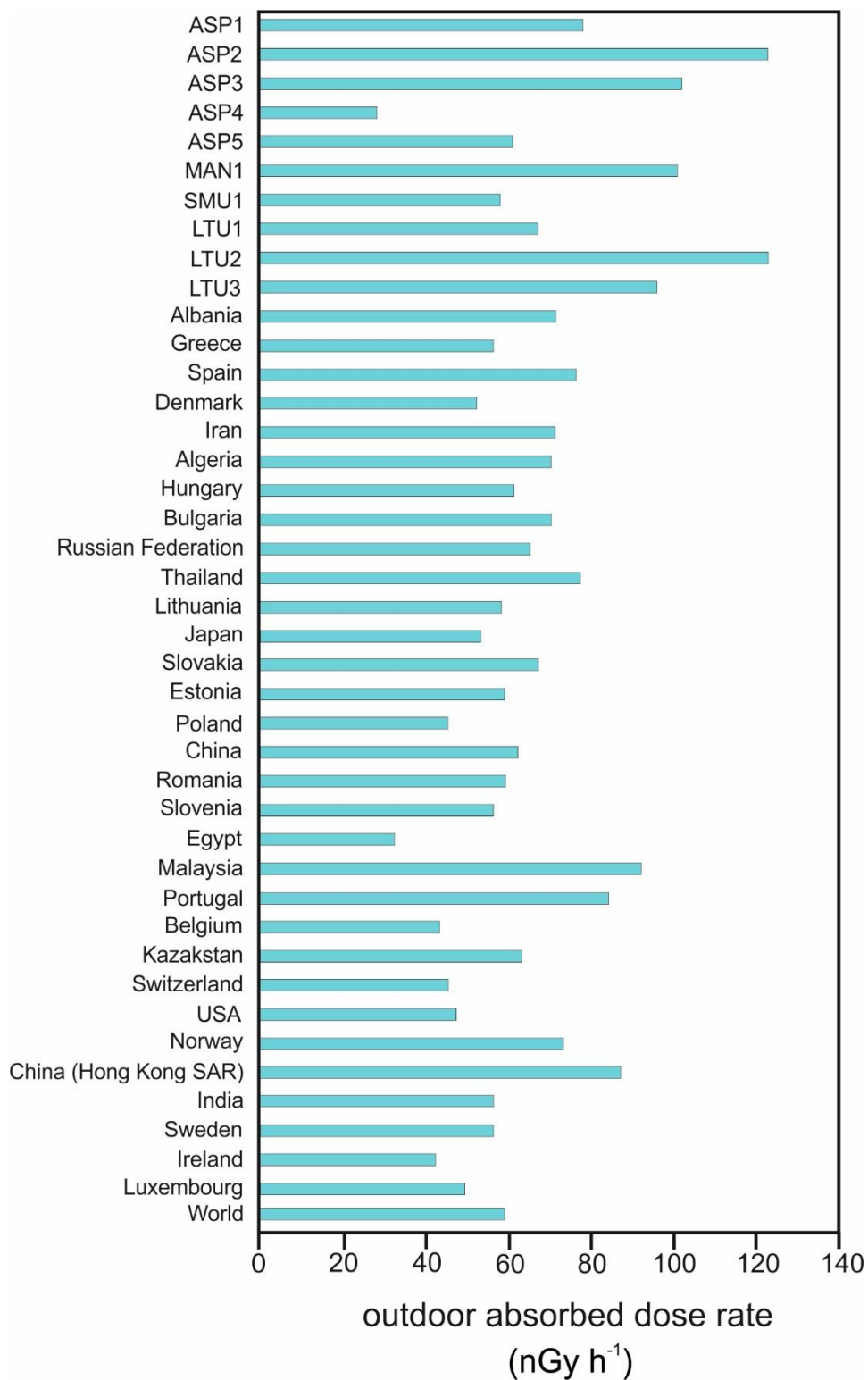


Figure 21. Absorbed dose rate outdoor calculated for the Peloritani rocks compared with that for other Countries and with the worldwide average (UNSCEAR, 2020 and references therein). Values for other countries were obtained by direct measurements and not through the ²²⁶Ra, ²³²Th and ⁴⁰K activity concentrations.

and LTU3 samples.

All the calculated $AEDE_{outdoor}$ values are higher than the worldwide average of 0.07 mSv y^{-1} (UNSCEAR, 2000), except that shown by the ASP4 sample. If we consider also the indoor component of the annual effective dose equivalent ($AEDE_{indoor}$), which can be calculated according to equation 19 by using an occupancy factor of 80%, the sum of $AEDE_{outdoor}$ (values shown in Table 5) and $AEDE_{indoor}$ (values not shown) for all rock samples is below the safety reference limit of 1 mSv y^{-1} adopted by ICRP (1991, 1999) and UNSCEAR (2008). Therefore, those natural materials are not hazardous for inhabitants who live in this area.

4.6.3 Hazard indexes

Among the hazard indexes, the gamma index (I_y) is the most used to evaluate the indoor hazard connected to the exposure to gamma radiation when rocks are used in construction.

The gamma index should be used as a screening tool in order to identify those materials that might produce increases higher than 1 mSv with respect to the annual effective dose. An increase of 1 mSv y^{-1} is achieved with I_y values of 1 if the material is used in bulk amounts, and with I_y values of 6 if the material is used as tiles, boards or other restricted uses (EC, 1999).

According to the Directive 2013/59/Euratom and to the Italian legislative decree no. 101/2020, if building materials produce gamma radiation increases up to 1 mSv y^{-1} , they should be exempted from restrictions.

The analysed rocks show I_y values lower than 1 (Table 6), then the building use should be allowed. However, some of the studied samples (i.e. ASP2, ASP3, MAN1, LTU2 and LTU3 samples) exhibit I_y values ranging from 0.76 to 0.98, slightly below the reference limit. For these rocks, additional measurements and controls are suggested. As regards the “Sabbie and ghiaie of Messina” formation, which is widely used in bulk amounts (as inert in concrete), we have to take into account that the mineralogical composition of these deposits varies from an area to another one in relationship with the prevailing lithology from which the sediments were locally eroded. For this reason, collecting a representative sample of the formation was impracticable. Since radiological properties of sediments are connected with those of the dismantled rocks

from which the sediments originated, I decided to evaluate only the parent rocks of the “Sabbie and ghiaie of Messina” (namely the ASP1, ASP2 and ASP3 samples). Since the parent rocks display a gamma index in the range of 0.62-0.98, the building use of the “Sabbie and ghiaie of Messina” is not harmful.

Other hazard indexes confirm that the Peloritani rocks can be used in construction without restrictions. The reference limit for the alpha index (I_α) and for the external (H_{ex}) and internal (H_{in}) hazard indexes is 1, whereas that for the radium equivalent index (Ra_{eq}) is 370 Bq kg⁻¹ (Beretka & Matthew, 1985; Rafique et al., 2014). All samples exhibit values below those limits (Table 6).

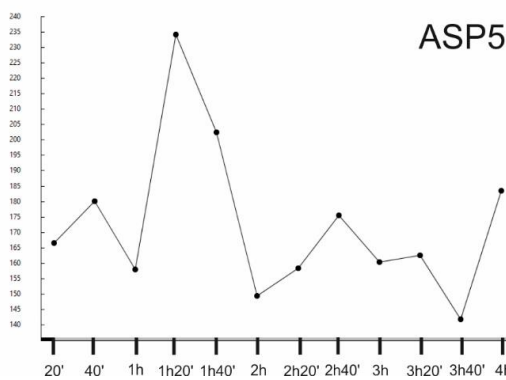
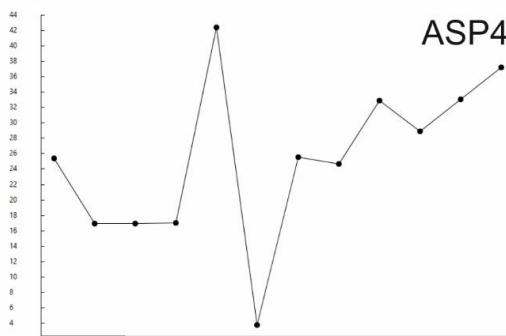
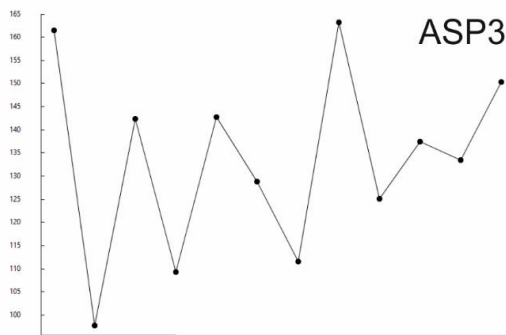
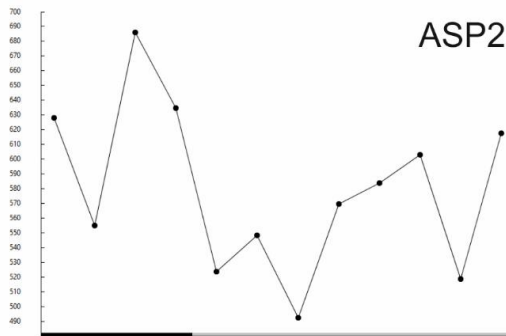
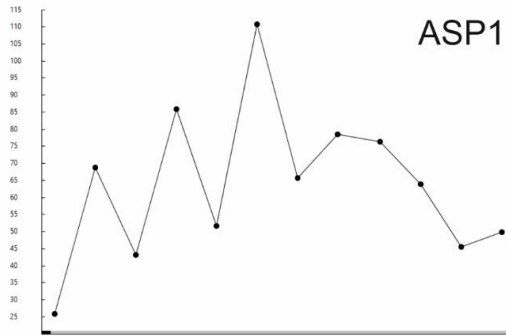
Table 6. Values of the hazard indexes for the Peloritani metamorphites: gamma index (I_γ), alpha index (I_α), radium equivalent index (Ra_{eq}), external hazard index (H_{ex}) and internal hazard index (H_{in}).

| Sample ID | I_γ | I_α | Ra_{eq} | H_{ex} | H_{in} |
|-----------|------------|------------|-----------|----------|----------|
| ASP1 | 0.62 | 0.09 | 156 | 0.42 | 0.47 |
| ASP2 | 0.98 | 0.23 | 259 | 0.7 | 0.82 |
| ASP3 | 0.81 | 0.2 | 215 | 0.58 | 0.69 |
| ASP4 | 0.22 | 0.14 | 61 | 0.17 | 0.24 |
| ASP5 | 0.48 | 0.09 | 119 | 0.32 | 0.37 |
| MAN1 | 0.81 | 0.2 | 213 | 0.58 | 0.68 |
| SMU1 | 0.46 | 0.13 | 122 | 0.33 | 0.4 |
| LTU1 | 0.53 | 0.17 | 142 | 0.38 | 0.47 |
| LTU2 | 0.98 | 0.24 | 251 | 0.68 | 0.81 |
| LTU3 | 0.76 | 0.28 | 205 | 0.55 | 0.71 |

4.6.4 Natural radioactivity due to radon

Experimental results for each sample are illustrated in Figure 22; the amount of ²²²Rn released from the samples into the air volume of the container (C_{Rn}) is also reported in Table 7. C_{Rn} varies from 25 ± 7 Bq m⁻³ of the ASP4 sample to 580 ± 35 Bq m⁻³ of the ASP2 sample

^{222}Rn
(Bq m⁻³)



^{222}Rn
(Bq m⁻³)

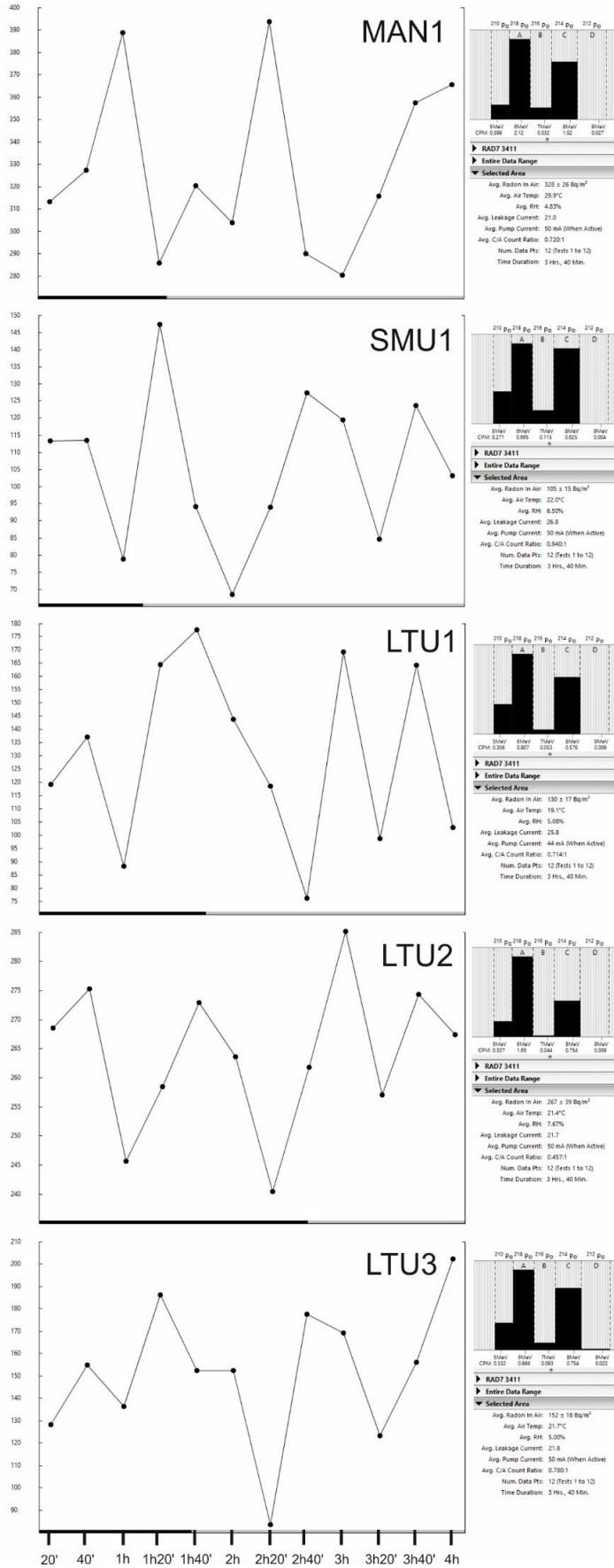


Figure 22. List of experimental results for the studied samples. The ^{222}Rn activity concentration, released from samples into the air volume of the container was measured after attaining the equilibrium between ^{226}Ra and ^{222}Rn by using a cycle of four hours composed of sub-cycles of 20 minutes.

As stated above, the emanation coefficient is a function of various factors, such as grain size, radium distribution, grain shape, temperature, moisture, and mineralogy (e.g. Sakoda et al., 2011; IAEA, 2013; Bikit et al., 2011; Zhang et al., 2019). Moreover, alteration and weathering processes also affect the emanation coefficient (Sato & Nakamura, 1993; Sakoda et al., 2008). All samples show similar experimental conditions (i.e. radium distribution, grain size, moisture and temperature), therefore the mineralogical content and the alteration degree are the only factors accountable for the different emanation coefficients among samples.

The ^{222}Rn emanation coefficient (ϵ), calculated for the crystalline samples through the equation 25, ranges from (0.63 ± 0.3) to $(8.27 \pm 1.6)\%$ (Table 7). These values lie within the representative literature range for soils and rocks (0.1-40%; Sakoda et al., 2011 and references therein).

The monzogranite (ASP1 sample) exhibits an emanation coefficient of $(2.44 \pm 0.9)\%$, which is very similar to that of granites unaffected by secondary alteration processes (~ 1 -2%; Sakoda et al., 2008; Arabi et al., 2016) as altered granites are usually characterized by $\epsilon > 20\%$ (Sakoda et al., 2008).

Emanation coefficients for orthogneiss (ASP2 sample) and paragneiss (ASP3 sample) were derived to be (8.27 ± 1.6) and $(2.30 \pm 0.7)\%$, respectively. Literature values for gneisses vary from 1 to 14% (Barretto 1973; Arabi et al., 2016) and the results of this study fall well within that range.

The amphibolite gneiss (ASP4 sample) displays the lowest emanation coefficient $(0.63 \pm 0.3\%)$. This value probably reflects the presence of amphibole in the ASP4 sample, since the emanation coefficient determined for amphibole mineral phases during experiments performed on single minerals is around 0.8% (Krupp et al., 2017).

The Aspromonte marble (ASP5 sample) was collected in the Capo Tindari area, where the presence of a regional tectonic system (“Aeolian-Tindari-Letojanni fault system”) allows the upward rise of deep fluids along the active tectonic lineaments (Giammanco

et al., 2008). These fluids could have altered the mineralogy of the crystalline rocks. In fact, during sampling and crushing activities, a rotten-eggs smell was detected. This is a typical feature of the occurrence of sulfurous gases, and it could be a strong evidence that Aspromonte marbles had been affected by a low degree alteration. In this case, secondary processes might have modified the pristine ^{222}Rn emanation properties of the ASP5 sample. However, the ^{222}Rn emanation coefficient of the ASP5 sample ($5.99 \pm 1.9\%$) falls within the typical range for carbonate rocks (limestones: 1.6-2.2% and 6.8-13.2%; Barretto, 1973 and Lee et al., 2018, respectively; marbles: 8.5% and 9.54-16.42%; El Afifi et al., 2006 and Misdaq & Amghar, 2005, respectively). Hence, alteration processes supposedly affecting marbles should have a marginal role.

The ε value calculated for the Mandanic Unit phyllite (MAN1 sample) was ($5.81 \pm 1.3\%$), which is similar to literature data for that type of rock (7.7%; Lee et al., 2018). The ^{222}Rn surface (E_S) and mass (E_M) exhalation rates calculated for the Peloritani samples are summarized in Table 7.

E_S and E_M values are in the range of (0.12 ± 0.03)-(2.75 ± 0.17) $\text{Bq m}^{-2} \text{h}^{-1}$ and (2.47 ± 0.69)-(54.02 ± 3.26) $\text{mBq kg}^{-1} \text{h}^{-1}$, respectively.

A comparison between the E_S values of the Peloritani rocks and those of a number of natural materials commonly used in construction in Italy was performed.

The orthogneiss (ASP2 sample) and the phyllite (MAN1 sample) show the highest ^{222}Rn surface exhalation rate (2.75 ± 0.17 and 1.56 ± 0.12 $\text{Bq m}^{-2} \text{h}^{-1}$, respectively). These values are very similar to those determined for many volcanic products coming from the Roman comagmatic province (Latium and Campania Region, Central Italy), as for instance the “Tufo Lionato”, “Peperino”, “Nemi Lava” and “Lapilli” from Colli Albani districts (0.86-1.40, 1.33-3.42, 2.23-2.48 and 2.41-4.01 $\text{Bq m}^{-2} \text{h}^{-1}$, respectively; Tuccimei et al., 2016). Moreover, the E_S of the Peloritani orthogneisses and phyllites is considerably lower than that of building materials showing a high attitude to release radon, such as the “Black pozzolana” from Colli Albani (37 $\text{Bq m}^{-2} \text{h}^{-1}$; Tuccimei et al., 2016), “Tufo rosso” from Vico district (5.47-17.06 $\text{Bq m}^{-2} \text{h}^{-1}$; Tuccimei et al., 2016) and “Tufo giallo napoletano” from Phlegraean Fields (2.66-10.33 $\text{Bq m}^{-2} \text{h}^{-1}$; Tuccimei et al., 2016). Thus, regarding the radon release, we should not consider the orthogneisses and the phyllites as a menace to public health.

The ASP5 sample (Aspromonte marble) displays a ^{222}Rn E_S of $(0.82 \pm 0.09) \text{ Bq m}^{-2} \text{ h}^{-1}$, which is rather high in comparison to common values for carbonate rocks used in construction in Italy (e.g. “Rosso Veronese” and “Travertino”: $0.04 \text{ Bq m}^{-2} \text{ h}^{-1}$ and $0.05\text{-}0.065 \text{ Bq m}^{-2} \text{ h}^{-1}$; Tuccimei et al., 2006), although marble samples analysed in previous studies exhibited surface exhalation rates (e.g. $0.74 \text{ Bq m}^{-2} \text{ h}^{-1}$; Kumar et al., 2014) quite similar to that of the Aspromonte marble.

Concerning the Late Variscan monzogranite (ASP1 sample), the E_S value of $0.30 \pm 0.05 \text{ Bq m}^{-2} \text{ h}^{-1}$ determined in this study is in agreement with data coming from the coeval granitoid rocks occurring in Sardinia ($0.11\text{-}0.91 \text{ Bq m}^{-2} \text{ h}^{-1}$; Dentoni et al., 2020), which are widely used in constructions as ornamental stones. Late Variscan plutonites intruding the crust of both Peloritani Mountains and Sardinia also show similar ^{226}Ra activity concentrations ($18 \pm 4 \text{ Bq kg}^{-1}$ for the ASP1 sample and 18 to 80 Bq kg^{-1} for the Sardinian granites; Dentoni et al., 2020). Therefore, as already suggested by Dentoni et al., (2020), it is plausible that the intrusive rocks generated within the continental crust of southern Europe (i.e. Sardinia, Sicily and Calabria) during the latest phase of the Variscan Orogeny share similar radiological features.

Table 7. ^{222}Rn released into the air volume of the container at equilibrium (C_{Rn}), ^{222}Rn emanation coefficients (ϵ), ^{222}Rn surface (E_S) and mass (E_M) exhalation rates for the metamorphic samples resulting from the experiment.

| Sample ID | mass of the sample (kg) | C_{Rn} (Bq m^{-3}) | ϵ (%) | E_S ($\text{Bq m}^{-2} \text{ h}^{-1}$) | E_M ($\text{mBq kg}^{-1} \text{ h}^{-1}$) |
|-----------|-------------------------|---------------------------------|----------------|---|---|
| ASP1 | 1.208 | 64 ± 11 | 2.44 ± 0.9 | 0.30 ± 0.05 | 6.38 ± 1.1 |
| ASP2 | 1.294 | 580 ± 35 | 8.27 ± 1.6 | 2.75 ± 0.17 | 54.02 ± 3.26 |
| ASP3 | 1.202 | 133 ± 17 | 2.30 ± 0.7 | 0.63 ± 0.08 | 13.33 ± 1.7 |
| ASP4 | 1.219 | 25 ± 7 | 0.63 ± 0.3 | 0.12 ± 0.03 | 2.47 ± 0.69 |
| ASP5 | 1.409 | 173 ± 19 | 5.99 ± 1.9 | 0.82 ± 0.09 | 14.80 ± 1.63 |
| MAN1 | 1.172 | 328 ± 26 | 5.81 ± 1.3 | 1.56 ± 0.12 | 33.73 ± 2.69 |
| SMU1 | 1.247 | 105 ± 15 | 2.80 ± 0.8 | 0.50 ± 0.07 | 10.15 ± 1.45 |
| LTU1 | 1.265 | 130 ± 17 | 2.51 ± 0.8 | 0.62 ± 0.08 | 12.39 ± 1.62 |
| LTU2 | 1.242 | 267 ± 39 | 3.72 ± 1.1 | 1.27 ± 0.19 | 25.91 ± 3.78 |
| LTU3 | 1.338 | 152 ± 18 | 1.68 ± 0.4 | 0.72 ± 0.09 | 13.69 ± 1.62 |

It is debated if the radium and/or uranium content is correlated or not when plotted against parameters such as the radon emanation coefficient and exhalation rates. According to Hassan et al. (2011), Pereira et al. (2012), Eakin et al. (2016) and Dentoni et al. (2020) no correlation exists, whereas Arabi et al. (2016) and Pinto et al. (2020) observed that ε and E increase with an increase in ^{226}Ra content.

As evidenced in Figure 23, the ^{226}Ra concentration is weakly correlated with the ^{222}Rn emanation coefficient, surface exhalation rate and mass exhalation rate. This feature testifies that the radon release from rocks mainly depends on mineralogical and physical characteristics.

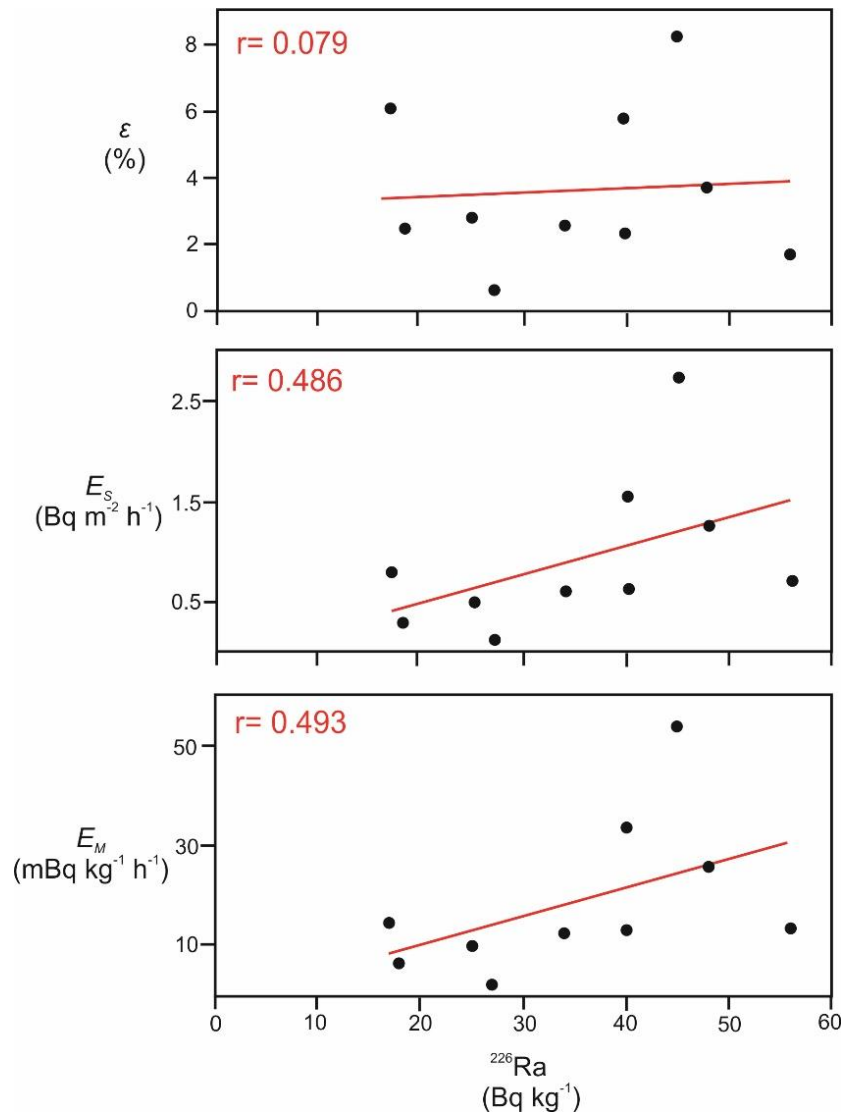


Figure 23. Relationship between ^{226}Ra activity concentration and ^{222}Rn emanation coefficient and exhalation rates; r is the Pearson's correlation coefficient.

4.6.5 Indoor radon

The indoor radon reference level adopted by the Directive 2013/59/Euratom and the Italian legislative decree 101/2020 is 300 Bq m^{-3} . The main part of the radon in the air inside dwellings, schools and workplaces derives from soil gas infiltration. Moreover, according to UNSCEAR (1993), the radon coming from building materials in dwellings located in a temperate climate is around 20% of the total indoor radon.

As a result, I believe that assessing the radon release from building materials can be useful to partially estimate the health hazard caused by indoor radon exposure. For this reason, a preliminary evaluation of the contribution to the indoor radon deriving from the use in constructions of the Peloritani rocks was performed.

The amount of indoor ^{222}Rn released from the crystalline rocks if used as building materials ($Ci_{Rn(bm)}$) was determined by equation 29 by using the calculated surface exhalation rates, a surface/volume ratio $S/V = 1.6 \text{ m}^{-1}$ (considering a room model of $4 \times 5 \times 2.8 \text{ m}^3$) and ventilation rates (λ_v) of 0.2, 0.63 and 2 h^{-1} (according to UNSCEAR 2000, λ_v varies from 0.2 to 2 h^{-1} with a geometric mean of 0.63 h^{-1}). The calculated $Ci_{Rn(bm)}$ are reported in Table 8. Only concentrations generated by a ventilation rate of 0.2 h^{-1} were discussed, because λ_v of 0.63 and 2 h^{-1} produce more conservative $Ci_{Rn(bm)}$ values.

The orthogneiss (ASP2 sample) shows the highest $Ci_{Rn(bm)}$ value (22.02 Bq m^{-3}) among all samples. The phyllite (MAN1 sample) and the felsic porphyroid (LTU2 sample) exhibit indoor radon activity concentrations higher than 10 Bq m^{-3} , whereas other samples do not produce $Ci_{Rn(bm)}$ values above 7 Bq m^{-3} .

Considering the indoor radon reference level adopted by the Italian legislation (300 Bq m^{-3}) and the contribution of 20% from building materials, the crystalline rocks should generate $Ci_{Rn(bm)}$ values below 60 Bq m^{-3} in order to reduce the health hazard. All analysed sampled exhibit $Ci_{Rn(bm)}$ values not exceeding the 60 Bq m^{-3} threshold; thus, their use in construction does not generate health risks due to indoor radon exposure. Furthermore, also the “Sabbie and ghiaie of Messina” formation are not hazardous, since their parent rocks (ASP1, ASP2 and ASP3 samples) release radon at low rates.

Table 8. The estimated indoor ^{222}Rn activity concentration ($C_{i\text{Rn}(bm)}$) and the annual effective dose ($Hi_{\text{Rn}(bm)}$) at different ventilation rates (λ_v).

| Sample ID | $C_{i\text{Rn}(bm)}$ (Bq m^{-3}) | | | $Hi_{\text{Rn}(bm)}$ ($\mu\text{Sv y}^{-1}$) | | |
|-----------|---|------------------|---------------|--|------------------|---------------|
| | $\lambda_v 0.2$ | $\lambda_v 0.63$ | $\lambda_v 2$ | $\lambda_v 0.2$ | $\lambda_v 0.63$ | $\lambda_v 2$ |
| ASP1 | 2.43 | 0.77 | 0.24 | 61 | 19 | 6 |
| ASP2 | 22.02 | 6.99 | 2.2 | 555 | 176 | 55 |
| ASP3 | 5.05 | 1.6 | 0.5 | 127 | 40 | 13 |
| ASP4 | 0.95 | 0.3 | 0.09 | 24 | 8 | 2 |
| ASP5 | 6.57 | 2.08 | 0.66 | 165 | 53 | 17 |
| MAN1 | 12.45 | 3.95 | 1.25 | 314 | 100 | 31 |
| SMU1 | 3.99 | 1.27 | 0.4 | 100 | 32 | 10 |
| LTU1 | 4.93 | 1.57 | 0.49 | 124 | 39 | 12 |
| LTU2 | 10.13 | 3.22 | 1.01 | 255 | 81 | 26 |
| LTU3 | 5.77 | 1.83 | 0.58 | 145 | 46 | 15 |

Equation 30 assesses the annual effective dose $Hi_{\text{Rn}(bm)}$ received by people due to the indoor ^{222}Rn exposure. As reported in Table 8, the calculated values considering $\lambda_v = 0.2 \text{ h}^{-1}$ do not exceed $555 \mu\text{Sv y}^{-1}$. Therefore, all values are well below the worldwide average ($1000 \mu\text{Sv y}^{-1}$, UNSCEAR, 2000).

The $C_{i\text{Rn}(bm)}$ and $Hi_{\text{Rn}(bm)}$ produced by the studied materials, represent only rough estimations because a few limitations should be taken into account:

- walls, the ceiling and the floor are considered to be exclusively composed of the analysed material (surface fractional usage $w_{si} = 100\%$);
- the “Sabbie and ghiaie of Messina” formation is widely used in construction. Unfortunately, collecting a representative sample was not possible since the deposits show a huge vertical and lateral mineralogical variability. Therefore, only their parent rocks (paragneisses, orthogneisses and monzogranites) were analysed;
- walls, the ceiling and the floor are assumed to be made up of materials in the same form as during the experiment, thereby in granular form; however, the

indoor radon concentration depends on radon diffusion length and radon surface exhalation, which can vary according to material fabric and texture. Therefore, the $Ci_{Rn(bm)}$ and $Hi_{Rn(bm)}$ values determined here should be attributed only to extreme and fictional situations, adopted to preliminarily evaluate the hazard connected with the building use of the crystalline rocks outcropping along the Peloritani Mountains.

In addition, I want to mention again that building materials account only for a part of the total indoor radon, which also depends on radon released from soils and domestic water (as already described in Section 4.5.5) as well as on other “external” factors (e.g. meteorological conditions, floor levels, and habits of inhabitants). Therefore, assessing the radon release from building materials provides only partial knowledge of the risk associated with the presence of radon in confined environments.

With this information in mind, it appears clear that carrying out a series of indoor radon measurements in dwellings, kindergartens, schools and workplaces in the studied area is strongly needed. This approach, coupled with the collection of geo-radiological data of soils and subsoils at the regional scale, represents the only strategy to properly evaluate the real risk to human health due to indoor radon (Giustini et al., 2022).

In this framework, starting from 2002 the Italian Health Ministry in cooperation with the Italian Regions has set up the “Piano Nazionale Radon” (PNR), which was conceived to mitigate the radon exposure to the population, especially in indoor environments. The PNR describes plans and remedial actions to apply in order to reduce the risk of cancer due to radon. Radiological data, such as the distribution of indoor radon concentration in Italian dwellings (data from Bochicchio et al., 1999), are also reported in the PNR, which proposes to drastically increase the number of observations over the years.

Unfortunately, the dataset for Sicily is really poor and no significant progress has been made in this field in the last 20 years. Even if indoor measurements were not performed in this study, I hope that radon data collected for crystalline rocks and soil gases (the argument will be treated in the next Chapter) will enrich the knowledge on the poorly investigated radon pollution in Sicily.

4.7 Concluding remarks

Igneous and metamorphic rocks widely outcrop along the Peloritani Mountains. Some of these lithologies have been broadly used in constructions, especially as inert material in concrete and cement mortar. Since these types of materials are usually prone to contain high amounts of natural radionuclides, a study was carried out in order to assess the potential radiological hazard for inhabitants.

Here are the main outputs obtained from this study:

- radiological analyses on the crystalline basement rocks of the Peloritani Mountains show that they are characterized by ^{226}Ra and ^{232}Th activity concentrations similar to those detected in other European Countries whereas the activity concentration of ^{40}K is higher than the worldwide average;
- radiological calculations prove that these rocks do not induce harmful effective doses originating from the gamma radiation emitted by terrestrial radioisotopes (^{226}Ra , ^{232}Th and ^{40}K);
- since the maximum acceptable level of total indoor radon adopted by the Italian legislation is 300 Bq m^{-3} and the contribution derived from building material is $\sim 20\%$, the proposed safety limit for the studied rocks is 60 Bq m^{-3} . Preliminary estimations highlight that those rocks are able to contribute to the indoor radon with values up to $\sim 22 \text{ Bq m}^{-3}$; therefore, if used in civil construction, they seem not to be dangerous in terms of radon releasing in confined environments;
- hazard indexes calculated for the studied samples (i.e. gamma index, alpha index, radium equivalent index and external and internal hazard indexes) confirm that their usage as building materials is not hazardous.

In conclusion, we can assume that the environmental impact and the radiological hazards for inhabitants, connected with the natural occurrence of igneous and metamorphic rocks along the Peloritani Mountains, are negligible. In addition, the use in the construction industry of these natural materials seems to be safe, and for this reason, they can be used without restrictions.

References

Angle4 Software (<https://www.angle4.com/>).

A. S. Arabi, I. I. Funtua, B. B. Dewu and A. M. Muhammad. Background Radiation and Radiological Hazard Associated with Local Building Materials around Zaria, Nigeria. *Radiochemistry*, **57**: 207-212, 2015.

A. S. Arabi, I. I. Funtua, B. B. Dewu, M. Y. Kwaya, E. K. Kurowska, A. M. Muhammad and M. L. Garba. NORM, radon emanation kinetics and analysis of rocks-associated radiological hazards. *Environmental Earth Sciences*, **75**, 689, 2016.

P. M. Barretto. Emanation Characteristics of Terrestrial and Lunar Materials and the ^{222}Rn Loss Effect on the U–Pb System Discordance. Ph. D thesis Rice University, 1973.

J. Beretka and P. J. Matthew. Natural radioactivity of Australian building materials, waste and by-products. *Health Physics*, **48**: 87-95, 1985.

I. Bikit, D. Mrda, S. Grujic and U. Kozmidic-Luburic. Granulation effects on the radon emanation rate. *Radiation. Protection Dosimetry*, **145**: 184-188, 2011.

F. Bochicchio, G. Campos Venuti, S. Piermattei, G. Torri, C. Nuccetelli, S. Risica and L. Tommasino. Results of the National survey on radon indoors in all the 21 Italian Regions. In: radon in living environments, Athens, Greece 19-23 April, 1999.

F. Caridi, M. D'Agostino, S. Marguccio, A. Belvedere, G. Belmusto, G. Marcianò, G. Sabatino and A. Mottese. Radioactivity, granulometric and elemental analysis of river sediments samples from the coast of Calabria, south of Italy. *The European Physical Journal Plus*, **131**: 136, 2016.

R. Cirrincione, E. Fazio, P. Fiannacca, G. Ortolano, A. Pezzino and R. Punturo. The Calabria Peloritani Orogen, a composite terrane in Central Mediterranean; its overall architecture and geodynamic significance for a pre-Alpine scenario around the Tethyan basin. *Periodico di Mineralogia*, **84**: 701-749, 2015.

S. De Martino, C. Sabbarese and G. Monetti. Radon emanation and exhalation rates from soils measured with an electrostatic collector. *Applied Radiation and Isotopes*, **49**: 407-413, 1998.

V. Dentoni, S. Da Pelo, M. M. Aghdam, P. Randaccio, A. Loi, N. Careddu and A. Bernardini. Natural radioactivity and radon exhalation rate of Sardinian dimension stones. *Construction and Building Materials*, **247**: 118377, 2020.

Directive 2013/59/EURATOM. Laying down basic safety standards for protection against the dangers arising from exposure to ionising radiation, and repealing Directives 89/618/Euratom, 90/641/Euratom, 96/29/Euratom, 97/43/Euratom and 2003/122/Euratom, 2013.

Durridge Company, RAD7, electronic radon detector user manual (<http://www.durridge.com>).

M. Eakin, S. J. Brownlee, M. Baskaran and L. Barbero. Mechanisms of radon loss from zircon: Microstructural controls on emanation and diffusion. *Geochimica et Cosmochimica Acta*, **184**: 212–226, 2016.

E. M. El Afifi, M. A. Hilal, S. M. Khalifa and H. F. Aly. Evaluation of U, Th, K and emanated radon in some NORM and TENORM samples. *Radiation Measurements*, **41**: 627-633, 2006.

EC. Radiation protection 112, Radiological Protection Principles Concerning the Natural Radioactivity of Building Materials, 1999.

S. Giammanco, M. Palano, A. Scaltrito, L. Scarfi and F. Sortino. Possible role of fluid overpressure in the generation of earthquake swarms in active tectonic areas: The case of the Peloritani Mts. (Sicily, Italy). *Journal of Volcanology and Geothermal Research*, **178**: 795-806, 2008.

F. Giustini, L. Ruggiero, A. Sciarra, S. E. Beaubien, S. Graziani, G. Galli, L. Pizzino, M. C. Tartarello, C. Lucchetti, P. Sirianni, P. Tuccimei, M. Voltaggio, S. Bigi and G. Ciotoli. Radon Hazard in Central Italy: Comparison among Areas with Different Geogenic Radon Potential. *International Journal of Environmental Research and Public Health*, **19**: 666, 2022.

N. M. Hassan, T. Ishikawa, M. Hosoda, K. Iwaoka, A. Sorimachi, S. K. Sahoo, M. Janik, C. Kranrod, H. Yonehara, M. Fukushi and S. Tokonami. The effect of water content on the radon emanation coefficient for some building materials used in Japan. *Radiation Measurements*, **46**: 232-237, 2011.

R. Hewamanna, C.S., Sumithrarachchi, P. Mahawatte, H. L. C. Nanayakkara and H. C. Ratnayake. Natural radioactivity and gamma dose from Sri Lankan clay bricks used in building construction. *Applied Radiation and Isotopes*, **54**: 365-369, 2001.

K. Krupp, M. Baskaran, and S.J. Brownlee, Radon emanation coefficients of several minerals: How they vary with physical and mineralogical properties, *American Mineralogist*, **102**: 1375-1383, 2017.

IAEA. Measurement and calculation of radon releases from NORM residues. Technical Reports Series n° 474 International Atomic Energy Agency Vienna, 2013.

ICRP. Recommendations of the International Commission on Radiological Protection 1990. ICRP Publication 60, 1991.

ICRP. International Commission on Radiological Protection. Protection of the public in situations of prolonged radiation exposure. ICRP Publication 82, 1999.

Italian Legislation, D. Lgs. 101/2020.

V. A. Leach, K. H. Lokan and L. J. Martin. A study of radiation parameters in an open-pit mine. *Health Physics*, **43**:363-375, 1982.

K. Y. Lee, S. H. Moon, Y. H. Oh, K. Ha and K. S. Ko. Determination of the radon emanation fraction from rocks by simple gamma-ray spectrometry. *J. Radioanal. Nucl. Chem*, **316**: 1307-1312, 2018.

M. A Misdag and A. Amghar. Radon and thoron emanation from various marble materials: impact on the workers. *Radiation Measurements*, **39**: 421-430, 2005.

Nordic. Naturally Occurring Radiation in the Nordic Countries—Recommendations. The Flag Book Series, The Radiation Protection Authorities in Denmark, Finland, Iceland, Norway and Sweden, Reykjavik, 2000.

D. Pereira, L. Neves, A. Pereira, M. Peinado, J. A. Blanco and J. J. Tejado. A radiological study of some ornamental stones: bluish granites from Extremadura (Spain). *Natural Hazards and Earth System Sciences*, **12**: 395-401, 2012.

M. P. Petropolous, M. J. Anagnostakis and S. Simopoulos. Building Materials Radon Exhalation rate: ERRICCA Intercomparison Exercise Results. *Science of the Total Environment*, **272**: 109-118, 2001.

Piano Nazionale Radon, 2002.

P.V. Pinto, K.S. Kumara and N. Karunakara, Mass exhalation rates, emanation coefficients and enrichment pattern of radon, thoron in various grain size fractions of monazite rich beach placers. *Radiation Measurements*, **130**: 106220, 2020.

M. Rafique, A. R. Khan, A. Jabbar, S. U. Rahman, S. J. A. Kazmi, T. Nasir, W. Arshed and Matiullah. Evaluation of radiation dose due to naturally occurring radionuclides in rock samples of different origins collected from Azad Kashmir. *Russian Geology and Geophysics*, **55**: 1103-1112, 2014.

S. Risica, C. Bolzan and C. Nuccetelli. Radioactivity in building materials: experimental methods, calculations and an overview of the Italian situation. In: radon in living environments, Athens, Greece 19-23 April, 1999.

D. Romano, F. Caridi, M. Di Bella, F. Italiano, S. Magazu, M. T. Caccamo, A. Tripodo, G. Faggio, R. Grillo, C. Triolo, G. Messina, A. Gattuso and G. Sabatino. Natural radioactivity of the crystalline basement rocks of the Peloritani Mountains (north-eastern Sicily, Italy): measurements and radiological hazard. *Radiation Protection Dosimetry*, **191**: 452-464 (2020).

G. Sabatino, M. Di Bella, F. Caridi, F. Italiano, D. Romano, S. Magazù, A. Gnisci, G. Faggio, G. Messina, S. Santangelo, F. Leonetti, and A. Tripodo. Radiological assessment, mineralogy and geochemistry of the heavy-mineral placers from the Calabrian coast (South Italy). *Journal of Instrumentation*, **14**: P05015, 2019.

J. Sato and T. Nakamura. Leaching of radon from weathered granite into water. *Radioisotopes*, **42**: 667-675, 1993.

A. Sakoda, K. Hanamoto, Y. Ishimori, T. Nagamatsu and T. K. Yamaoka. Radioactivity and radon emanation fraction of the granites sampled at Misasa and Badgastein. *Applied Radiation and Isotopes*, **66**: 648-652, 2008.

A. Sakoda and Y. Ishimori. Mechanisms and Modeling Approaches of Radon Emanation for Natural Materials. *Japanese Journal of Health Physics*, **52**: 296-306, 2017.

A. Sakoda, Y. Ishimori and K. A. Yamaoka. Comprehensive review of radon emanation measurements for mineral, rock, soil, mill tailing and fly ash. *Applied Radiation and Isotopes*, **69**: 1422-1435, 2011.

E. Srinivasa, D. R. Rangaswamy and J. Sannappa. Assessment of radiological hazards and effective dose from natural radioactivity in rock samples of Hassan district, Karnataka, India. *Environmental Earth Sciences*, **78**: 431, 2019.

S. Stoulos, M. Manolopoulou and C. Papastefanou. Assessment of natural radiation exposure and radon exhalation from building materials in Greece. *Journal of Environmental Radioactivity*, **69**: 225-240, 2003.

P. Tuccimei, M. Moroni and D. Norcia. Simultaneous determination of ^{222}Rn and ^{220}Rn exhalation rates from building materials used in Central Italy with accumulation chambers and a continuous solid state alpha detector: Influence of particle size, humidity and precursors concentration. *Applied Radiation and Isotopes*, **64**: 254-263, 2006.

P. Ujic, I. Celikovic, A. Kandic, I. Vukanac, M. Durasevic, D. Dragosavac and Z. Zunic. Internal exposure from building materials exhaling ^{222}Rn and ^{220}Rn as compared to external exposure due to their natural radioactivity content. *Applied Radiation and Isotopes*, **68**: 201-206, 2010.

UNSCEAR. Report to the general assembly of the United Nations with scientific annexes. United Nations New York, 1993.

UNSCEAR. Report to general assembly of the United Nations Scientific Committee on the effects of atomic radiation. United Nations New York, 2000.

UNSCEAR. Report to the general assembly. Annex B exposures of the public and workers from various sources of radiation. New York, 2008.

W. Zhang, Y. Zhang and Q. Sun. Analyses of Influencing Factors for Radon Emanation and Exhalation in Soil. *Water, Air, & Soil Pollution*, **230**: 16, 2019.

Chapter V - Soil gas radon and hazard assessment

5.1 Introduction

In the last decades, a great number of studies testifying the strong relationship between tectonic activity and anomalous emission of endogenous gases (e.g. carbon dioxide, methane, helium and radon) were performed (e.g. Irwin and Barnes, 1980; Zhiguan, 1991; Klusman, 1993; Lombardi et al., 1996; Zhang and Sanderson, 1996; Ciotoli et al., 1998, 1999, 2005, 2007, 2016; Baubron et al., 2002; Claesson et al., 2004; Fu et al., 2005; Tansi et al., 2005; Lombardi and Voltattorni 2010; Quattrocchi et al., 2012; Yuce et al., 2014; Voltattorni et al., 2014; Khattak et al., 2016; Kumar et al., 2016; Sciarra et al., 2015, 2018; Iovine et al., 2017; Chen et al., 2018). Regarding radon, anomalous activities in soil are defined as those concentrations exceeding the background value (mostly depending on the soil- ^{226}Ra content and the radon emanation coefficient).

Tectonic activity is responsible for seismic events, which are triggered by the sudden release of geodynamic stresses accumulated for years. Earthquakes occur along fractures located in the Earth's crust that are called faults.

Faults are permeable, and for this reason, they can be crossed by water and gases. Earthquakes, micro-seismicity (i.e. seismic events with magnitude less than zero) and creeping processes (i.e. aseismic movements along faults) lead to the mechano-chemical generation (i.e. due to rock ruptures) of crustal gases. The high crustal permeability along faults systems allows the upward migration of those gases toward the Earth's surface (e.g. Italiano et al., 2008). Moreover, faults act as preferential pathways for gases originating deeper in the mantle or produced by thermal energy (Kissin and Pakhomov, 1969; Gianelli, 1985). As a result, we can definitively state that faults and fractures favour the upward migration of deep gases and their release into aquifers and the atmosphere.

Recently, endogenous fluids, and particularly radon, have assumed a prominent role in the mainframe of the earthquake precursors. Even though a reliable seismic tracer has not been detected yet, several cases of radon anomalies connected with the occurrence of seismic events have been documented. (see Igarashi et al., 1995; Yasuoka et al., 1997, 2005; Kawada et al., 2007; Yang et al., 2005; Skelton et al., 2014; Zhou et al., 2016; Barberio et al., 2020). Exhaustive reviews about the role of

radon as a precursor are represented by the following papers: Friedmann (2012), Immè and Morelli (2012), Riggio and Santulin (2015), Woith (2015) and Tomer et al. (2016).

As described in Chapter III, northeastern Sicily, from a geophysical point of view, is defined as a complicated geodynamic puzzle where intense tectonic activity, strong seismic events and high earthquake density rates take place. Since high soil-radon concentrations generally occur in seismic areas, the Peloritani Mountains can be considered as a potential hazardous zone for radiation exposure due to radon.

In addition, it is important to remark that radon degassing from soils is widely considered as the main contributor to indoor radon (see Chapter IV). For this reason, measuring the soil-radon concentration represents the first important step towards a proper mitigation strategy.

Taking into account those evidences, a series of soil-radon concentration measurements were performed along the Tyrrhenian margin of northeastern Sicily, in the sector including the alluvial plain of Milazzo and Barcellona and the reliefs of Castoreale, Rodi Milici and Furnari (see Section 5.3). Here, around 100,000 people currently live. Moreover, the area including Castoreale, Rodi Milici and Furnari municipalities results to be one of the most seismically active zones in southern Italy. All those features make this area a perfect natural laboratory where to perform soil-radon investigations. Moreover, I want to stress on the fact that no works regarding natural radioactivity due to soil-radon have been previously carried out for the Peloritani Mountains. Therefore, findings and considerations reported in this Chapter represent the first detailed study made available to the scientific community.

The main objectives of this study are:

- evaluating the radiological hazard for population deriving from radon emissions from soils. For this purpose, the so-called “radon index” was derived by considering the amount of soil-radon as well as soil permeability;
- identifying the role of lithology and faults on the migration mechanisms of radon through the Earth’s upper crust. This target was assessed by analysing the spatial properties of soil-radon concentration together with the geological and tectonic features.

5.2 Radon migration through the Earth's crust

Radon is exhaled from rocks by alpha recoil and (minor) by diffusion, as delineated in Section 4.3. Moreover, laboratory experiments demonstrated that the amount of radon released from rocks increases during failures and/or microcracking under stresses (e.g. Holub and Brady 1981; Hishinuma et al., 1999; Tuccimei et al., 2010, 2015; Mollo et al., 2011; Nicolas et al., 2014; Wei et al., 2018). The same phenomenon presumably occurs during fault ruptures and microseismicity.

Once radon is free to move, what kind of mechanisms influence the migration of radon from depth to the Earth's surface? An extensive paper, resuming the main processes governing the migration mechanisms in the geosphere was provided by Etiope and Martinelli (2002).

In general, gas migration occurs by diffusion (i.e. due to concentration gradients) or by advection (i.e. under the influence of external forces such as pressure gradients).

As described by Fick's law, the diffusive flux (F_d ; $M L^{-2} T^{-1}$) is directly related to the concentration gradient according to the equation:

$$F_d = -D_m \nabla C \quad [31]$$

where $-D_m$ is the molecular diffusion coefficient ($L^2 T^{-1}$), which depends on the physical properties of the medium, and ∇C is the concentration gradient ($M L^{-4}$).

Since in porous media the real gas path is tortuous and not linear, and the volume where the gas circulates is reduced, the molecular diffusion coefficient in Fick's law is substituted by the bulk diffusion coefficient (D), which is calculated as follows:

$$D = \frac{D_m \cdot n}{\tau} \quad [32]$$

where τ is the tortuosity factor and n is the air-filled porosity. For soils, the n/τ ratio can be estimated from the Fang and Moncrieff (1999) equation:

$$\frac{n}{\tau} = n^{2a} \left(\frac{n}{n_t} \right)^2 \quad [33]$$

where n_t is the total porosity of the medium and a is an empirical coefficient determined from the following relation (Millington and Shearer, 1971):

$$n^{2a} + (1 - n)^a = 1 \quad [34]$$

On the other hand, the advective flux (F_a ; $M L^{-2} T^{-1}$) depends on the gas concentration (C ; $M L^{-3}$) and velocity (v ; $L T^{-1}$) as follows:

$$F_a = Cv \quad [35]$$

For porous media, velocity is calculated from the relation:

$$v = -\frac{k}{\mu} \nabla P \quad [36]$$

where k (L^2) is the intrinsic permeability, μ ($M L^{-1} T^{-1}$) is the gas viscosity and ∇P is the pressure gradient ($M L^{-2} T^{-2}$).

When advection and diffusive processes coexist, the total flux (F_t) of a gas species is simply expressed as the sum of advective and diffusive aliquots:

$$F_t = F_d + F_a = -D\nabla C + Cv \quad [37]$$

If we want to quantitatively describe a system characterized by the occurrence of both diffusion and advection, we have to invoke the mass conservation law:

$$\text{div}(F_t) + \frac{dC}{dt} = 0 \quad [38]$$

that in this case demonstrates that the temporal change of gas concentration of gas (dC/dt) corresponds to the spatial change of the total flux ($\text{div}(F_t)$). By combining equations 37 and 38, and assuming that F_a and D are constants, the advective-diffusion equation is obtained:

$$v\nabla C - D\nabla^2 C = \frac{dC}{dt} \quad [39]$$

Concerning radon released by rocks, it can travel by diffusion only a few meters until its specific activity decreases to less than 1%, with respect to the initial value. Moreover, rare gases such as radon and helium, cannot form a macroscopic amount of gas that is able to react to pressure gradients and move autonomously. This is due to the fact that their concentration in subsurface environments is too small.

Differently, the greater subsurface amount of other gaseous species including CO_2 , CH_4 and N_2 , allows the formation of large gas domains that can “carry” rare gases toward the Earth’ surface over long distances (Fig. 24).

Those gases are called “carrier gases”, and the mixture formed by primary (i.e. carrier gases) and secondary (i.e. rare gases) components is known as “geogas” (Kristiansson and Malmqvist, 1987; Etiope and Lombardi, 1996). Van der Waals forces are responsible for the “wedding” between the carrier and rare gases.

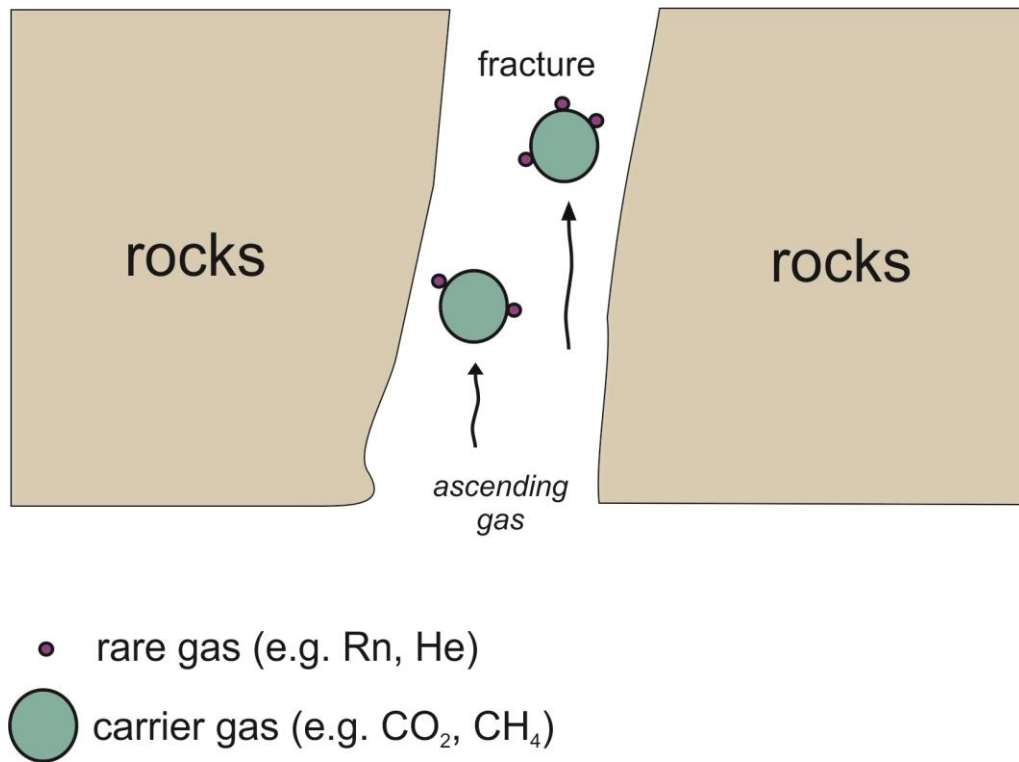


Figure 24. Simplified and intuitive scheme representing the key role of carrier gases (e.g. CO₂ and CH₄) in redistributing radon. Rock fractures, characterizing the Earth's crust, act as pathways for ascending carrier gases moving towards the Earth's surface by advection; CO₂ and CH₄ are able to transport radon and other rare gases over long distances (modified from Romano et al., 2021).

Therefore, according to Etiope and Martinelli (2002), transport and redistribution of radon and other rare gases toward the Earth's surface rely on the occurrence of carrier gases.

Besides active fault zones, the presence of high radon concentrations is persistent in volcanic areas, where magmatic gases (mainly CO₂), deriving from degassing magma bodies residing in the Earth's crust, transport radon along fractures affecting volcanic edifices, generating subaerial fumaroles and diffuse degassing areas.

In Figure 25 we can observe that surface emission of geogas (carrier gases together with passively transported radon) takes place in the proximity of fault planes and fracture zones. Usually, these geophysical features occur in volcanic and tectonic areas.

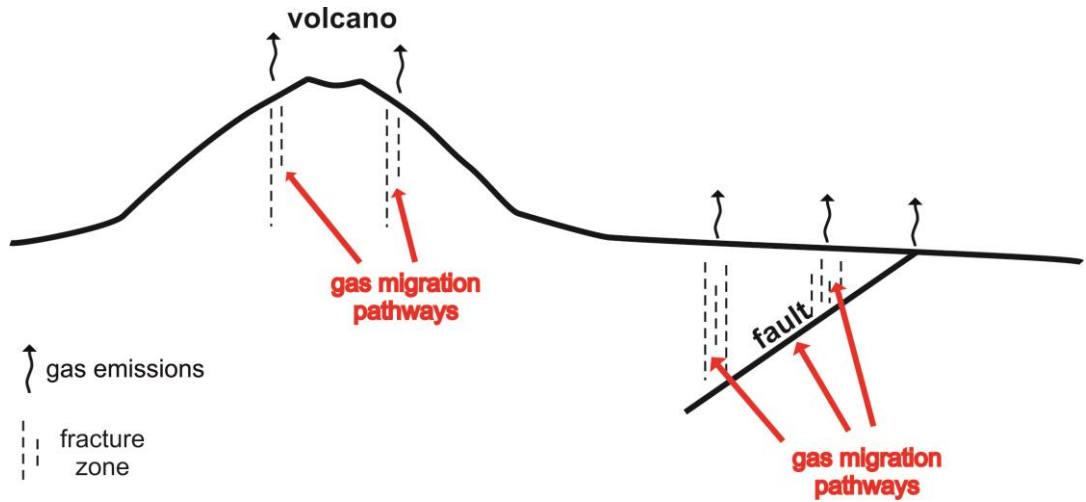


Figure 25. Carrier and rare gases are able to reach the Earth's surface and disperse into the atmosphere by migrating along permeable zone such as faults and fractures (modified from Romano et al., 2021). The most common places, where geogenic gases are released from the Earth's surface, are active and dormant volcanoes and seismogenic areas.

5.3 Measurement locations

Soil-radon measurements were performed in 172 sites along the Tyrrhenian margin of NE Sicily. The investigated area (131 km²) is depicted in Figure 26 and it involves the territory of ten municipalities (Barcellona Pozzo di Gotto, Castoreale, Furnari, Mazzarrà S.Andrea, Merì, Milazzo, Pace del Mela, Rodi Milici, S.Filippo del Mela, Terme Vigliatore). The sampling density was 1.3 sample km⁻².

Locations of the radon measurement sites are plotted in Figure 26B, whereas the population of municipalities is shown in Table 9.

Table 9. The population of each municipality located within the investigated area (data were collected from ISTAT, 2019).

| Municipality | Population | Municipality | Population |
|---------------------------|------------|--------------------|------------|
| Barcellona Pozzo di Gotto | 40,263 | Milazzo | 29,884 |
| Castoreale | 2,240 | Pace del Mela | 6,152 |
| Furnari | 3,863 | Rodi Milici | 1,968 |
| Mazzarrà S.Andrea | 1,411 | S.Filippo del Mela | 6,770 |
| Merì | 2,346 | Terme Vigliatore | 7,223 |

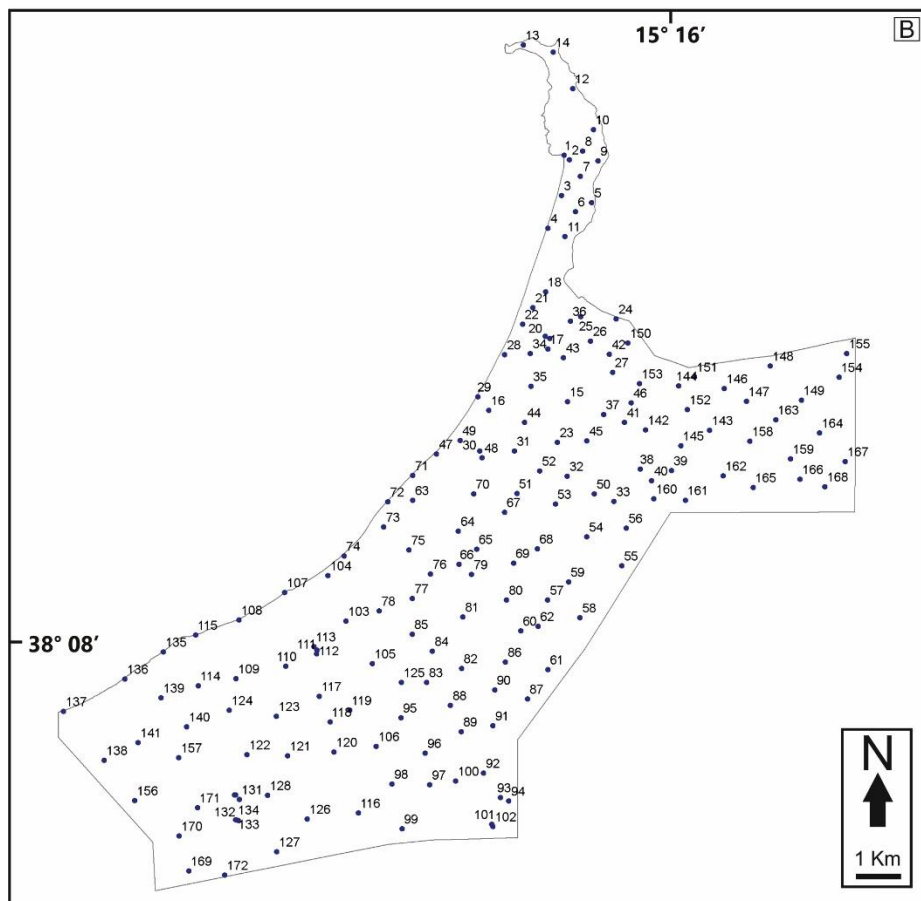


Figure 26. A) The investigated area (highlighted in red) where soil-radon measurements were carried out, is located along a portion of the Tyrrhenian margin of NE Sicily, and it covers about 131 km²; B) location of the 172 sampling sites within the investigated area (coordinates are listed in Table 11).

5.4 Method

5.4.1 Soil-radon measurements

5.4.1.1 Techniques

^{222}Rn and ^{220}Rn (thoron) activity concentration measurements in soils were performed by using the RAD7 DurrIDGE. A full description of how the instrument works is provided in Chapter IV.

In order to pump out the soil gas, a hollow probe with an inner diameter of 0.6 cm was hammered into the soil at a determinate depth. The probe was connected to a drying tube filled with drierite (CaSO_4), and then to the RAD7 (Fig. 27). A pump located inside the RAD7 extracts the soil gas from the inlet placed at the bottom of the probe at a flow rate of around 0.5 L m^{-1} . The inlet valve of the RAD7 was equipped with a millipore filter ($0.5 \mu\text{m}$) which is able to block dust and other decay products. When the soil gas arrives in the RAD7 internal chamber the radon concentration is measured. After that, the gas was discharged into the atmosphere through the outlet valve. Drierite allows the relative humidity in the internal chamber to quickly bring down below 10%. In these conditions, the measure has the maximum efficiency since excessive humidity inside the chamber makes it more difficult to maintain the high insulation. The instrument settings were: Sniff Mode, 5 min cycle, 00 recycle, Thoron ON and pump AUTO. In this configuration, the ^{222}Rn and ^{220}Rn activity concentrations were determined, at cycles (i.e. counting periods) of 5 minutes each, from the ^{218}Po peak at 6.00 MeV and from the ^{216}Po peak at 6.78 MeV, respectively. The RAD7 sensitivity shows a range of $4\text{-}750000 \text{ Bq m}^{-3}$.

In each site, a series of measurement cycles of 5 minutes was carried out until the secular equilibrium between ^{218}Po and ^{222}Rn is attained (it takes around 10 minutes). Theoretical and experimental data demonstrated that the ^{222}Rn concentration increases during the first four 5-min counting periods, whereas the fifth cycle exhibits a concentration value similar to that of the fourth one. Therefore, in order to determine the soil- ^{222}Rn concentration, the initial 3 cycles (15 min total) were ignored. The ^{222}Rn concentration was finally determined by considering the results of the first two consecutive 5-min cycles (measured after the end of the third counting period) having a standard deviation below 15% with respect to the highest measured value (Castelluccio, 2010). A different approach was used with ^{220}Rn . The

equilibrium between ^{216}Po and ^{220}Rn is attained in a few seconds, and for this reason, thoron activity concentration was determined by considering the values of all the 5-min cycles except the first one (Castelluccio, 2010). The radon and thoron concentrations were calculated by averaging the cumulative spectrum over the selected 5-min cycles.

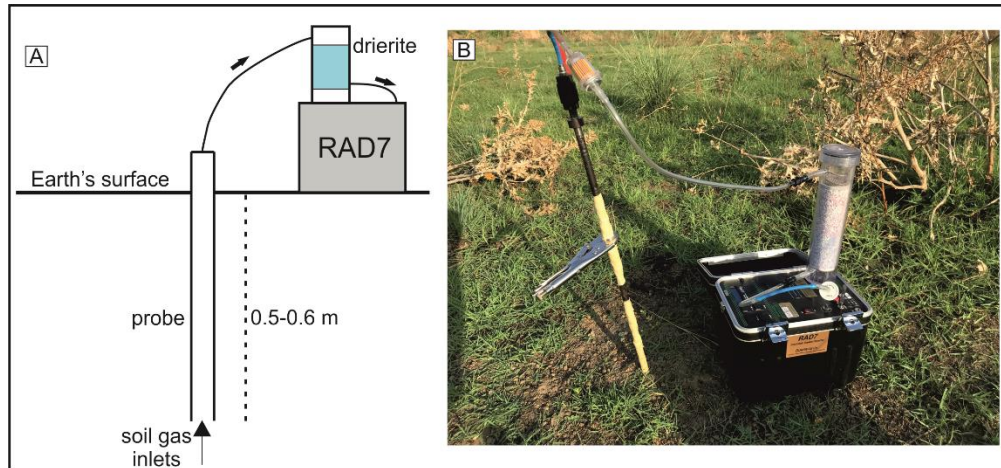


Figure 27. The soil-radon measurement setup: scheme (A) and picture (B). See the text for the description.

Because of the short half-life of thoron (56 s), a great number of atoms decay during the path from the soil to the RAD7 internal chamber. Then, the measured ^{220}Rn concentration must be corrected (RAD7 Manual).

The true ^{220}Rn activity concentration (C_0 , kBq m^{-3}) in soils is calculated as follows:

$$C_0 = C_M e^{\lambda t} \quad [40]$$

where C_M (kBq m^{-3}) is the ^{220}Rn concentration measured by the RAD7, λ is the ^{220}Rn constant decay (0.0124 s^{-1}) and t (s) is the travel time from the measurement depth to the RAD7. The travel time is calculated by the following formula:

$$t = \frac{V}{Q} \quad [41]$$

where V (L) is the effective volume of the measurement setup and Q is the pump rate (0.5 L m^{-1}). The term $e^{-\lambda t}$ in equation 40, determined for the setup used in this work, is equal to 2.8.

The RAD7 used for this Thesis (ID number 3411) had been calibrated in the DurrIDGE firmware in Sheffield (UK) just before the onset of measurement activities.

According to the manufacturer, the RAD7 shows a high stable calibration; the typical annual drift is less than 2%, and the Durrige company suggest sending the instrument to the firmware for recalibration around once a year. All measurements carried out for this Thesis were performed with a perfectly calibrated RAD7.

5.4.1.2 Uncertainties

Radon values measured by the RAD7 in every counting cycle are associated to uncertainty expressed as 2σ (confidence interval of 95%). Errors reflect estimations based on counting statistics. It is known that radioactive decays obey Poisson statistics, where the standard deviation (σ) is the square root of the count. However, Poisson statistics underestimate the uncertainty at low counts. According to the RAD7 Manual, in order to compensate for this drift, the RAD7 defines σ as equal to $1 + \text{SQR}(N+1)$, where N is the number of counts.

5.4.1.3 Spatial and environmental parameters affecting the soil radon concentration

Obviously, the main factors controlling the soil radon concentration are: i) the content of radium and thorium in the solid matrix; ii) the presence of advective flows carrying deep-seated geogenic gases.

Furthermore, spatial and environmental parameters also influence the radon concentration. Depth is one of those parameters. It is clear that close to the Earth's surface, radon-free atmospheric air enters the soil-interstitial air diluting the radon concentration. This sort of "mixing" effect decreases with increasing depth. Literature studies (Jonsson, 2001; Kristiansson & Malmqvist, 1982) demonstrated that soil radon concentration increases with increasing depth down to around 2 m beneath the soil-air interface. In this context, also soil fabric and texture show a prominent role by controlling the dimension and shape of interstitial spaces.

Unfortunately, inserting the soil probe at a depth >2 m is impracticable. In addition, a worldwide shared protocol setting a uniform sampling-depth does not exist.

Some studies focused on soil-radon analysis reported sampling depths ≥ 0.7 m (e.g. Szabo et al., 2014; Sciarra et al., 2018; Elio et al., 2019a; Bini et al., 2020). Conversely, other studies highlighted that soil air samples were collected at depths in

the range of 0.4-0.6 m (e.g. Ciotoli et al., 1998, 1999; Neri et al., 2011, 2014; Voltattorni et al., 2014; Khattak et al., 2016; D'Alessandro et al., 2018).

Measurements carried out for this Ph.D. were conducted at depths of 0.5-0.6 m in all sites. The main reason is that where clay lithologies crop out, sediments located more than 0.6 m below the ground surface are compacted and lowly permeable, making it difficult to pump a sufficient amount of air to perform a reliable analysis. The identical phenomenon sometimes occurs when sampling sites are located in moderately permeable soils.

It was demonstrated that seasonal parameters, including temperature and soil moisture, have an important role on soil-radon concentration. In order to reduce the effect of seasonal variability, all measurements were carried out in 2020 and 2021, in the dry and warm season (in 2020: from May to September; in 2021: in April and May). Measurements were carried out between 7:00 am to 7:00 pm, except in August, when the hottest hours (i.e. atmospheric temperature $>30^{\circ}\text{C}$) were avoided. Moreover, soil sampling was not performed during windy days.

5.4.2 Statistical properties: Exploratory Data Analysis

Exploratory Data Analysis (EDA) helps to evaluate data variabilities and the central tendency. The most common parameters used for this purpose are the minimum, value, lower quartile, median, upper quartile, maximum value, average (i.e. arithmetic mean), mode, standard deviation and range.

In addition, values of ^{222}Rn and ^{220}Rn concentrations measured on different geological formations were plotted in “box plot” diagrams (i.e. “box and whiskers” diagrams). Histograms were also plotted with the purpose of analysing the frequency distribution of radon.

Moreover, evaluating the Rn concentration background value is a fundamental step to identify potential radon anomalies. One of the most reliable methods used for geophysical data is the statistical approach by means of normal probability plot (NPP) as described in Sinclair (1974, 1991). Recently, a great number of studies enhanced the role of the NPP analysis as a good method to identify anomaly thresholds (e.g. Ciotoli et al., 2007; Sciarra et al., 2015, 2018; Yuce et al 2017; D'Alessandro et al., 2018). NPPs are graphical techniques that evaluate if a dataset

shows a normal distribution or not. Data are sorted and plotted against a theoretical normal distribution. If data are normally distributed, the graph should approximate a straight line; every deviation or curve indicate departures from normality (Fig. 28).

Normal order statistic medians (N_i) symbolize the theoretical normal distribution plotted vs data; N_i are computed as:

$$N_i = G(U_i) \quad [42]$$

where G is the inverse of the cumulative normal distribution function and U are the uniform order statistic medians calculated as follows:

$$U_i = \begin{cases} 1 - U_n & i = 1 \\ (i - 0.3175)/(n + 0.365) & i = 2, 3, \dots, n - 1 \\ 0.5^{1/n} & i = n \end{cases} \quad [43]$$

The whole radon dataset was plotted in a NPP Plot Graph and the different populations (i.e., background and anomalous values) were identified in correspondence of the inflection points of the curvature by visual analysis (Fig. 29).

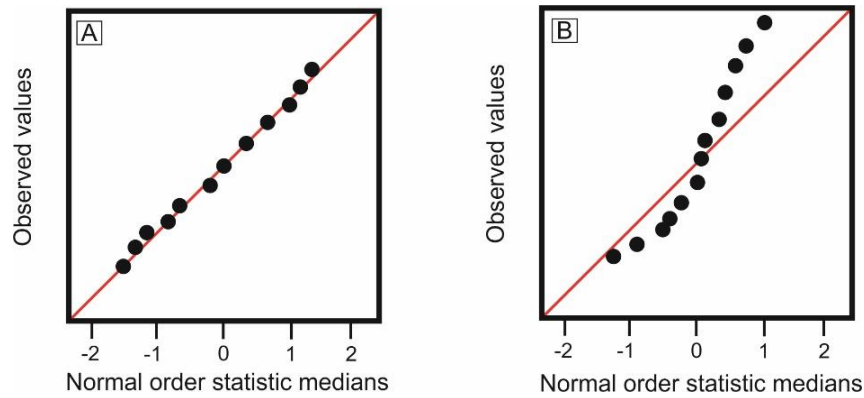


Figure 28. NPPs of dataset normally distributed (A) and not normally distributed (B).

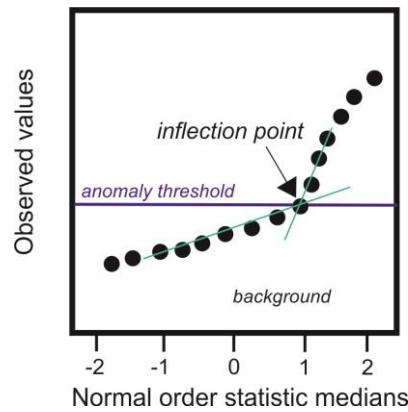


Figure 29. NPPs are used to identify different populations among geophysical data.

5.4.3 Geostatistics: data interpolation

The main objective of geostatistics is to estimate unknown values falling between known values, here represented by the collected soil-radon concentrations. This process, which is called interpolation, generates continuous maps.

Interpolation methods were widely used in the radon “field” with this purpose (e.g. Kemski et al 2001; Bossew and Lettner, 2002, 2005; Cinelli et al., 2014; Szabo et al., 2014; Elio et al., 2019a).

According to Dubois and Bossew (2006), radon concentrations and other risk-related parameters can be considered as realisations of random functions that are spatially continuous and auto-correlated, and therefore they can be interpolated (i.e. values can be estimated at unsampled sites).

Here, the inverse distance weighting function (IDW) was used to produce prediction maps of soil-radon concentration. The IDW is one of the most suitable interpolation methods for soil radon mapping (Dubois and Bossew, 2006), and it was used in several recent works such as Kemski et al. (2001) and Elio et al. (2019a,b).

The IDW is a deterministic method that estimates unknown values by averaging sampled points in the neighbourhood of the prediction location. The measured values that are closer to the unknown site have more influence and greater weight in comparison to those farther away. The interpolated value z at unsampled location x is calculated as follows (Bivand et al., 2008):

$$z(x) = \frac{\sum_{i=1}^n w(x_i)z_i(x_i)}{\sum_{i=1}^n w(x_i)} \quad [44]$$

where x_i is the location of a known value z_i , and w is the weight computed according to their distance to the interpolation location:

$$w(x_i) = ||x_i - x||^{-p} \quad [45]$$

with $||\cdot||$ indicating the Euclidean distance and p is the inverse distance weighting power.

ArcGIS 10.2 ESRI (Geostatistical Wizard belonging to the Geostatistical Analyst tool) was used for the IDW interpolation under the supervision of Dr. Alessandro Gattuso. Radon prediction maps for the studied area were generated by predicting soil-radon concentrations over cells of 250 x 250 m.

5.4.4 Soil permeability

Determining the permeability of soils is a top priority if we want to assess the hazard induced by soil-radon. Highly permeable soils allow radon atoms to be easily released to the atmosphere and buildings, whereas low permeability soils act as a natural shield against radon exhalation. Even low radon concentrations in highly permeable soil might be harmful if edifices are not provided by adequate protections. In this work, a permeability class was associated with each lithological formation cropping out in the studied area. Three permeability classes have been defined: low, medium and high.

The class assignment was made according to hydrological information and classification provided by the PAI (Piano Assetto Idrogeologico) realized for the Sicilian Region (<http://www.sitr.regione.sicilia.it/pai>), which considered fabric, texture, granulometry and fracture networks of rocks and soil.

A permeability map was therefore created for the investigated zone.

5.4.5 Radon hazard

Buildings are in strict contact with the soil environment, which is the main source of indoor radon. A way to assess the health risk caused by the gas radon has become a concern since it was discovered its carcinogenic potential. The most important successes in this field were obtained in the Czech Republic, where in the last 30 years, a method for radon risk classification for building sites was published and improved (Kulajita et al., 1990; Barnet et al., 1994; Neznal et al., 2004; Barnet et al., 2008).

Le level of risk is based on soil gas measurements coupled with permeability evaluation. Two ways can be followed: if *in-situ* permeability measurements are performed, the radon potential (RP) is determined (Neznal et al., 2004). On the other hand, if the permeability is assessed without carrying on direct measurements (i.e. by “expert” evaluation), the radon index (RI) is calculated (Kulajita et al., 1990; Neznal et al., 2004). As evidenced in the former paragraph, soil permeability in this work was evaluated by analysing the petrographic characteristics of rocks and loose sediments, namely by means of “expert” evaluations. Therefore, only the RI was calculated.

The soil- ^{222}Rn activity concentration and the “expert” evaluation of soil permeability (i.e. given as low, medium, or high) allow us to assess the RI of a building site by using the classification scheme of Table 10. The RI categories are three: low, medium, and high.

In order to investigate the radon risk for the studied area, a RI map was produced by using the permeability and radon prediction maps. For each 250 x 250 m cell having a ^{222}Rn concentration value determined by interpolation (see Section 5.4.3), a permeability class was attributed by considering the permeability degree observed at the centre of the cell. The RI category for each 250 x 250 m cell was determined coupling the two parameters (i.e. permeability and ^{222}Rn concentration) in agreement with the scheme of Table 10.

Table 10. RI assessment (Neznal et al., 2004).

| Radon index (RI) category | Soil ^{222}Rn concentration, C_{Rn} (kBq m ⁻³) | | |
|------------------------------|--|--------------------------|--------------------------|
| | Low | $C_{Rn} < 30$ | $C_{Rn} < 20$ |
| Medium | $30 \leq C_{Rn} \leq 100$ | $20 \leq C_{Rn} \leq 70$ | $10 \leq C_{Rn} \leq 30$ |
| High | $C_{Rn} \geq 100$ | $C_{Rn} \geq 70$ | $C_{Rn} \geq 30$ |
| | low | medium | high |
| | permeability | | |

RI maps became very important as a recent change in the Italian Legislation occurred. The legislative decree no. 101/2020, which transposed the 2013/59 Euratom directive, introduced for the first time in Italy a specific indoor radon limit for private dwellings (maximum acceptable concentration of 300 Bq m⁻³). Formerly, only indoor radon in public edifices, schools and workplaces had been regulated by law. Therefore, the leg. decree no. 101/2020 represents a huge step regarding indoor radon mitigation.

Since no previous radon data exist for the Tyrrhenian coast of northeastern Sicily, the RI map produced here acts as the first preliminary instrument against radon hazard. The RI map can be used in civil engineering and architecture in the field of new housing construction or to mitigate the risk of pre-existing dwellings.

5.4.6 CO₂ measurements in soil gas

Due to the covid19 pandemic restrictions taking place in Italy during 2020 and 2021, it was not possible to measure the carbon dioxide (CO₂) percentage in soil gas during the soil-Rn measurement survey. However, late in the Summer of 2021 (i.e. the second half of August), I was able to measure the soil-CO₂ content in a few selected sites where the Rn concentration had been already measured, by using the portable instrumentation of INGV-Palermo.

The CO₂ content in soil gas was determined by adopting the so-called “active” method (Gurrieri and Valenza, 1988). A probe of a section of 2,5 cm² is inserted in the soil at a depth of 0.5 m (Fig. 30). Soil gas enters the probe from five different inlets located at different depths. Soil gas is pumped at a constant flux of ~ 1.5 L m⁻¹ and finally enter an infrared gas analyser (IRGA) where the CO₂ percentage (vol. %) is measured. The right CO₂ concentration value of the analysed gas is taken when it reaches the steady state, namely a constant value (generally after 30 s of pumping).

The working principle of the infrared gas analyser is determining the CO₂ concentration through the absorption by carbon dioxide of different frequencies of infrared light. A sample chamber is exposed to an infrared source that irradiates the gas sample. An infrared detector measures the attenuation of the specific CO₂ wavelengths, which are selected by an optical filter; the attenuation of these wavelengths determine the CO₂ concentration.

According to the Beer-Lambert law, the optical attenuation induced by a single and uniform gas species is described by the followed equation:

$$A = \varepsilon \cdot l \cdot C \quad [46]$$

where A is the absorbance, ε is the molar attenuation coefficient of the gas species, l is the optical length path of the beam of light and C is the concentration of the gas species.

If more gas species are involved, equation 46 becomes:

$$A = \sum_{i=1}^N A_i = \sum_{i=1}^N \varepsilon_i \int_0^l C_i(z) dz \quad [47]$$

The IRGA was calibrated at INGV-Palermo by the INGV staff in the person of Dr. Santo Cappuzzo.

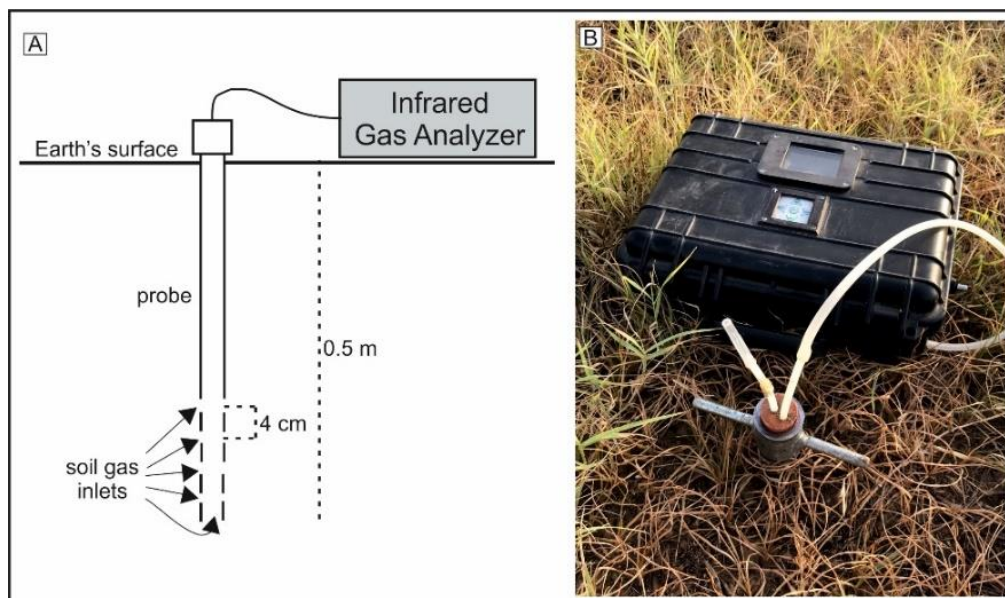


Figure 30. A) scheme of the setup used for measuring the CO₂ concentration in soil gas (modified from Camarda et al., 2006); B) picture of the CO₂ measurement setup.

5.5 Results and Discussion

5.5.1 Soil-gas radon concentration and statistical analysis

Soil-²²²Rn (radon) and ²²⁰Rn (thoron) concentrations measured at each sampling site are listed in Table 11 along with site coordinates, site lithologies and ²²⁰Rn/²²²Rn ratios. Experimental measurement patterns and spectra are reported in Appendix 1.

Table 12 shows the statistical features of soil-radon and -thoron concentrations as well as those of ²²⁰Rn/²²²Rn ratios. ²²²Rn concentration ranges between (0.69 ± 0.2) kBq m⁻³ in site #4 and (81.3 ± 2.5) kBq m⁻³ in site #153, whereas ²²⁰Rn concentration varies from (2.63 ± 0.6) kBq m⁻³ in site #11 to (123.48 ± 5) kBq m⁻³ in site #94. The ratio between ²²⁰Rn and ²²²Rn ranges from 0.4 (site #171) to 22.76 (site #118).

Soil-²²²Rn concentrations measured in NE Sicily were compared (Table 13) with literature values obtained for Italy (Beaubien et al., 2003) and other European countries (Dubois, 2005 and references therein; Vaupotic, 2012). The average value of the whole Peloritani dataset (12.37 kBq m⁻³) is lower with respect to Italian and European averages (ranging from 18.5 kBq m⁻³ of Lithuania to 75 kBq m⁻³ of Austria). However, I want to stress on the fact that this comparison should be viewed only as a rough evaluation since measurements in various countries were performed at different sampling depth and it is known that depth is probably the most important

Table 11. List of radon and thoron concentrations measured in soil gas samples collected in NE Sicily. Sampling date, site coordinates (UTM WGS84 zone 33 N), $^{220}\text{Rn}/^{222}\text{Rn}$ ratios and the type of lithology outcropping in the sampling site are also reported. Site locations are plotted in the map in Figure 27B. Lithology labels: BEA: beach deposits; FD: fluvial deposits; TER: marine and fluvial terraces composed of metamorphic clasts; TUF: cineritic tuffs; RA: recent alluvial sediments; MES: “sabbie and ghiaie” of Messina; QC: Quaternary clays; PPC: Plio-Pleistocene calcarenites; MMT; Middle Miocene terrigenous sediments; CC: Cretaceous clays; FLY: Capo d’Orlando flysch; ASP: Aspromonte metamorphic Unit.

| #Site | Date (dd/mm/yyyy) | North | East | ^{222}Rn (kBq m ⁻³) | ^{220}Rn (kBq m ⁻³) | $^{220}\text{Rn}/^{222}\text{Rn}$ | Lithology |
|-------|----------------------|---------|--------|---|---|-----------------------------------|-----------|
| 1 | 19/05/2020 | 4233044 | 521107 | 2.88 ± 0.4 | 4.34 ± 0.7 | 1.51 | BEA |
| 2 | 25/05/2020 | 4232759 | 521243 | 6.7 ± 0.76 | 61.6 ± 3.1 | 9.19 | RA |
| 3 | 26/05/2020 | 4232074 | 521040 | 2.08 ± 0.4 | 13.44 ± 1.1 | 6.46 | RA |
| 4 | 30/05/2020 | 4231238 | 520712 | 0.69 ± 0.2 | 6.1 ± 0.9 | 8.85 | BEA |
| 5 | 30/05/2020 | 4231863 | 521784 | 10.12 ± 0.8 | 79.8 ± 3.9 | 7.89 | ASP |
| 6 | 30/05/2020 | 4231617 | 521375 | 4.85 ± 0.6 | 16.35 ± 1.6 | 3.37 | ASP |
| 7 | 01/06/2020 | 4232539 | 521503 | 9.54 ± 0.8 | 42 ± 2.8 | 4.4 | ASP |
| 8 | 01/06/2020 | 4233084 | 521612 | 7.2 ± 0.7 | 31.08 ± 2.2 | 4.32 | TER |
| 9 | 01/06/2020 | 4232930 | 521942 | 1.71 ± 0.34 | 23.52 ± 2.1 | 13.75 | ASP |
| 10 | 01/06/2020 | 4233696 | 521834 | 4 ± 0.5 | 12.15 ± 1.5 | 3.04 | TER |
| 11 | 01/06/2020 | 4231071 | 521115 | 2.08 ± 0.4 | 2.63 ± 0.6 | 1.27 | ASP |
| 12 | 04/06/2020 | 4234623 | 521367 | 14 ± 1 | 97.44 ± 6.2 | 6.96 | TER |
| 13 | 04/06/2020 | 4235776 | 520098 | 35.5 ± 1.6 | 123.2 ± 5 | 3.47 | TUF |
| 14 | 04/06/2020 | 4235642 | 520856 | 32.2 ± 1.5 | 97.16 ± 6.2 | 3.02 | TUF |
| 15 | 11/06/2020 | 4226962 | 521195 | 9.16 ± 0.8 | 23.02 ± 2.1 | 2.51 | RA |
| 16 | 11/06/2020 | 4226753 | 519244 | 8.63 ± 0.8 | 28.06 ± 2.3 | 3.25 | RA |
| 17 | 11/06/2020 | 4228273 | 520694 | 12.43 ± 0.9 | 21.59 ± 2 | 1.74 | RA |
| 18 | 11/06/2020 | 4229716 | 520632 | 7.28 ± 0.7 | 36.12 ± 3.6 | 4.96 | RA |
| 19 | 11/06/2020 | 4228540 | 520749 | 27.4 ± 1.4 | 31.19 ± 2.5 | 1.14 | RA |
| 20 | 11/06/2020 | 4228560 | 520696 | 18.65 ± 0.9 | 53.2 ± 2.8 | 2.85 | RA |
| 21 | 12/06/2020 | 4229302 | 520330 | 11.41 ± 0.9 | 72.24 ± 3.6 | 6.33 | RA |
| 22 | 12/06/2020 | 4228848 | 520058 | 9.08 ± 0.8 | 24.08 ± 2.2 | 2.65 | RA |
| 23 | 12/06/2020 | 4225964 | 520929 | 6.13 ± 0.6 | 33.04 ± 2.5 | 5.39 | RA |
| 24 | 15/06/2020 | 4229006 | 522423 | 1.21 ± 0.3 | 5.04 ± 0.8 | 4.17 | BEA |
| 25 | 15/06/2020 | 4229082 | 521512 | 12.74 ± 0.9 | 87.64 ± 4.2 | 6.88 | RA |
| 26 | 15/06/2020 | 4228497 | 521726 | 10.51 ± 0.8 | 25.23 ± 1.6 | 2.4 | RA |
| 27 | 15/06/2020 | 4227731 | 522233 | 39.4 ± 1.7 | 99.12 ± 4.5 | 2.52 | RA |
| 28 | 17/06/2020 | 4228138 | 519645 | 0.74 ± 0.2 | 13.83 ± 1.6 | 18.69 | RA |
| 29 | 17/06/2020 | 4227080 | 518991 | 2.4 ± 0.4 | 10.36 ± 1.4 | 4.32 | BEA |
| 30 | 17/06/2020 | 4225717 | 519048 | 8.55 ± 0.8 | 54.88 ± 3.4 | 6.42 | RA |
| 31 | 17/06/2020 | 4225737 | 519887 | 30.2 ± 1.5 | 47.6 ± 3.1 | 1.58 | RA |

| #Site | Date (dd/mm/yyyy) | North | East | ²²² Rn (kBq m ⁻³) | ²²⁰ Rn (kBq m ⁻³) | ²²⁰ Rn/ ²²² Rn | Lithology |
|-------|----------------------|---------|--------|---|---|--------------------------------------|-----------|
| 32 | 17/06/2020 | 4225126 | 521162 | 5.49 ± 0.6 | 27.64 ± 2.3 | 5.03 | FD |
| 33 | 17/06/2020 | 4224501 | 522264 | 5.79 ± 0.6 | 18.48 ± 1.9 | 3.19 | FD |
| 34 | 19/06/2020 | 4228161 | 520222 | 2.83 ± 0.4 | 35.76 ± 2.6 | 12.63 | RA |
| 35 | 19/06/2020 | 4227330 | 520275 | 3.47 ± 0.5 | 39.76 ± 3.9 | 11.46 | RA |
| 36 | 19/06/2020 | 4228918 | 521186 | 33.5 ± 1.5 | 42 ± 2.8 | 1.25 | RA |
| 37 | 24/06/2020 | 4226635 | 522091 | 8.7 ± 0.8 | 110.88 ± 4.8 | 12.74 | RA |
| 38 | 24/06/2020 | 4225270 | 522976 | 21.7 ± 1.2 | 116.2 ± 4.8 | 5.35 | RA |
| 39 | 24/06/2020 | 4225230 | 523758 | 31.2 ± 1.5 | 49.84 ± 3.1 | 1.6 | MES |
| 40 | 27/06/2020 | 4225020 | 523252 | 33.8 ± 1.6 | 81.76 ± 3.9 | 2.42 | RA |
| 41 | 27/06/2020 | 4226400 | 522575 | 51.6 ± 1.9 | 106.96 ± 4.8 | 2.07 | RA |
| 42 | 27/06/2020 | 4228141 | 522218 | 37.1 ± 1.7 | 84.84 ± 4.2 | 2.29 | RA |
| 43 | 29/07/2020 | 4228103 | 520998 | 18.4 ± 1.1 | 56.28 ± 3.4 | 3.06 | RA |
| 44 | 02/07/2020 | 4226451 | 520126 | 5.69 ± 0.6 | 27.44 ± 2.3 | 4.82 | RA |
| 45 | 02/07/2020 | 4226001 | 521667 | 6.39 ± 0.7 | 32.34 ± 2.5 | 5.06 | RA |
| 46 | 02/07/2020 | 4226935 | 522738 | 22.2 ± 1.3 | 121.24 ± 5 | 5.46 | RA |
| 47 | 03/07/2020 | 4225650 | 517970 | 1.98 ± 0.4 | 6.3 ± 0.9 | 3.18 | BEA |
| 48 | 03/07/2020 | 4225537 | 519131 | 2.4 ± 0.4 | 23.32 ± 2.1 | 9.72 | RA |
| 49 | 03/07/2020 | 4226041 | 518487 | 8.5 ± 0.8 | 6.83 ± 1.1 | 0.8 | FD |
| 50 | 10/07/2020 | 4224672 | 521833 | 2 ± 0.4 | 36.51 ± 2.4 | 18.26 | RA |
| 51 | 10/07/2020 | 4224688 | 519940 | 11.37 ± 0.9 | 52.92 ± 3 | 4.65 | RA |
| 52 | 10/07/2020 | 4225249 | 520471 | 7.02 ± 0.7 | 14.84 ± 1.7 | 2.11 | FD |
| 53 | 10/07/2020 | 4224461 | 520898 | 17.5 ± 1.1 | 54.32 ± 3.4 | 3.10 | RA |
| 54 | 11/07/2020 | 4223622 | 521663 | 13.48 ± 0.9 | 37.83 ± 2.7 | 2.81 | RA |
| 55 | 11/07/2020 | 4222912 | 522528 | 9.21 ± 0.8 | 69.72 ± 3.6 | 7.57 | MMT |
| 56 | 11/07/2020 | 4223815 | 522630 | 12.77 ± 0.9 | 64.96 ± 3.6 | 5.09 | MES |
| 57 | 13/07/2020 | 4222070 | 520691 | 10.68 ± 0.9 | 25.31 ± 2.2 | 2.37 | MMT |
| 58 | 13/07/2020 | 4221626 | 521487 | 8.29 ± 0.7 | 31.92 ± 2.2 | 3.85 | CC |
| 59 | 13/07/2020 | 4222502 | 521210 | 6.84 ± 0.7 | 88.76 ± 4.2 | 12.98 | MMT |
| 60 | 14/07/2020 | 4221290 | 520046 | 15.8 ± 1.1 | 64.12 ± 3.6 | 4.06 | MES |
| 61 | 14/07/2020 | 4220334 | 520693 | 1.21 ± 0.3 | 22.48 ± 2.1 | 18.58 | CC |
| 62 | 14/07/2020 | 4221408 | 520457 | 6.79 ± 0.7 | 48.72 ± 3.1 | 7.18 | MES |
| 63 | 22/07/2020 | 4224539 | 517346 | 11.39 ± 0.9 | 54.32 ± 3.4 | 4.77 | RA |
| 64 | 22/07/2020 | 4223729 | 518470 | 14 ± 1 | 53.2 ± 2.8 | 3.8 | RA |
| 65 | 22/07/2020 | 4223311 | 518928 | 18.1 ± 1.1 | 72.52 ± 3.6 | 4.01 | RA |
| 66 | 22/07/2020 | 4222948 | 518527 | 7.78 ± 0.7 | 30.46 ± 2.4 | 3.92 | RA |
| 67 | 23/07/2020 | 4224222 | 519630 | 6.29 ± 0.7 | 26.80 ± 2.3 | 4.26 | RA |
| 68 | 23/07/2020 | 4223313 | 520433 | 9.06 ± 0.8 | 37.32 ± 2.7 | 4.12 | RA |
| 69 | 23/07/2020 | 4222957 | 519840 | 8.4 ± 0.8 | 37.66 ± 2.7 | 4.48 | RA |
| 70 | 23/07/2020 | 4224681 | 518859 | 13.11 ± 0.9 | 39.70 ± 2.8 | 3.03 | RA |
| 71 | 24/07/2020 | 4225134 | 517366 | 1.79 ± 0.3 | 13.16 ± 1.4 | 7.35 | BEA |
| 72 | 24/07/2020 | 4224439 | 516722 | 2.59 ± 0.4 | 12.6 ± 1.5 | 4.86 | BEA |

| #Site | Date (dd/mm/yyyy) | North | East | ²²² Rn (kBq m ⁻³) | ²²⁰ Rn (kBq m ⁻³) | ²²⁰ Rn/ ²²² Rn | Lithology |
|-------|----------------------|---------|--------|---|---|--------------------------------------|-----------|
| 73 | 24/07/2020 | 4223854 | 516643 | 9.77 ± 0.8 | 81.76 ± 3.9 | 8.37 | RA |
| 74 | 24/07/2020 | 4223120 | 515654 | 2.4 ± 0.4 | 12.18 ± 1.5 | 5.08 | BEA |
| 75 | 27/07/2020 | 4223298 | 517288 | 8.24 ± 0.7 | 35.92 ± 2.6 | 4.36 | RA |
| 76 | 27/07/2020 | 4222670 | 517786 | 12.65 ± 0.9 | 57.4 ± 3.3 | 4.54 | RA |
| 77 | 27/07/2020 | 4222102 | 517356 | 12.09 ± 0.9 | 27.3 ± 2.3 | 2.26 | RA |
| 78 | 27/07/2020 | 4221775 | 516535 | 10.19 ± 0.8 | 35.11 ± 2.6 | 3.45 | MES |
| 79 | 28/07/2020 | 4222683 | 518811 | 6.08 ± 0.6 | 22.48 ± 2.1 | 3.7 | RA |
| 80 | 28/07/2020 | 4222062 | 519672 | 10.34 ± 0.8 | 48.44 ± 3.1 | 4.68 | RA |
| 81 | 28/07/2020 | 4221647 | 518581 | 7.31 ± 0.7 | 36.04 ± 2.4 | 4.93 | MES |
| 82 | 31/07/2020 | 4220375 | 518579 | 6.55 ± 0.7 | 42 ± 2.8 | 6.41 | QC |
| 83 | 31/07/2020 | 4220008 | 517684 | 2.88 ± 0.4 | 18.73 ± 1.9 | 6.5 | PPC |
| 84 | 31/07/2020 | 4220789 | 517844 | 13.74 ± 1 | 96.6 ± 4.5 | 7.03 | MES |
| 85 | 31/07/2020 | 4221222 | 517343 | 7.64 ± 0.7 | 47.04 ± 4.2 | 6.16 | QC |
| 86 | 03/08/2020 | 4220521 | 519656 | 10.04 ± 0.8 | 47.04 ± 3.1 | 4.69 | MES |
| 87 | 03/08/2020 | 4219617 | 520186 | 4.1 ± 0.5 | 61.88 ± 3.1 | 15.09 | CC |
| 88 | 03/08/2020 | 4219453 | 518283 | 10.38 ± 0.8 | 27.89 ± 2.3 | 2.69 | PPC |
| 89 | 03/08/2020 | 4218796 | 518556 | 1.09 ± 0.3 | 12.35 ± 1.5 | 11.33 | PPC |
| 90 | 04/08/2020 | 4219851 | 519403 | 16.6 ± 1.1 | 64.96 ± 3.6 | 3.91 | RA |
| 91 | 04/08/2020 | 4218957 | 519337 | 7.35 ± 0.7 | 55.16 ± 3.4 | 7.5 | PPC |
| 92 | 04/08/2020 | 4217778 | 519093 | 2.97 ± 0.5 | 6.47 ± 1.1 | 2.18 | PPC |
| 93 | 04/08/2020 | 4217154 | 519531 | 21.1 ± 1.2 | 53.48 ± 3.4 | 2.53 | MMT |
| 94 | 04/08/2020 | 4217074 | 519737 | 17.3 ± 1.1 | 123.48 ± 5 | 7.14 | ASP |
| 95 | 25/08/2020 | 4219140 | 517065 | 2.98 ± 0.4 | 9.8 ± 1.1 | 3.29 | PPC |
| 96 | 28/08/2020 | 4218288 | 517665 | 38.6 ± 1.7 | 54.32 ± 3.4 | 1.41 | MMT |
| 97 | 28/08/2020 | 4217490 | 517782 | 21.6 ± 1.2 | 69.72 ± 3.6 | 3.23 | PPC |
| 98 | 28/08/2020 | 4217476 | 516842 | 2.64 ± 0.4 | 11.45 ± 1.5 | 4.34 | PPC |
| 99 | 28/08/2020 | 4216358 | 517056 | 1.63 ± 0.3 | 35.5 ± 2.6 | 21.78 | CC |
| 100 | 29/08/2020 | 4217573 | 518404 | 6.28 ± 0.7 | 19.88 ± 1.9 | 3.17 | TER |
| 101 | 29/08/2020 | 4216498 | 519334 | 10.56 ± 0.8 | 34.61 ± 2.6 | 3.28 | TER |
| 102 | 29/08/2020 | 4216430 | 519408 | 12.94 ± 0.9 | 37.04 ± 2.7 | 2.86 | TER |
| 103 | 31/08/2020 | 4221544 | 515712 | 5.7 ± 0.6 | 56.56 ± 4.8 | 9.92 | RA |
| 104 | 31/08/2020 | 4222660 | 515264 | 9.4 ± 0.8 | 22.18 ± 2.1 | 2.36 | RA |
| 105 | 31/08/2020 | 4220484 | 516361 | 6.83 ± 0.7 | 38.08 ± 2.7 | 5.58 | RA |
| 106 | 31/08/2020 | 4218451 | 516457 | 10.42 ± 0.8 | 32.4 ± 2.5 | 3.11 | RA |
| 107 | 05/09/2020 | 4222235 | 514196 | 0.92 ± 0.2 | 3.28 ± 0.7 | 3.56 | BEA |
| 108 | 05/09/2020 | 4221568 | 513059 | 1.4 ± 0.3 | 5.07 ± 0.9 | 3.62 | BEA |
| 109 | 05/09/2020 | 4220117 | 512992 | 15 ± 1 | 39.12 ± 2.7 | 2.61 | MES |
| 110 | 05/09/2020 | 4220416 | 514218 | 7.2 ± 0.7 | 40.07 ± 2.8 | 5.57 | MES |
| 111 | 05/09/2020 | 4220725 | 514984 | 15 ± 1 | 44.8 ± 2.8 | 2.99 | MES |
| 112 | 05/09/2020 | 4220793 | 514983 | 9.05 ± 0.8 | 51.24 ± 3.6 | 5.66 | MES |
| 113 | 06/09/2020 | 4220899 | 514916 | 15 ± 1 | 24.98 ± 2.2 | 1.67 | MES |

| #Site | Date (dd/mm/yyyy) | North | East | ²²² Rn (kBq m ⁻³) | ²²⁰ Rn (kBq m ⁻³) | ²²⁰ Rn/ ²²² Rn | Lithology |
|-------|----------------------|---------|--------|---|---|--------------------------------------|-----------|
| 114 | 09/09/2020 | 4219943 | 512032 | 5.48 ± 0.6 | 10.36 ± 1.4 | 1.89 | FD |
| 115 | 09/09/2020 | 4221185 | 511998 | 2.13 ± 0.4 | 7.19 ± 1.2 | 3.38 | BEA |
| 116 | 09/09/2020 | 4216803 | 516010 | 6.11 ± 0.7 | 53.48 ± 3.1 | 8.75 | RA |
| 117 | 10/09/2020 | 4219672 | 515047 | 1.47 ± 0.3 | 15.62 ± 1.7 | 10.63 | PPC |
| 118 | 10/09/2020 | 4219038 | 515325 | 2.03 ± 0.4 | 46.2 ± 2.4 | 22.76 | QC |
| 119 | 10/09/2020 | 4219287 | 515756 | 5.15 ± 0.6 | 51.8 ± 3.1 | 10.06 | PPC |
| 120 | 10/09/2020 | 4218295 | 515411 | 10.18 ± 0.8 | 65.8 ± 3.6 | 6.46 | PPC |
| 121 | 10/09/2020 | 4218210 | 514268 | 29.9 ± 1.5 | 71.4 ± 3.6 | 2.39 | CC |
| 122 | 10/09/2020 | 4218237 | 513265 | 8.05 ± 0.7 | 54.6 ± 3.4 | 6.78 | CC |
| 123 | 10/09/2020 | 4219178 | 513991 | 4.04 ± 0.5 | 43.26 ± 2.6 | 10.71 | CC |
| 124 | 10/09/2020 | 4219315 | 512827 | 8.25 ± 0.7 | 31.36 ± 2.2 | 3.8 | PPC |
| 125 | 11/09/2020 | 4220011 | 517084 | 10.83 ± 0.9 | 56.84 ± 3.4 | 5.25 | PPC |
| 126 | 11/09/2020 | 4216650 | 514744 | 9.4 ± 0.8 | 27.1 ± 2.3 | 2.88 | RA |
| 127 | 11/09/2020 | 4215831 | 513997 | 2.68 ± 0.4 | 24.81 ± 2.2 | 9.26 | FLY |
| 128 | 16/09/2020 | 4217228 | 513782 | 11.26 ± 0.9 | 82.04 ± 3.4 | 7.29 | FLY |
| 129 | 16/09/2020 | 4217246 | 512943 | 3.6 ± 0.5 | 42.22 ± 2.6 | 11.73 | CC |
| 130 | 16/09/2020 | 4217245 | 512963 | 3.55 ± 0.5 | 20.78 ± 1.8 | 5.85 | CC |
| 131 | 16/09/2020 | 4217093 | 513037 | 3.91 ± 0.5 | 66.92 ± 3.6 | 17.12 | CC |
| 132 | 16/09/2020 | 4216605 | 513041 | 5.12 ± 0.6 | 16.6 ± 1.8 | 3.24 | CC |
| 133 | 16/09/2020 | 4216623 | 512992 | 1.57 ± 0.3 | 13.08 ± 1.6 | 8.33 | CC |
| 134 | 16/09/2020 | 4216618 | 512982 | 1.13 ± 0.3 | 24 ± 2.2 | 21.24 | CC |
| 135 | 01/04/2021 | 4220768 | 511198 | 1.19 ± 0.3 | 3.78 ± 0.7 | 3.18 | BEA |
| 136 | 01/04/2021 | 4220104 | 510239 | 1.02 ± 0.3 | 8.51 ± 1.2 | 8.35 | BEA |
| 137 | 01/04/2021 | 4219298 | 508733 | 0.92 ± 0.2 | 8.76 ± 1.3 | 9.53 | BEA |
| 138 | 01/04/2021 | 4218085 | 509747 | 5.3 ± 0.6 | 28.67 ± 2.7 | 5.41 | MMT |
| 139 | 02/04/2021 | 4219640 | 511134 | 26.3 ± 1.4 | 28.03 ± 2.4 | 1.07 | RA |
| 140 | 02/04/2021 | 4218936 | 511774 | 5.93 ± 0.6 | 18.54 ± 1.9 | 3.13 | PPC |
| 141 | 02/04/2021 | 4218543 | 510567 | 3 ± 0.4 | 3.64 ± 0.8 | 1.21 | PPC |
| 142 | 12/04/2021 | 4226289 | 523082 | 64.8 ± 2.2 | 72.8 ± 3.9 | 1.12 | RA |
| 143 | 12/04/2021 | 4226264 | 524703 | 16.7 ± 1.1 | 61.32 ± 3.3 | 3.67 | MES |
| 144 | 12/04/2021 | 4227350 | 523924 | 6.86 ± 0.7 | 21.08 ± 2.1 | 3.07 | RA |
| 145 | 12/04/2021 | 4225865 | 523984 | 17.5 ± 1.1 | 28.98 ± 2.4 | 1.66 | RA |
| 146 | 14/04/2021 | 4227274 | 525060 | 24.5 ± 1.3 | 16.94 ± 1.8 | 0.69 | MES |
| 147 | 14/04/2021 | 4226953 | 525597 | 27.8 ± 1.4 | 53.2 ± 3.3 | 1.91 | RA |
| 148 | 14/04/2021 | 4227839 | 526198 | 6.79 ± 0.7 | 25.37 ± 2 | 3.74 | QC |
| 149 | 14/04/2021 | 4226989 | 526965 | 15 ± 1 | 49.28 ± 3.1 | 3.29 | MES |
| 150 | 26/04/2021 | 4228416 | 522669 | 78.6 ± 2.4 | 78.4 ± 3.9 | 1 | RA |
| 151 | 26/04/2021 | 4227578 | 524318 | 36.8 ± 1.6 | 35.84 ± 2.7 | 0.97 | RA |
| 152 | 26/04/2021 | 4226776 | 524131 | 27.5 ± 1.4 | 39.2 ± 2.8 | 1.43 | RA |
| 153 | 28/04/2021 | 4227395 | 522964 | 81.3 ± 2.5 | 71.68 ± 3.9 | 0.88 | RA |
| 154 | 28/04/2021 | 4227572 | 527895 | 18.2 ± 1.1 | 25.48 ± 2.2 | 1.4 | RA |

| #Site | Date (dd/mm/yyyy) | North | East | ^{222}Rn (kBq m ⁻³) | ^{220}Rn (kBq m ⁻³) | $^{220}\text{Rn}/^{222}\text{Rn}$ | Lithology |
|-------|----------------------|---------|--------|---|---|-----------------------------------|-----------|
| 155 | 28/04/2021 | 4228152 | 528082 | 6.03 ± 0.6 | 22.54 ± 2.1 | 3.74 | RA |
| 156 | 30/04/2021 | 4217086 | 510497 | 0.98 ± 0.3 | 5.91 ± 1.1 | 6.03 | CC |
| 157 | 30/04/2021 | 4218149 | 511585 | 7.2 ± 0.7 | 49.56 ± 3.1 | 6.88 | MES |
| 158 | 09/05/2021 | 4225977 | 525698 | 13.71 ± 1 | 58.24 ± 3.4 | 4.25 | MES |
| 159 | 09/05/2021 | 4225544 | 526684 | 21.7 ± 1.2 | 45.08 ± 3.1 | 2.08 | MES |
| 160 | 10/05/2021 | 4224568 | 523323 | 19.6 ± 1.2 | 33.18 ± 2.5 | 1.69 | MES |
| 161 | 10/05/2021 | 4224523 | 524094 | 22.5 ± 1.3 | 45.92 ± 3 | 2.04 | MES |
| 162 | 10/05/2021 | 4225106 | 525057 | 13.31 ± 0.9 | 46.76 ± 3.1 | 3.51 | MES |
| 163 | 10/05/2021 | 4226548 | 526291 | 69.3 ± 2.3 | 44.52 ± 3 | 0.64 | MES |
| 164 | 10/05/2021 | 4226194 | 527412 | 13.65 ± 1 | 34.77 ± 2.6 | 2.55 | MES |
| 165 | 11/05/2021 | 4224843 | 525735 | 13.62 ± 0.9 | 29.99 ± 2.4 | 2.2 | MES |
| 166 | 11/05/2021 | 4225025 | 526932 | 10.51 ± 0.8 | 31.5 ± 2.5 | 3 | MES |
| 167 | 11/05/2021 | 4225483 | 528051 | 6.56 ± 0.7 | 42 ± 2.8 | 6.4 | MMT |
| 168 | 12/05/2021 | 4224876 | 527536 | 11 ± 0.9 | 29.04 ± 2.4 | 2.64 | MMT |
| 169 | 14/05/2021 | 4215328 | 511853 | 4.03 ± 0.5 | 25.59 ± 2.2 | 6.35 | FLY |
| 170 | 14/05/2021 | 4216215 | 511592 | 1.08 ± 0.3 | 19.49 ± 1.6 | 18.04 | RA |
| 171 | 14/05/2021 | 4216873 | 512055 | 19.2 ± 1.1 | 7.62 ± 1.2 | 0.4 | FD |
| 172 | 14/05/2021 | 4215232 | 512695 | 12.44 ± 0.9 | 31.75 ± 2.5 | 2.55 | RA |

Table 12. Statistics of soil-radon and -thoron activity concentrations (kBq m⁻³) and $^{220}\text{Rn}/^{222}\text{Rn}$ ratio of the 172 sites.

| Statistics | N | Min | Lower quartile | Median | Upper quartile | Max | Mean | Standard deviation | Range |
|-----------------------------------|-----|------|----------------|--------|----------------|--------|-------|--------------------|--------|
| ^{222}Rn | 172 | 0.69 | 4.08 | 8.66 | 14.25 | 81.3 | 12.37 | 13.29 | 80.61 |
| ^{220}Rn | 172 | 2.63 | 22.48 | 35.88 | 54.32 | 123.48 | 40.74 | 26.66 | 120.85 |
| $^{220}\text{Rn}/^{222}\text{Rn}$ | 172 | 0.4 | 2.59 | 3.91 | 6.46 | 22.76 | 5.29 | 4.3 | 22.36 |

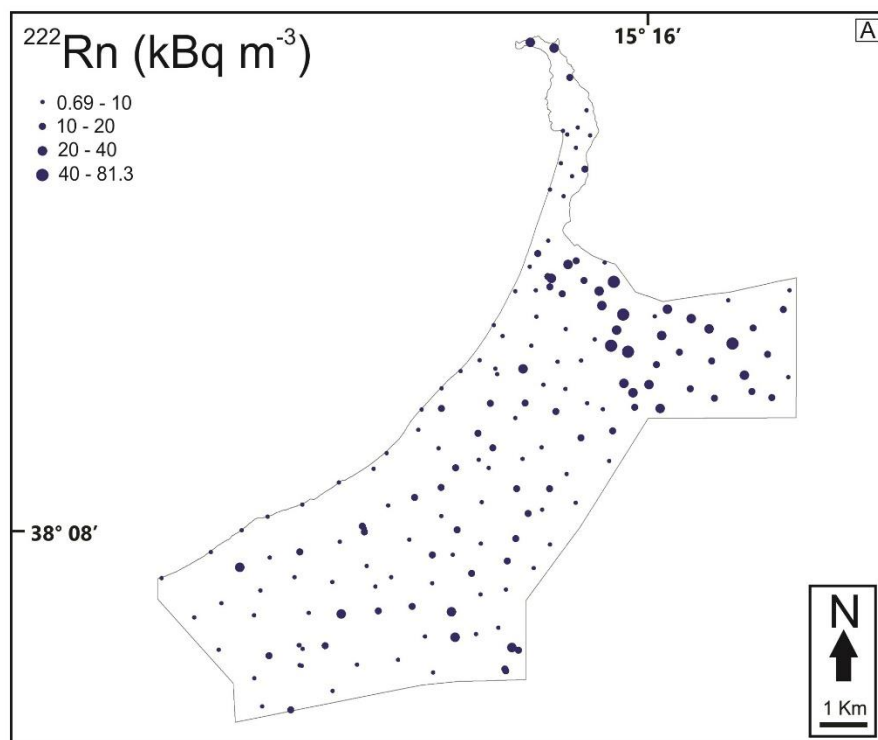
parameter regulating radon concentration in soils (radon concentration increases with increasing depth; see Section 5.4.1.3).

Figure 31 shows the distribution maps of ^{222}Rn and ^{220}Rn and that of the $^{220}\text{Rn}/^{222}\text{Rn}$ ratio. Soil- ^{222}Rn and ^{220}Rn concentrations are higher in the eastern sector of the investigated area, where all the ^{222}Rn values higher than 40 kBq m⁻³ and most of the ^{220}Rn values above >100 kBq m⁻³ have been detected (Fig. 31A and B).

Concerning the $^{220}\text{Rn}/^{222}\text{Rn}$ ratio (Fig. 31C), values in the western sector result often above 3 (up to 22.76) whereas in the eastern sector they are usually comprised between 0.4 and 3.

Table 13. Soil- ^{222}Rn activity concentration (kBq m^{-3}) obtained in this work compared to that measured in Italy and other European countries (data from: ^aBeaubien et al., 2003; ^bVaupotic, 2012; ^cDubois, 2005 and references therein).

| ^{222}Rn | Min | Max | Mean |
|-----------------------------|------|-------|-------|
| NE Sicily (this work) | 0.69 | 81.3 | 12.37 |
| Italy ^a | 0.4 | 1200 | 26.6 |
| Slovenia ^b | 1 | 200 | 40.9 |
| France ^c | - | 598 | 58 |
| Germany ^c | <5 | >1000 | 55 |
| Austria ^c | 40 | 600 | 75 |
| Czech Republic ^c | 1 | 1664 | 28.08 |
| Estonia ^c | 1 | 2224 | 62.5 |
| Lithuania ^c | 1 | 60 | 18.5 |
| Latvia ^c | 2 | 52 | - |
| Luxembourg ^c | - | 120 | 45 |
| Poland ^c | 3.2 | 89 | 38.73 |
| Slovakia ^c | 0.5 | 712 | 21.6 |



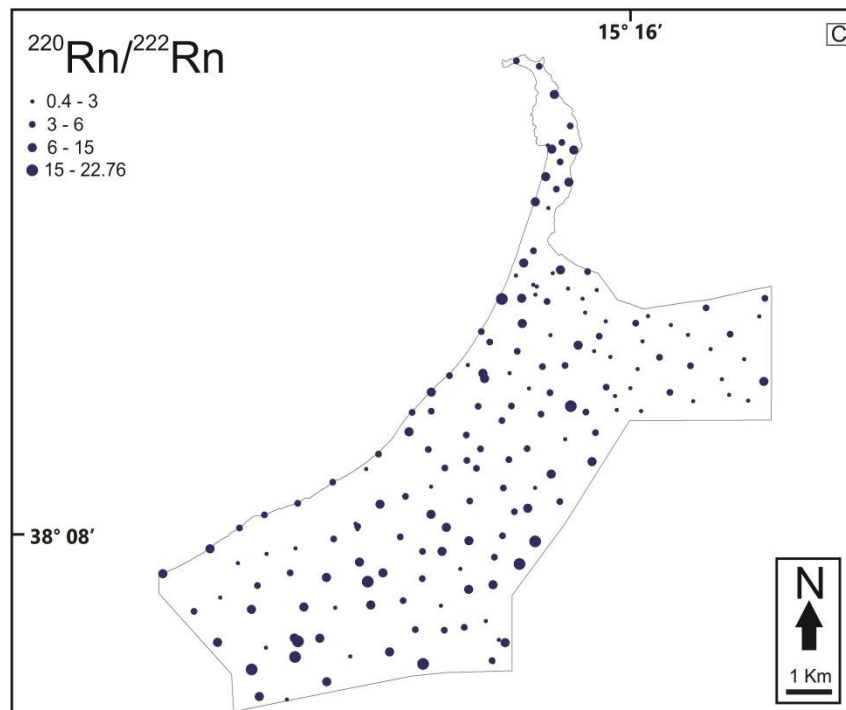
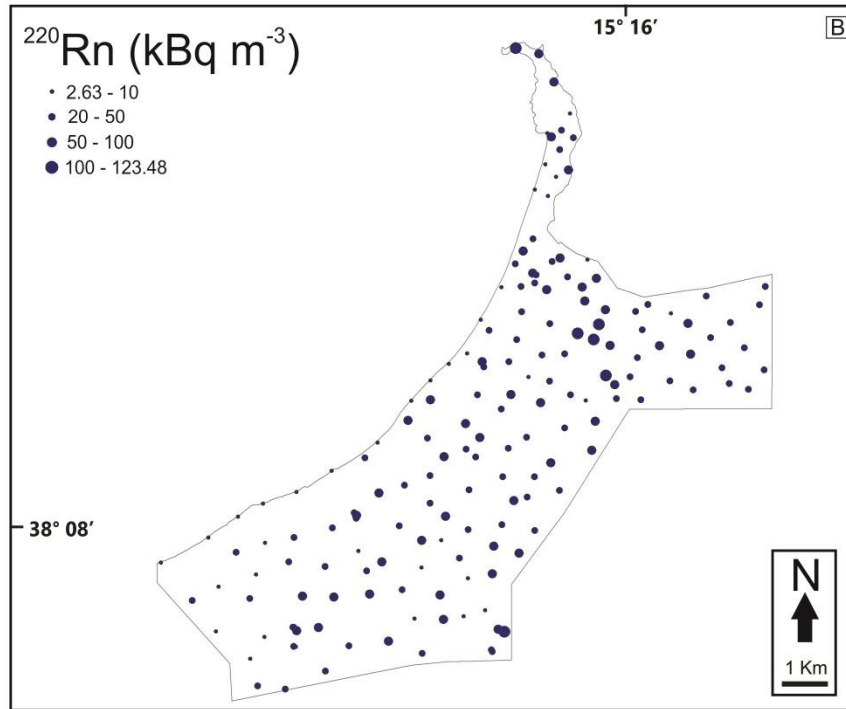


Figure 31. Distribution maps of ^{222}Rn (A) and ^{220}Rn (B) concentrations and $^{220}\text{Rn}/^{222}\text{Rn}$ ratios (C) at all the 172 sampling locations. ^{222}Rn and ^{220}Rn are higher in the eastern portion of the area whereas the $^{220}\text{Rn}/^{222}\text{Rn}$ ratio shows the opposite trend, being higher in the western sector.

Table 14. The number of measurements for each lithology.

| Lithology | No.of measurements |
|--|--------------------|
| beach deposits (BEA) | 14 |
| fluvial deposits (FD) | 6 |
| marine and fluvial terraces (TER) | 6 |
| cineritic tuffs (TUF) | 2 |
| recent alluvial sediments (RA) | 68 |
| “sabbie and ghiaie” of Messina (MES) | 26 |
| Quaternary clays (QC) | 4 |
| Plio-Pleistocene calcarenites (PPC) | 15 |
| Middle Miocene terrigenous sediments (MMT) | 8 |
| Cretaceous clays (CC) | 14 |
| Capo d’Orlando flysch (FLY) | 3 |
| Aspromonte Unit (ASP) | 6 |
| Total | 172 |

Measurements were performed in soils belonging to twelve different lithologies. Recent alluvial sediments were the most analysed lithology (68 measurements), whereas the poorest investigated formations were the cineritic tuffs (outcropping only in the northern tip of the Milazzo Peninsula), the Capo d’Orlando flysch and the quaternary clays (Table 14).

As already mentioned, Rn concentration in soil gas depends on various factors. All measurements were performed at the same depth (0.5-0.6 m) and at similar temperatures and soil moisture. In this condition, Rn concentration depends on four parameters:

- soil permeability;
- U and Th amounts in soil;
- soil texture and fabric;
- presence of advective flow linked to the uprising of deep gases;

I want to remark that permeability, U-Th abundance, texture and fabric are exclusively a function of lithology.

Box plots (Fig. 32) evidence a robust lithological control on ^{222}Rn and ^{220}Rn concentrations. The beach sediments (BEA) exhibit the lowest Rn concentration. This is due to the fact that the absence of a fine-grained matrix favours gas exchanges between soil and atmosphere causing the dilution of radon beneath the

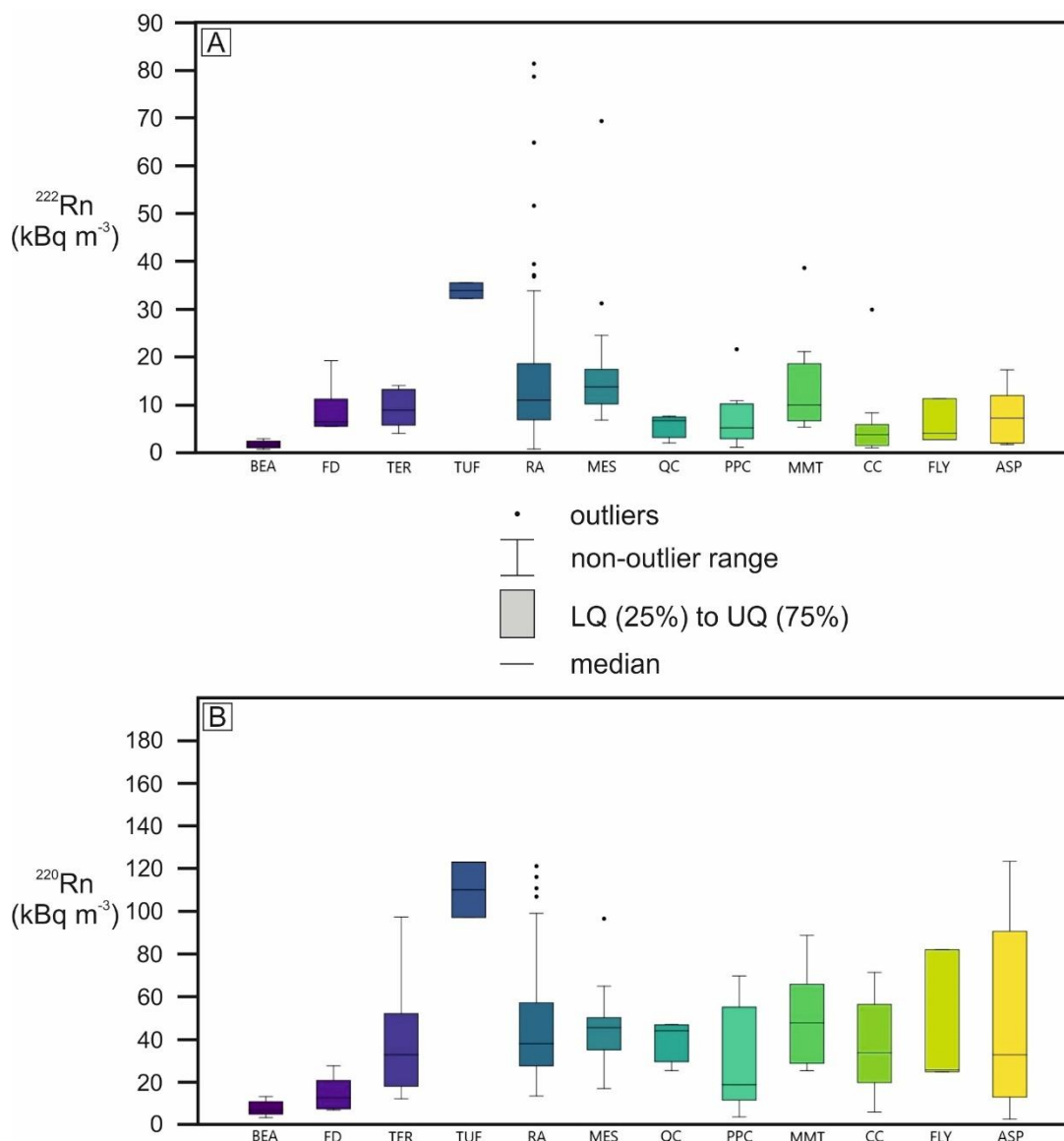


Figure 32. Box plots of the soil ^{222}Rn and ^{220}Rn activity concentration collected on the different lithologies outcropping in the study area.

ground surface. Low Rn values were also measured in clay lithologies (CC and QC) because of their low permeability, and in carbonate rocks (PPC), which presumably display the lowest U and Th content among the investigated rocks.

On the other hand, cineritic tuffs (TUF), which originated from hydromagmatic eruption occurred at the Island of Vulcano (Aeolian Islands; Lucchi et al., 2008), show the highest median by far. This feature probably reflects the high U and Th concentration that commonly characterizes the volcanic product emitted from the Vulcano Island (De Astis et al., 1997).

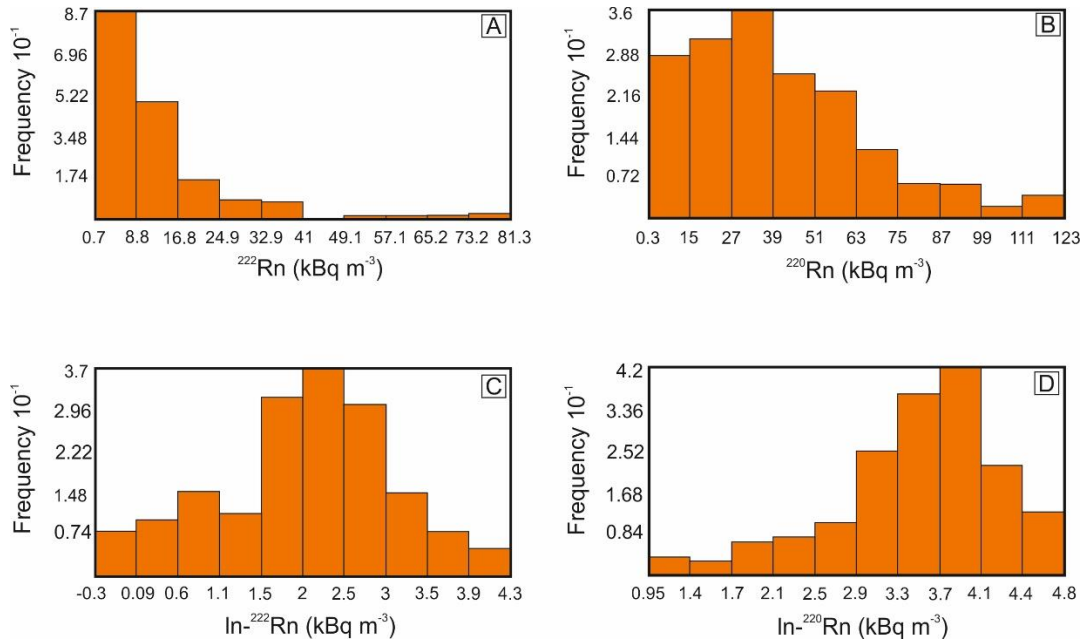


Figure 33. Histogram of: (A) radon concentrations; (B) thoron concentrations; (C) radon \ln -transformed values; (D) thoron \ln -transformed values.

Histograms of ^{222}Rn and ^{220}Rn concentrations are depicted in Figure 33. Both datasets do not follow a normal distribution; ^{222}Rn values exhibit a J shape (Fig. 33A) whereas ^{220}Rn histogram is right-skewed (Fig. 33B). Histograms of \ln -transformed data illustrate that $\ln-^{222}\text{Rn}$ concentrations (Fig. 33C) approximate a \ln -normal distribution even if a bimodal behaviour can be observed since a slight peak at 0.6-1.1 $\ln-^{222}\text{Rn}$ (kBq m^{-3}) occurs along with the main peak at 2-2.5 $\ln-^{222}\text{Rn}$ (kBq m^{-3}). Conversely, $\ln-^{220}\text{Rn}$ transformed data are skewed to the left (Fig. 33D).

Also NNPs (Fig. 34) confirm that ^{222}Rn and ^{220}Rn concentrations are not normally distributed. However, NNPs were used to recognize Rn anomalous concentrations by identifying the anomaly threshold value, which is placed in correspondence of the inflection point (i.e. change in direction of curvature) of the NPP.

The anomaly threshold represents the limit between background concentrations (depending on permeability, U-Th content, texture and fabric of soil) and anomalous values (connected to the occurrence of deep gases uprising along faults and fractures). Here, outliers on the up end of NNPs are treated as anomalies since several authors confirmed that they usually indicate real gas anomalies (Bertolo and Verdi,

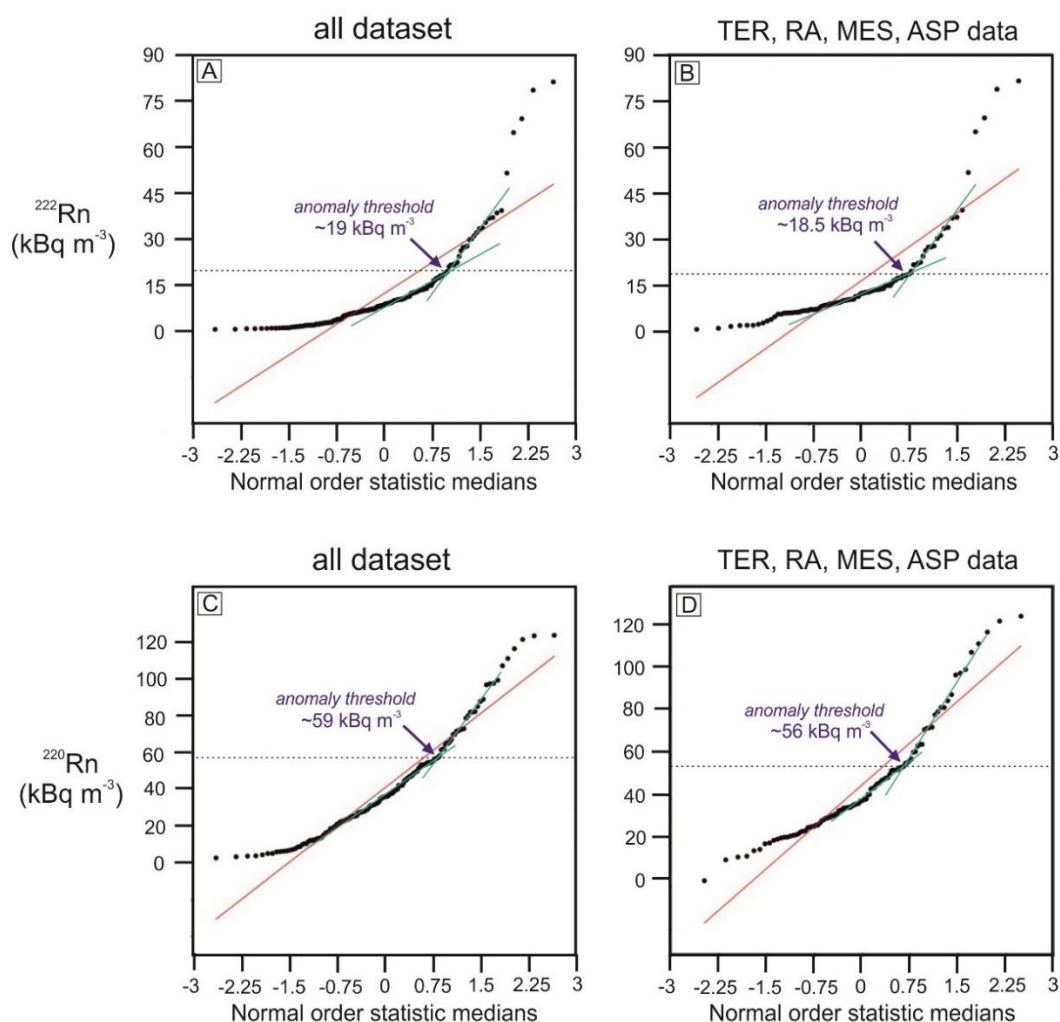


Figure 34. Normal probability plots (NPPs) for ^{222}Rn and ^{220}Rn soil gas concentrations: (A) and (C) for the whole dataset; (B) and (D) for values collected in TER, RA, MES and ASP lithologies. The anomaly threshold is fixed at the inflection point, which marks the intersection of straight lines (in green) approximating different segments of NPPs.

2001; Kemski et al., 2001; Tóth et al., 2006; Bossew et al., 2008; Appleton et al., 2011; Szabo et al 2014; Yuce et al., 2017). Even if many approaches have been proposed to distinguish among different populations (e.g. by using the interquartile range or the mean value plus two standard deviations; Beaubron et al., 2002; Beaubien et al., 2003; Fu et al., 2005), NPPs are currently considered as the best method (Yuce et al., 2017; Sciarra et al., 2015, 2018).

Concerning Rn-soil analyses, it is intuitive that determining the anomaly threshold through NPPs is more reliable if soils, where measurements are performed, have similar permeability, radiological (i.e. U and Th contents) and petrological (i.e.

texture and fabric) properties. As a result, three of the four major parameters governing the Rn concentration in the soil would be rather uniform among all measurements sites, and all differences in Rn concentration would be presumably related to the presence of deep contributions due to advective fluid transport.

For this reason, ^{222}Rn and ^{220}Rn NPPs were drawn for the whole database (Fig. 34A and C) and for measurements carried out in TER, RA, MES and ASP (Fig. 34B and D), because these lithologies exhibit comparable permeability, radiological and petrological characteristics.

According to NPPs, ^{222}Rn values higher than $\sim 19 \text{ kBq m}^{-3}$ are defined as anomalies. More precisely, for TER, RA, MES and ASP lithologies, the ^{222}Rn anomaly threshold is set at $\sim 18.5 \text{ kBq m}^{-3}$.

Concerning ^{220}Rn , the anomaly threshold results to be $\sim 59 \text{ kBq m}^{-3}$. Then, soil gas concentrations higher than the threshold value should be considered as anomalies. For TER, RA, MES and ASP lithologies, the selected threshold signal is $\sim 56 \text{ kBq m}^{-3}$.

Unfortunately, ^{220}Rn NPPs are more or less linear, and it was not possible to define a clear inflection point. For this reason, the anomaly threshold determined for ^{220}Rn should be only viewed as a raw estimation.

5.5.2 Interpolation and radon maps

^{222}Rn , ^{220}Rn and $^{220}\text{Rn}/^{222}\text{Rn}$ data were interpolated and three prediction maps were produced. Soil-gas predictions across the studied area were found for cells of 250 x 250 m. IDW interpolation (see Section 5.4.3) was carried out with an inverse distance weighting power of 2. Moreover, 15 and 10 were set as the maximum and the minimum number of nearest observations located within a distance of 3000 m. Prediction and contour maps for ^{222}Rn , ^{220}Rn and $^{220}\text{Rn}/^{222}\text{Rn}$ ratio are shown in Figures 35, 36 and 37, respectively.

The studied area is characterised by low to high soil-gas Rn concentrations, which do not show a perfect correlation with geological formations or with mapped faults (Fig. 38). Prediction maps for ^{222}Rn and ^{220}Rn (Fig. 35 and 36) display that higher Rn concentrations are located on the eastern side of the studied area, in agreement with previous remarks.

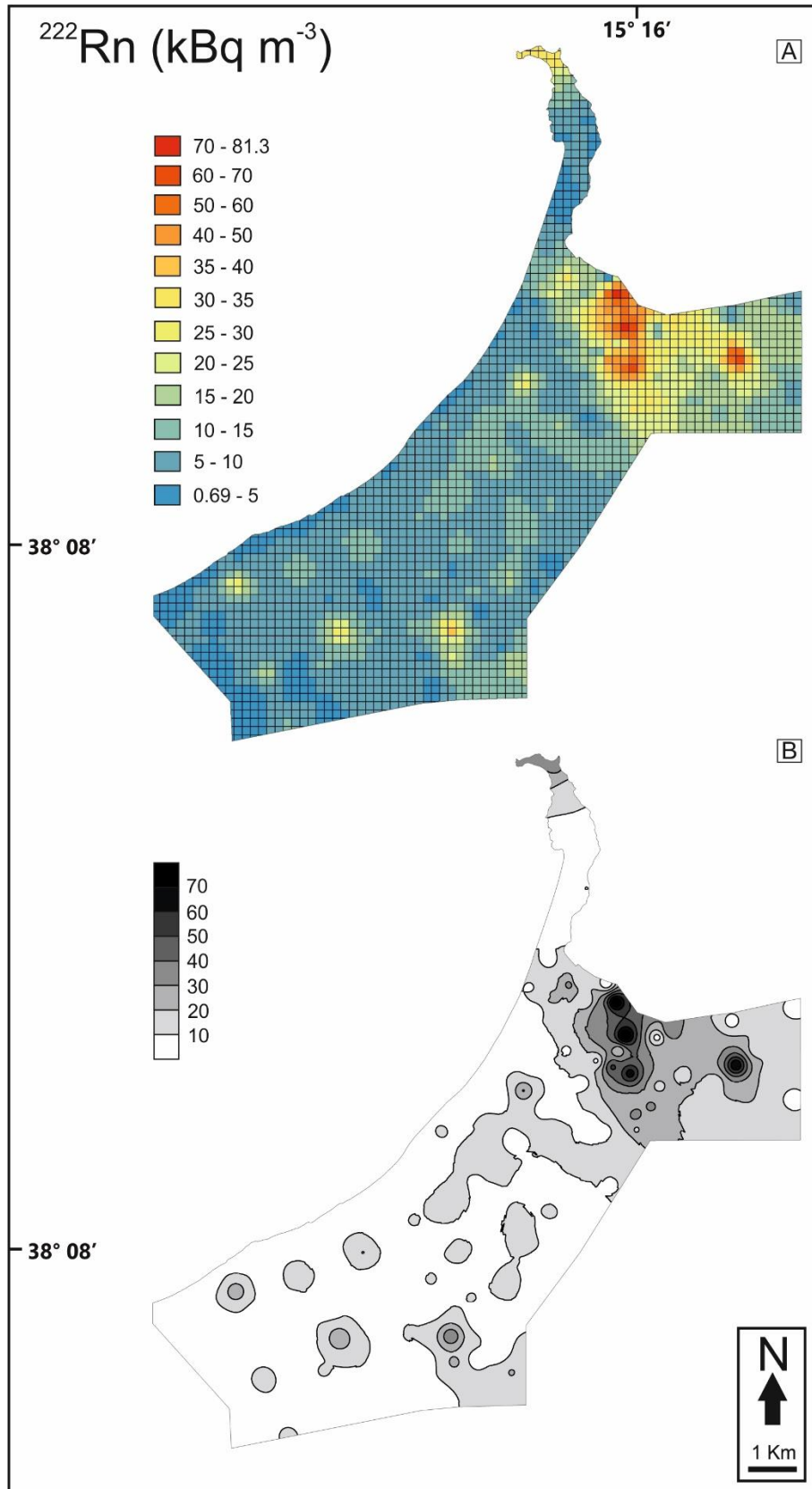


Figure 35. Prediction map (IDW interpolation; $idp=2$, $n_{min}=10$, $n_{max}=15$) for 250 x 250 m cells (A) and contour map (B) for soil-²²²Rn concentration (kBq m⁻³).

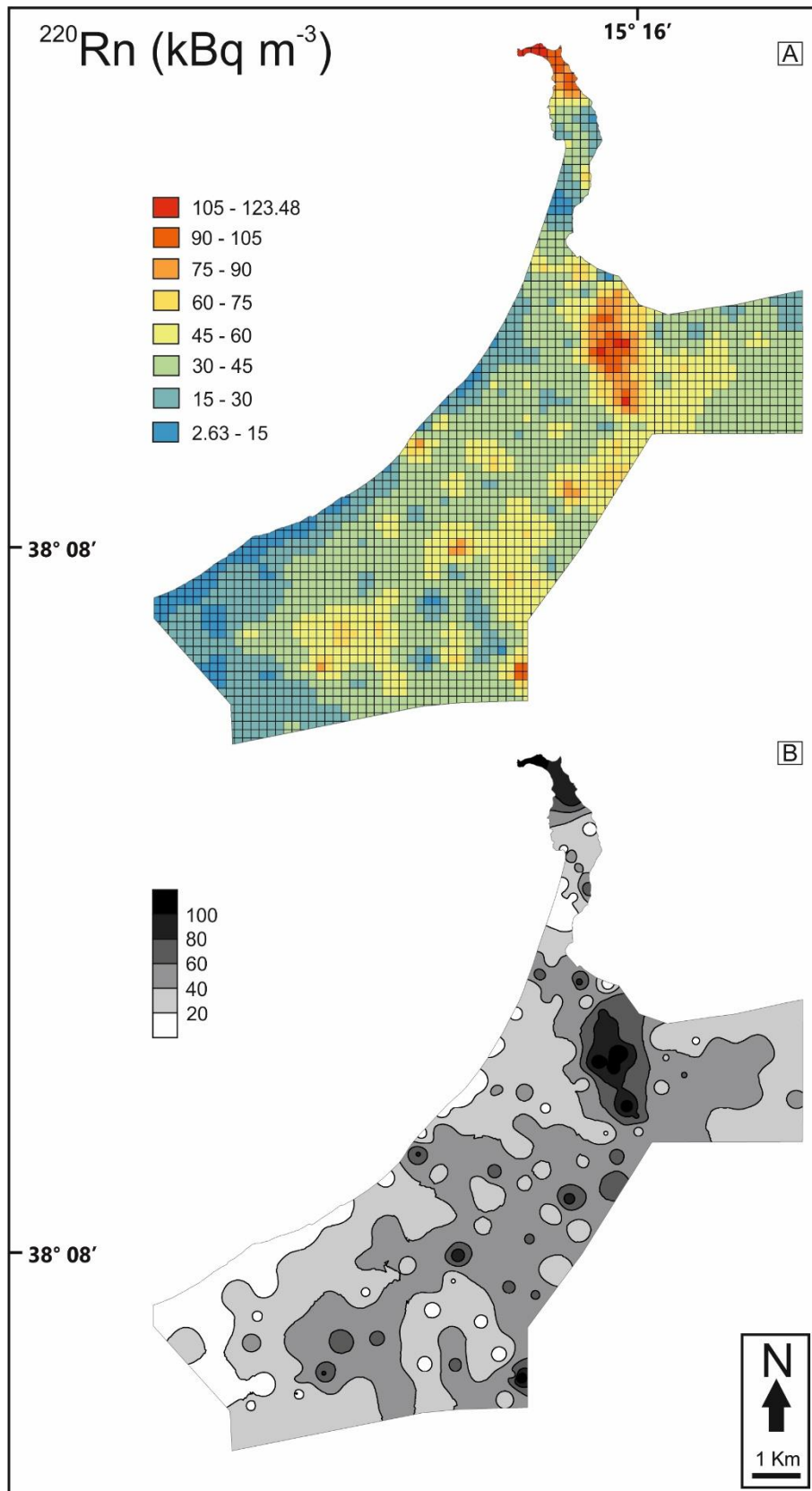


Figure 36. Prediction map (IDW interpolation; $idp=2$, $n_{min}=10$, $n_{max}=15$) for 250 x 250 m cells (A) and contour map (B) for soil- ^{220}Rn concentration (kBq m^{-3}).

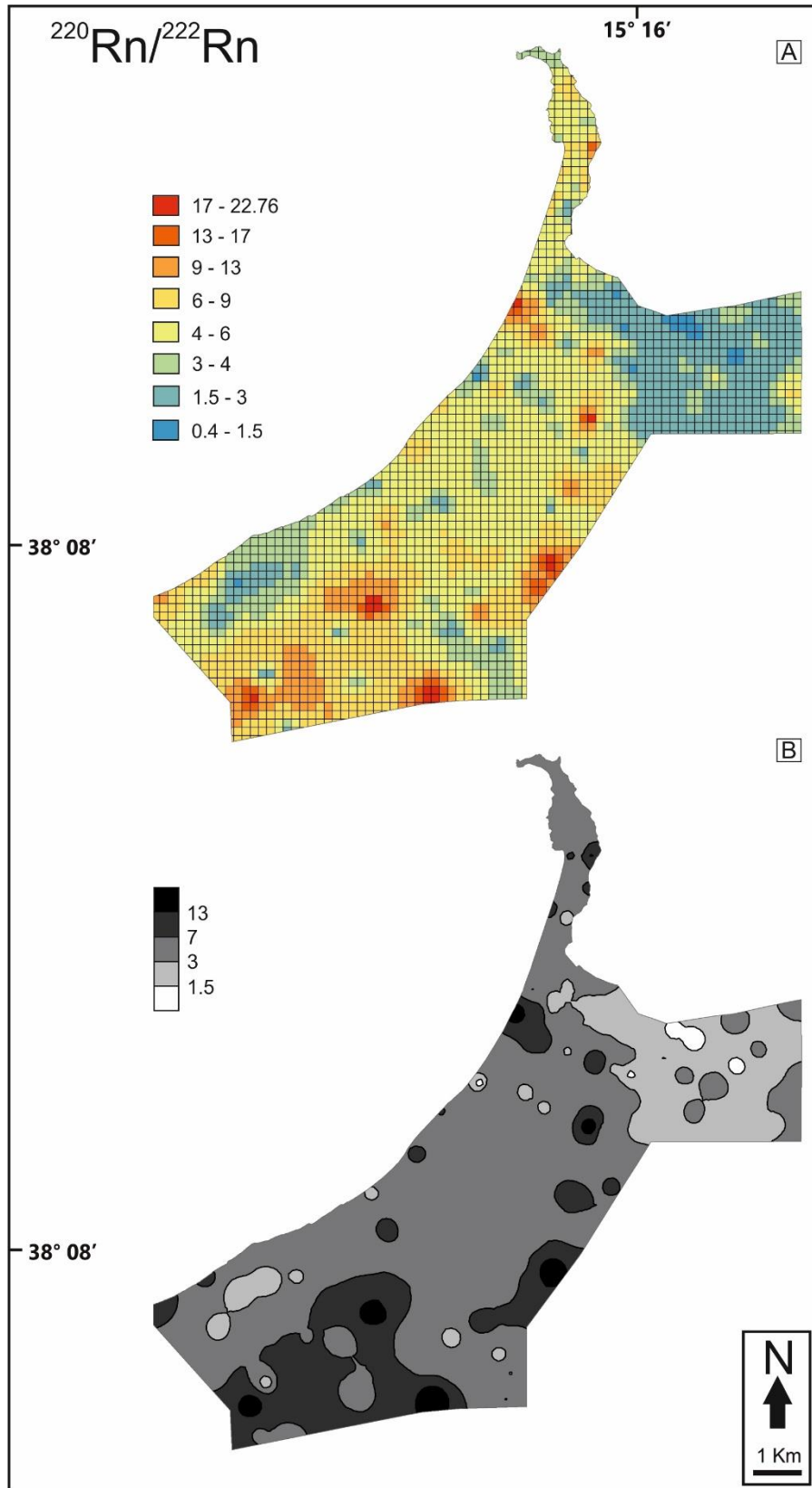


Figure 37. Prediction map (IDW interpolation; $idp=2$, $n_{min}=10$, $n_{max}=15$) for 250 x 250 m cells (A) and contour map (B) for soil- $^{220}\text{Rn}/^{222}\text{Rn}$ ratio.

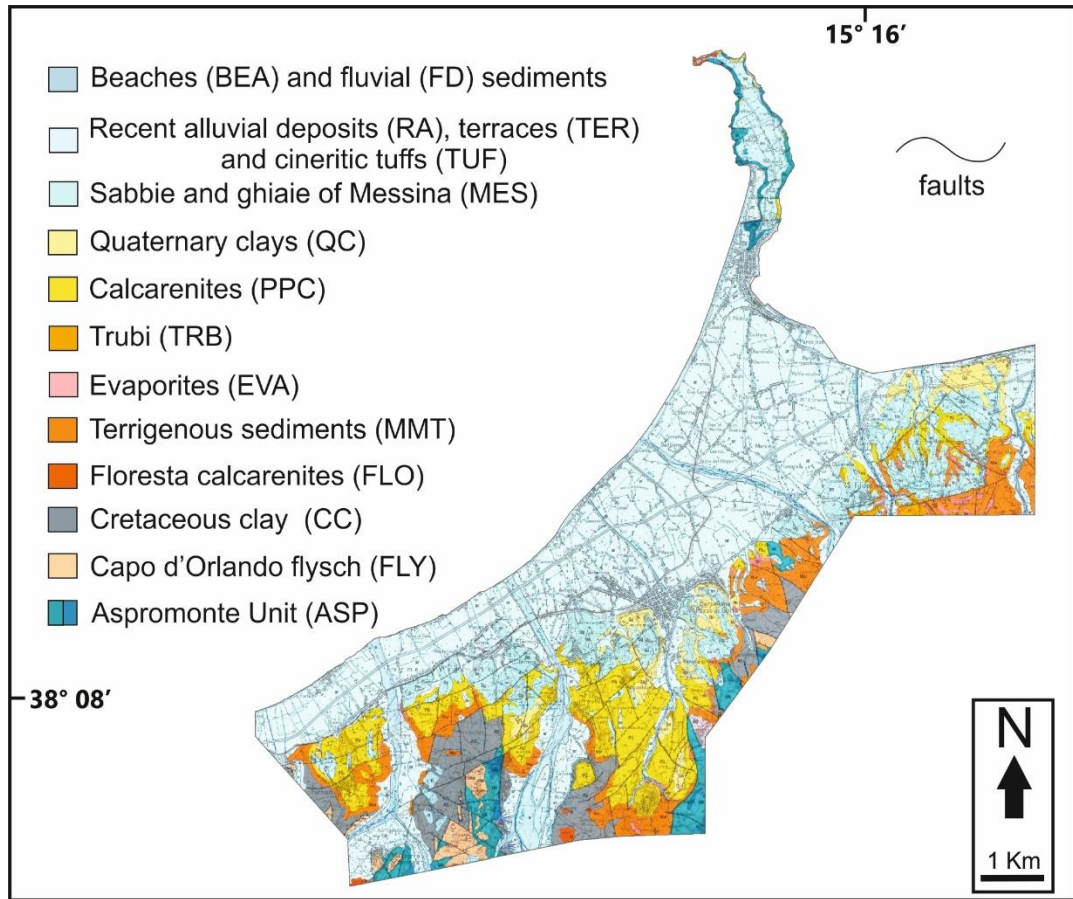


Figure 38. Sketch of the geological map of the studied area (modified from Lentini et al. 2000).

5.5.3 Hazard assessment

5.5.3.1 Radon Index

Firstly, a permeability map was created by taking into account the hydrogeological features of each of the fifteen geolithological formations outcropping in the investigated area. Hydrogeological information was supplied by the Sicilian PAI service, and are freely available online at the website “<http://www.sitr.regione.sicilia.it/pai>”. Accordingly, lithologies were divided into three different permeability classes: high, medium and low permeability (Table 15). Five lithologies out of fifteen were classified as highly permeable, six as moderately permeable, and four show a low permeability.

The most permeable lithologies are those represented by loose-grained sediments, which favour fluid migrations over long distances.

Conversely, lowly permeable ones are those characterized by the occurrence of a fine

Table 15. Permeability classification, as high, medium and low, of the different formations outcropping in the studied area. The classification was performed in agreement with the hydrogeological information provided from the PAI (Piano Assetto Idrogeologico) service for Sicily.

| Permeability class | Lithologies |
|--------------------|--|
| high | “sabbie and ghiaie” of Messina, recent alluvial sediments, marine and fluvial terraces, fluvial deposits, beach deposits |
| medium | Aspromonte Unit, Capo d’Orlando flysch, Floresta calcarenites, Middle Miocene terrigenous sediments, evaporites, Plio-Pleistocene calcarenites |
| low | Cretaceous clays, Trubi, Quaternary clays, cineritic tuffs |

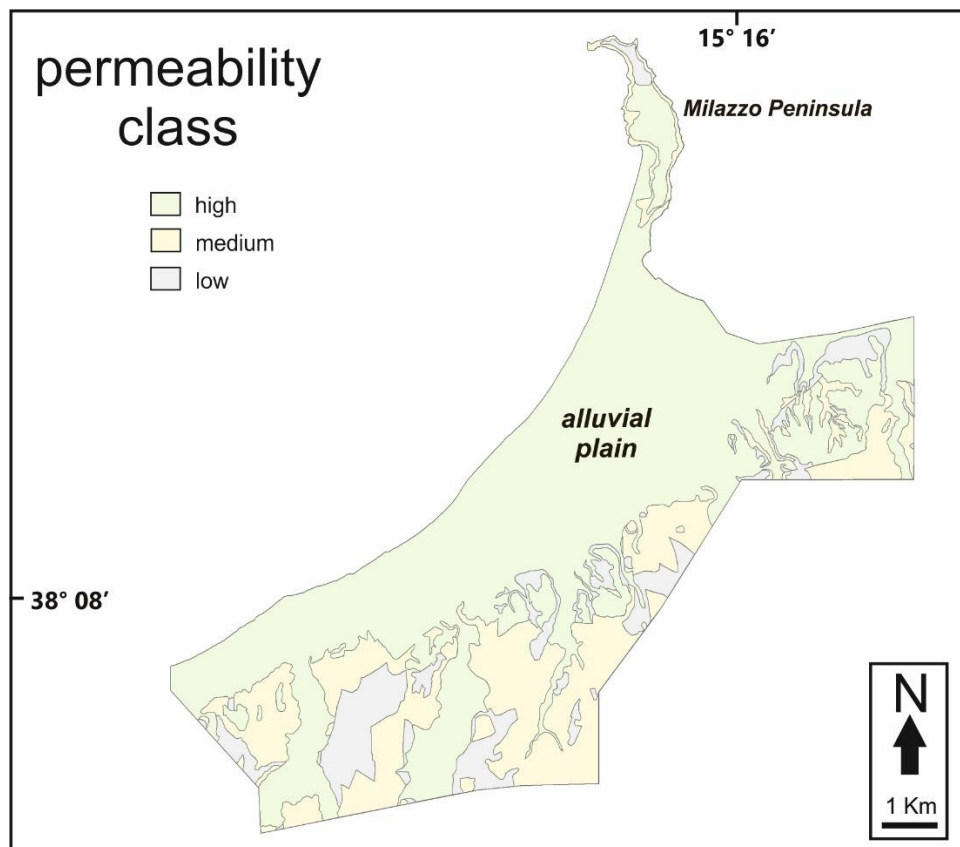


Figure 39. Permeability map of the studied area.

-grained matrix, which prevents fluid circulation. Concerning hard lithologies, they show a moderate hydraulic conductivity due to fracturation and cracking induced by tectonic stress.

Moreover, the geological map of the province of Messina (Fig. 38, Lentini et al., 2000) was used as a base map to draw physical limits among different lithologies.

The permeability map is shown in Figure 39. The coastal zone, dominated by the alluvial plain of Milazzo and Barcellona, is a high permeable area. Southwards, where the hilly reliefs of the Peloritani Mountains take place, a wide permeability fluctuation exists: high permeable zones are located along stream valleys, whereas hills are mostly marked by medium and low permeability areas. The Milazzo peninsula exhibits high permeability soils, except for the northern termination, where the presence of thin layers of cineritic tuffs at the top of the strata succession provokes drastic permeability decreases.

As regards the assessment and mitigation of radiological hazards due to soil-Rn, it is important to remark that permeability has to be evaluated for the uppermost soil/rock strata as edifices interact with the superficial portion of the ground. High permeability strata promote geogases circulation, whereas impermeable or semi-permeable layers tend to protect and isolate buildings.

After having obtained permeability information and soil-²²²Rn concentrations for 250 x 250 m cells, the RI category expressed as high, medium or low (Neznal et al., 2004) was calculated for each 250 x 250 m cell according to the procedure described in Section 5.4.5.

Because of the longest half-life of ²²²Rn (3.82 d) in comparison to that of ²²⁰Rn (55.6 s), only the former isotope is considered for the RI calculation (Neznal et al., 2004; Barnet et al., 2008).

Taking into account the large half-life discrepancy between the two Rn isotopes, it is strongly believed that the effective dose induced by thoron and its progeny is considerably less than that provoked by radon (Barnet et al., 2008), and for this reason, the contribution of thoron is usually neglected. Nevertheless, recent papers (e.g. Nguyen-Thuy et al., 2019) pointed out that significant human health risks could be also derived from indoor thoron inhalation.

The RI map is shown in Figure 40 whereas in Table 16 (first column) is reported the aerial extent of each RI category. The majority of the studied area (~69%) has been classified as low hazardous (low-RI), while high-RI zones cover about ~4%.

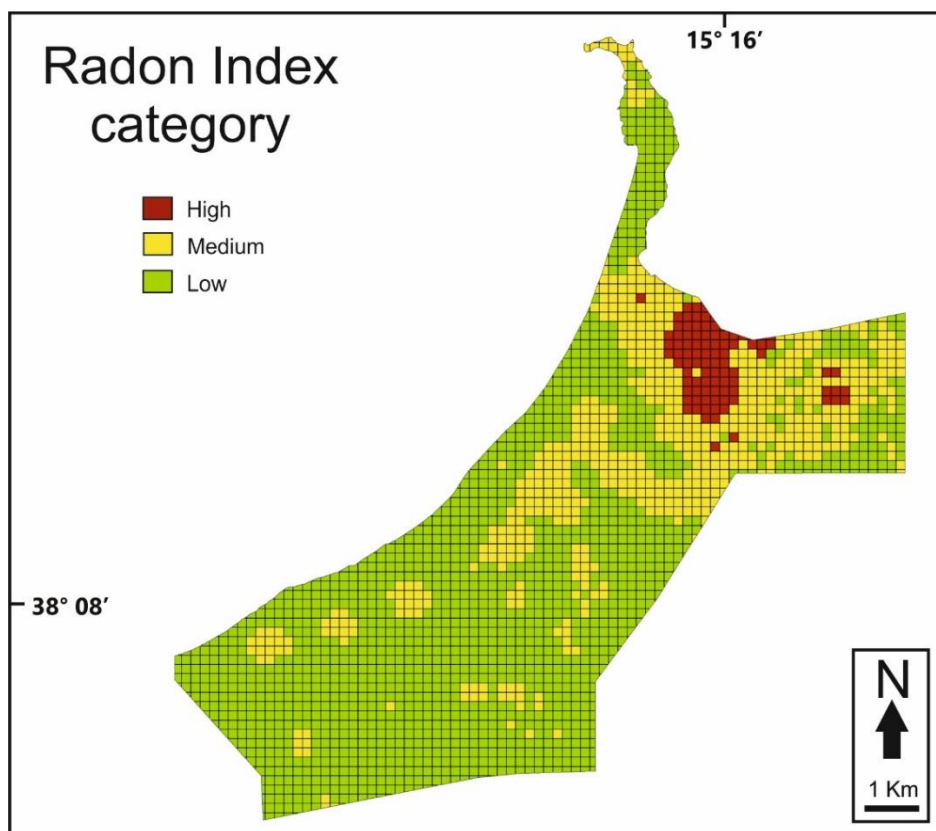


Figure 40. Radon Index map of the studied area. RI categories are calculated for 250 x 250 m cells accordingly to the method reported in Section 5.4.5.

Table 16. Aerial extents of the three Radon Index categories: a) for the whole area; b) for the urban areas as illustrated in Figure 41.

| RI category | a) whole studied area | b) urban areas |
|-------------|-----------------------|----------------|
| high | 4% | 2% |
| medium | 27% | 38% |
| low | 69% | 60% |

The rest of the studied area (~27%) displays a medium hazard. High-RI areas are located on the Milazzo side of the alluvial plain. Conversely, the western side of the studied area is almost exclusively represented by a low-RI category.

In order to better evaluate the Rn hazard for the population, the location of urban centres within the investigated area was superimposed to the RI map (Fig. 41).

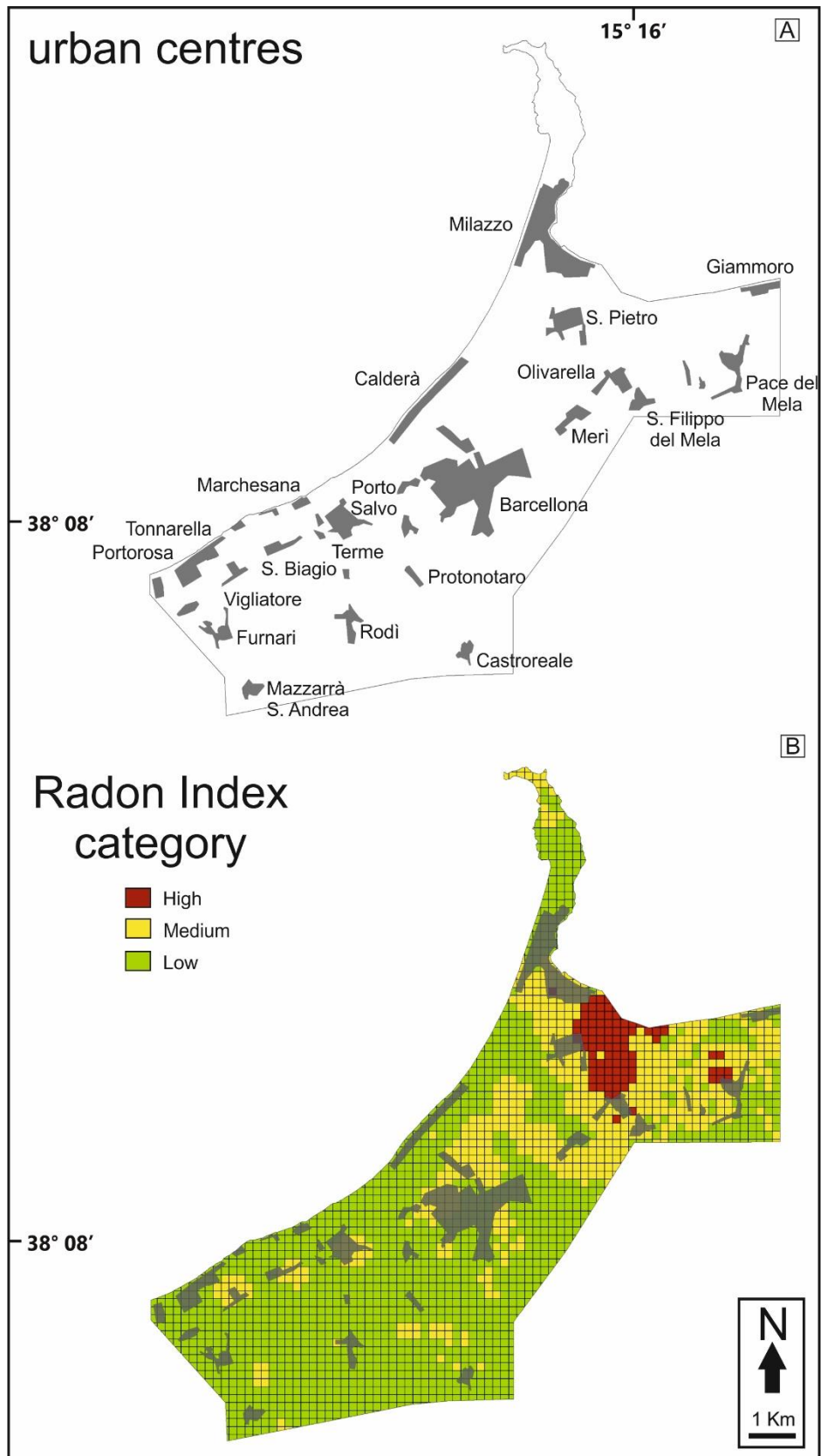


Figure 41. A) Locations and aerial extents of urban centres; B) RI map of Figure 40 and superimposed locations of urban areas.

A total population of around 100,000 people currently live in the area, and assessing the radiological hazard connected to radon could be vital. Considering only the urban areas (see the second column in Table 16), approximately 2% of the area has been classified at high risk, whereas medium- and low-RI categories account for around 38 and 60%, respectively.

As evidenced in Table 16, the hazard assessment determined for urban centres does not completely match the classification obtained for the whole area. Urban centres are marked by less high and low-RI areas in comparison to those recorded for the whole area classification, as well as they show a moderate increase of medium-RI cells. The lower number of low-RI cells within urban areas can be explained by the fact that large portions of low risk “alluvial” areas have been assigned to plant nurseries and cultivation instead of construction.

Considering all those information, we can preliminarily classify the investigated area as low-mild hazardous for the population. With the aim of confirming the latter assumption, a further evaluation approach was used, namely, the method suggested by the SSI (Swedish Radiation Protection Authority), which rely only on soil- ^{222}Rn activity concentration (see Dubois, 2005 and Castelluccio et al., 2012). The SSI method divided areas in three different risk classes (Table 17): low risk areas ($\text{soil-}C_{222\text{Rn}} < 10 \text{ kBq m}^{-3}$), normal risk areas ($10 \text{ kBq m}^{-3} < \text{soil-}C_{222\text{Rn}} < 50 \text{ kBq m}^{-3}$) and high risk areas ($\text{soil-}C_{222\text{Rn}} > 50 \text{ kBq m}^{-3}$).

Being the mean soil- ^{222}Rn concentration among all the 172 sites equal to 12.37 kBq m^{-3} (Table 12), the SSI approach evidenced that the studied area is characterized by a normal radiological risk due to radon.

By coupling outcomes derived from RI and SSI methods, we can affirm that the health hazard connected to soil-radon is essentially low to moderate for people living along the Tyrrhenian margin of NE Sicily.

However, a high-RI cluster is located next to the urban areas of Milazzo, S. Pietro, S. Filippo del Mela and Pace del Mela (Fig. 41). Here, not many edifices exist today, but we cannot completely rule out the possibility that this area could be designated for future urban expansion and development.

Table 17. The evaluation method proposed by the Swedish Radiation Protection Authority (after Dubois, 2005).

| Risk classification | Soil-Rn concentration (kBq m ⁻³) | Technical building requirements |
|---------------------|--|--|
| high | >50 | Radon safe construction, such as thicker, reinforced concrete foundation or ventilation below the foundation |
| medium | 10-50 | Radon protective construction. No apparent fissures or leaks in the foundation |
| low | <10 | traditional |

5.5.3.2 RI maps used in the field of indoor hazard mitigation

As already mentioned in Section 5.4.5, the Italian legislative decree no. 101/2020 not only regulates the indoor radon levels in schools, workplaces and public edifices, but also, for the first time, introduced a limit for private buildings where people live.

According to the legislative decree no. 101/2020 (*Art. 12*), the indoor Rn concentration limits are:

- annual average value of 300 Bq m⁻³ for existing private buildings and workplaces (also schools and public edifices);
- annual average value of 200 Bq m⁻³ for new private buildings to build after December 31st 2024.

Concerning workplaces, schools and public edifices (*Art. 16*), radon investigations must involve underground spaces, thermal baths and specific high-risk workplaces, whereas basements and ground floors are evaluated only if edifices are situated within the so-called “risky areas”. On the other hand, for private buildings (*Art. 19*), indoor measurements have to be carried out only if buildings are located within the “risky areas” (defined in the *Art. 11* of the 101/2020 D. Lgs. as those areas where indoor Rn levels can be higher than the reference limit), which have not been identified yet by the Italian Regions. If private buildings are located outside the “risky areas”, they are exempted from every hazard evaluation.

In this framework, the RI map produced in this work (Fig. 40) might serve as a preliminary tool adopted to define the radon hazard for existing and new (i.e. future)

edifices. As a result, RI maps can be used to detect the “risky areas” of the 101/2020 D. Lgs (*Art. 11*), where indoor Rn measurements are mandatory. Clearly, the “risky areas” should be correlated to the high-RI category zones.

I believe that RI maps should be used to perform first-level screenings, and further investigations are needed within high-RI zones, both in case of existing and future edifices. For instance, a series of *in-situ* soil-Rn measurements could be performed across the building area. In addition, the attitude of soils to be crossed by endogenous gases could be evaluated through direct permeability measurements, instead of using the indirect “expert” evaluation (see Section 5.4.5).

However, two limitations must be considered:

- it is important to remark that RI maps should be used only for preliminary hazard assessment because unknown values determined with interpolation might have high uncertainties.
- soil-Rn concentration is exposed to seasonal fluctuations. Hence, the RI category can be underestimated if measurements are performed during the season characterized by a lower Rn concentration in the soil (see Castelluccio et al., 2012). The solution to this issue is to collect soil gases both in winter and in summer. The most troublesome condition (namely, when soil-Rn concentrations are higher) will be picked as a reference as the most prudent option is generally considered the best way to assess natural hazards.

5.5.4 Geophysical and tectonic implications

5.5.4.1 Radon vs thoron: deep degassing vs shallow circulation

The soil-gas composition usually reflects the mixing of two components: gases equilibrated at shallow levels and deep gases uprising in a regime of advective transport (Sciarra et al. 2018).

The remarkable difference in the half-lives of radon (3.8 d) and thoron (56 s) is responsible for the different migration distances covered by the two isotopes. Thoron is produced at shallow levels (i.e. within the soil), while radon originates both from soils and from deep sources (Huxol et al., 2013; Ciotoli et al., 2016). Therefore, the ^{220}Rn vs ^{222}Rn ratio indicates the transport type of soil gas as well as its relative time of migration, as fast or slow.

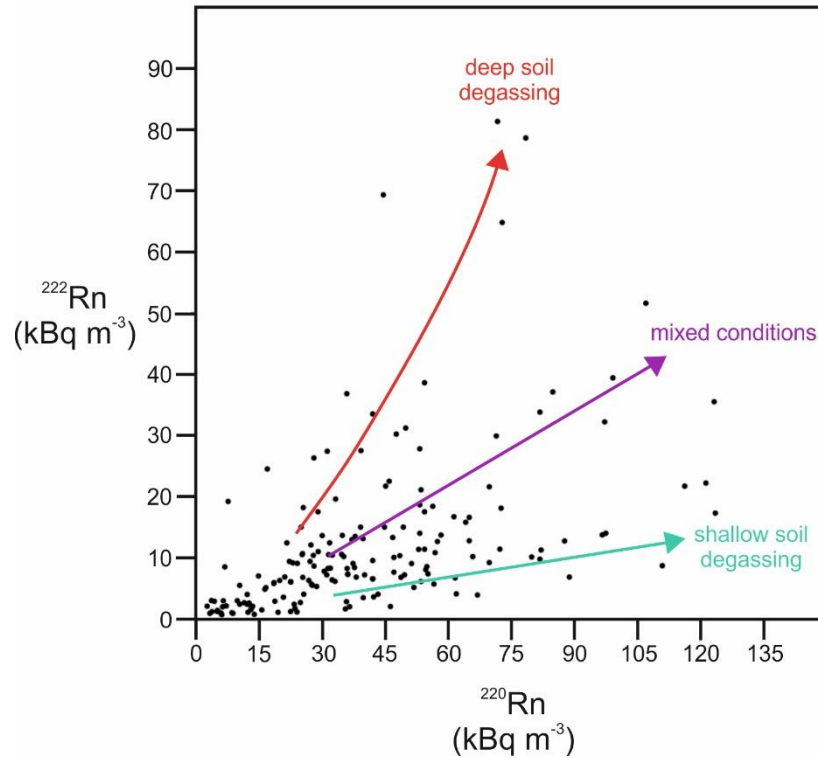


Figure 42. Diagram of ^{220}Rn vs ^{222}Rn activity concentrations measured in northeastern Sicily. The diagram highlights the distinction among three different populations representing deep soil degassing, shallow circulation and combined circumstances.

For these reasons, the ^{220}Rn vs ^{222}Rn ratio can be used as a marker to discriminate soil Rn emanation (high $^{220}\text{Rn}/^{222}\text{Rn}$) from deep-originated Rn transported to the surface with carrier gases (low $^{220}\text{Rn}/^{222}\text{Rn}$), as already proposed in recent works (e.g. Elio et al., 2015; Sciarra et al., 2018; D'Alessandro et al., 2018 and Bini et al., 2020).

In Figure 42 are plotted the soil- ^{220}Rn vs ^{222}Rn activities measured in the 172 sampling points. Three different populations can be observed in the plot. Low $^{220}\text{Rn}/^{222}\text{Rn}$ ratios (red arrow) are connected to a predominant advective gas-carrying transport mechanism. In contrast, high $^{220}\text{Rn}/^{222}\text{Rn}$ ratios (green arrow) suggest that radon atoms in soil gas are formed at shallow levels travelling by diffusion in porous soils.

Moreover, medium $^{220}\text{Rn}/^{222}\text{Rn}$ ratios (purple arrow) are indicative of mixing between shallow and deep sources; the lower will be the ratio, the more abundant will be the deep component with respect to the shallow one.

These results testify the presence of Rn anomalies linked to deep gases uprising along faults. In addition, the ^{222}Rn anomaly threshold (i.e. the value representing the onset of a deep advective contribution) fixed at $\sim 19 \text{ kBq m}^3$ by interpreting NPPs (Fig. 34) is consistent with the fact that in the ^{220}Rn vs ^{222}Rn plot, the transition from only shallow circulation to mixed condition (i.e. shallow + deep advective degassing) roughly occurs at ^{222}Rn values between ~ 12 and $\sim 25 \text{ kBq m}^3$. This consideration strengthens the goodness of those results, despite the fact that the distribution of Rn data in three different populations, as evidenced in the ^{220}Rn vs ^{222}Rn graph (Fig. 42), does not clearly emerge from NPPs (Fig. 34).

5.5.4.2 CO₂ percentage in soil: preliminary data

Late in August 2021, the soil-CO₂ content was measured with the “active” method (see Section 5.4.6) in 7 of the 172 sites previously investigated for the soil-Rn concentration. The 7 selected sites (# 27, 36, 39, 41, 142, 153 and 163; see locations in Figure 26 and coordinates in Table 11) represent those locations where high radon concentrations and low $^{220}\text{Rn}/^{222}\text{Rn}$ ratios were previously documented. The main aim is to understand if carbon dioxide is the carrier gas where soil-Rn degassing has a deep signature.

Besides the soil-CO₂ percentage, the ^{222}Rn activity concentration was measured a second time at the same site in order to assess if a correlation between CO₂ and ^{222}Rn exists. In this framework, the ^{222}Rn concentration was determined through the RAD7 by using the CO₂ probe (Figure 30), which is composed of 5 different gas inlets located at different depths, and the most superficial of them is located at a depth of 0.34 m. At the same time, it was not possible to assess the correct travel time of soil air from sampling depth to the RAD7 chamber, and for this reason, the ^{220}Rn concentration was not determined.

^{222}Rn concentrations measured with the CO₂ probe setup resulted lower than those determined during the soil-Rn measurement survey that had been previously carried out by using a probe hammered at depths of 0.5-0.6 m having only one gas inlet located at the bottom (see Sections 5.4.1.1 and 5.4.1.3). This outcome is completely in agreement with the assumption that Rn concentration increased with increasing depth (see Section 5.4.1.3). In addition, the 2021 summer was very hot and dry,

causing the development of small and narrow desiccation cracks within the uppermost part of the soil. This phenomenon might have led to a larger dilution of soil gas with atmospheric air, provoking the decrease of the original CO₂ and Rn levels.

The measured soil-CO₂ content (coupled with the ²²²Rn concentration) was 1.22% (14.5 kBq m⁻³), 1.12% (9.3 kBq m⁻³), 1.05% (6.3 kBq m⁻³), 1.36% (25.9 kBq m⁻³), 1.21% (23 kBq m⁻³), 1.11% (20.4 kBq m⁻³) and 1.03% (9.5 kBq m⁻³) at sites 27, 36, 39, 41, 142, 153 and 163, respectively. These CO₂ concentrations are well above the atmosphere (~400 ppm) by two orders of magnitude.

Normally, the CO₂ concentration in soil is higher than that of the atmosphere because of biogenic and geogenic contributions. It usually ranges between 0.2 and 4% (Rose et al., 1979). In geothermal/hydrothermal areas connected to the presence of magmatic bodies at depth, where the pressure gradient transport (i.e. advection) is significant, the soil CO₂ concentration is typically above 10% (Pearce, et al., 2004; D'Alessandro et al., 2018; Bini et al., 2020). Concerning neotectonic settings, where active and seismogenic faults promote the generation and uprising of deep gases, the CO₂ percentage in soil air actually show a wide range of values. For instance, Ciotoli et al. (1999) along the Ofanto Valley (southern Italy), Ciotoli et al. (2007) in the Fucino Plain (central Italy) and Yuce et al (2017) in Turkey measured soil-CO₂ values up to 15-20%, whereas values up to 5-8% were observed by Lombardi and Voltattorni (2010) and Voltattorni et al. (2014) in the Marche Region (central Italy) and Greece, respectively. On the other hand, Sciarra et al. (2015) and Xiang et al. (2020) detected CO₂ values below 1.5% along active faults located in the Sila Massif (southern Italy) and in the Tianshan Mountains (China), respectively.

The soil-CO₂ content measured in the Peloritani Mountains for this Ph.D. Thesis (1.03-1.36%) fall within the common soil air range. However, these values might be underestimated due to dilution phenomena triggered by the occurrence of desiccation cracks in the soil. Furthermore, the dissolution of large volumes of carbon dioxide in groundwaters before reaching the vadose zone (Ciotoli et al., 2007) may have caused a general reduction of CO₂ levels in the soil. The dissolution effect should not be neglected, especially within the alluvial plain, where the water table can show depths

of 5/10 meters below the ground level depending on the local stratigraphic setting (Dr. Antonio Torre, personal communication).

The CO₂ percentage and the ²²²Rn activity concentration (measured by using the CO₂ probe) show a significant positive correlation (Pearson's correlation coefficient of 0.798). This feature might be the expression of a probable presence of CO₂ acting as a deep carrier gas for Rn. Moreover, soil-CO₂ contents between 1 and 1.5% are compatible with tectonically active environments, as documented by Sciarra et al. (2015) and Xiang et al. (2020).

However, it is clear that these rough considerations are founded only on very preliminary data. Only very few sites were analysed for the carbon dioxide content, and for this reason, it is impossible to determine if the measured CO₂ values should be considered anomalous or not. In this framework, it is undeniable that the three future keys to improving the comprehension of the physical dynamics connected to the gas migration are: i) increasing the number of soil-CO₂ measurements; ii) determining the source of the deep CO₂ (crust vs mantle) through isotope analyses; iii) measuring additional soil-gas parameters (i.e. CH₄ and He contents and CO₂ flux).

5.5.4.3 Type and location of radon anomalies

Anomalies, due to gas uprising along deep tectonic lineaments, can show different shapes depending on faults geometry and soil permeability. According to Ciotoli et al. (1999, 2005 and 2007), the most common types of gas anomalies are linear, spot and diffuse shaped (Fig. 43). Linear soil gas anomalies, typically several meters long, reflect the presence of tectonic faults, which favour gas leaks by increasing rock/soil permeability. Diffuse (or halo) anomalies often occur at intersections of two or more tectonic structures, where wide fracture zones allow great volumes of deep gases to reach the Earth's surface. Moreover, since permeability properties can be discontinuous along a tectonic lineament (e.g. Lombardi et al., 1996; Etiope et al., 2005; Ciotoli et al., 1998; Ciotoli et al., 2005), spot anomalies can be generated where permeability is much higher than that of surrounding zones. Spot anomalies occur as lonely points characterized by high concentration values.

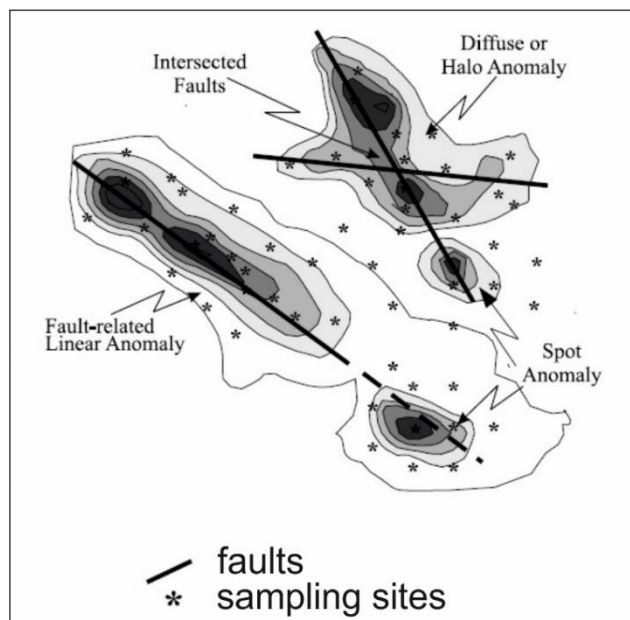


Figure 43. The most common types of soil anomalies are caused by the presence of tectonic lineaments (modified after Ciotoli et al., 2007).

Locations of radon and thoron anomalous values, as recognized from NPPs (Fig. 34; namely ^{222}Rn and ^{220}Rn concentrations above 19 and 59 kBq m⁻³, respectively), are illustrated in Figure 44A and B, respectively. Data show that an anomalous Rn zone occurs in the eastern part of the studied area. Here, diffuse anomalies indicate the existence of a ~NW-SE oriented trend. On the contrary, in the western part, only scattered spot anomalies are present.

Moreover, radon and thoron values were combined with $^{220}\text{Rn}/^{222}\text{Rn}$ ratios. Sites where the $^{220}\text{Rn}/^{222}\text{Rn}$ ratio is low closely coincide with sites where radon concentrations are higher than the anomaly threshold (Fig. 44C). The ~NW-SE striking structure is clearly detectable by observing contour lines and locations of Rn anomalies and low $^{220}\text{Rn}/^{222}\text{Rn}$ values (Fig. 44A, B and C).

In Figure 44D is depicted the map that reassumes all the localities where abnormal radon was identified. The map is produced by taking into account only sites where at least two of these three conditions, indicating deep gas uprising, were identified: i) ^{222}Rn anomaly; ii) ^{220}Rn anomaly; iii) low $^{220}\text{Rn}/^{222}\text{Rn}$.

The radiological analyses performed in this study show that ^{222}Rn , ^{220}Rn and $^{220}\text{Rn}/^{222}\text{Rn}$ values are in good agreement. Therefore, I believe that the results obtained from the soil-Rn survey are reliable.

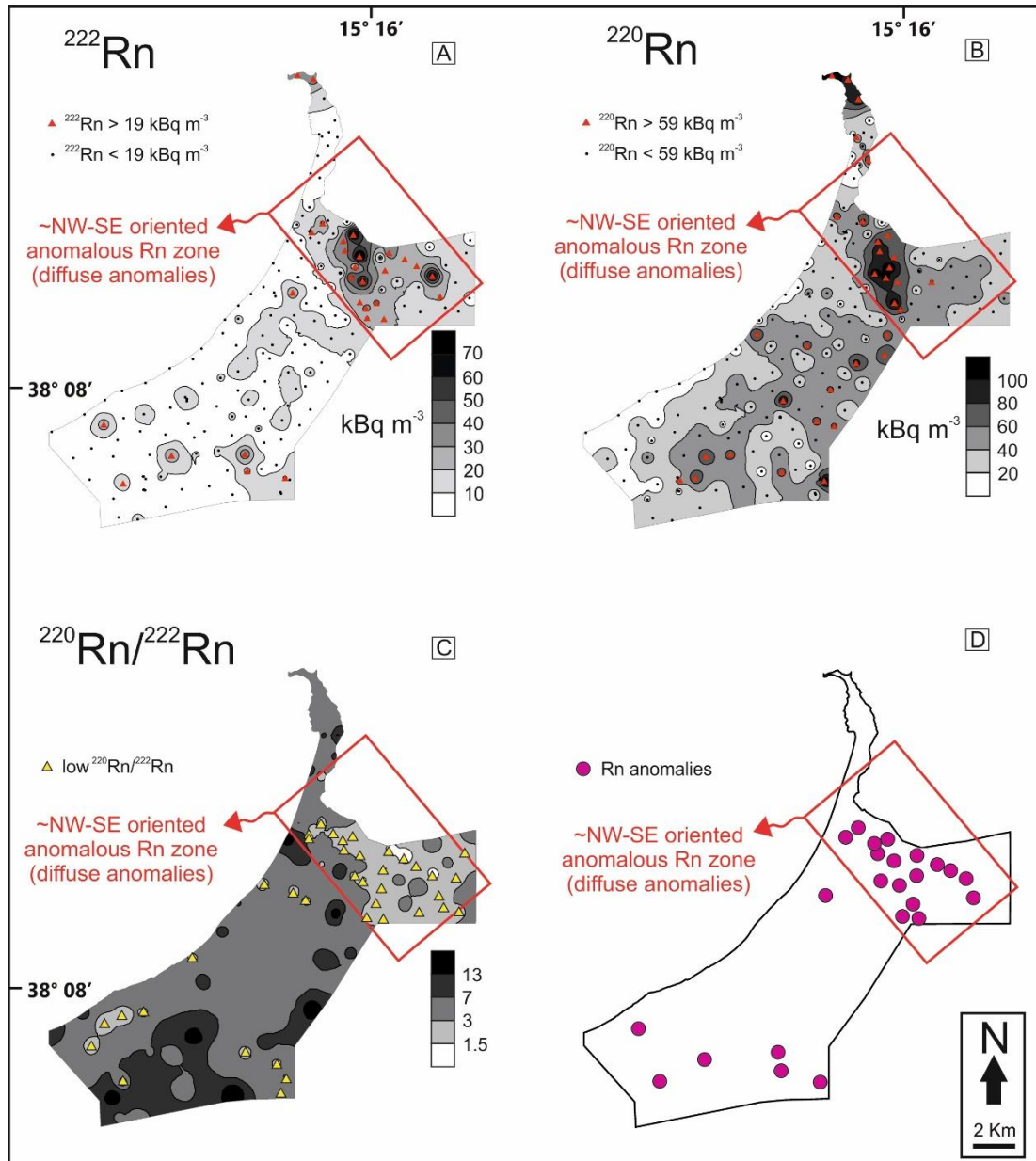


Figure 44. Contour maps showing the distribution of soil-²²²Rn (A) and ²²⁰Rn (B) anomalies as well as low ²²⁰Rn/²²²Rn sites (C). Figure D represents the Rn anomalies recap map obtained considering only sites where at least two of the three following conditions occurs: i) ²²²Rn anomaly; ii) ²²⁰Rn anomaly; iii) low ²²⁰Rn/²²²Rn. A ~NW-SE oriented region, marked by diffuse Rn degassing, occurs in the eastern side of the studied area. On the western side only spot anomalies were detected.

I want to stress on the fact that coupling ²²²Rn, ²²⁰Rn and ²²⁰Rn/²²²Rn data represents the key tool for the correct understanding of the complex factors ruling gas circulation beneath the Earth's surface.

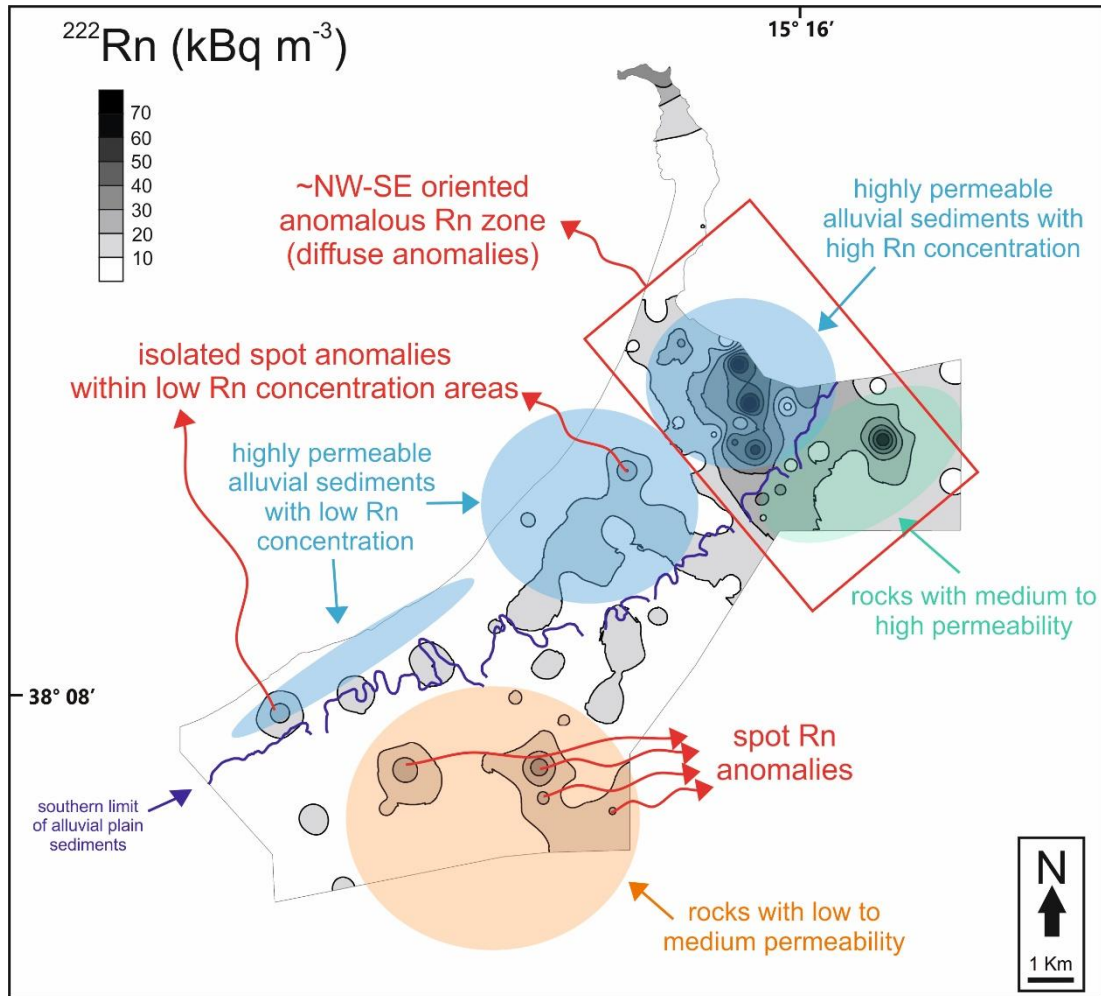


Figure 45. Soil- ^{222}Rn contour map showing that a ~NW-SE oriented region characterized by the presence of Rn diffuse anomalies was recognized in the eastern part of the studied area. Highly permeable alluvial sediments sampled along the anomalous Rn zone show higher soil-Rn concentrations (soil- $C_{222\text{Rn}}$ up to $\sim 80 \text{ kBq m}^{-3}$) than those situated westwards (soil- $C_{222\text{Rn}}$ below 20 kBq m^{-3} ; except rare and isolated spot anomaly). This feature can be explained through the occurrence in the eastern portion of the area, of a fault zone that is able to favour the uprising of crustal/mantle gases. Conversely, in the western side of the area, where rocks with low to medium permeability occur, Rn degassing is represented by a number of spot anomalies (soil- $C_{222\text{Rn}}$ up to $\sim 40 \text{ kBq m}^{-3}$).

This approach is perfectly suitable if extensive measurements of other geogenic gases (e.g. CO_2 , CH_4 , He, etc) cannot be performed.

It is important to note that the tectonic effect on soil-Rn concentration appears evident in the highly permeable alluvial plain sediments (Fig. 45). Along the ~NW-

SE oriented anomalous zone that was detected in the eastern sector of the investigated area, alluvial deposits show extremely high Rn concentrations (soil- C_{222Rn} up to $\sim 80 \text{ kBq m}^{-3}$). On the other hand, Rn concentrations are considerably lower (soil- C_{222Rn} below 20 kBq m^{-3}) in the alluvial sediments situated farther to the West, except uncommon isolated spot anomalies (soil- $C_{222Rn} \sim 25\text{-}30 \text{ kBq m}^{-3}$). All Quaternary alluvial sediments, deposited along the Tyrrhenian margin of the Peloritani Mountains, share similar permeability, U and Th content as well as texture and fabric. Under those conditions, the higher Rn concentration detected in the eastern sector of the area is certainly connected to the existence of a wide fault zone promoting the uprising of deep-originated gases. A further constraint about the role of tectonics on soil-Rn concentration arises from Iovine et al. (2017), who determined the soil- ^{222}Rn level in the Calabria region (same lithological and geodynamical environment of NE Sicily). The ^{222}Rn values measured by Iovine et al. (2017) along active faults (up to 90 kBq m^{-3}) are comparable with those documented in the eastern part of the studied area (anomaly range: $19\text{-}81.3 \text{ kBq m}^{-3}$). Moreover, even if different lithologies are involved, also Ciotoli et al. (2007) in the Fucino Plain (central Italy) and Yuce et al. (2017) in the Amik Basin (SE Turkey) recorded similar ^{222}Rn ranges for active faults ($26\text{-}119$ and $17\text{-}84 \text{ kBq m}^{-3}$, respectively). Conversely, in the western sector of the studied area, where rocks often exhibit low to medium permeability, a different radiological behaviour was outlined. Here, no diffuse degassing occurs (Fig. 45) and the release of radon is expressed only through a number of spot anomalies (soil- C_{222Rn} up to $\sim 40 \text{ kBq m}^{-3}$).

5.5.4.4 The meaning of Radon anomalies within the regional geodynamic framework

As highlighted in Chapter III, the Aeolian-Tindari-Letojanni fault system (ATLFS) marks the transition from the compressional domain involving the southern Tyrrhenian Sea and the active ESE-ONO extension occurring in southern Calabria. The ATLFS is a NNW-SSE trending right-lateral transtensional zone extending from the Aeolian Islands to the Ionian Sea (Goes et al., 2004; Billi et al., 2006; Palano et al., 2012, 2015; Barreca et al., 2014, 2019).

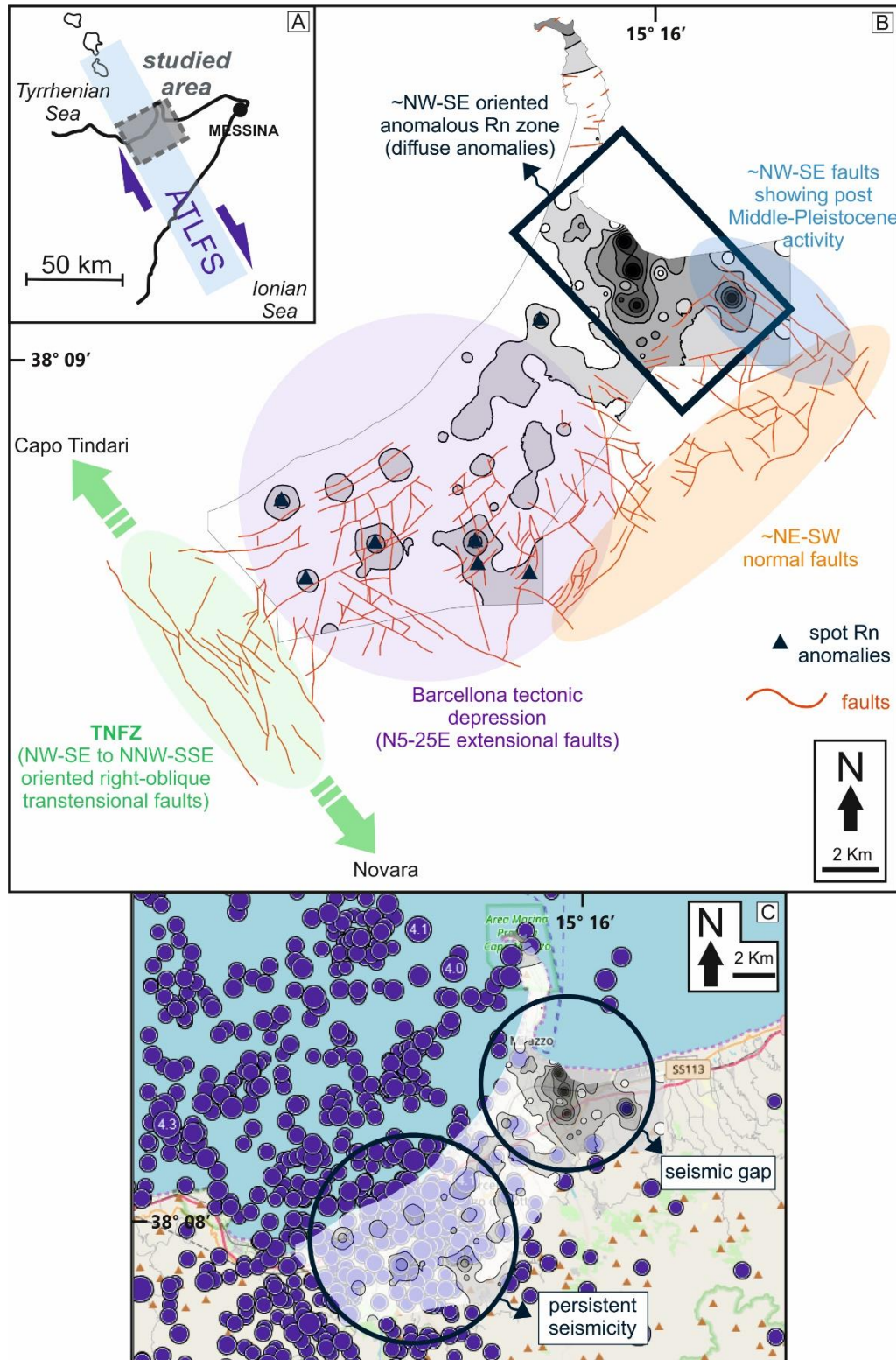


Figure 46. A) The studied area (in grey) falls within the onshore sector of the ATLFS; B) three sets of faults affect this portion of northeast Sicily (^{222}Rn contour map is in the background). The first set is composed of a swarm of right oblique (transtensional) faults referred to the TNFZ extending from Capo Tindari to the Novara village, the second set of

faults, exhibiting N5-25E strike and normal kinematics, characterizes the Barcellona tectonic depression, and the third set of faults is composed of NE-SW trending extensional faults. Spot Rn-anomalies located within the Barcellona depression are often situated at the intersection between N5-25E and NE-SW trending faults, whereas the ~NW-SE Rn degassing zone detected in the eastern part of the studied area is marked by the occurrence of ~NW-SE faults showing post-Middle Pleistocene activity; C) by superimposing the ^{222}Rn contour map upon the earthquakes map (seismic events occurred from 1985 to 2020 with hypocentral depth 0-40 km and $M > 2$; INGV catalogue; <http://terremoti.ingv.it>), it can be observed that diffuse Rn degassing takes place where seismicity is scarce (seismic gap).

In this context, the investigated area represents the northern edge of the mainland sector of the ATLFS (Fig. 46A). Here, according to Cultrera et al. (2017a,b), three different populations of faults occur (Fig. 46B). The main set of faults is represented by the Tindari-Novara fault zone (TNFZ; Cultrera et al 2017a,b), which includes right-oblique (transtensional) faults oriented NW-SE to NNW-SSE, extending from Capo Tindari to the village of Novara for a total length of ~20 km. These faults exhibit strong evidences of Holocene deformation (Billi et al., 2006; De Guidi et al., 2013). The second set of faults, exhibiting N5-25E orientation and normal kinematics, affects the Barcellona tectonic depression controlling the drainage pattern of this zone. Moreover, the third set of faults, composed of ~NE-SW trending normal faults, extends northeasternwards from the southern boundary of the Barcellona tectonic depression. This set of faults shows signs of Quaternary activity (Cultrera et al., 2017b).

The ~NW-SE oriented Rn degassing zone detected in the eastern part of the studied area involves different lithologies (Fig. 45). The greatest portion of the degassing zone affects the Holocene alluvial plain, whose sediments prevent identifying any active fault. On the other hand, the southernmost portion of the degassing zone is formed by Plio-Quaternary rocks. Here, previous works (e.g. Lentini et al., 2000; Carbone et al., 2011) recognized the occurrence of a number of ~NW-SE trending faults that locally cut Middle Pleistocene sediments (Fig. 46B). Therefore, the fact that the strike of the anomalous Rn zone (~NW-SE) is roughly coincident with that of major tectonic lineaments (Fig. 46B) strengthen the hypothesis that tectonic forces drive the Rn degassing in this area. A different scheme was observed in the western

part of the studied area (i.e. within the Barcellona tectonic depression), where soil-Rn activity concentration is generally low. Here, scattered spot anomalies are often located along the N5-25E normal faults, especially at the intersection with ~NE-SW trending lineaments (Fig. 46B). A similar assertion was already mentioned by Cultrera et al. (2017b), who stated that the N5-25E set of faults could probably favour the presence of thermal springs and gas vents.

Moreover, an analysis of the recorded seismicity was carried out referring to the INGV catalogue (<http://terremoti.ingv.it>) by selecting events with a maximum hypocentral depth of 40 Km and $M > 2$.

The analysis displays that the highest earthquake density rate is situated in the western part of the studied area (Fig. 46C). Here, seismic events are mostly characterized by focal solutions with normal kinematics and ~NE-SW striking nodal planes (see Cultrera et al., 2017b and references therein) whereas hypocentral depths are commonly concentrated between 5 and 15 km.

Surprisingly, as illustrated in Figure 46C, the highest soil-Rn activity concentrations were measured where the number of earthquakes is very low (i.e. seismic gap). Conversely, where the earthquake density rate is high and seismicity is persistent (thereby in the western sector of the studied area), Rn values are considerably lower, except for the presence of a number of spot anomalies (Fig. 46C).

Concerning the offshore sector of the ATLFS, recent geophysical and morpho-batimetric investigations (Cultrera et al., 2017a,b) revealed that a swarm of ~NW-SE oriented right-lateral transtensional faults (Vulcano-Milazzo fault zone: VMFZ; Fig. 47) occur in the Gulf of Patti. Here, seismicity shows the same seismogenic depth of that located in the mainland sector but different kinematics, as plane solutions exhibit ~NW-SE striking nodal planes and dextral strike-slip motions. Cultrera et al. (2017a,b) pointed out that seismic profiles acquired along the VMFZ reported only the extensional component. The strike-slip component is instead inferred by the dextral kinematics evidenced by the focal solution of the $M_w=6.1$ earthquake recorded in the Gulf of Patti on 15 April 1978 (Gasparini et al., 1982, 1985; Rovida et al., 2011) and by the 3.6 mm y^{-1} of right-lateral motion taking place along the ATLFS (Palano et al., 2012).

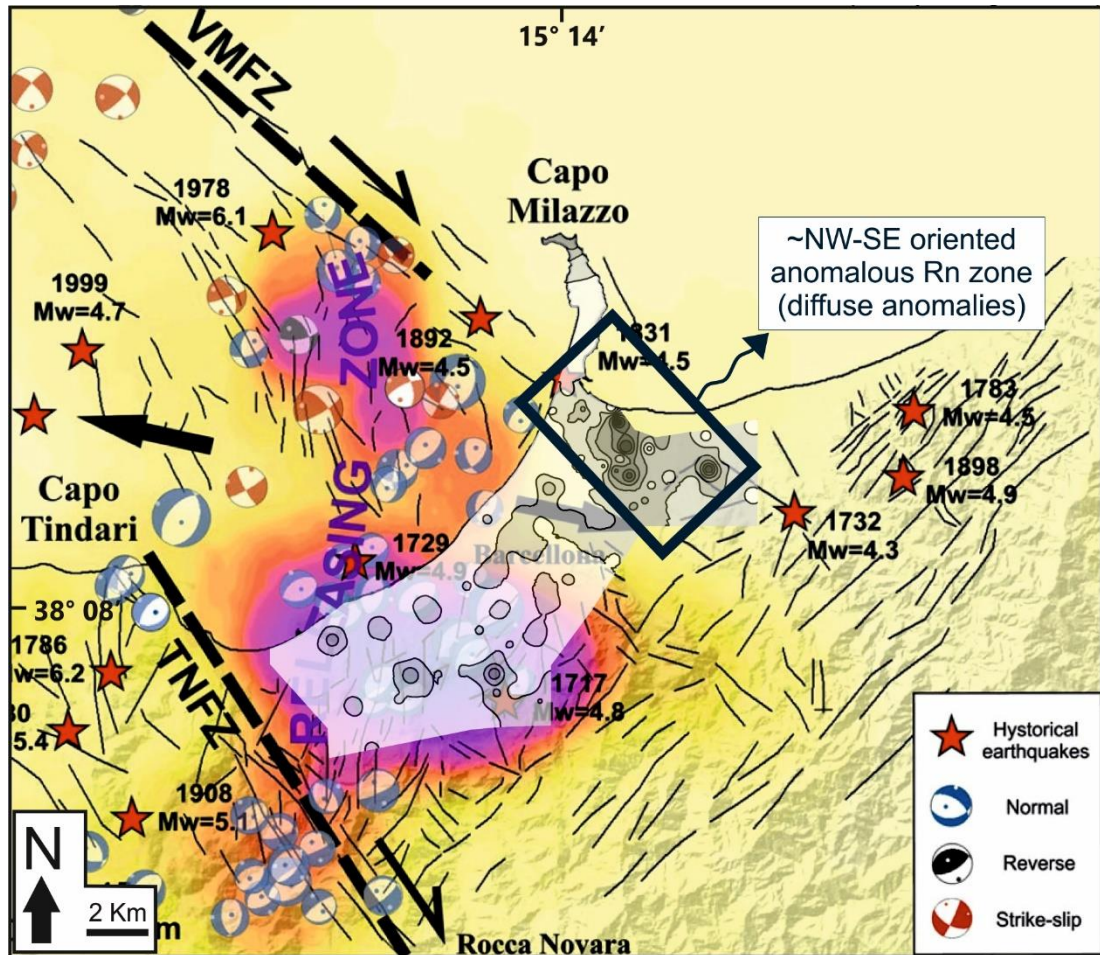


Figure 47. Tectonic reconstruction for the Gulf of Patti and its onshore sector as proposed by Cultrera et al. (2017a) by merging offshore and onshore data. Here, NW–SE trending right-lateral transtensional fault zones (TNFZ and VMFZ) contribute to the dextral motion occurring along the ATLFS (total motion of 3.6 mm yr^{-1} ; Palano et al., 2012). Moreover, an extensional zone formed in the relay area between TNFZ and VMFZ. The ^{222}Rn contour map superimposes the tectonic reconstruction of Cultrera et al. (2017a). The ~NW-SE oriented anomalous Rn zone is located adjacent to the VMFZ, suggesting a probable tectonic connection between the two segments (modified from Cultrera et al., 2017a).

Astonishingly, the Rn anomalous zone documented in the eastern portion of the studied area through soil-Rn investigations is located adjacent to the VMFZ, and it is supposed to act as its on-land prosecution (Fig. 47). Both features are tied along a ~NW-SE direction.

Further evidence of this tectonic link is provided by seismic events. Hypocentres of a series of moderate and major earthquakes ($3 < M < 6.5$), documented both

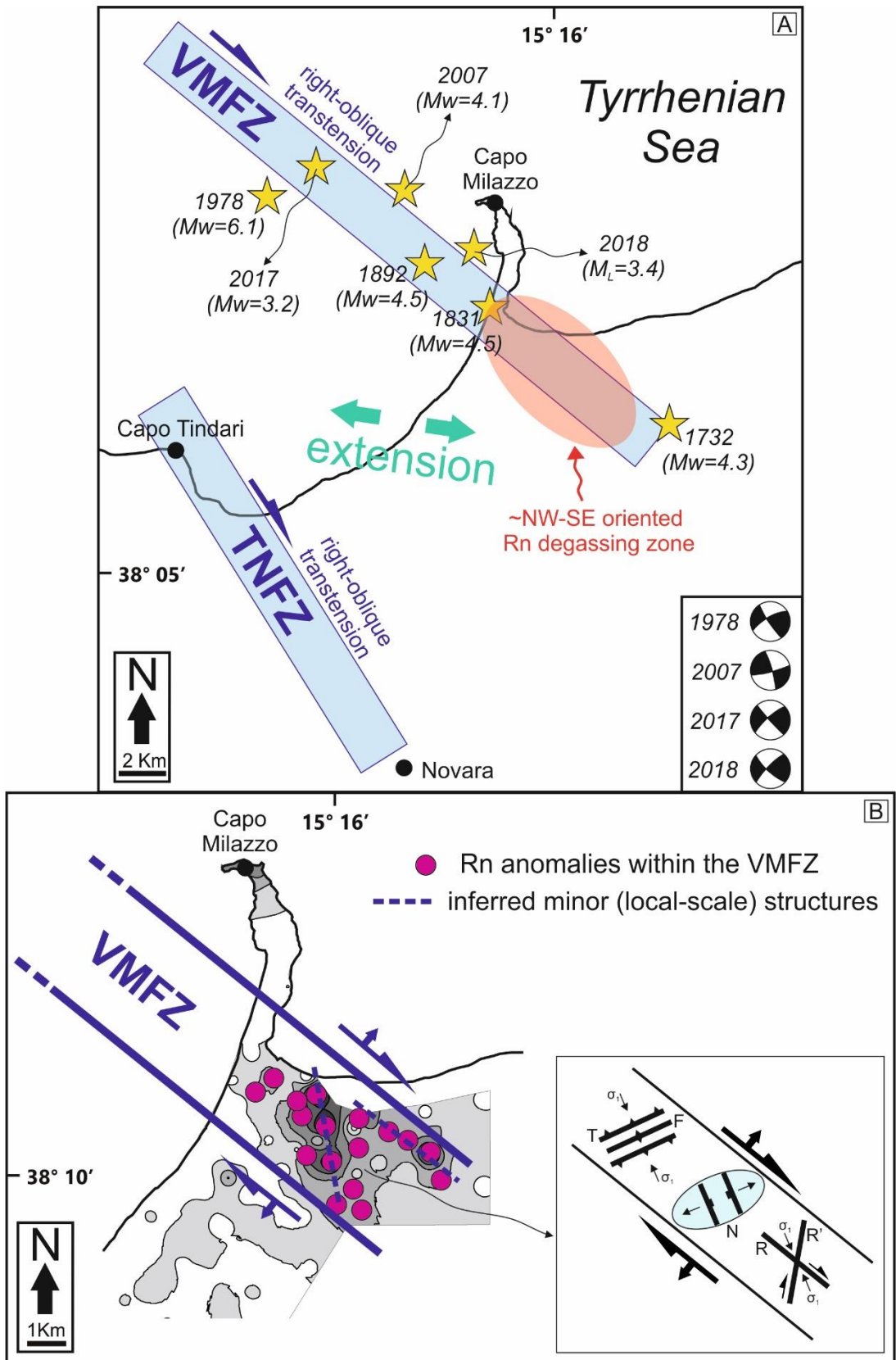


Figure 48. A) The anomalous Rn degassing zone (pale red area), detected in the eastern part of the studied area, is reasonably the result of gas uprising occurring along a swarm of

faults and fractures. It can be interpreted as the on-land prosecution of the VMFZ of Cultrera et al. (2017a,b), which was thought to be confined only in the offshore sector of the Gulf of Patti. In this framework, both segments presumably act as a unique fault zone characterized by right-oblique transtensional deformation. A series of recent (INGV catalogue: <http://terremoti.ingv.it>) and historical (Rovida et al., 2011: <http://emidius.mi.ingv.it/CPTI>) earthquakes (yellow stars) with moderate and high magnitude ($3 < M < 6.5$), document a ~NW-SE alignment of hypocentres that roughly marks the VMFZ and its on-land prolongation. Focal solutions exhibit strike-slip kinematics and ~NW-SE oriented nodal plane (1978 earthquake: Gasparini et al., 1982; 2007, 2017 and 2018 earthquakes: Scognamiglio et al., 2006). According to Cultrera et al. (2017a), the kinematic setting of the area is represented by two major transtensional fault zones (TNFZ and VMFZ) showing right-oblique motion and ~NW-SE direction, while an extensional area developed between the two major right-lateral fault zones; B) if we assume a right-oblique transtensional deformation for the on-land prosecution of the VMFZ, Rn anomalies alignments could indicate minor tectonic structures with normal and/or strike-slip kinematics (²²²Rn contour map is in the background). The small window reports orientations of subsidiaries minor structures within a transtensional domain (after Sanderson and Marchini, 1984): F, wrench fold; N, normal fault; R and R': Riedel and conjugate Riedel shears; T: reverse fault.

offshore and onshore, are aligned along a NW-SE direction, in close proximity to the VMFZ and its assumed on-land prolongation (Fig. 48A). Besides the $M_w=6.1$, 1978 major event, additional constraints on the role of the right lateral deformation arise from focal solutions of recent earthquakes observed in the Gulf of Patti (i.e. the $M_w=4.1$ event on 18 August 2007, the $M_w=3.2$ event on 21 September 2017 and $M_w=3.4$ event on 25 April 2018; <http://terremoti.ingv.it>). They indicate, in agreement with the 1978 earthquake, dextral kinematics on NW-SE oriented nodal planes (Scognamiglio et al., 2006). Moreover, historical earthquakes struck the mainland during the XVIII and XIX centuries ($M_w=4.3$, 1732 and $M_w=4.5$, 1831; Rovida et al., 2011). Hypocentres occurred roughly within the Rn degassing zone (Fig. 48A), underlining the seismogenic potential of this sector despite the low-rate seismicity registered in the past 35 years.

After those considerations, the VMFZ, as depicted by Cultrera et al. (2017a,b), and the anomalous Rn zone detected in this Ph.D. Thesis, might be carefully interpreted

as a rather unique major fault zone running along a ~NW-SE direction from the Vulcano Island to the town of Milazzo for a total length of at least 20 km (Fig. 48A). It is noteworthy that alluvial sediments, which are largely diffused where intense Rn degassing was recognized, prevent achieving accurate information on kinematics and direction of buried faults (see Wang et al., 2010). However, seismic profiles, focal solutions and GPS data clearly indicate a right-lateral transtensional deformation along the VMFZ (Cultrera et al., 2017a,b). Then, if we consider the VMFZ and its on-land prolongation acting as a unique fault zone, a right-lateral transtension can be prudently assumed for the whole tectonic element (Fig. 48A). Under this theoretical circumstance, alignments inferred from locations of high-Rn sites can be interpreted as minor extensional faults and/or strike-slip Riedel shears (Fig. 48B). Unfortunately, the sampling grid was too loose to constrain <5 km long tectonic features; then, local-scale (i.e. minor) lineaments illustrated in Figure 48B have to be viewed only from a purely speculative perspective.

The occurrence of a NW-SE trending structure in the eastern part of the studied area, where radon is widely degassing, could match with recent geophysical observations including gravimetric data (Palano et al., 2015). The Bouguer anomaly map of NE Sicily shows a sudden increase in the anomaly values (around 40 mGal) taking place south of the Milazzo Peninsula (Fig. 49A; after Palano et al., 2015). Moreover, density contrast maps document a high-density body, roughly aligned along a NW-SE direction, located around the Milazzo Peninsula down to depths of around 12-15 km (Fig. 49B; after Palano et al., 2015). Even if P-wave velocity models (Figure 4 of Palano et al., 2015) do not reveal any clear anomaly, gravimetric observation could be consistent with the activity of a ~NW-SE oriented tectonic lineament running from the coast of Milazzo to the hilly reliefs of the Peloritani Chain.

After all those evidences, both “lithological” and “tectonic” effects are here retained to be responsible for the different Rn concentrations measured in soils. To summarize, as already asserted, the studied area is divided into two sectors. In the western one (hilly reliefs of Castroreale and Rodi Milici villages; “W” zone in Fig. 50) the effective migration of endogenous gas is prevented by the lowly-moderately permeable rocks outcropping in this area. Here, diffuse degassing has not been recognized even though seismicity shows a very high rate. Soil-²²²Rn

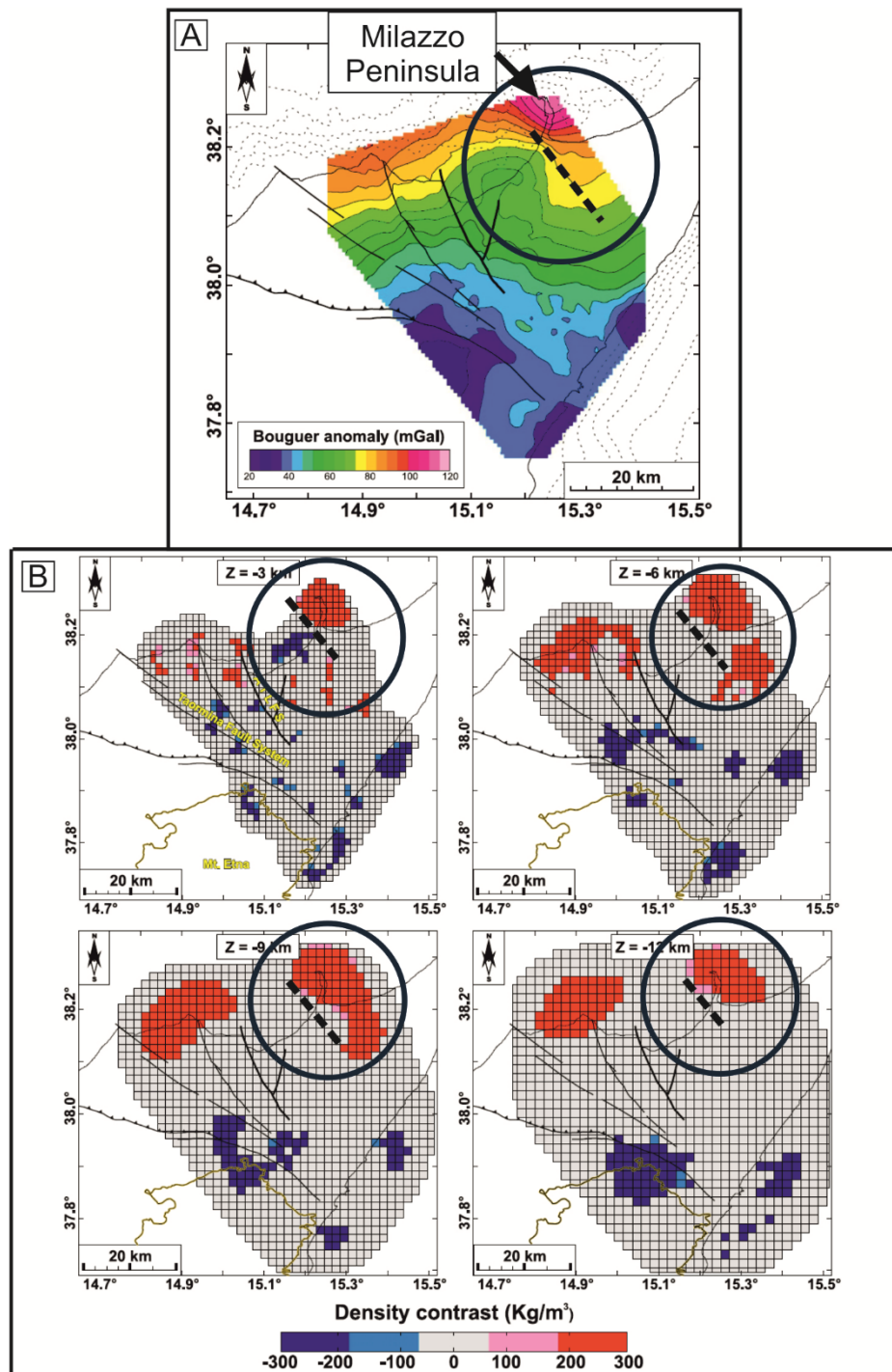


Figure 49. Gravimetric maps of NE Sicily (after Palano et al., 2015): A) Bouguer anomaly map where it is evident a huge increase in the anomaly value (around 40 mGal) occurring south to the Milazzo Peninsula along a NW-SE trend; B) density contrast maps (3-12 km depths) depicting a high-density body around the Milazzo Peninsula that it is stretched along a NW-SE direction. The proposed tectonic lineament is indicated with the dashed line.

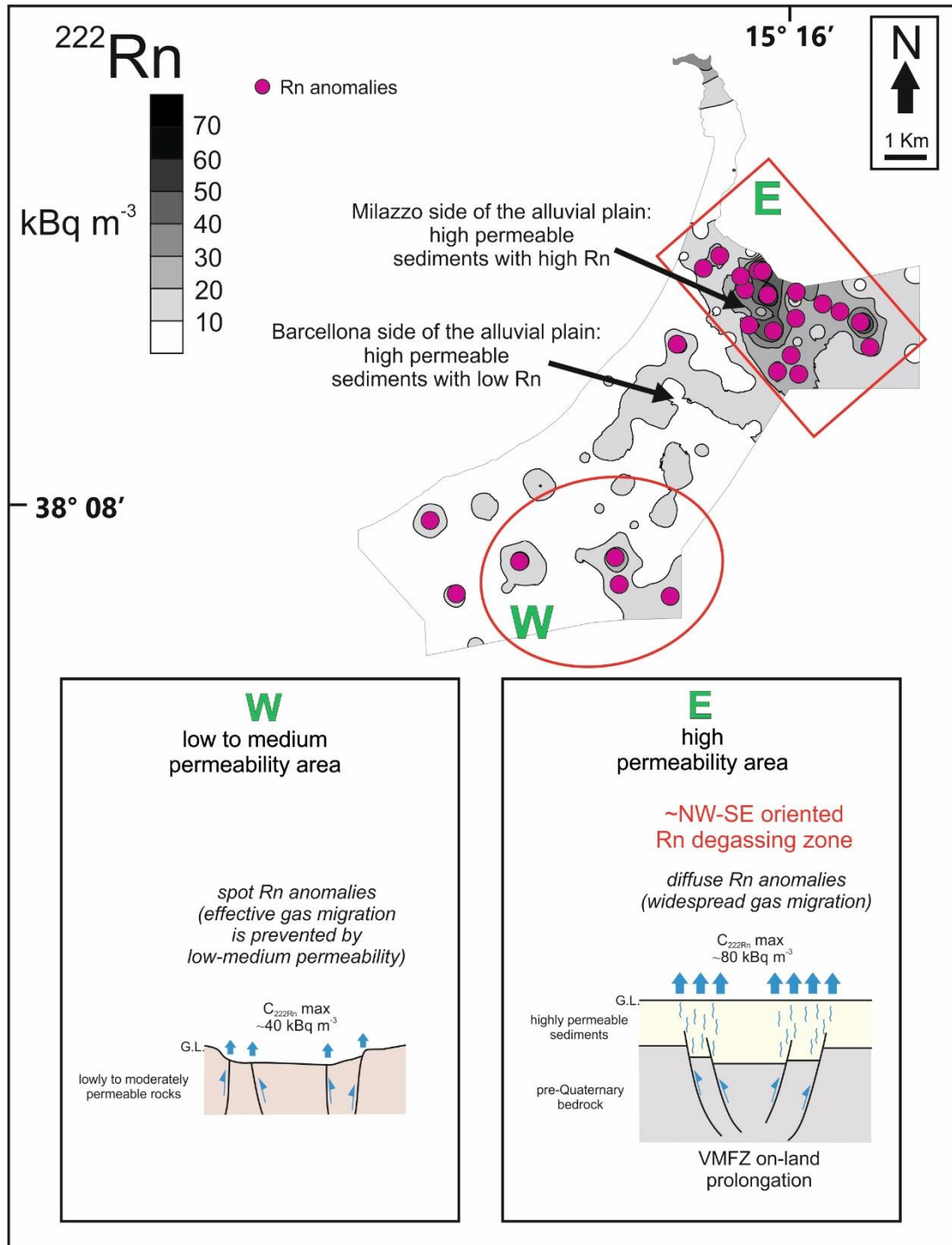


Figure 50. As already stated, two sectors with different characteristics were recognized in the investigated area. The ^{222}Rn contour map put in evidence that in the western sector (“W” zone) only spot anomalies were detected. Here, the lowly to moderately permeable rocks prevent the effective migration of geogenic gases, which takes place only along unsealing faults, especially at fault intersections. In the eastern sector (“E” zone), the high permeability of Quaternary alluvial and transitional sediments favour the gas transport to

the Earth's surface. Here, widespread gas migration occurs along faults and fractures related to the NW-SE oriented on-land prolongation of the VMFZ. Conversely, a weak gas migration was detected farther to the West. This is testified by the fact that the high-permeable alluvial sediments located in the Eastern sector of the studied area (i.e. in the Milazzo side of the alluvial plain) show Rn levels that are considerably higher than those situated farther to the West (i.e. in the Barcellona side of the alluvial plain).

concentrations up to $\sim 40 \text{ kBq m}^{-3}$ have been documented as spot anomalies, and gas migration takes place along non-sealing faults or within highly-fractured domains (i.e. at fault intersections). Lowly and moderately permeable rocks that are affected by low degrees of tectonic deformation did not show anomalous Rn concentrations. The eastern sector ("E" zone in Fig. 50), mostly situated in the Milazzo side of the Holocene alluvial plain, is a high permeability-dominated area where diffuse anomalies (^{222}Rn levels up to $\sim 80 \text{ kBq m}^{-3}$) were identified despite the low-rate seismicity. Here, widespread gas migration occurs along faults and fracture ascribed to a fault segment belonging to the VMFZ. The effectiveness of the gas transport is favoured by the high permeability and porosity of the alluvial and transitional sediments overlying the pre-Quaternary bedrock. Alternatively, the alluvial sediments located farther to the west (i.e. in the Barcellona side of the Holocene alluvial plain; see Fig. 50) show low Rn concentrations. The radiological difference between alluvial sediments occurring in separate localities must be related to the "tectonic" effect as in the eastern sector of the studied area faults and joints are affected by an intense uprising of deep-originated gases while a weak gas migration takes place further west.

As regards the activity of the proposed on-land continuation of the VMFZ, the lack of high-rate seismicity (Fig. 46C) may account for an aseismic (i.e. creeping) fault or for a "silent" (i.e. locked, un-slipped) segment in the interseismic phase. The presence of historical earthquakes (i.e. $M_w=4.3$, 1732 and $M_w=4.5$, 1831; Fig. 48A) together with the slow deformation rate (see Palano et al., 2015) and the lack of low-density and low-velocity bodies at depth (see Palano et al., 2015), strongly suggest defining this tectonic structure as a "silent" fault segment.

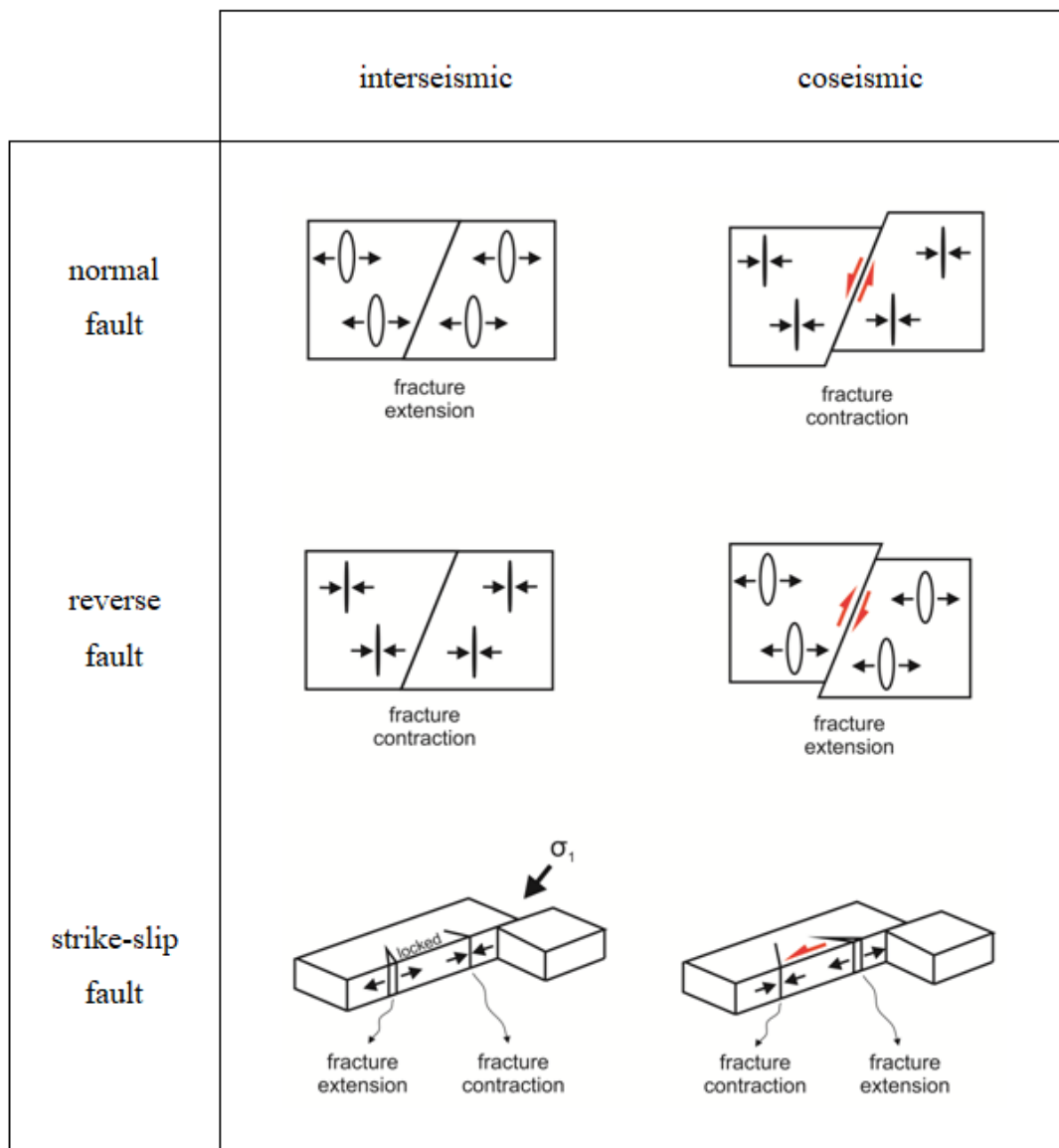


Figure 51. Interseismic and coseismic models for normal, reverse and strike-slip faults (after Muir-Wood and King, 1993; Muir-Wood 1994; Seront et al., 1998; Doglioni et al., 2014). Normal faults exhibit higher permeability during the interseismic period because of the positive dilation involving fractures and pore space. During the coseismic stage, permeability decreases due to collapsing fractures. An opposite style is assumed for reverse faults, as fractures result open and highly permeable during coseismic ruptures. Strike-slip kinematics permit the contemporaneous presence of dilated and contracted domains, both in interseismic and coseismic phases.

This assumption is justified by the fact that the permeability of a fault zone, and then the capacity of being permeated by gases, depends on its kinematics and activity. As

illustrated in Figure 51, normal faults show a higher permeability during the interseismic stage since fractures and pore spaces undergo elastic dilation (Muir-Wood and King 1993; Muir-Wood 1994; Seront et al., 1998; Doglioni et al., 2014). During coseismic ruptures, fractures are instantaneously closed and the general permeability decreases as void volume is lost. The opposite behaviour occurs for reverse faults (Muir-Wood and King 1993; Muir-Wood 1994; Doglioni et al., 2014) whereas strike-slip faults allow the existence of both extension and contraction areas (Doglioni et al., 2014), which alternate each other when the activity phase switches from interseismic to coseismic (Fig. 51). Following those rules, transtensional settings should exhibit permeability conditions that are a mix between those generated by normal and strike-slip regimes. Under those circumstances, transtensional environments at interseismic stages, such as the proposed onshore segments of the VMFZ, are characterized by high permeability domains resulting in a high degassing rate from soils. Hence, the Rn anomalies recognized along the studied tectonic segment fully supports its “silent” (i.e. interseismic) significance.

As proof, degassing phenomena linked to locked normal, transtensional and strike-slip faults have been widely documented worldwide. King et al. (1993, 1996) measured soil-Rn anomalous values along a locked segment of the S. Andreas fault (California, USA). In the Ghab basin (Western Syria), where several historical earthquakes have been documented even though seismic quiescence characterizes the last 100 years, Al-Hilal and Abdul-Wahed (2018) identified high soil-Rn increases correlated with the presence of a silent fault segment belonging to the Dead Sea fault system. Moreover, Sun et al. (2017) demonstrated the negative correlation between the carbon monoxide concentration in soil and the slip rate of a normal fault situated in the Shanxi zone (northern China), emphasizing the fact that the permeability of normal faults tends to increase during interseismic periods due to the opening of cracks.

Interestingly, recently geological and geophysical investigations carried out further south, along the Ionian margin of the Peloritani Mountains, identified a NW-SE trending “silent” fault zone (known as Rocca Novara-Capo S.Alessio fault belt; Barreca et al., 2019) marking the southern boundary of the ATLFS from the Novara village to the Ionian Sea. The on-land segment of the VMFZ shares several

geophysical characteristics with the Rocca Novara-Capo S.Alessio fault belt (e.g. the transtensional motion, the position at the edge of the ATLFS, the paucity of seismic events, the slow strain-rate and the absence of ductile low-velocity and low-density bodies at depth), and for this reason, it could be considered as its northern equivalent. In my opinion, further analyses should be done to better understand the relevant role of the silent transtensional fault branches bounding the ATLFS. I believe that the focus should be put on seismological hazards. Major silent faults have to be treated as potentially active faults that are capable of generating destructive earthquakes depending on their length (Wells and Coppersmith, 1994) as already explained by Cultrera et al. (2017b) and Barreca et al. (2019). Despite the fact that seismicity has been scarce in the last 35 years, the seismic potential of the main recognized Rn degassing zone is strongly testified by historical earthquakes $M > 4$ occurring in 1732 and 1831. Moreover, all along the Milazzo Peninsula, two uplifted Holocene shorelines were identified (Scicchitano et al., 2011). They were probably deformed by coseismic displacements attributed to earthquakes that occurred during the IV and the IX century, enhancing the debate concerning the seismological risk in the studied area. Therefore, it seems clear that performing advanced multidisciplinary investigations (e.g. geological, geophysical, geochemical) results to be crucial to assess a correct seismic-risk management for one of the most populated areas within the central Mediterranean.

5.6 Concluding remarks

As already reported in the Introduction of this Chapter, the Tyrrhenian margin of northeastern Sicily is one of the most tectonically active areas in Italy. Usually, those regions are considered hazard-prone areas in terms of radiological exposure to radon. Because of that, radiological prospections in soils were performed in the sector of northeastern Sicily that includes the Holocene alluvial plain of Milazzo and Barcellona and the hilly reliefs of Castoreale and Rodi Milici villages. The primary targets of the study are evaluating the hazard for inhabitants caused by the exposure to radon degassed from soils, and understanding if, and how, lithology and fault zones affect radon concentration in soil gas.

Results show that soil- ^{222}Rn and ^{220}Rn concentrations within the studied area increase eastwards whereas the $^{220}\text{Rn}/^{222}\text{Rn}$ ratio behaves the opposite. The so-called Radon Index (RI) was used to assess the radon risk classification, and it was calculated by considering ^{222}Rn levels and soil permeability features. RI values demonstrate that the radiological hazard for the population living in the investigated area is low to moderate, except for a cluster situated near the urban area of Milazzo where the risk is higher.

Future goals in this field could involve a series of indoor Rn measurements, to carry out in order to confirm the goodness of the results obtained from the hazard evaluation proposed in this work, especially since the Italian legislative decree no. 101/2020 introduced for the first time an indoor radon concentration limit (300 Bq m^{-3}) for private buildings. Moreover, the RI classification could be employed as a strategic preliminary tool in civil engineering in the field of hazard mitigation for existing and new buildings.

As regards the geophysical point of view, it appears clear that both “lithological” (resulting from permeability features, U and Th content and fabric/texture of soil) and “tectonic” (due to advective flows of endogenous gases along fractures and faults) effects contribute to the Rn concentration measured in soil.

Following the results of the radon survey, the studied area can be divided into two sectors. The western one (hilly reliefs of Castoreale and Rodi Milici villages) is characterized by the occurrence of lowly to moderately permeable soils, which prevent the effective gas migration from deep environments to the Earth’s surface. Here, anomalous Rn sites were identified as spot anomalies located only where rocks are more fractured and permeable, namely at fault intersections. In the eastern sector (mostly composed of the alluvial plain of Milazzo), where highly permeable sediments occur, diffuse Rn anomalies were detected. It testifies a widespread gas migration of deep-originated gases along fractures and buried faults, favoured by the high permeability of the Quaternary sediments.

The “tectonic” effect is evident in the eastern sector of the studied area, where soil-Rn levels measured in the alluvial deposits are considerably higher in comparison to those determined for the analogous sediments outcropping further west. This detail can only be explained through the presence of an additional contribution to the

background concentration, derived from endogenous Rn uprising along faults and associated structures. This assumption is supported by the fact that in the eastern sector: i) $^{220}\text{Rn}/^{222}\text{Rn}$ ratios show a deep signature; ii) soil-Rn values are identical to those measured within fault zones located in the northern part of the Calabrian arc by previous studies; iii) soil-CO₂ concentrations determined together with Rn are compatible with a tectonically active environment.

The Rn degassing zone identified in the eastern sector is oriented along a ~NW-SE direction, and it is located adjacent to the Vulcano-Milazzo fault zone (VMFZ), a tectonic element with transtensional kinematics running from the Island of Vulcano to the Tyrrhenian coast of NE Sicily. In this framework, the tectonic structures promoting the gas migration probably represent the on-land prolongation of the VMFZ.

The proposed tectonic link seems to be confirmed by the presence of: i) an offshore-onshore alignment of seismic events $M > 3$ located in proximity to the VMFZ and the Rn degassing zone; ii) a number of ~NW-SE trending faults showing recent activity located where widespread Rn degassing occurs. Therefore, we can prudently envisage a structural configuration where the two tectonic segments act as a unique ~NW-SE trending fault zone.

Moreover, the slow deformation rate, the lack of ductile layers at depth, the presence of historical earthquakes together with the recent paucity of recorded seismicity, and the condition of enhanced permeability affecting interseismic stages, allow us to consider the onshore prolongation of the VMFZ as a “silent” fault segment.

Taking into account this information, I believe that the next step should be to refine the gas migration model proposed in this work. For instance, future activities such as performing further soil-CO₂ measurements, evaluating soil concentrations of other key gas (e.g. CH₄ and He) and determining if endogenous gases have a crustal or a mantle signature, are essentials in order to achieve the aforementioned purpose. In addition, since this area is retained to be at high seismic risk, geophysical investigation (e.g. active and passive seismic methods) are helpful to obtain data about the location and the activity of buried faults located beneath the Holocene alluvial plain of Milazzo and Barcellona.

References

- M. Al-Hilal and M.K. Abdul-Wahed. Soil gas radon measurements for investigating the actual status of seismic quiescence along the bounding fault of the Ghab pull-apart basin in western Syria. *Geofísica International*, **57**(3):177-187, 2018.
- J.D. Appleton, J.C.H. Miles and M. Young. Comparison of Northern Ireland radon maps based on indoor radon measurements and geology with maps derived by predictive modelling of airborne radiometric and ground permeability data. *Science of the Total Environment*, **409**:1572-1583, 2011.
- M.D. Barberio, F. Gori, M. Barbieri, A. Billi, F. Casalati, S. Franchini, L. Lorenzetti and M. Petitta. Optimization of dissolved Radon monitoring in groundwater to contribute to the evaluation of the seismic activity: an experience in central-southern Italy. *SN Applied Sciences* **2**:Article Number 1392, 2020.
- I. Barnet. Radon risk classification for building purposes in the Czech Republic. In: BARNET I. – NEZNAL M., Eds: Radon investigation in the Czech Republic, 5, 18–24. – Czech Geol. Survey and RADON v.o.s., Prague, 1994.
- I. Barnet, P. Pacherova and M. Neznal. Radon in geological environment—Czech experience *Czech Geological. Survey Special Papers*, **19**:19–28, 2008.
- G. Barreca, V. Bruno, F. Cultrera, M. Mattia, C. Monaco and L. Scarfi. New insights in the geodynamics of the Lipari–Vulcano area (Aeolian Archipelago, southern Italy) from geological, geodetic and seismological data. *Journal of Geodynamics*, **82**:150–167, 2014.
- G. Barreca, L. Scarfi, F. Gross, C. Monaco and G. De Guidi. Fault pattern and seismotectonic potential at the south-western edge of the Ionian Subduction System (southern Italy): New field and geophysical constraints. *Tectonophysics*, **761**:31.45, 2019.
- J.C. Baubron, A. Rigo and J.P. Toutain. Soil gas profiles as a tool to characterize active tectonic areas: the Jaut Pass example (Pyrenees, France). *Earth and Planetary Science Letters*, **196**:69-81, 2002.
- S.E. Beaubien, G. Ciotoli and S. Lombardi. Carbon dioxide and radon gas hazard at the Alban hill area (Central Italy). *Journal of Volcanology and Geothermal Research*, **123**:63–80, 2003.
- A. Bertolo and L. Verdi. Validation of a geographic information system for the evaluation of the soil radon exhalation potential in South-Tyrol and Veneto (Italy). *Radiation Protection Dosimetry*, **97**:321-332, 2001.

A. Billi, G. Barberi, C. Faccenna, G. Neri, F. Pepe, and A. Sulli. Tectonics and seismicity of the Tindari Fault System, southern Italy: crustal deformations at the transition between ongoing contractional and extensional domains located above the edge of a subducting slab. *Tectonics*, **25**(2), Article Number 2006, 2006.

G. Bini, G. Chiodini, C. Lucchetti, P. Moschini, S. Caliro, S. Mollo, J. Selva, P. Tuccimei, G. Galli and O. Bachmann. Deep versus shallow sources of CO₂ and Rn from a multi-parametric approach: the case of the Nisyros caldera (Aegean Arc, Greece). *Scientific Reports*, **10**:Article Number 13782, 2020.

R.S. Bivand, E.J. Pebesma and V. Gómez-Rubio. *Applied spatial data analysis with R*. Springer, New York, 2008.

P. Bossew and H. Lettner. *Statistische Analyse von Radondaten*. Report to the Austrian Ministry of Social Affairs & Generations. Vienna, 2002.

P. Bossew and H. Lettner. Definition of the Radon potential, its spatial properties over Austria and mapping of its levels and the related risk. Presentation, Radon workshop, Lausanne, 2005.

P. Bossew, G. Dubios and T. Tollefsen. Investigations on indoor Radon in Austria, part 2: geological classes as categorical external drift for spatial modeling of the Radon potential. *Journal of Environmental Radioactivity*, **99**:81-97, 2008.

M. Camarda, S. Gurrieri and M. Valenza. CO₂ flux measurements in volcanic areas using the dynamic concentration method: Influence of soil permeability. *Journal of Geophysical Research*, **111**:Article Number B05202, 2006.

S. Carbone, A. Messina, F. Lentini and E. Macaione. *Carta Geologica d'Italia alla Scala 1:50.000*. Foglio 587 Milazzo e 600 Barcellona Pozzo di Gotto. ISPRA-Regione Siciliana, S.EL.CA., Firenze, 2011.

M. Castelluccio. Soil radon concentration survey in Caffarella Valley test site (Rome). Ph.D. Thesis in Geodynamics at the "Roma Tre" University, 2011.

M. Castelluccio, G. Giannella, C. Lucchetti, M. Moroni and P. Tuccimei. Classification Of Radon Hazard In Urban Planning Focused To Risk Management. *Italian Journal of Engineering Geology and Environment*, **2**:5-15, 2012.

Z. Chen, Y. Li, Z. Liu, J. Wang, X. Zhou and J. Du. Radon emission from soil gases in the active fault zones in the Capital of China and its environmental effects. *Scientific Reports*, **8**:Article Number 16772, 2018.

G. Cinelli, L. Tositti, B. Capaccioni, E. Brattich and D. Mostacci. Soil gas radon assessment and development of a radon risk map in Bolsena, Central Italy. *Environmental Geochemistry & Health*, **37**:305–319, 2015.

G. Ciotoli, M. Guerra, S. Lombardi and E. Vittori. Soil gas survey for tracing seismogenic faults: a case study in the Fucino Basin, Central Italy. *Journal of Geophysical Research*, **103**:23781–23794, 1998.

G. Ciotoli, G. Etiope, M. Guerra and S. Lombardi. The detection of concealed faults in the Ofanto basin using the correlation between soil gas fracture surveys. *Tectonophysics*, **299**:321-332, 1999.

G. Ciotoli, S. Lombardi, S. Morandi and F. Zarlenga. A multidisciplinary statistical approach to study the relationships between helium leakage and neotectonic activity in a gas province: the Vasto Basin, Abruzzo-Molise (central Italy). *AAPG Bulletin*, **88**(3):355-372, 2005.

G. Ciotoli, S. Lombardi and A. Annunziatellis. Geostatistical analysis of soil gas data in a high seismic intermontane basin: Fucino Plain, central Italy. *Journal of Geophysical Research*, **112**:Article Number B05407, 2007.

G. Ciotoli, A. Sciarra, L. Ruggiero, A. Annunziatellis and S. Bigi. Soil gas geochemical behaviour across buried and exposed faults during the 24 August 2016 central Italy earthquake. *Annals of Geophysics* **59**:Fast Track 5, 2016.

L. Claesson, A. Skelton, C. Graham, C. Dietl, C.M. Morth, P. Torssander and I. Kockum. Hydrogeochemical changes before and after a major earthquake. *Geology* **32**(8):641-644, 2004.

F. Cultrera, G. Barreca, P. Burrato, L. Ferranti, C. Monaco, S. Passaro, F. Pepe and L. Scarfi. Active faulting and continental slope instability in the Gulf of Patti (Tyrrhenian side of NE Sicily, Italy): a field, marine and seismological joint analysis. *Natural Hazards*, **86**:253–272, 2017a.

F. Cultrera, G. Barreca, L. Ferranti, C. Monaco, F. Pepe, S. Passaro, G. Barberi, V. Bruno, P. Burrato, M. Mattia, C. Musumeci and L. Scarfi. Structural architecture and active deformation pattern in the northern sector of the Aeolian-Tindari-Letojanni fault system (SE Tyrrhenian Sea-NE Sicily) from

integrated analysis of field, marine geophysical, seismological and geodetic data. *Italian Journal of Geosciences* **136**(3):399-417, 2017b.

W. D'Alessandro, L. Brusca, D. Cinti, A.L. Gagliano, M. Longo, G. Pecoraino, H. Pfanz, L. Pizzino, A. Raschi and N. Voltattorni. Carbon dioxide and radon emissions from the soils of Pantelleria island (Southern Italy). *Journal of Volcanology and Geothermal Research* **362**:49-63, 2018.

G. De Astis, L. La Volpe, A. Peccerillo and L. Civetta. Volcanological and petrological evolution of Vulcano island (Aeolian Arc, southern Tyrrhenian Sea). *Journal of Geophysical Research*, **102**(B4):8021-8050, 1997.

G. De Guidi, G. Lanzafame, M. Palano, G. Puglisi, A. Scaltrito and L. Scarfi. Multidisciplinary study of the Tindari Fault (Sicily, Italy) separating ongoing contractional and extensional compartments along the active Africa–Eurasia convergent boundary. *Tectonophysics* **588**:1–17, 2013.

C. Doglioni, S. Barba, E. Carminati and F. Riguzzi. Fault on v-off versus coseismic fluids reaction. *Geoscience Frontiers* **5**:767-780, 2014.

G. Dubois. An overview of radon surveys in Europe. Radioactivity environmental monitoring emissions and health unit institute for environment and sustainability. JRC—European commission 2005.

G. Dubois and P. Bossew. From babel to the round table of Camelot: On setting up a common language and objective for European radon risk mapping. Part I. Radon risk maps, different maps for different purposes. In: I. Barnet, M. Neznal and P. Pacherova (Eds.) *Proceedings of the 8th international workshop on the geological aspect of radon risk mapping*, Prague, Czech Republic, 2006.

Durridge Company. RAD 7, electronic radon detector user manual. 2018.

D. Nguyễn-Thùy, H. Nguyễn-Văn, J.P. Schimmelmann, N.T.Á. Nguyễn, K. Doiron and A. Schimmelmann. ^{220}Rn (Thoron) Geohazard in Room Air of Earthen Dwellings in Vietnam. *Geofluids*, Volume 2019: Article Number 7202616, 2019.

J. Elío, M.F. Ortega, B. Nisi, L.F. Mazadiego, O. Vaselli, J. Caballero and F. Grandia. CO_2 and Rn degassing from the natural analog of Campo de Calatrava (Spain): implications for monitoring of CO_2 storage sites. *International Journal of Greenhouse Gas Control*, **32**:1-14, 2015.

- J. Elío, Q. Crowley, R. Scanlon, J. Hodgson and S. Long. Rapid radon potential classification using soil-gas radon measurements in the Cooley Peninsula, County Louth, Ireland. *Environmental Earth Sciences* **78**: Article Number 359, 2019a.
- J. Elío, G. Cinelli, P. Bossew, J.L. Gutiérrez-Villanueva, T. Tollefsen, M. De Cort, A. Nogarotto and R. Braga. The first version of the Pan-European Indoor Radon Map. *Natural Hazards and Earth System Sciences*, **19**:2451-2464, 2019b.
- G. Etiope and S. Lombardi. Laboratory simulation of geogas microbubble flow. *Environmental Geology* **27**:226–232, 1996.
- G. Etiope and G. Martinelli. Migration of carrier and trace gases in the geosphere: an overview. *Physics of the Earth and Planetary Interiors*, **129**(3-4):185-204, 2002.
- G. Etiope, M. Guerra and A. Raschi. Carbon dioxide and radon geohazards over a gas-bearing fault in the Siena Graben (Central Italy). *Terrestrial, Atmospheric and Oceanic Sciences*, **16**:885–896, 2005.
- Directive 2013/59/EURATOM. Laying down basic safety standards for protection against the dangers arising from exposure to ionising radiation, and repealing Directives 89/618/Euratom, 90/641/Euratom, 96/29/Euratom, 97/43/Euratom and 2003/122/Euratom, 2013.
- C. Fang and J.B. Moncrieff. A model for soil CO₂ production and transport 1: Model development. *Agricultural and Forest Meteorology* **95**: 225–236, 1999.
- H. Friedmann. Radon In Earthquake Prediction Research. *Radiation Protection Dosimetry*, **149**(2):177–184, 2012.
- C.C. Fu, T.F. Yang, V. Walia and C.H. Chen. Reconnaissance of soil gas composition over the buried fault and fracture zone in southern Taiwan. *Geochemical Journal*, **39**:427-439, 2005.
- C. Gasparini, G. Iannaccone, P. Scandone and R. Scarpa. Seismotectonics of the Calabrian Arc. *Tectonophysics*, **82**:267-286, 1982.
- C. Gasparini, G. Iannaccone, R. Scarpa. Fault-plane solutions and seismicity of the Italian peninsula. *Tectonophysics*, **117**:59-78, 1985.
- G. Gianelli. On the origin of geothermal CO₂ by metamorphic processes. *Bollettino Società Geologica Italiana* **104**:575–584, 1985.

S. Goes, D. Giardini, S. Jenny, C. Hollenstein, H.G. Kahle and A. Geiger. A recent tectonic reorganization in the south-central Mediterranean. *Earth and Planetary Science Letters*, **226**(3-4):335-345, 2004.

S. Gurrieri and M. Valenza. Gas transport in natural porous medium: a method for measuring soil CO₂ flows from the ground in volcanic and geothermal areas. *Rendiconti Società Italiana di Mineralogia e Petrologia*, **43**:1151-1158, 1988.

T. Hishinuma, T. Nishikawa, T. Shimoyama, M. Miyajima, Y. Tamagawaì and S. Okabe. Emission of radon and thoron due to the fracture of rock. *Il Nuovo Cimento C, Year 1999*(3-4):523-528, 1999.

R.F. Holub and B.T. Brady. The effect of stress on radon emanation from rock, *Journal of Geophysical Research* **86**:1776–1784, 1981.

S. Huxol, M.S. Brennwald, R. Henneberger and R. Kipfer. ²²⁰Rn/²²²Rn Isotope Pair as a Natural Proxy for Soil Gas Transport. *Environmental Science & Technology* **47**:14044–14050, 2013.

G. Igarashi, S. Saeki, N. Takahata, K. Sumikawa, S. Tasaka, Y. Sasaki, M. Takahashi and Y. Sano. Ground-Water Radon Anomaly Before the Kobe Earthquake in Japan. *Science* **269**(5220):60-61, 1995.

G. Immè and D. Morelli. Radon as Earthquake Precursor, *Earthquake Research and Analysis - Statistical Studies, Observations and Planning*, Dr Sebastiano D'Amico (Ed.), ISBN: 978-953-51-0134-5, 2012.

INGV earthquakes catalogue, <http://terremoti.ingv.it>.

G. Iovine, I. Guagliardi, C. Bruno, R. Greco, A. Tallarico, G. Falcone, F. Lucà and G. Buttafuoco. Soil-gas radon anomalies in three study areas of central-northern Calabria (southern Italy). *Natural Hazards* **91**:193–219, 2018.

W.P. Irwin and I. Barnes. Tectonic relation of carbon dioxide discharges and earthquakes. *Journal of Geophysical Research* **85**: 3115-3121, 1980.

ISTAT, 2019 Istituto Nazionale di Statistica

- F. Italiano, G. Martinelli and P. Plescia. CO₂ Degassing over Seismic Areas: The Role of Mechanochemical Production at the Study Case of Central Apennines. *Pure and Applied Geophysics*, **165**:75–94, 2008.
- G. Jonsson. Soil radon depth dependence. *Radiation Measurements*, 34:415-418, 2001.
- Y. Kawada, H. Nagahama, Y. Omori, Y. Yasuoka, T. Ishikawa, S. Tokonami and M. Shinogi. Time-scale invariant changes in atmospheric radon concentration and crustal strain prior to a large earthquake. *Nonlinear Processes in Geophysics*, **14**:123–130, 2007.
- J. Kemski, A. Siehl, R. Stegemann and M. Valdivia-Manchego. Mapping the geogenic radon potential in Germany. *Science of the Total Environment*, **272**:217-230, 2001.
- N.U. Khattak, M.A. Khan, N. Ali, F. Ahmed and M. Tahir Shah. Recognition and characterization of a tectonically active Karak Thrust using radon measurement technique in the Southern Kohat Plateau, Pakistan. *Journal of Himalayan Earth Sciences Volume 49(2)*:40-49, 2016.
- C.Y. King, W. Zhang and B.S. King. Radon anomalies on three kinds of faults in California. *Pure and Applied Geophysics*, **141**:111–124 1993.
- C.Y. King, B.S. King, W.C. Evans and W. Zhang. Spatial radon anomalies on active faults in California. *Applied Geochemistry* **11**:497-510, 1996.
- I.G. Kissin and S.I. Pakhomov. Geochemistry of Carbon Dioxide in Deep Zones of the Underground Hydrosphere. *Geokhimiya*, Year 1969(4): 460–471, 1969.
- R.W. Klusman. *Soil Gas and Related Methods for Natural Resource Exploration*, John Wiley, New York, 1993.
- K. Kristiansson and L. Malmqvist. Evidence for non-diffusive transport of ²²²Rn the ground and a new physical model for the transport. *Geophysics* **47**:1444-1452, 1982.
- K. Kristiansson and L. Malmqvist. Trace elements in the geogas and their relation to bedrock composition. *Geoexploration* **24**:517–53, 1987.
- V. Kulajta, M. Matolin, V. Vesely and I. Barnet. A proposal of the Radon Risk Classification of Foundation Soils. In: I. Barnet (Eds), *Radon investigations in Czechoslovakia*, Czech Geological Survey, Prague, 1990.

A. Kumar, V. Walia, T.F. Yang, C.C. Fu, S. Singh, B.S. Bajwa and V. Arora. Soil ^{222}Rn Concentration, CO_2 and CH_4 Flux Measurements around the Jwalamukhi Area of North-West Himalayas, India. *Radiation Protection Dosimetry*, **171**(2):262-266, 2016.

Italian Legislation, D. Lgs. 101/2020

F. Lentini, S. Carbone, M. Grasso, A. Di Stefano, M. Romeo and A. Messina. Carta Geologica della Provincia di Messina 1:50,000, S.EL.CA. Firenze, Italy, 2000.

S. Lombardi and N. Voltattorni. Rn, He and CO_2 soil gas geochemistry for the study of active and inactive faults. *Applied Geochemistry*, **25**:1206–1220, 2010.

S. Lombardi, G. Etioppe, M. Guerra, G. Ciotoli, P. Grainger, G. A. Duddridge, F. Gera, V. Chiantore, R. Pensieri, P. Grindrod and M. Impey. The Refinement of Soil Gas Analysis as a Geological Investigative Technique. Final Report EC Contract No. FI2WCT91e0064. 4th R&D Programme on “Management and Storage of Radioactive Waste” (1990e1994) Part a, Task 4: “Disposal of Radioactive Waste”. Official publication of the European Communities no. EUR 16929 EN, 1996.

F. Lucchi, C.A. Tranne, G. De Astis, J. Keller, R. Losito and W. Morche. Stratigraphy and significance of Brown Tuffs on the Aeolian Islands (southern Italy). *Journal of Volcanology and Geothermal Research*, **177**:49–70, 2008.

S. Mollo, P. Tuccimei, M.J. Heap, S. Vinciguerra, M. Soligo, M. Castelluccio, P. Scarlato and D.B. Dingwell. Increase in radon emission due to rock failure: An experimental study. *Geophysical Research Letters*, 38: Article Number L14304, 2011

R. Muir Wood. Earthquakes, strain-cycling and the mobilization of fluids. Geological Society, London, Special Publications, **78**:85-98, 1994.

R. Muir Wood and G.C.P. King. Hydrologic signatures of earthquake strain. *Journal of Geophysical Research*, **98**:22035-22068, 1993.

M. Neri, S. Giammanco, E. Ferrera, G. Patanè and V. Zanon. Spatial distribution of soil radon as a tool to recognize active faulting on an active volcano: the example of Mt. Etna (Italy). *Journal of Environmental Radioactivity*, **102**:863-870, 2011.

M. Neri, E. Ferrera, S. Giammanco, G. Patanè and V. Zanon. Un metodo per riconoscere faglie attive sepolte mediante misure areali di radon dal suolo *Geologia dell’Ambiente*, n. 2, 2014.

M. Neznal, N. Neznal, M. Matolin, I. Barnet and J. Miksova. The New Method for Assessing the Radon Risk of Building Sites. In: Czech Geol. Survey Special Papers, 16. Czech Geological Survey, Prague, 2004.

A. Nicolas, F. Girault, A. Schubnel, É. Pili, F. Passelègue, J. Fortin, and D. Deldicque. Radon emanation from brittle fracturing in granites under upper crustal conditions, *Geophysical Research Letters*, **41**:5436–5443, 2014.

PAI (Piano Assetto Idrogeologico), Sicilian Region, <http://www.sitr.regione.sicilia.it/pai>.

M. Palano, L. Ferranti, C. Monaco, M. Mattia, M. Aloisi, V. Bruno, F. Cannavò and G. Siligato. GPS velocity and strain fields in Sicily and southern Calabria, Italy: Updated geodetic constraints on tectonic block interaction in the central Mediterranean. *Journal of Geophysical Research*, **117**, Article Number B0740, 2012.

M. Palano, D. Schiavone, M. Loddo, M. Neri, D. Presti, R. Quarto, C. Totaro and G. Neri. Active upper crust deformation pattern along the southern edge of the Tyrrhenian subduction zone (NE Sicily): Insights from a multidisciplinary approach. *Tectonophysics*, **657**:205–218, 2015.

J. Pearce, I. Czernichowski-Lauriol, S. Lombardi, S. Brune, A. Nador, J. Baker, H. Pauwels, G. Hatziyannis, S. Beaubien, E. Faber. A review of natural CO₂ accumulations in Europe as analogues for geological sequestration. *Geol. Soc. Spec. Publ.* **233**, 29-41, 2004.

F. Quattrocchi, A. Pizzi, S. Gori, P. Boncio, N. Voltattorni and A. Sciarra. The contribution of fluid geochemistry to define the structural pattern of the 2009 L'Aquila seismic source. *International Journal of Geosciences*, **131**:448-458, 2012.

A. Riggio and M. Santulin. Earthquake forecasting: a review of radon as seismic precursor. *Bollettino di Geofisica Teorica ed Applicata*, **56**: 95-114, 2015.

D. Romano, G. Sabatino, M. Di Bella, F. Italiano, M.T. Caccamo, A. Tripodo and S. Magazu. Natural radioactivity and radiological hazard for humans: A simple introduction for newbies and students. New perspectives and innovative teaching methods. *Atti Accademia Peloritana dei Pericolanti, Cl. Sci. Fis. Mat. Nat.*, **99**: No. S1, A39, 2021.

A.W. Rose, H.E. Hawkes, J.S. Webb. *Geochemistry in Mineral Exploration*, 2nd ed..Academic Press, London, UK, **95**,1979.

A. Rovida, R. Camassi, P. Gasperini and M. Stucchi. CPTI11, the 2011 version of the Parametric Catalogue of Italian Earthquakes, 2011. INGV, Milano, Bologna, <http://emidius.mi.ingv.it/CPTI>.

D.J. Sanderson and W.R.D. Marchini. Transpression. *Journal of Structural Geology*, **6**(5):449-458, 1984.

A. Sciarra, A. Fascetti, A. Moretti, B. Cantucci, L. Pizzino, S. Lombardi and I. Guerra. Geochemical and radiometric profiles through an active fault in the Sila Massif (Calabria, Italy). *Journal of Geochemical Exploration*, **148**:128-137, 2015.

A. Sciarra, A. Mazzini, S. Inguaggiato, F. Vita, M. Lupi and S. Hadi. Radon and carbon gas anomalies along the Watakosek Fault System and Lusi mud eruption, Indonesia. *Marine and Petroleum Geology*, **90**:77-90, 2018.

G. Scicchitano, C.R. Spampinato, L. Ferranti, F. Antonioli, C. Monaco, M. Capano, C. Lubritto. Uplifted Holocene shorelines at Capo Milazzo (NE Sicily, Italy): Evidence of co-seismic and steady-state deformation. *Quaternary International*, **232**:201-213, 2011.

L. Scognamiglio, E. Tinti, M. Quintiliani. Time Domain Moment Tensor (TDMT) Data set. Istituto Nazionale di Geofisica e Vulcanologia (INGV). <https://doi.org/10.13127/TDMT>, 2006.

B. Seront, T.F. Wong, J.S. Caine, C.B. Forster and R.L. Bruhn. Laboratory characterisation of hydromechanical properties of a seismogenic fault system. *Journal of Structural Geology*, **20**:865-881, 1998.

A. Skelton, M. Andren, H. Kristmannsdottir, G. Stockmann, C.M. Morth, A. Sveinbjornsdottir, S. Jonsson, E. Sturkell, H.R. Guorunardottir, H. Hjartarson, H. Siegmund and I. Kockum. Changes in groundwater chemistry before two consecutive earthquakes in Iceland. *Nature Geoscience*, **7**(10):752-756, 2014.

A.J. Sinclair. Selection of threshold values in geochemical data using probability graphs. *Journal of Geochemical Exploration*, **3**:129-149, 1974.

A.J. Sinclair. A fundamental approach to threshold estimation in exploration geochemistry: probability plots revisited. *Journal of Geochemical Exploration*, **41**:1-22, 1991.

- Y. Sun, X. Zhou, G. Zheng, J. Li, H. Shi, Z. Guo and J. Du. Carbon monoxide degassing from seismic fault zones in the Basin and Range province, west of Beijing, China. *Journal of Asian Earth Sciences*, **149**:41–48, 2017.
- K.Z. Szabo, G. Jordan, A. Horvath and C. Szabo. Mapping the geogenic radon potential: methodology and spatial analysis for central Hungary. *Journal of Environmental Radioactivity*, **129**:107-120, 2014.
- C. Tansi, A. Tallarico, G. Iovine, M. Folino Gallo and G. Falcone. Interpretation of radon anomalies in seismotectonic and tectonic-gravitational settings: the south-eastern Crati graben (Northern Calabria, Italy). *Tectonophysics*, **396**:181-193, 2005.
- A.Tomer. Radon as a Earthquake Precursor: A Review. *International Journal of Science, Engineering and Technology*, **4**:815-822, 2016.
- E. Tóth, K. Hamori, M. Minda. Indoor radon in Hungary (lognormal mysticism). In: I. Barnet, M. Neznal and P.Pacherová (Eds.), *Radon Investigations in the Czech Republic XI and the 8th International Workshop on the Geological Aspects of Radon Risk Mapping*. Prague, 2006.
- P. Tuccimei, S. Mollo, S. Vinciguerra, M. Castelluccio, and M. Soligo. Radon and thoron emission from lithophysae-rich tuff under increasing deformation: An experimental study. *Geophysical Research Letters*, **37**: Article Number L05305, 2010.
- P. Tuccimei, S. Mollo, M. Soligo, P. Scarlato, and M. Castelluccio. Real-time setup to measure radon emission during rock deformation: implications for geochemical surveillance. *Geoscientific Instrumentation, Methods and Data Systems*, **4**:111–119, 2015.
- J. Vaupotic. Review Of Radon Research In Slovenia. Sources and Measurements of Radon and Radon Progeny Applied to Climate and Air Quality Studies Proceedings of a technical meeting held in Vienna, organized by the International Atomic Energy Agency and co-sponsored by the World Meteorological Organization, 2012.
- N. Voltattorni, D. Cinti, L. Pizzino and A. Sciarra. Statistical approach for the geochemical signature of two active normal faults in the western Corinth Gulf Rift (Greece). *Applied Geochemistry*, **51**:86–100, 2014.
- L.Wang , T. Xianguo and L. Chunlai. Research Of Radon Transportation Model To Investigate Buried Fault. Conference: 18th International Conference on Nuclear Engineering, 2010.

- J. Wei, P. Cui, Z. Chen, B. Yao, C. Zheng, B. Jia and X. Wang. Experimental study on radon exhalation characteristics of coal samples under varying gas pressures. *Results in Physics*, **10**:1006–1014, 2018.
- D.L. Wells and K.J. Coppersmith. New empirical relationships among magnitude, rupture length, rupture width, rupture area, and surface displacement. *Bulletin of Seismological Society of America*, **84**:974–1002, 1994.
- H. Woith. Radon earthquake precursor: A short review. *The European Physical Journal Special Topics*, **224**:611-627, 2015.
- Y. Xiang, X. Sun, D. Liu, L. Yan, B. Wang and X. Gao. Spatial Distribution of Rn, CO₂, Hg, and H₂ Concentrations in Soil Gas Across a Thrust Fault in Xinjiang, China. *Frontiers in Earth Sciences*, **8**: Article Number 554924, 2020.
- T.F. Yang, V. Walia, L.L. Chyi, C.C. Fu, C.H. Chen, T.K. Liu, S.R. Song, C.Y. Lee and M. Lee. Variations of soil radon and thoron concentrations in a fault zone and prospective earthquakes in SW Taiwan. *Radiation Measurements*, **40**:496-502, 2005.
- Y. Yasuoka and M. Shinogi. Anomaly in atmospheric radon concentration: a possible precursor of the 1995 Kobe, Japan, earthquake. *Health Physics*, **72**(5):759–761, 1997.
- Y. Yasuoka, T. Ishii, S. Tokonami, T. Ishikawa, Y. Narazaki and M. Shinogi. Radon anomaly related to the 1995 Kobe earthquake in Japan. *International Congress Series* **1276**: 426–427, 2005.
- G. Yuce, F. Italiano, W. D'Alessandro, T.H. Yalcin, D.U. Yasin, A.H. Gulbay, N.N. Ozyurt, B. Rojay, V. Karabacak, S. Bellomo, L. Brusca, T. Yang, C.C. Fu, C.W. Lai, A. Ozacar and V. Walia. Origin and interactions of fluids circulating over the Amik Basin (Hatay-Turkey) and relationships with the hydrologic, geologic and tectonic settings. *Chemical Geology*, **388**:23-39, 2014.
- G. Yuce, C.C. Fu, W. D'Alessandro, A.H. Gulbay, C.W. Lai, S. Bellomo, T.F. Yang, F. Italiano and V. Walia. Geochemical characteristics of soil radon and carbon dioxide within the dead sea fault and karasu fault in the amik basin (Hatay), Turkey. *Chemical Geology*, **469**:129-146, 2017.
- X. Zhang and D.J. Sanderson. Numerical modeling of the effects of fault slip on fluid flow around extensional fault. *Journal of Structural Geology*, **18**:109-122, 1996.

S. Zhiguan. A study on the origin of fault gases in western Yunnan. *Earthquake Research in China*, **5**(1):45-52, 1991.

X. Zhou, Z. Chen and Y. Cui. Environmental impact of CO₂, Rn, Hg degassing from the rupture zones produced by Wenchuan Ms 8.0 earthquake in western Sichuan, China. *Environmental Geochemistry and Health*, **38**:1067–1082, 2016.

Chapter VI - Radon in groundwater

6.1 Introduction

As highlighted in Section 5.2, radon and other rare gases move over long distances by advection if carried by large gas domains composed of species such as CO₂, CH₄ and N₂. In porous and/or fractured media, another process that is responsible for radon transportation is gas dissolution in groundwaters. This process is known as “water-phase advection” (Etiope and Martinelli, 2002). Gases dissolved in water are passively transported, and move at the same velocity as water. Darcy’s equation allows us to calculate the velocity as follows:

$$v = K \cdot I \quad [48]$$

where K is the hydraulic conductivity and I is the hydraulic gradient.

Radon concentration in water saturating porous rocks and soils can be expressed by the following equation (Andrews, 1977):

$$Rn = \frac{A \cdot Ra \cdot r}{f} \cdot \left[1 - e\left(\frac{-x}{v}\right)\right] \cdot e\left(\frac{-x'}{v'}\right) \quad [49]$$

where A is the emanation coefficient of rocks, Ra is the radium activity concentration of rocks, r is the rock density, f is the fractional pore space, v and v' are the velocities of groundwater within hosting rocks and after leaving the aquifer, respectively and x and x' are the distance covered by groundwater within hosting rocks and after leaving the aquifer, respectively.

Radon is slightly soluble in water and when dissolves it tends to form structures called clathrates, of the type of Rn·6H₂O (see Nesmeyanov, 1974). Radon solubility depends on pH; for instance, high values of pH value (above 7) tend to destabilize clathrates destroying them and allowing the phase change from liquid to gas (Gasparini and Veltri, 1987).

Therefore, it is obvious that radon solubility increases at low pH. Acidification of water in continental environments is usually induced by carbon dioxide dissolution. Active and recent tectonic lineaments, such as those involving the continental crust of the Peloritani Mountains, are characterized by CO₂-rich gases uprising along fault planes and cracks. Those gases dissolve in groundwater provoking modifications of physical and chemical parameters (T, pH, Eh, etc.). Thus, we might expect to detect geochemical anomalies in groundwaters collected close to fault zones.

Furthermore, in northeastern Sicily, groundwater coming from natural springs and wells is carried to towns and served as domestic (i.e. drinking) water for human consumption (i.e. tap water).

In Section 4.5.5 is highlighted that radon dissolved in domestic water is one of the contributors to indoor radon. A fraction of dissolved radon in domestic water is released into the air (i.e. de-emanated) when water is used for bathing, showering, laundry, etc., and is inhaled by people. The part of radon that remains dissolved in water is ingested when water is drunk increasing the probability to develop cancer (see Chapter 1). According to UNSCEAR (2000), the worldwide averages of annual effective doses induce by inhalation and ingestion of ^{222}Rn in water are 0.025 and 0.002 mSv y^{-1} , respectively.

The radiological hazard connected to radionuclides dissolved in domestic water is often neglected by authorities. In addition, no data are present in literature about the “radiological” quality of groundwater for northeastern Sicily. For these reasons, several groundwater samples were collected along the Tyrrhenian margin of the Peloritani Mountains in order to determine the activity concentration of dissolved ^{222}Rn . Fresh water was sampled from wells and natural springs and the ^{222}Rn levels were measured by using the RAD7 + RAD H₂O setup.

The main goals of this part of the Thesis are:

- determining if geophysical parameters affect the dissolved radon concentration in groundwaters.
- estimating the annual effective dose received by people due to ingestion of ^{222}Rn dissolved in groundwaters and evaluating the radiological hazard.

6.2 Method

6.2.1 Sampling locations

A total of 70 groundwater samples were collected from wells and natural springs. Locations of sampled sites are plotted in Figure 52 and listed in Table 18 along with the type of sample. The ^{222}Rn concentration was measured along with temperature, pH and electrical conductivity. Water samples for radon concentration measurements were collected in 40 ml vials, taking care that no air bubbles were in vials. A label stating the date, the time and the site ID was applied to vials just after the sampling.

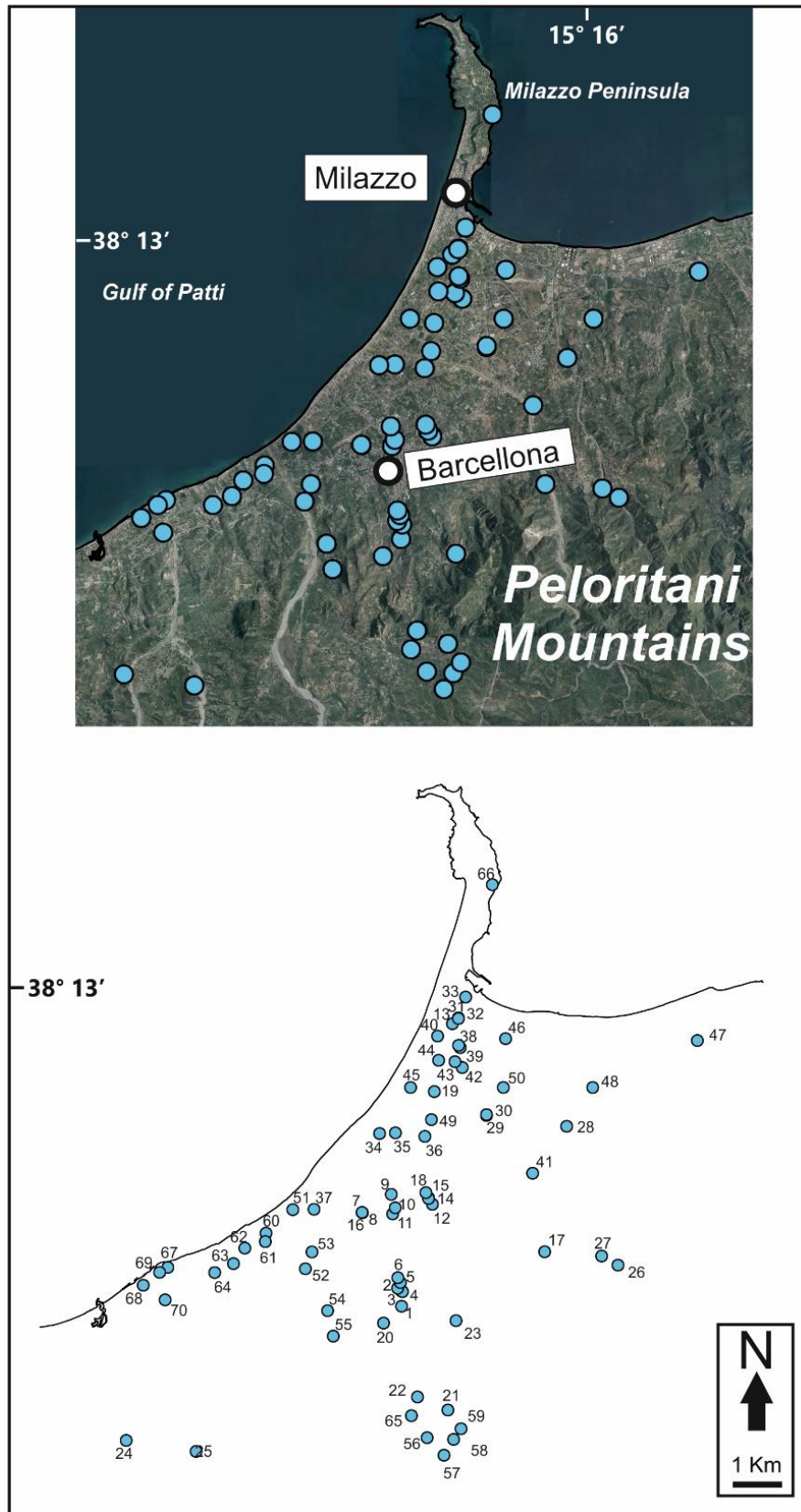


Figure 52. Location of the 70 sites where the groundwater was collected (coordinates are listed in Table 18).

Table 18. List of sampling site coordinates (UTM WGS84 zone 33 N). Sampling date is also reported along with the type of sample (Wd: domestic water well belonging to Barcellona [BRC] or Milazzo [MLZ] municipality; W= private well; S= natural spring). Site locations are plotted on map in Figure 52.

| #Site | Type | Location | Date (dd/mm/yyyy) | North | East |
|-------|------|-----------------------------|----------------------|---------|--------|
| 1 | Wd | Due Mulini - BRC | 22/06/2020 | 4219788 | 519116 |
| 2 | Wd | S. Venera 1 - BRC | 22/06/2020 | 4220347 | 518997 |
| 3 | Wd | Nuovo dx Longano - BRC | 22/06/2020 | 4220259 | 519111 |
| 4 | Wd | S. Venera 2 - BRC | 22/06/2020 | 4220244 | 519146 |
| 5 | Wd | Saia Riti Basso - BRC | 22/06/2020 | 4220527 | 519080 |
| 6 | Wd | Via Isonzo Nuovo - BRC | 22/06/2020 | 4220676 | 519003 |
| 7 | Wd | Aia Scarpaci 1 - BRC | 25/06/2020 | 4222711 | 517899 |
| 8 | Wd | Aia Scarpaci 3 - BRC | 25/06/2020 | 4222699 | 517906 |
| 9 | Wd | Nuovo S. Andrea - BRC | 25/06/2020 | 4223257 | 518796 |
| 10 | Wd | Macello S. Andrea - BRC | 25/06/2020 | 4222845 | 518921 |
| 11 | Wd | S. Andrea - BRC | 25/06/2020 | 4222654 | 518837 |
| 12 | Wd | Petraro 1 - BRC | 25/06/2020 | 4222949 | 520074 |
| 13 | W | / | 27/06/2020 | 4228552 | 520697 |
| 14 | Wd | Petraro 2 - BRC | 30/06/2020 | 4223152 | 519950 |
| 15 | Wd | Petraro 3 - BRC | 30/06/2020 | 4223138 | 519952 |
| 16 | Wd | Aia Scarpaci 2 - BRC | 30/06/2020 | 4222708 | 517899 |
| 17 | Wd | Femminamorta - BRC | 30/06/2020 | 4221475 | 523554 |
| 18 | Wd | Petraro 4 - BRC | 30/06/2020 | 4223313 | 519872 |
| 19 | W | / | 02/07/2020 | 4226451 | 520130 |
| 20 | Wd | Gurafi - BRC | 08/07/2020 | 4219266 | 518554 |
| 21 | Wd | Nuovo Praga - BRC | 08/07/2020 | 4216559 | 520557 |
| 22 | Wd | Praga - BRC | 08/07/2020 | 4216916 | 519584 |
| 23 | Wd | Nuovo Kappa - BRC | 08/07/2020 | 4219338 | 520809 |
| 24 | W | / | 21/09/2020 | 4215601 | 510579 |
| 25 | W | / | 21/09/2020 | 4215281 | 512754 |
| 26 | Wd | Santa Lucia 2 - MLZ | 22/10/2020 | 4221066 | 525819 |
| 27 | Wd | Santa Lucia 1 - MLZ | 22/10/2020 | 4221352 | 525316 |
| 28 | Wd | San Filippo-Corriolon - MLZ | 22/10/2020 | 4225359 | 524238 |
| 29 | Wd | Fiumarella 3 - MLZ | 22/10/2020 | 4225711 | 521746 |
| 30 | Wd | Fiumarella 2 - MLZ | 22/10/2020 | 4225736 | 521746 |
| 31 | Wd | Contura 4 - MLZ | 22/10/2020 | 4228740 | 520879 |
| 32 | Wd | Contura 2 - MLZ | 22/10/2020 | 4228724 | 520880 |
| 33 | Wd | Zirilli - MLZ | 22/10/2020 | 4229389 | 521093 |
| 34 | W | / | 23/02/2021 | 4225157 | 518436 |
| 35 | W | / | 23/02/2021 | 4225162 | 518933 |
| 36 | W | / | 23/02/2021 | 4225061 | 519838 |
| 37 | W | / | 23/02/2021 | 4222798 | 516389 |

| #Site | Type | Location | Date (dd/mm/yyyy) | North | East |
|-------|------|----------------------|----------------------|---------|--------|
| 38 | W | / | 05/02/2021 | 4227864 | 520912 |
| 39 | W | / | 05/02/2021 | 4227821 | 520933 |
| 40 | W | / | 05/02/2021 | 4228179 | 520232 |
| 41 | W | / | 05/02/2021 | 4223921 | 523181 |
| 42 | W | / | 17/02/2021 | 4227202 | 520997 |
| 43 | W | / | 17/02/2021 | 4227381 | 520787 |
| 44 | W | / | 17/02/2021 | 4227410 | 520261 |
| 45 | W | / | 18/02/2021 | 4226599 | 519372 |
| 46 | W | / | 18/02/2021 | 4228094 | 522345 |
| 47 | W | / | 18/02/2021 | 4228034 | 528279 |
| 48 | W | / | 19/02/2021 | 4226597 | 525042 |
| 49 | W | / | 19/02/2021 | 4225588 | 520048 |
| 50 | W | / | 26/02/2021 | 4226581 | 522265 |
| 51 | W | / | 01/03/2021 | 4222789 | 515744 |
| 52 | W | / | 01/03/2021 | 4220981 | 516149 |
| 53 | W | / | 01/03/2021 | 4221475 | 516320 |
| 54 | S | Porto Salvo | 01/03/2021 | 4219639 | 516822 |
| 55 | S | Protonotaro | 01/03/2021 | 4218868 | 517002 |
| 56 | S | Madonna dell'Udienza | 03/03/2021 | 4215698 | 519900 |
| 57 | S | S. Gaetano | 03/03/2021 | 4215158 | 520439 |
| 58 | S | Nipotelle | 03/03/2021 | 4215637 | 520721 |
| 59 | S | Foleo | 03/03/2021 | 4215980 | 520957 |
| 60 | W | / | 05/03/2021 | 4222053 | 514905 |
| 61 | W | / | 08/03/2021 | 4221780 | 514899 |
| 62 | W | / | 08/03/2021 | 4221610 | 514250 |
| 63 | W | / | 08/03/2021 | 4221122 | 513908 |
| 64 | W | / | 08/03/2021 | 4220846 | 513324 |
| 65 | S | Acqua ruggiata | 13/03/2021 | 4216428 | 519371 |
| 66 | S | S. Opolo | 13/03/2021 | 4232877 | 521915 |
| 67 | W | / | 30/03/2021 | 4220984 | 511857 |
| 68 | W | / | 30/03/2021 | 4220432 | 511119 |
| 69 | W | / | 30/03/2021 | 4220825 | 511612 |
| 70 | W | / | 06/04/2021 | 4219993 | 511787 |

6.2.2 Temperature, pH, and conductivity measurements

Temperature (T; °C), pH, and electrical conductivity (C; mS cm⁻¹) of water samples were determined directly *in situ* by using an electronic multiparametric system probe (YSI 556 MPS; Fig. 53 and 54). The probe was calibrated in the laboratory before every sampling survey by using buffer solutions.



Figure 53. Sampling activity. Water samples for dissolved radon measurements were stored in vials and analysed in the laboratory. T, pH and C is measured in situ by using a multiparametric probes immersed in water.



Figure 54. The YSI 556 multiparametric system probe. T, pH and C measurements were carried out by inserting the probes directly into the water sample.

6.2.3 Radon concentration measurement in water samples

The concentration of dissolved ^{222}Rn in groundwaters was calculated by using the RAD7 Durrige at the laboratories of the University of Messina. An exhaustive description of the device characteristics and functioning can be found in Chapter IV of the Thesis.

Measurements were performed by the RAD7 + RAD H₂O setup (Fig 55). The RAD H₂O is an accessory that enables to measure ^{222}Rn concentrations in water over a range of 0.37-14800 Bq L⁻¹ (RAD H₂O Manual). The process of measuring radon in water by coupling the RAD7 and the RAD H₂O is known as “emanometry” (see Caridi et al., 2016 and Caridi and Belmusto, 2018). The 40 ml vial containing the groundwater sample is connected with a small dryer unit filled with drierite and with the RAD7, forming a closed air loop (Fig. 55).

The RAD7 + RAD H₂O provides results after a 30 minutes analysis (Protocol Wat-40). For this reason, only the alpha particles emitted by ^{218}Po were counted for ^{222}Rn detection. This is due to the fact that secular equilibrium between ^{218}Po and ^{222}Rn is achieved after just 10 minutes, whereas ^{216}Po and ^{222}Rn reach the equilibrium after 3 hours. The Wat-40 analysis was preceded by a drying step, resulting in the decrease of relative humidity inside the RAD7 chamber down to 6/7%.

The RAD7 internal pump operated automatically for the first 5 minutes of the Wat-40 analysis, aerating the sample and distributing the radon that was in the water throughout the loop. During, the aeration, the dissolved ^{222}Rn was stripped from the water forming a separate gaseous phase. After that, the RAD7 waited for a further 5-min to allow the establishment of the ^{218}Po - ^{222}Rn equilibrium, and then, it counted for four 5-min cycles. The radon concentration in the water was directly calculated by considering the cumulative spectrum over the four 5-min cycles (RAD H₂O Manual). Measurements were carried out following the operative procedure MET-37 of the Italian Institute for the Environmental Protection and Research (ISPRA, 2015).

According to Caridi et al. (2016) and Caridi and Belmusto (2018), radon emanometry measurements with RAD7 + RAD H₂O setup provide reliable results, which are in good agreement with those obtained with other techniques such as LCS and high-resolution gamma-ray spectrometry.

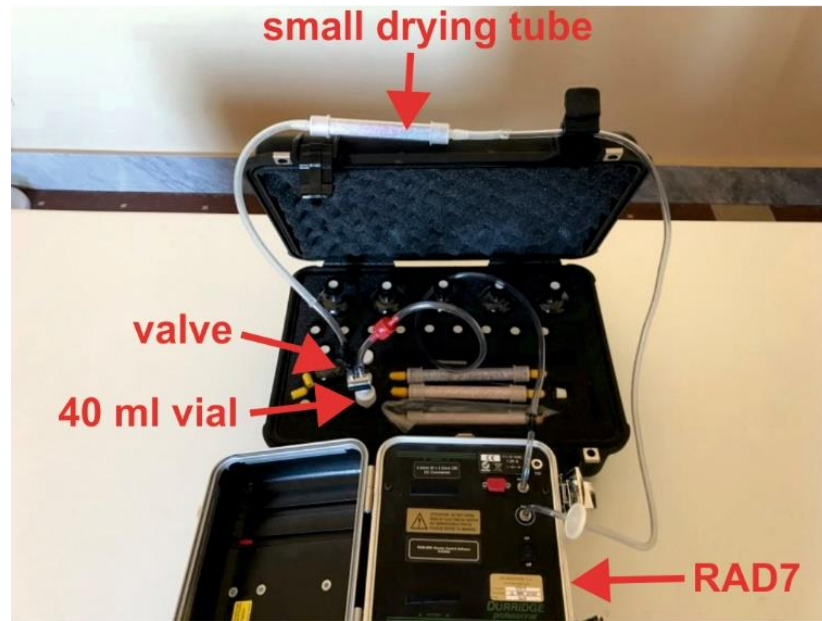


Figure 55. The RAD7 + RAD H₂O setup.

Since the exponential decay leads to the decreasing of the number of ²²²Rn atoms in water (equation 3; Chapter II), the corrected radon concentration was obtained by multiplying the value determined by emanometry for a decay correction factor (DCF), which depends on the amount of time elapsed from the sampling activity to the analysis (Table 19). All the collected samples were analysed within 48 hours from the time of sampling, in order to avoid the correction for ²²⁶Ra (Papastefanou, 2002). Uncertainties of radon measurements performed by the RAD7 spectrometer are expressed as 2σ (see Section 5.4.1.2). Moreover, two aliquots of groundwater were collected for each site and the ²²²Rn concentration resulted from the mean average of the two measures. The uncertainty (*M*) was calculated according to the propagation of error theory as follows:

$$M = \sqrt{(m_1^2 + m_2^2 + \dots + m_N^2)/N^2} \quad [50]$$

where *m* is the uncertainty of the single measurement and *N* is the number of measurements.

6.2.4 Dosimetry

The total annual effective dose due to ingestion of ²²²Rn in groundwater samples (*H_{ing}*), expressed in μSv y⁻¹, was calculated taking into account the activity concentration of

dissolved ^{222}Rn in water (CRn_w in Bq L^{-1}) and the dose conversion factor of radon according to the following equation (Caridi et al 2016; Caridi and Belmusto 2018):

$$H_{ing} = DCF_{ing} \cdot CRn_w \cdot I_w \cdot 365 \quad [51]$$

where DCF_{ing} is the conversion factor of ^{222}Rn in water samples by adults ($3,5 \times 10^{-9} \text{Sv Bq}^{-1}$) whereas I_w is the daily water consumption rate (2 l d^{-1} according to WHO, 2004).

Table 19. Decay correction factors (RAD H₂O Manual).

| hours | DCF | hours | DCF | hours | DCF | hours | DCF |
|-------|-------|-------|-------|-------|-------|-------|-------|
| 1 | 1.008 | 2 | 1.015 | 3 | 1.023 | 4 | 1.031 |
| 5 | 1.038 | 6 | 1.046 | 7 | 1.054 | 8 | 1.062 |
| 9 | 1.070 | 10 | 1.078 | 11 | 1.087 | 12 | 1.95 |
| 13 | 1.103 | 14 | 1.112 | 15 | 1.120 | 16 | 1.128 |
| 17 | 1.137 | 18 | 1.146 | 19 | 1.154 | 20 | 1.163 |
| 21 | 1.172 | 22 | 1.181 | 23 | 1.190 | 24 | 1.199 |
| 25 | 1.208 | 26 | 1.217 | 27 | 1.226 | 28 | 1.236 |
| 29 | 1.234 | 30 | 1.254 | 31 | 1.264 | 32 | 1.273 |
| 33 | 1.283 | 34 | 1.293 | 35 | 1.303 | 36 | 1.312 |
| 37 | 1.322 | 38 | 1.332 | 39 | 1.343 | 40 | 1.353 |
| 41 | 1.363 | 42 | 1.373 | 43 | 1.384 | 44 | 1.394 |
| 45 | 1.405 | 46 | 1.415 | 47 | 1.426 | 48 | 1.437 |

6.3 Results and Discussion

6.3.1 Distribution of ^{222}Rn dissolved in groundwaters

^{222}Rn concentrations measured in water samples are listed in Table 20 together with temperature, pH, electrical conductivity and the annual effective dose due to ingestion. Experimental measurement spectra are reported in Appendix 2. In table 21 are reported the statistical parameters of dissolved radon concentrations.

^{222}Rn activity concentration ranges between (1.6 ± 1.1) Bq L^{-1} in site #12 and (57.5 ± 5.3) Bq L^{-1} in site #17. Median, average value and standard deviation result to be 21.5, 22.1 and 11.3 Bq L^{-1} , respectively. The electrical conductivity of water samples is in the range of 0.483-1.409 mS cm^{-1} whereas the pH varies from ~6 to ~8.5.

It is noteworthy to remark that radon levels in groundwater mostly depend on hydrogeological, mechanical and mineralogical features of the hosting rocks. For instance, great relevance is ascribed to grain size, fracturing degree and U and Th

content. Grain size and fracturing usually control the depth and time of residence of groundwater within the rocks.

Positive radon anomalies can be related to Rn input due to the uprising of deep originated gases across the upper crust of the Earth, whereas negative radon anomalies occur where groundwaters are in contact with the atmosphere and radon transfers from water to the air.

Regarding the hydrogeography of northeastern Sicily, the close proximity of the Peloritani reliefs to the coastline produces an articulate hydrogeological architecture evidencing a strong interaction between surface and underground waters.

The main parameters affecting groundwater circulation are geology (i.e. lithological features) and tectonic lineaments (Coltro et al 1980; Ferrara 1987; Barbagallo et al., 1993). Aquifers in the high-grade metamorphic rocks of the Aspromonte Unit (see Chapter III) rely on fractures to contain and move groundwater. Local alteration phenomena affecting crystalline rocks are capable of increasing the permeability. Concerning the alluvial plain of Milazzo and Barcellona, the high porosity and permeability of alluvial sediments account for the development of wide and large aquifers. For this reason, the main volume of groundwater intended for human consumption and agricultural activities is currently extracted from alluvial sediments. In addition, it is clear that tectonic faults and joints provoke increases in permeability due to the mechanic fracturing of rocks within fault zones and their surroundings.

According to Coltro et al. (1980), Ferrara (1987) and Barbagallo et al. (1993), the circulation of groundwaters and surface waters in the Tyrrhenian side of the Peloritani Mountains can be resumed as follows.

The greatest part of the annual precipitation feeding groundwaters occurs at high altitudes along the Peloritani Range. Meteoric water infiltrates into high-grade metamorphic rocks and water-rock interaction at low temperatures leads to chemical exchanges between hosting rocks and water. After that, water is released to surface circulation through a great number of natural springs. Once surface water reaches the alluvial plain, a part of it infiltrates again flowing as subriverbed water feeding alluvial aquifers. The thickness of alluvial sediments in the Milazzo-Barcellona Holocene plain increases northwards, and the maximum value is around 100 m close to the coastline (Ferrara, 1999).

Table 20. List of Temperature (T), pH, electrical conductivity (C) and dissolved ^{222}Rn concentration measured in groundwater samples (n.s.: not sampled; n.m.: not measured.). Annual effective dose due to ingestion (H_{ing}) is also listed. The location and coordinates of sites are shown in Figure 52 and listed in Table 18.

| #Site | T (°C) | C (mS cm ⁻¹) | pH | ^{222}Rn 1 st aliquot (Bq L ⁻¹) | ^{222}Rn 2 nd aliquot (Bq L ⁻¹) | average ^{222}Rn (Bq L ⁻¹) | H_{ing} (μSv y ⁻¹) |
|-------|-----------|-----------------------------|-----|--|--|--|--|
| 1 | 17.3 | 0.718 | 7.8 | 13.2 ± 3.6 | 10.4 ± 3.2 | 11.8 ± 2.4 | 30.1 |
| 2 | 16.3 | 0.686 | 7.8 | 35.2 ± 5.9 | 29.9 ± 5.4 | 32.5 ± 4 | 83.1 |
| 3 | 18 | 0.75 | 7.8 | 23.4 ± 5.1 | 21.2 ± 4.9 | 22.3 ± 3.6 | 57.1 |
| 4 | 17 | 0.75 | 7.8 | 22.7 ± 4.7 | 19.6 ± 4.4 | 21.2 ± 3.2 | 54.1 |
| 5 | 16.7 | 0.71 | 8 | 30.9 ± 5.9 | 35.1 ± 6.3 | 32 ± 4.3 | 84.3 |
| 6 | 16.4 | 0.688 | 8.1 | 36.8 ± 6.5 | 34.9 ± 6.2 | 35.8 ± 4.5 | 91.5 |
| 7 | 22.6 | 0.874 | 7.7 | 30.2 ± 5.4 | 23.2 ± 4.7 | 26.7 ± 3.6 | 68.3 |
| 8 | 18.2 | 0.83 | 7.7 | 29.9 ± 5.3 | 31.8 ± 5.5 | 30.9 ± 3.8 | 78.9 |
| 9 | 18.9 | 1.050 | 7.8 | 30.9 ± 5.4 | 25.5 ± 4.9 | 28.2 ± 3.6 | 72 |
| 10 | 18 | 0.913 | 8 | 27.4 ± 5.6 | 22.6 ± 5.1 | 25 ± 3.8 | 63.9 |
| 11 | 17.6 | 0.831 | 8.1 | 25.9 ± 5.4 | 23.5 ± 5.1 | 24.7 ± 3.7 | 63.2 |
| 12 | 28 | 0.918 | 8.6 | 2.6 ± 1.9 | 0.5 ± 1 | 1.6 ± 1.1 | 4 |
| 13 | 19.5 | 0.879 | 6.9 | 8.8 ± 2.9 | 6.1 ± 2.6 | 7.4 ± 2 | 19 |
| 14 | 20.4 | 0.969 | 8.3 | 22.5 ± 4.7 | 29.5 ± 5.4 | 26 ± 3.6 | 66.4 |
| 15 | 19.3 | 0.96 | 8.3 | 26.8 ± 5.6 | 22.8 ± 5.1 | 24.8 ± 3.8 | 63.3 |
| 16 | 18.3 | 0.83 | 7.8 | 38.9 ± 6.6 | 35.5 ± 6.4 | 37.2 ± 4.6 | 95 |
| 17 | 17.8 | 0.483 | 8.5 | 54.2 ± 7.3 | 60.7 ± 7.7 | 57.5 ± 5.3 | 146.8 |
| 18 | 19 | 1.117 | 8.2 | 29.7 ± 5.8 | 25.9 ± 5.5 | 27.8 ± 4 | 71 |
| 19 | 17 | 0.691 | 8.7 | 28.9 ± 5.3 | 25.6 ± 4.9 | 27.2 ± 3.6 | 69.6 |
| 20 | 19.9 | 0.937 | 7.9 | 10.2 ± 3.2 | n.s. | 10.2 ± 3.2 | 26.1 |
| 21 | 21.7 | 1.063 | 7.9 | 30.2 ± 5.9 | 40.3 ± 6.7 | 35.3 ± 4.5 | 90.1 |
| 22 | 20.7 | 0.737 | 8 | 43.3 ± 7 | 37.1 ± 6.4 | 40.2 ± 4.7 | 102.7 |
| 23 | - | 0.851 | 7.4 | 25.4 ± 5.2 | 19.3 ± 4.6 | 22.4 ± 3.5 | 57.1 |
| 24 | 14.6 | 0.587 | 7.2 | 38.9 ± 6.6 | 31.4 ± 5.8 | 35.2 ± 4.4 | 89.8 |
| 25 | 19.8 | 0.976 | 6.8 | 43.2 ± 6.9 | 43.9 ± 6.9 | 43.6 ± 4.9 | 111.4 |
| 26 | 19.5 | 0.487 | 8.3 | 31.6 ± 5.4 | 31 ± 5.5 | 31.3 ± 3.8 | 80.1 |
| 27 | 17.4 | 0.519 | 8 | 31 ± 5.8 | 32.9 ± 5.9 | 32 ± 4.2 | 81.6 |
| 28 | 16.9 | 0.827 | 7.6 | 45.6 ± 6.9 | 48.4 ± 7.2 | 47 ± 5 | 120 |
| 29 | 16.4 | 0.519 | 7.5 | 17.8 ± 4.4 | 19.2 ± 4.6 | 18.5 ± 3.2 | 47.2 |
| 30 | 16.2 | 0.529 | 7.4 | 22.4 ± 4.9 | 19.4 ± 4.6 | 20.9 ± 3.4 | 53.4 |
| 31 | 17.4 | 0.612 | 7.3 | 23.1 ± 5.1 | 21.3 ± 5 | 22.2 ± 3.6 | 56.7 |
| 32 | 16.8 | 0.616 | 7.3 | 17.9 ± 1.8 | 16.3 ± 1.6 | 17.1 ± 1.2 | 43.7 |
| 33 | 18.9 | 0.661 | 7.2 | 23 ± 2 | 21.4 ± 1.9 | 22.2 ± 1.4 | 56.8 |
| 34 | 19 | 1.203 | 6.4 | 10.3 ± 3 | 8.3 ± 2.7 | 9.23 ± 2.1 | 23.8 |
| 35 | 20 | 1.088 | 6.7 | 14.6 ± 3.7 | 15 ± 3.7 | 14.9 ± 2.6 | 38 |
| 36 | 18.2 | 0.733 | 6.5 | 5.6 ± 2.3 | 3.4 ± 1.8 | 4.5 ± 1.4 | 11.5 |
| 37 | 16.4 | 1.067 | 6.7 | 8.4 ± 2.8 | 9.1 ± 2.9 | 8.8 ± 2 | 22.5 |

| #Site | T (°C) | C (mS cm ⁻¹) | pH | ²²² Rn 1 st aliquot (Bq m ⁻³) | ²²² Rn 2 nd aliquot (Bq m ⁻³) | average ²²² Rn (Bq L ⁻¹) | H _{ing} (μSv y ⁻¹) |
|-------|-----------|-----------------------------|------|--|--|--|--|
| 38 | 15.9 | 0.74 | 6.5 | 24.7 ± 4.9 | 28 ± 5.2 | 26.4 ± 3.6 | 67.4 |
| 39 | 20.6 | 0.737 | 6.7 | 21.2 ± 4.6 | 22.4 ± 4.9 | 21.8 ± 3.4 | 55.7 |
| 40 | 17.3 | 0.668 | 6.6 | 16.3 ± 4.2 | 14.1 ± 3.9 | 15.2 ± 2.9 | 38.9 |
| 41 | 16.3 | 0.506 | 6.6 | 21.2 ± 4.7 | 17.9 ± 4.4 | 19.5 ± 3.2 | 49.9 |
| 42 | 16.3 | 0.59 | 6.4 | 30.2 ± 5.3 | 29.7 ± 5.3 | 29.9 ± 3.7 | 76.5 |
| 43 | 16 | 0.746 | 6.6 | 22.9 ± 4.6 | 20.9 ± 4.4 | 21.9 ± 3.2 | 55.9 |
| 44 | 16.1 | 0.572 | 6.7 | 21.1 ± 4.5 | 20.5 ± 4.4 | 20.8 ± 3.1 | 53.2 |
| 45 | 17.8 | 0.809 | 6.4 | 24.5 ± 4.7 | 25.2 ± 4.7 | 24.8 ± 3.3 | 63.4 |
| 46 | 17.4 | 0.989 | 6.3 | 11.5 ± 3.1 | 12.6 ± 3.4 | 12 ± 2.3 | 30.7 |
| 47 | 18 | 0.836 | 6.6 | 10.2 ± 3.1 | 12.6 ± 3.3 | 11.4 ± 2.3 | 29.1 |
| 48 | 17.2 | 1.409 | 6.3 | 6.9 ± 2.5 | 6.3 ± 2.4 | 6.6 ± 1.7 | 16.8 |
| 49 | 16.7 | 0.536 | 6.5 | 18.5 ± 4 | 18.4 ± 4.1 | 18.4 ± 2.9 | 47.1 |
| 50 | 18 | 0.88 | 6.7 | 11.3 ± 3.2 | 12.6 ± 3.5 | 11.9 ± 2.4 | 30.5 |
| 51 | 17 | 0.915 | 6.6 | 13.5 ± 3.5 | 13 ± 3.4 | 13.2 ± 2.5 | 33.8 |
| 52 | 17 | 0.903 | 6.8 | 57 ± 8 | 54.5 ± 7.8 | 55.8 ± 5.6 | 142.5 |
| 53 | 16 | 1.168 | 6.7 | 15 ± 3 | 18.1 ± 3.9 | 16.6 ± 2.8 | 42.3 |
| 54 | 18 | 0.988 | 6.9 | 4.9 ± 2.3 | 60.9 ± 2.4 | 5.5 ± 1.7 | 14.1 |
| 55 | 18 | 0.888 | 7 | 8.8 ± 3 | 8.1 ± 3 | 8.4 ± 2.1 | 21.5 |
| 56 | 11 | 0.578 | n.m. | 11.3 ± 3.2 | 11.3 ± 3.2 | 11.3 ± 2.3 | 28.9 |
| 57 | 12 | 0.778 | n.m. | 21.4 ± 4. | 20.2 ± 4.2 | 20.8 ± 3.1 | 53.1 |
| 58 | 11.2 | 0.259 | n.m. | 22.8 ± 4.9 | 26.2 ± 5.2 | 24.5 ± 3.6 | 62.6 |
| 59 | 12.1 | 0.151 | n.m. | 15.9 ± 4.1 | 15.3 ± 4 | 15.6 ± 2.9 | 40 |
| 60 | 16.3 | 0.809 | 7.5 | 26.9 ± 5 | 24.7 ± 4.7 | 25.8 ± 3.4 | 65.9 |
| 61 | 15.8 | 0.717 | 7.5 | 28.1 ± 5.4 | 29.1 ± 5.6 | 28.6 ± 3.9 | 73.1 |
| 62 | 18.2 | 0.981 | 7.4 | 21.9 ± 4.9 | 19.1 ± 4.5 | 20.5 ± 3.3 | 52.4 |
| 63 | 18.6 | 1.328 | 6.9 | 15.1 ± 3.9 | 18.3 ± 4.4 | 16.7 ± 3 | 42.6 |
| 64 | 18.2 | 0.815 | 7.7 | 12.3 ± 3.7 | 16.2 ± 4.2 | 14.2 ± 2.8 | 36.3 |
| 65 | 10.7 | 0.545 | 6.7 | 15.7 ± 3.8 | 18.7 ± 4.2 | 17.2 ± 2.8 | 43.9 |
| 66 | 17 | 1.36 | 7.5 | 5.8 ± 2.3 | 6.7 ± 2.4 | 6.3 ± 1.7 | 16 |
| 67 | 18 | 0.712 | 7.3 | 16.9 ± 4.3 | 17.2 ± 4.3 | 17 ± 3 | 43.5 |
| 68 | 15.6 | 0.705 | 7.3 | 15 ± 4 | 16.8 ± 4.3 | 15.9 ± 2.9 | 40.6 |
| 69 | 16.5 | 0.665 | 7.3 | 23.9 ± 5.1 | 24.3 ± 5.1 | 24.1 ± 3.6 | 61.5 |
| 70 | 15.4 | 0.655 | 7.7 | 13.6 ± 3.8 | 10.7 ± 3.3 | 12.2 ± 2.5 | 31.1 |

Table 21. Statistics of dissolved ²²²Rn concentrations in groundwaters (Bq L⁻¹).

| Statistics | N | Min | Lower quartile | Median | Upper quartile | Max | Mean | Standard deviation | Range |
|-------------------|----|-----|----------------|--------|----------------|------|------|--------------------|-------|
| ²²² Rn | 70 | 1.6 | 14.4 | 21.5 | 27.6 | 57.5 | 22.1 | 11.3 | 55.9 |

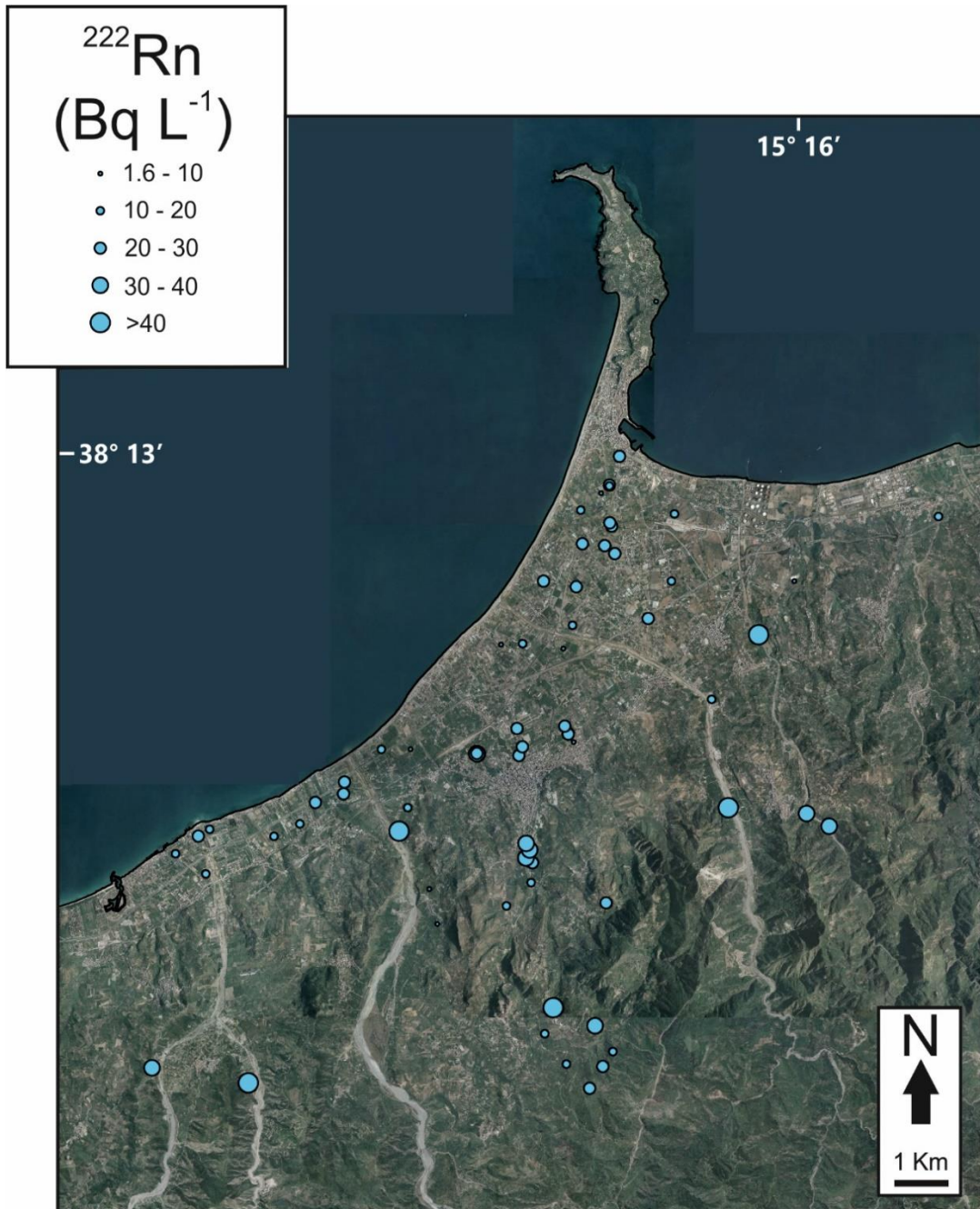


Figure 56. Distribution of ^{222}Rn concentration in wells and natural springs along the Tyrrhenian margin of NE Sicily.

The geographic distribution of groundwater ^{222}Rn activity concentration is shown in Figure 56. Radiological data from wells and springs are poorly correlated with radon and thoron concentrations measured in soils (see Chapter V), suggesting that the dynamic ruling the amount of radioactivity in groundwaters is complicated to decipher.

In order to discriminate ^{222}Rn anomalous values from the background concentration, the graphical technique of normal probability plots (see Chapter V) was tentatively used. Unfortunately, points approximate a linear distribution (not shown), so it was not possible to determine a clear ^{222}Rn anomaly cutoff. Moreover, dissolved radon and other measured parameters (temperature, electrical conductivity and pH) are uncorrelated.

Nevertheless, a series of considerations can be made. It emerges that the average ^{222}Rn concentration of water samples collected from the eight natural springs (seven sites located in the mountains and hills around Castoreale and one located in the Milazzo Peninsula) is lower than that calculated from well waters (13.7 vs 23.2 Bq L⁻¹). Reasonably, it might be explained with the fact that water discharged from natural springs interacts with the atmosphere in the shallowest part of the aquifer, losing part of radon (D'Alessandro and Vita, 2003).

The lowest ^{222}Rn content was found in the water sample collected from the well "Petraro 1" (# 12). Since the temperature of the sample (28°C) is considerably higher in comparison to that measured in other sites, probably the groundwater collected from the well "Petraro 1" has spent an unknown amount of time in a surface container where radon decayed and temperature increased.

Surprisingly, no radon-rich water was detected in sites located close to the thermal area of Terme Vigliatore, where warm CO₂-rich waters occur together with gas discharge vents (Italiano et al., 2019). Probably, if a free gas phase is present, radon can be easily stripped out, lowering the pristine Rn activity concentration (D'Alessandro and Vita, 2003).

Generally, if we consider groundwaters derived only from wells, it seems clear that the ^{222}Rn activity concentration results lower in the sector occupied by the Milazzo-Barcellona alluvial plain and higher in groundwater sampled along fluvial valleys and in the crystalline hilly reliefs. Different hypotheses can be invoked to explain the phenomenon. It could be related to a geological "effect", as hydraulic properties are different between clastic alluvial deposits and fractured high-grade metamorphites, or because alluvial aquifers are affected by intense mixing processes involving subriverbed waters that formerly experienced radon-loss due to interaction with the atmosphere. In addition, the alluvial and hilly sectors are inevitably characterized by

Table 22. Comparison among the ^{222}Rn activity concentration in groundwaters (Bq L^{-1}) of northeastern Sicily and that measured in Southern Italy and other parts of the World (data from: ^aCaridi and Belmusto, 2021; ^bPizzino et al., 2004; ^cD'Alessandro and Vita, 2003; ^dInguaggiato et al., 2000; ^eDongarrà et al., 1995; ^fPereira et al., 2015; ^gTrautmannsheime et al., 2002; ^hRavikumar and Somashekar, 2014; ⁱCorrea et al., 2014; ^lDarko et al., 2010).

| Location | Min | Max | Mean | Geology |
|---|------|-------|------|--------------------------|
| NE Sicily (this work) | 1.6 | 57.5 | 22.1 | crystalline and alluvial |
| Southern Calabria (Southern Italy) ^a | 1.6 | 94 | 24.4 | crystalline and alluvial |
| Southern Calabria (Southern Italy) ^b | <1 | 180 | - | crystalline and alluvial |
| Etna (Southern Italy) ^c | 1.8 | 52.7 | 11.8 | volcanic |
| Ischia (Southern Italy) ^d | 26 | 249 | 89.2 | volcanic |
| Western Sicily (Southern Italy) ^e | 0.1 | 50.7 | 4.6 | carbonate |
| Nisa (Portugal) ^f | 17 | 3856 | 934 | crystalline |
| Ciudad Rodrigo (Spain) ^f | 1.4 | 1609 | 381 | crystalline |
| Bavaria (Germany) ^g | - | 1220 | - | crystalline |
| Sankey tank (India) ^h | 7.2 | 11.43 | - | crystalline |
| Malathahalli (India) ^h | 11.7 | 381.2 | - | crystalline |
| Curitiba (Brazil) ⁱ | 1.6 | 215 | - | crystalline |
| Greater Accra (Ghana) ^l | 2.15 | 28.7 | 8.1 | crystalline |

a different residence time of water in the hosting rocks, which lead to different amounts of radon transferred from rocks to groundwaters due to water-rock interaction.

6.3.2 Comparison of radon levels measured in the Peloritani groundwaters with other areas

The ^{222}Rn concentration measured in groundwaters of NE Sicily was compared with data obtained for other areas (Table 22).

Concerning Italy, dissolved radon concentrations determined in groundwaters of Southern Calabria (Aspromonte and Serre Massifs) by Pizzino et al. (2004) and Caridi and Belmusto (2021) are almost identical to those observed in the Peloritani Mountains. This feature was predictable since the two areas show similar lithological and geophysical characters.

Contrastingly, volcanic areas exhibit distinct behaviours. For instance, ^{222}Rn concentrations measured around the Mount Etna edifice (D'Alessandro and Vita,

2003) are comparable to those characterizing NE Sicily, whereas measurements carried out in the Island of Ischia displayed higher Rn concentrations (Inguaggiato et al., 2000). Moreover, aquifers in carbonate rocks usually show low Rn concentrations (e.g. Dongarrà et al., 1995 for limestones and dolostones of Western Sicily).

As regards other countries, several data are available in literature for radon contents in crystalline-rock aquifers.

Very high values were detected in some areas of Germany, Spain and Portugal (Trautmannsheime et al., 2002 and Pereira et al., 2015) where Variscan metamorphites and granites represent the dominant lithology. Radon concentration values measured in groundwater circulating within the coeval crystalline rocks of the Calabrian Arc (Pizzino et al., 2004; Caridi and Belmusto, 2021; this work) deviate from the typical signature of European Variscan rocks. This discrepancy could be related to the higher degree of tectonization showed by Variscan rocks outcropping in southern Italy since they were widely involved in the Alpine Orogeny as opposed to those occurring in central Iberia and in central Europe. This assumption relies on the fact that intense tectonization and fracturing usually intensify water-rock interaction processes culminating in an enhanced radon exchange between rock and water phases. In addition, the rainfall behaviour in major islands located within the Mediterranean Sea is rather different from that affecting the rest of Europe. Probably, precipitations play an important role in the physical processes governing radon dilution and/or enrichment in groundwater.

On the other hand, aquifers in granites of India (Ravikumar and Somashekar, 2014) and in ancient crystalline rocks of Brazil (Correa et al., 2014) and Ghana (Darko et al., 2010) show similar or slightly higher levels of dissolved ^{222}Rn in comparison to those measured in this study.

6.3.3 Radiological Hazard

The use of domestic (i.e. tap) water derived from local aquifers as drinking water is common around the world. Radionuclides in domestic water produce internal exposure when water is ingested, inhaled or used as part of the food chain (Duenas et al., 1999). The latter contribution is often neglected, whereas the effect of domestic water on radon inhalation is usually considered as part of the more general framework of indoor

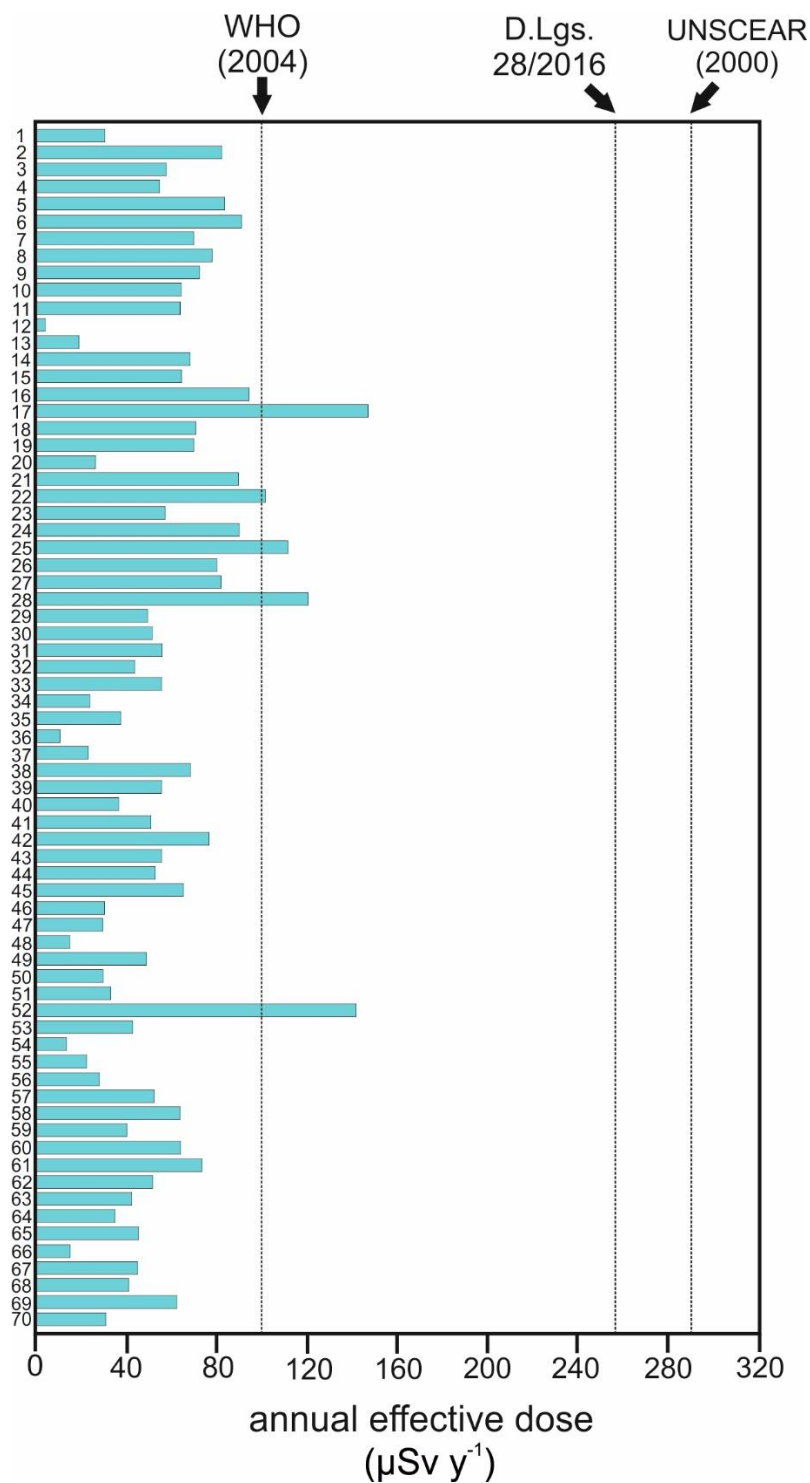


Figure 57. Annual effective doses induced to adults living in the studied area by ingestion of ²²²Rn in groundwater. The calculated doses are compared with the reference value of 100 μSv y⁻¹ set by WHO (2004), with the dose value corresponding to the reference parameter of 100 Bq L⁻¹ adopted by the Italian legislation (legislative decree no. 28/2016) and with the average worldwide value of 290 μSv y⁻¹ due to ingestion of radionuclides in food and drinking water (UNSCEAR, 2000).

radon concentration exposure (UNSCEAR, 2000). Therefore, only the radiological impact generated by the intake of radon by ingestion will be treated here.

In table 20 are listed the annual effective doses induced by ingestion (H_{ing}) of domestic water by an individual adult living in the studied area. H_{ing} values, calculated with equation 51, vary from 4 to 146.8 $\mu\text{Sv y}^{-1}$.

As depicted in Figure 57, the calculated annual effective doses were compared with the following reference levels: i) 100 $\mu\text{Sv y}^{-1}$, which is the recommended effective dose level due to intake of radionuclides in drinking water proposed by the World Health Organization (WHO, 2004); ii) 255 $\mu\text{Sv y}^{-1}$, which is the effective dose value corresponding to the recommended level of 100 Bq L^{-1} set by the Council Directive 2013/51/Euratom and by the Italian legislation (legislative decree no. 28/2016); iii) 290 $\mu\text{Sv y}^{-1}$, which, according to UNSCEAR (2000), is the average worldwide dose received by people due to ingestion of radioisotopes contained in food and drinking water.

All the annual effective doses calculated for groundwaters from northeastern Sicily are lower than the average worldwide value. Moreover, they do not exceed the dose value corresponding to the concentration limit of 100 Bq L^{-1} set by the Italian legislation and by the 2013/51/Euratom Directive.

However, five samples (sites # 17, 22, 25, 28, 52) induce effective doses higher than the recommended limit of 100 $\mu\text{Sv y}^{-1}$ set by the World Health Organization guidance level for radionuclides in drinking water (WHO, 2004). Despite this fact, WHO (2004) pointed out that drinking water exceeding the limit of 100 $\mu\text{Sv y}^{-1}$ should not be considered unsuitable for consumption, even if further investigations, including repeated additional sampling, are needed in order to evaluate if a possible radiological health risk really exists.

After these considerations, it can be argued that groundwaters collected in the studied area should be regarded as safe for drinking and other domestic purposes. In addition, it appears that no remedial actions are needed.

From a more general perspective, it can be assumed that the health risk due to radon dissolved in groundwater circulating in the alluvial deposits and crystalline rocks of the Calabrian Arc is probably low. Nevertheless, further analyses are required in order to better constrain the radiological hazard as some samples show annual effective

doses exceeding the reference limit of $100 \mu\text{Sv y}^{-1}$ set by the World Health Organization.

6.4 Concluding remarks

In this Chapter, it was evaluated the activity concentration of ^{222}Rn dissolved in groundwaters from northeastern Sicily.

Results show that groundwater ^{222}Rn levels are similar to those determined in Southern Calabria by previous studies. On the other hand, radon concentrations measured in aquifers located within Variscan crystalline rocks of Central Europe and the Iberian Peninsula are systematically higher.

The ^{222}Rn activity concentration was preferentially higher in samples collected along fluvial valleys and in the crystalline hilly reliefs, whereas groundwater sampled in the Milazzo-Barcellona alluvial plain exhibits lower values. This dissimilarity is presumably related to the different mechano-physical properties characterizing aquifers in alluvial deposits and metamorphites in terms of hydraulic properties, depth and time of residence of water within the hosting rocks and occurrence of mixing phenomena with Rn-degassed waters.

Moreover, the measurement of the ^{222}Rn activity concentration in groundwater allows us to assess the extent of internal exposure doses received by the population due to radiation coming from the consumption of domestic water. All the ^{222}Rn activity concentrations measured in the analysed water are below 100 Bq L^{-1} , which represent the reference limit set by the Italian legislation and by the 2013/51/Euratom Directive. In addition, the annual effective dose induced by ingestion is lower than the worldwide average.

Finally, it can be assumed that groundwaters in northeastern Sicily can be safely used as domestic waters and no remedial actions are needed.

However, ^{222}Rn concentrations measured in water collected directly from the captation point might be different from that resulting in the point of use. Adsorption of radium from old distribution networks could produce an increase of radon, while the transport from wells/springs to dwellings causes a radon reduction due to the radioactive decay. Therefore, I believe that further analyses should be performed on tap water, with the

aim to evaluate the effective radiological hazard affecting people living in the studied area.

References

J. N. Andrews. Radiogenic and inert gases in groundwater. In: Paquet, H., Tardy Y. (Eds.), Proceedings of the Second Symposium on Water–Rock Interaction. Strasbourg: 334–342, 1977.

M. Barbagallo, V. Ferrara and A. Pennisi. Lineamenti idrogeologici e vulnerabilità all'inquinamento degli acquiferi della fascia costiera tirrenica del Messinese (versante settentrionale dei M. Peloritani – Sicilia NE). Atti Congr. ANDIS '93, Palermo - Torre Normanna 21-23 September 1993, 1:17-31, 1993.

F. Caridi, M. D'Agostino, A. Belvedere, S. Marguccio and G. Belmusto. Radon radioactivity in groundwater from the Calabria region, south of Italy. JINST, **11**, Article ID P05012, 2016.

F. Caridi and G. Belmusto. Radon radioactivity measurements in underground water: A comparison between different diagnostics techniques. Cogent Physics **5**, Article ID1480134, 2018.

F. Caridi and G. Belmusto. Assessment of the public effective dose due to the ^{222}Rn radioactivity in drinking water: results from the Calabria region, southern Italy. JINST, **16**, Article ID P02033, 2021.

R. Coltro, V. Ferrara and C. Roda. Relazione tra acque superficiali e falde subalvee nelle fiumare. Atti 4° Conv. Int. Acque sotterranee, Acireale 17-21 February 1980, 3: 211-237, 1980.

J. N. Corrêa, S. A. Paschuk, J. Kappke, A. F. N. Perna, A. C. França, H. R. Schelin and V. Denyak. Measurements of ^{222}Rn activity in well water of the Curitiba metropolitan area (Brazil). Radiation Physics and Chemistry, **104**: 108-111, 2014.

W. D'Alessandro and F. Vita. Groundwater radon measurements in the Mt. Etna area. Journal of Environmental Radioactivity, **65**(2): 187–201, 2003.

O. Darko, O. K. Adukpo, J. J. Fletcher, A. R. Awudu and F. Otoo. Preliminary studies on ^{222}Rn concentration in ground water from selected areas of the Accra metropolis in Ghana. Journal of Radioanalytical and Nuclear Chemistry, **283**(2): 507-512, 2010.

Directive 2013/51/EURATOM. Laying down requirements for the protection of the health of the general public with regard to radioactive substances in water intended for human consumption.

G. Dongarra, S. Hauser, P. Censi and M. Brai. Water chemistry, $\delta^{13}\text{C}$ values and ^{222}Rn activity in groundwaters of western Sicily. *Nuclear Geophysics*, **9**(5): 461-470, 1995

C. Duenas, M. C. Fernandez, J. Carretero, E. Liger and S. Canete. ^{226}Ra and ^{222}Rn concentrations and doses in bottled waters in Spain. *Journal of Environmental Radioactivity*, **45**(3):283–290, 1999.

Durridge Company, RAD7, electronic radon detector user manual (<http://www.durridge.com>).

G. Etiope and G. Martinelli. Migration of carrier and trace gases in the geosphere: an overview. *Physics of the Earth and Planetary Interiors*, **129**(3-4):185-204, 2002.

V. Ferrara. Aspetti connessi alla vulnerabilità degli acquiferi alluvionali nei bacini dei corsi d'acqua minori della Sicilia nord-orientale. *Atti Conv. "I corsi d'acqua minori dell'Italia Appenninica – Aspetti ecologici e gestionali. Aulla 22-24 June 1987, Boll. Mus. St. Nat. Lunigiana*, 1987.

V. Ferrara. Vulnerabilità all'inquinamento degli acquiferi dell'area Peloritana (Sicilia Nord Orientale); Pitagora, GNDICI-CNR n. 1946; Pitagora Editore: Bologna, Italy, 1–119. 1999.

P. Gasparini and C. Veltri. Radon: un precursore dei terremoti? In: Boschi, E., Dragoni, M. (Eds.), *Aree sismogenetiche e rischio sismico in Italia*, Ettore Majorana Centre for Scientific Culture. Istituto Nazionale di Geofisica, Lausanne: 585–609, 1987.

S. Inguaggiato, G. Pecoraino and F. D'Amore. Chemical and isotopical characterisation of fluid manifestations of Ischia Island (Italy). *Journal of Volcanology and Geothermal Research*, **99**(1-4): 151–178, 2000.

Italian Institute for the Environmental Protection and Research. ISPRA (2015). *Manual of the operative procedures for environmental radioactivity measurements*

Italian Legislation, D. Lgs. 28/2016.

F. Italiano, P. Bonfanti and S. R. Maugeri. Evidence of Tectonic Control on the Geochemical Features of the Volatiles Vented along the Nebrodi-Peloritani Mts (Southern Apennine Chain, Italy). *Geofluids*, special Volume, Article ID 6250393, 2019.

A. Nesmeyanov. *Radiochemistry*. Mir Publisher, Moscow: 644, 1974.

C. Papastefanou. An overview of instrumentation for measuring radon in soil gas and groundwaters. *Journal of Environmental Radioactivity*, **63**(3): 271-283, 2002.

A. J. S. C. Pereira, M. D. Pereira, L. J. P. F. Neves, J. M. M. Azevedo and A. B. A. Campos. Evaluation of groundwater quality based on radiological and hydrochemical data from two uraniferous regions of Western Iberia: Nisa (Portugal) and Ciudad Rodrigo (Spain). *Environmental Earth Sciences*, **73**: 2717–2731, 2015.

L. Pizzino, P. Burrato, F. Quattrocchi and G. Valensise. Geochemical signatures of large active faults: The example of the 5 February 1783, Calabrian earthquake (southern Italy). *Journal of Seismology*, **8**: 363–380, 2004.

P. Ravikumar and R.K. Somashekar. Determination of the radiation dose due to radon ingestion and inhalation. *International Journal of Environmental Science and Technology*, **11**(2): 493-508, 2014.

M. Trautmannsheime, W. Schindlmeier and K. Hübel. Radon exposure levels of the staff in the drinking water supply facilities in Bavaria, Germany. *International Congress Series*, **1225**: 81–86, 2002.

UNSCEAR. Report to general assembly of the United Nations Scientific Committee on the effects of atomic radiation. United Nations New York, 2000.

World Health Organization, Guidelines for drinking water quality. Vol 1: Recommendations, third edition, WHO, Geneva Switzerland (2004).

Chapter VII – Summary and conclusions

All of the collected data clearly supports the general conclusion that the portion of northeastern Sicily investigated in this Ph.D. Thesis is an area where the background radiation level is not enhanced by natural factors. Hence, the radiological hazard for the living population appears to be rather low.

In detail, the gamma radiation originating from terrestrial radionuclides occurring in soils and rocks seems not to be harmful. In addition, radon concentrations measured in groundwater are lower than the reference value of 100 Bq L⁻¹ set by the Italian legislation (legislative decree no. 28/2016) as well as effective doses due to ingestion are found to be below the worldwide average. Moreover, radon and gamma radiation released from natural materials when they are used in construction do not provoke health threats.

Concerning radon in soil gases, analyses reveal that the radiological hazard for inhabitants is generally low to moderate. The only exception is a ~NW-SE oriented zone characterized by the presence of diffuse radon anomalies (²²²Rn concentrations up to ~80 kBq m⁻³) where the risk is higher. These anomalies are reasonably generated by the uprising of deep-originated fluid along tectonic lineaments.

Recent works (e.g. Italiano et al., 2019) put in evidence that northeastern Sicily is affected by a regional degassing of CO₂-dominated fluids related to the presence of lithospheric faults. Some geochemical features (e.g. isotopic compositions ³He/⁴He and δ¹³C_{CO2}) suggest that fluids are the result of a mix between crustal and mantle-derived volatiles.

Preliminary soil-CO₂ investigations, carried out where radon anomalies were detected, show that CO₂ levels are compatible with the occurrence of advective fluxes of deep-originated fluids. In this context, carbon dioxide acts as a deep carrier gas for radon.

The “tectonic” nature of those radon anomalies is supported by the trend of the ²²⁰Rn/²²²Rn ratio, which discriminates between a shallow (high ratio) and a deep (low ratio) signature. Accordingly, the lowest ²²⁰Rn/²²²Rn values were determined right within the ~NW-SE oriented degassing zone.

In addition, the anomalous radon concentrations measured in northeastern Sicily are identical to those documented by Iovine et al. (2017) along the active and seismogenic faults occurring in central and northern Calabria.

The widespread degassing is further favoured by the high permeability of the Quaternary sediments cropping out over the Tyrrhenian margin of the Peloritani Mountains.

From a geophysical point of view, the ~NW-SE oriented degassing zone is located within the Barcellona-Milazzo alluvial plain, and it is adjacent to the Vulcano-Milazzo fault zone (VMFZ, Cultrera et al., 2017a,b), a tectonic element belonging to the Aeolian-Tindari-Letojanni System (Fig. 47). The VMFZ is a ~NW-SE trending transtensional lineament situated in the Gulf of Patti and running from the Island of Vulcano to the Tyrrhenian margin of Sicily. In this geodynamic context, the fault segment responsible for the radon degassing probably represents the on-land prolongation of the VMFZ toward the SE.

The tectonic link seems to be validated by an offshore-onshore alignment of historical and recent $M > 3$ earthquakes and by a number of normal/transtensional faults cutting Late Quaternary sediments, which rest in proximity to the VMFZ and its proposed on-land prolongation (Fig. 46, 47, 48).

After those considerations, it is clear that the hypothesis postulated by Italiano et al. (2019) on the genesis of the regional degassing in northeastern Sicily is coherent with the results collected in this work. Mantle volatiles are generated in response to the depressurization of the upper mantle triggered by the fault activity of the Aeolian-Tindari-Letojanni System. Tectonic deformation with normal/transtensional kinematics enhances the vertical permeability, allowing mantle-derived fluids to be driven toward the Earth's surface along faults planes and joints. The high radon concentration detected in soils reflects the fact that during their ascent, mantle volatiles (rich in ^3He) are mixed with crustal-derived fluids (rich in ^4He and radon) presumably produced by thermo-mechanical processes.

The slow strain rate, the presence of historical earthquakes and the low seismicity rate allow defining the potential tectonic element that promotes the radon degassing documented in this Thesis as a “silent” fault segment in the interseismic phase.

Nevertheless, faults at the interseismic stage can effectively stimulate gas migration. According to Muir-Wood and King (1993), Muir-Wood (1994) and Seront et al. (1998), the interseismic period of normal faults is accompanied by joint opening and pore space dilation, resulting in an increase in permeability. On the contrary, the coseismic release is associated with crack closure and a decrease in permeability. As proof, several episodes of radon anomalies related to locked faults have been broadly recorded worldwide, not only in extensional domains, but also in transtensional and strike-slip ones (e.g. King et al., 1993, 1996; Al-Hilal and Abdul-Wahed, 2018; Sun et al., 2017).

It is noteworthy to underline that the collected data reflect the state of the natural degassing taking place at the sampling time. Therefore, data compose an instantaneous portrait that describes only a very short time span. Future events, such as increased seismicity or destructive earthquakes, may strongly modify the degassing rate. Enhancement of vertical permeability along the lithosphere, induced by seismo-tectonic activity, can trigger sudden and unexpected injections of radioactive fluids into the shallow crust and then into the atmosphere, generating a high radiological risk for the living population.

The area investigated for this Ph.D. Thesis covers only a limited portion of the regional domain currently deformed by the Aeolian-Tindari-Letojanni System. Given the fact that a strong relationship exists between radiological hazard and tectonic setting, it is considered appropriate to perform physical-radiological analyses also in the adjacent areas, especially those where high magnitude earthquakes were recorded (e.g. the 1978, $M_w=6.1$ Gulf of Patti and the 1908, $M>7$ Messina and Reggio Calabria).

The original feature of this work was to emphasize the concept of “temporal variation” of radiological parameters (e.g. radon concentration in soils), which in response to tectonic pulses and seismogenic processes it may assume a primary role in human health protection, independently from the associated seismic risk. Moreover, it is obvious that this approach can be applied worldwide, mostly for regions affected by tectonic and seismic activity.

In conclusion, I believe that carrying out a series of indoor radon measurements in dwellings, schools, kindergartens and workplaces as well as deploying a number of

monitoring stations with continuous data recording and transmission in key areas of northeastern Sicily could be very useful.

These tools may represent an important step towards a clever mitigation strategy focused on the radiological hazard due to natural sources, a threat that has often been underestimated until now.

References

M. Al-Hilal and M.K. Abdul-Wahed. Soil gas radon measurements for investigating the actual status of seismic quiescence along the bounding fault of the Ghab pull-apart basin in western Syria. *Geofísica International*, **57**(3):177-187, 2018.

F. Cultrera, G. Barreca, P. Burrato, L. Ferranti, C. Monaco, S. Passaro, F. Pepe and L. Scarfi. Active faulting and continental slope instability in the Gulf of Patti (Tyrrhenian side of NE Sicily, Italy): a field, marine and seismological joint analysis. *Natural Hazards*, **86**:253–272, 2017a.

F. Cultrera, G. Barreca, L. Ferranti, C. Monaco, F. Pepe, S. Passaro, G. Barberi, V. Bruno, P. Burrato, M. Mattia, C. Musumeci and L. Scarfi. Structural architecture and active deformation pattern in the northern sector of the Aeolian-Tindari-Letojanni fault system (SE Tyrrhenian Sea-NE Sicily) from integrated analysis of field, marine geophysical, seismological and geodetic data. *Italian Journal of Geosciences* **136**(3):399-417, 2017b.

C.Y. King, W. Zhang and B.S. King. Radon anomalies on three kinds of faults in California. *Pure and Applied Geophysics*, **141**:111–124 1993.

C.Y. King, B.S. King, W.C. Evans and W. Zhang. Spatial radon anomalies on active faults in California. *Applied Geochemistry* **11**:497-510, 1996.

G. Iovine, I. Guagliardi, C. Bruno, R. Greco, A. Tallarico, G. Falcone, F. Lucà and G. Buttafuoco. Soil-gas radon anomalies in three study areas of central-northern Calabria (southern Italy). *Natural Hazards* **91**:193–219, 2018.

Italian Legislation, D. Lgs. 28/2016.

F. Italiano, P. Bonfanti and S. R. Maugeri. Evidence of Tectonic Control on the Geochemical Features of the volatiles Vented along the Nebrodi-Peloritani Mts (Southern Apennine Chain, Italy). *Geofluids*, special Volume, Article ID 6250393, 2019.

R. Muir Wood. Earthquakes, strain-cycling and the mobilization of fluids. Geological Society, London, Special Publications, **78**:85-98, 1994.

R. Muir Wood and G.C.P. King. Hydrologic signatures of earthquake strain. Journal of Geophysical Research, **98**:22035-22068, 1993.

B. Seront, T.F. Wong, J.S. Caine, C.B. Forster and R.L. Bruhn. Laboratory characterisation of hydromechanical properties of a seismogenic fault system. Journal of Structural Geology, **20**:865-881, 1998.

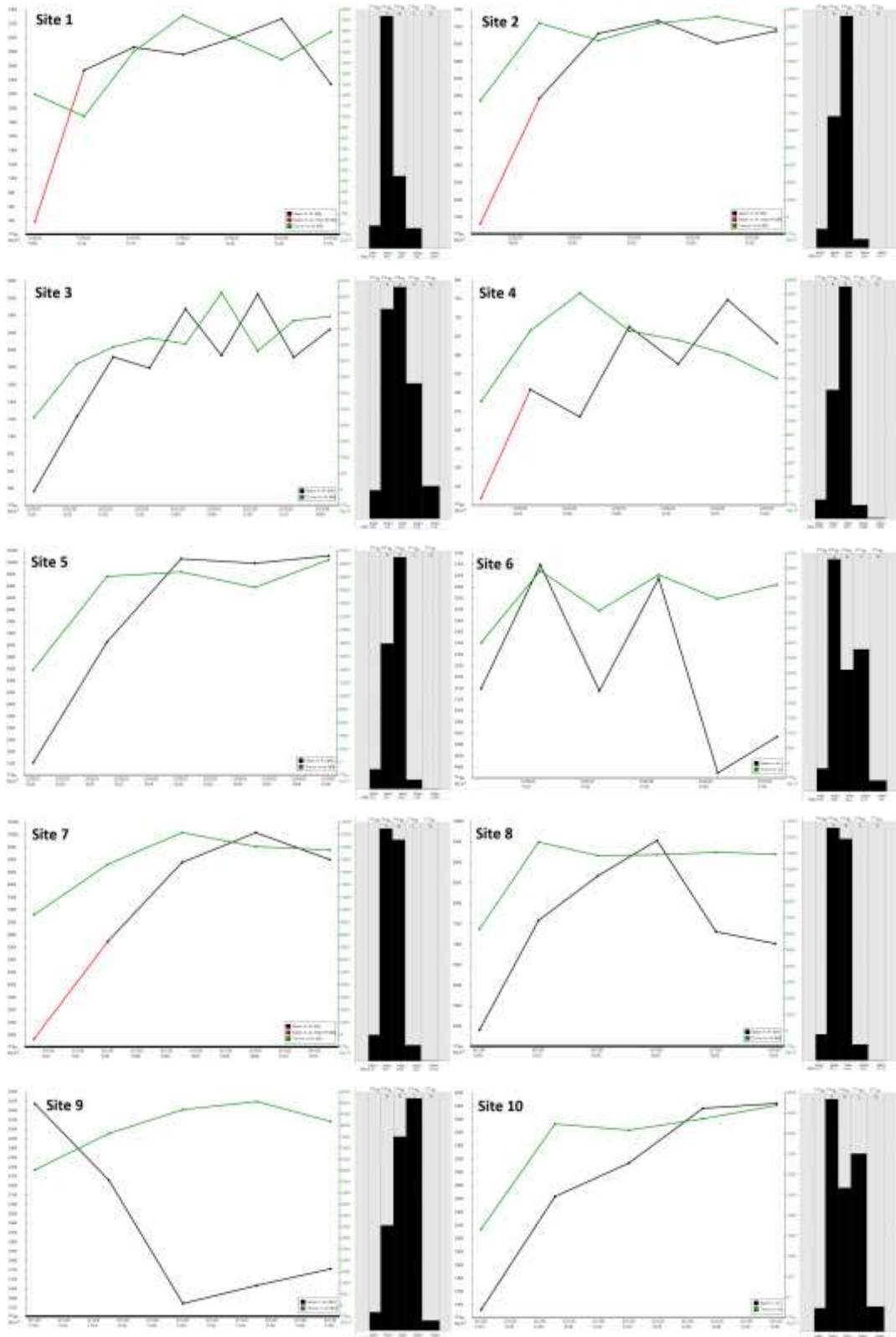
Y. Sun, X. Zhou, G. Zheng, J. Li, H. Shi, Z. Guo and J. Du. Carbon monoxide degassing from seismic fault zones in the Basin and Range province, west of Beijing, China. Journal of Asian Earth Sciences, **149**:41-48, 2017.

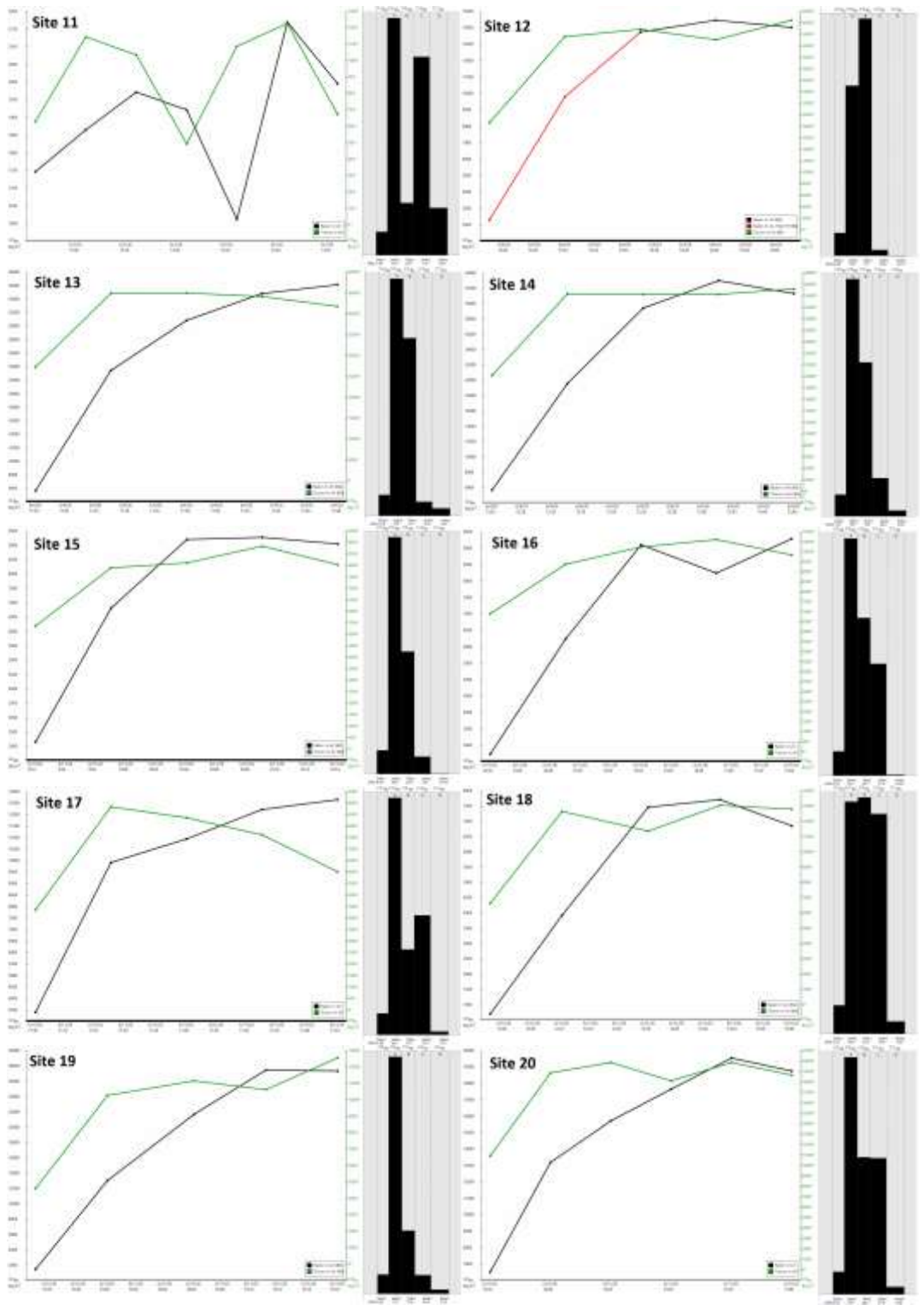
Acknowledgements

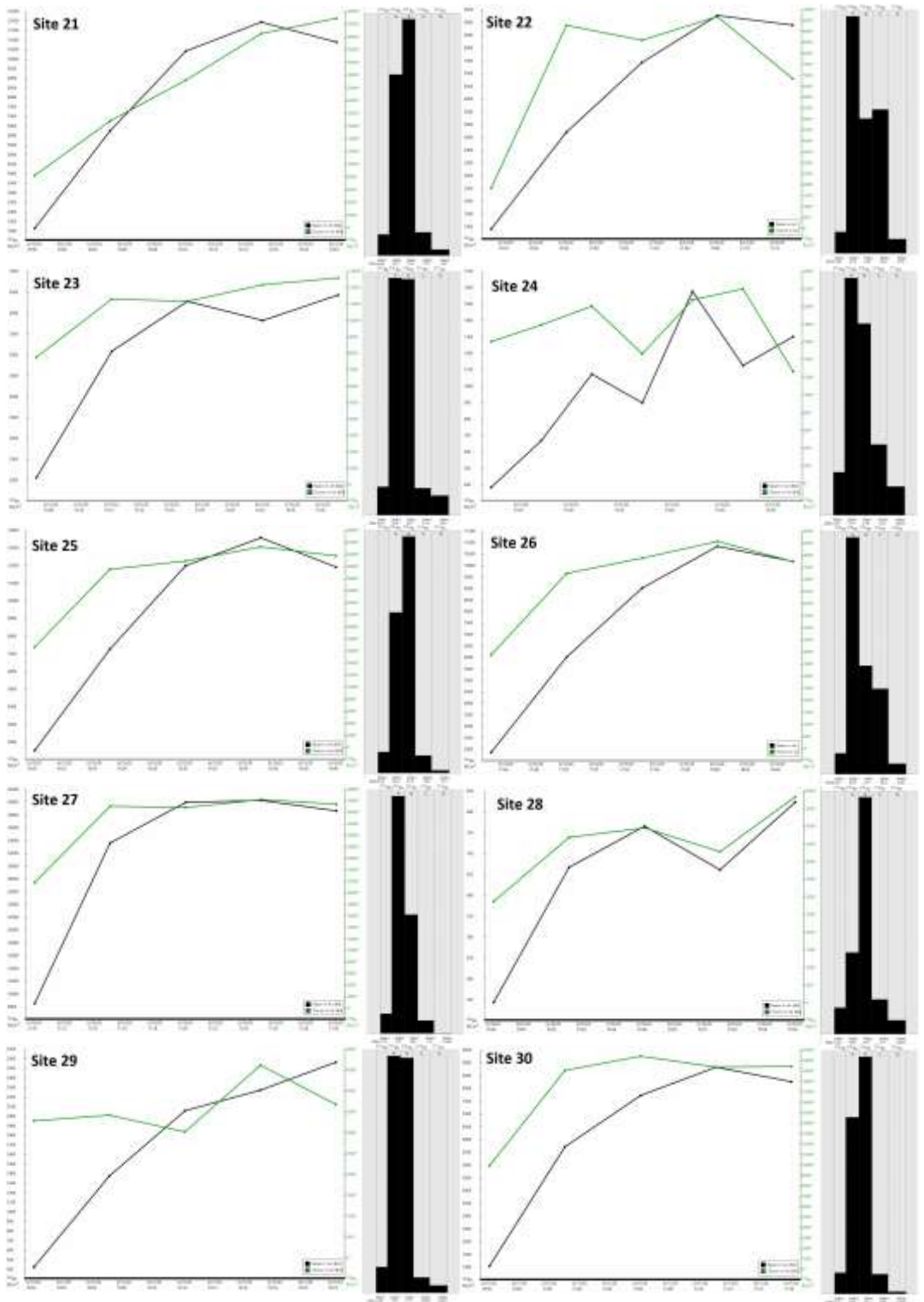
First and foremost I want to underline that this Thesis was funded by the FSE (Fondo Sociale Europeo) operational program (OP) for Sicily 2014-2020.

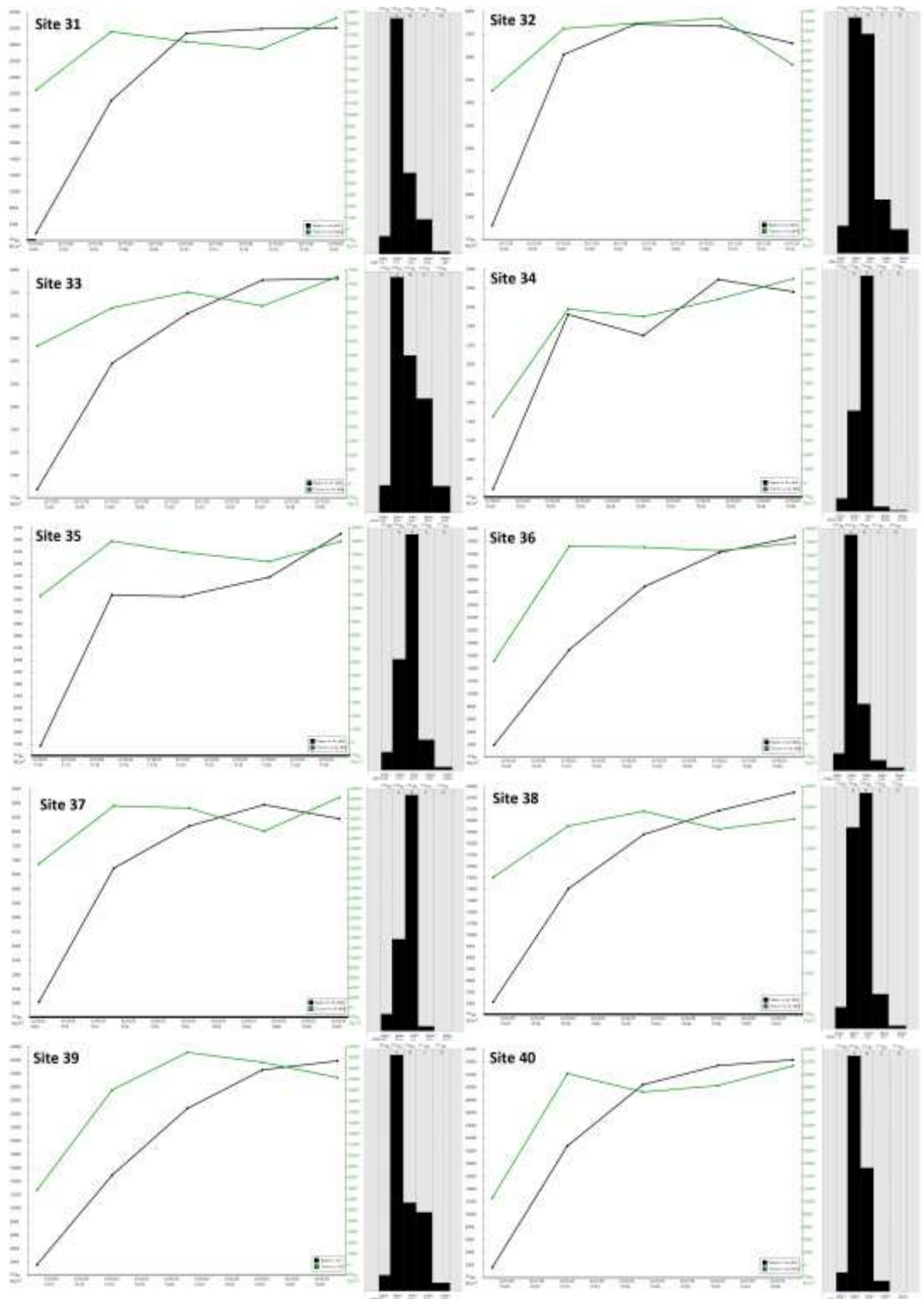
Moreover, I wish to thank: i) Brigitte Di Salvo, Carmelo Allegra, Marco Fiumara, Davide Calabrò, Gianluca Lazzaro, Giuseppe Nania, Andrea Maio, Daniele Torre and Antonio Torre for their support during the fieldwork; ii) Marcella Di Bella, Francesco Caridi, Janja Vaupotic, Maria Teresa Caccamo, Alessandro Tripodo, Alessandro Gattuso and Fabrizio Cultrera for their precious suggestion that improved the quality of the Thesis; iii) all the owners of the sampled wells as well as those of the land fields where soil measurements were performed; iv) the technical staffs of the Milazzo and Barcellona municipalities for their assistance and help.

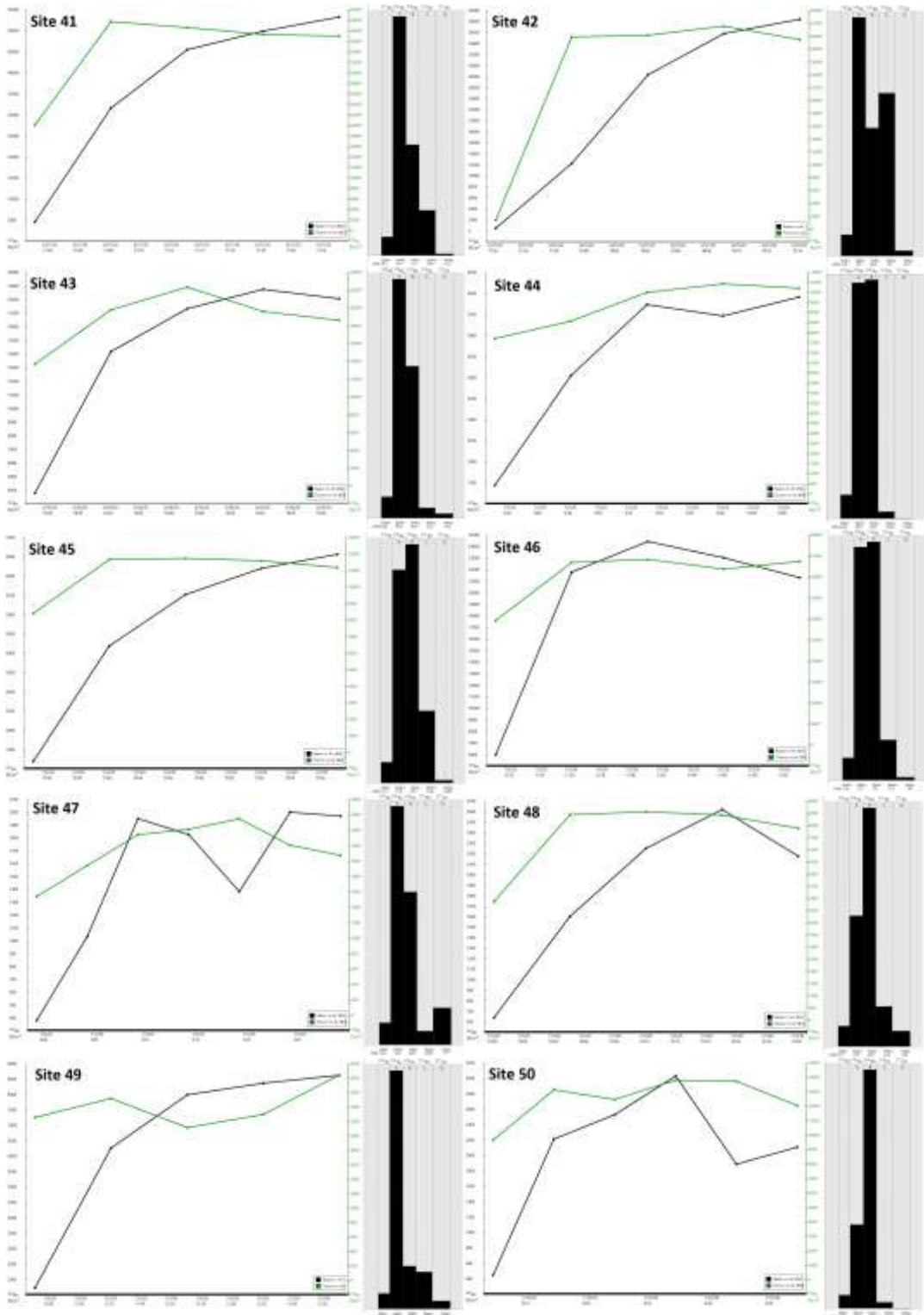
Appendix 1 - Soil-Rn spectra

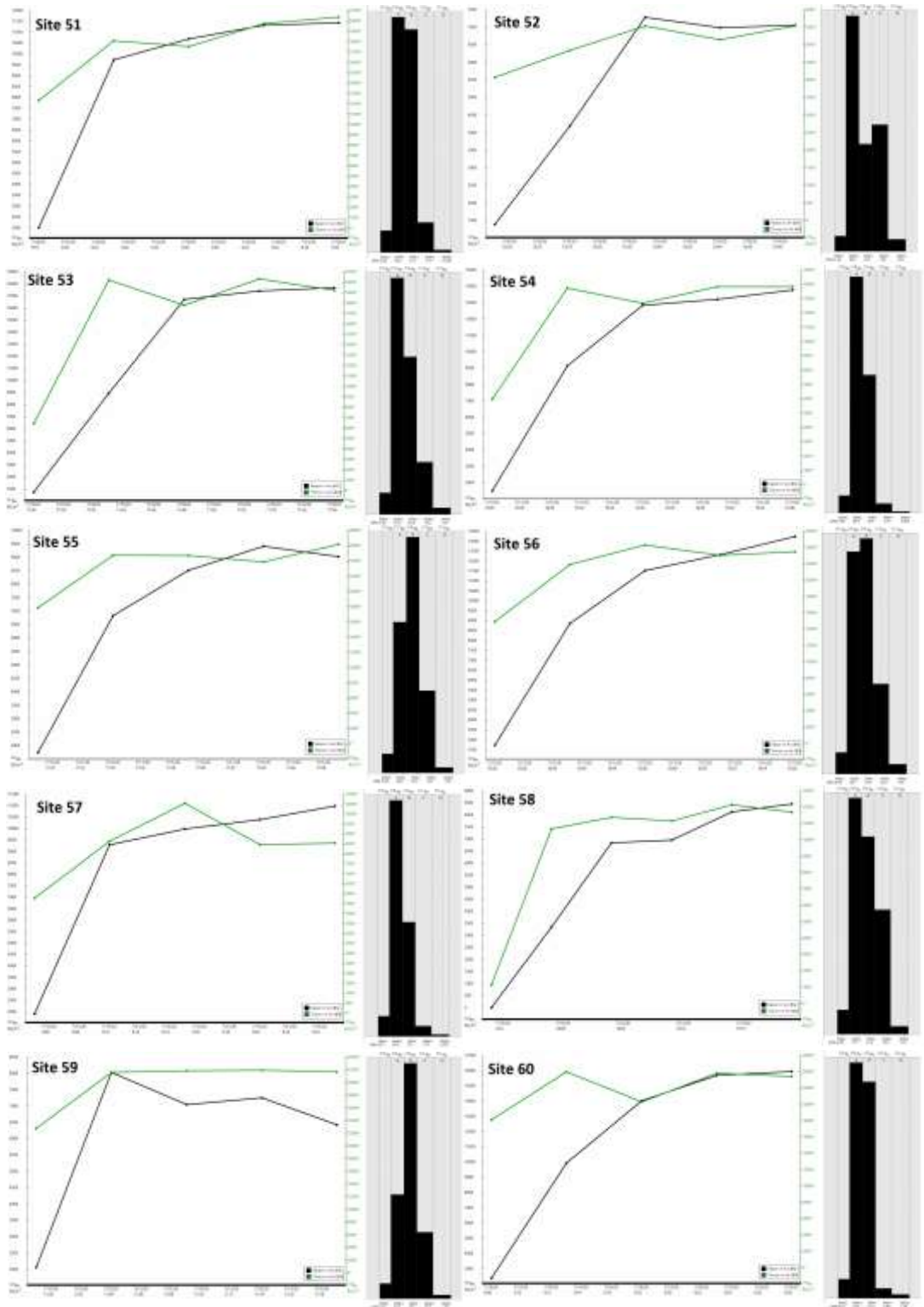


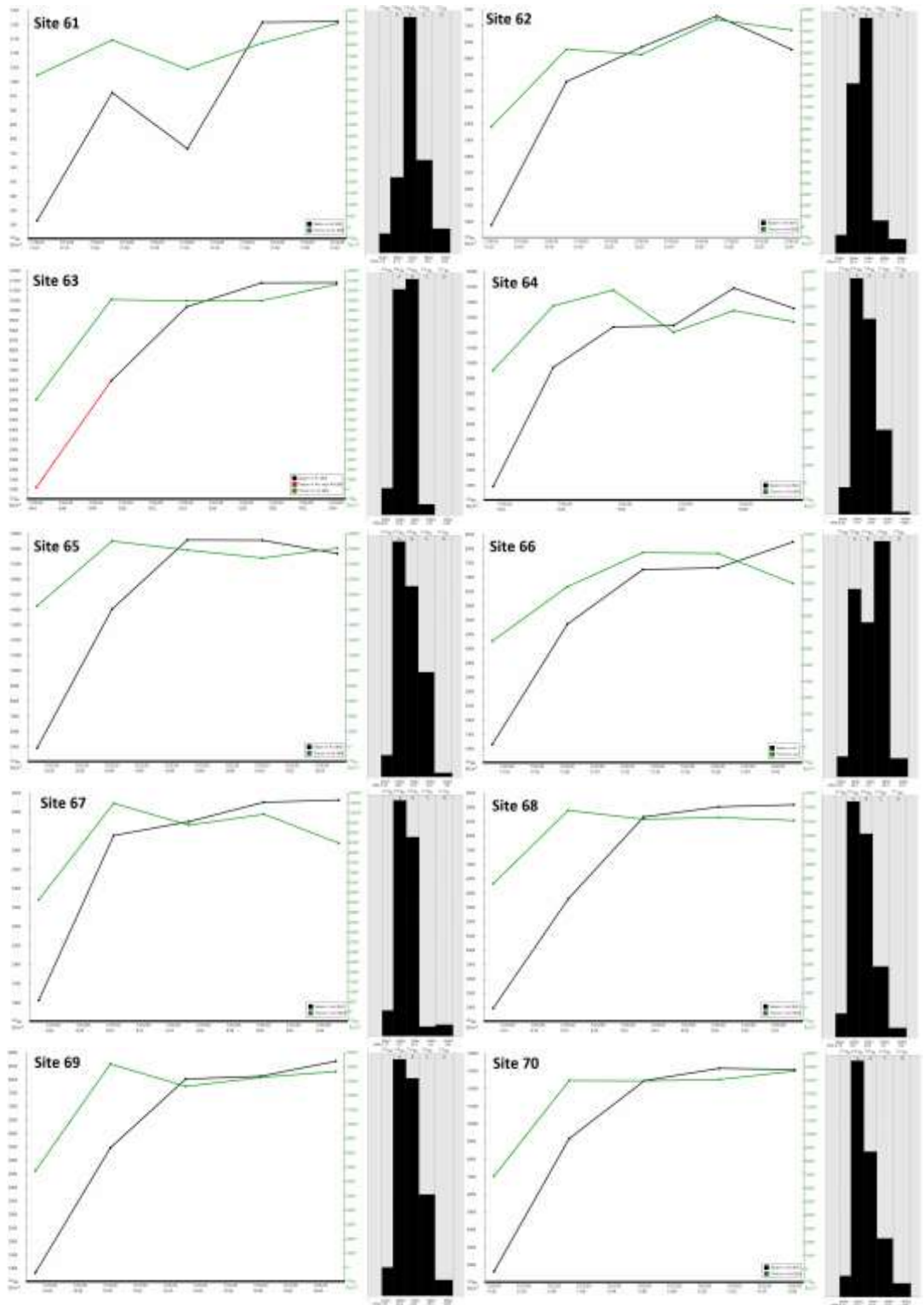


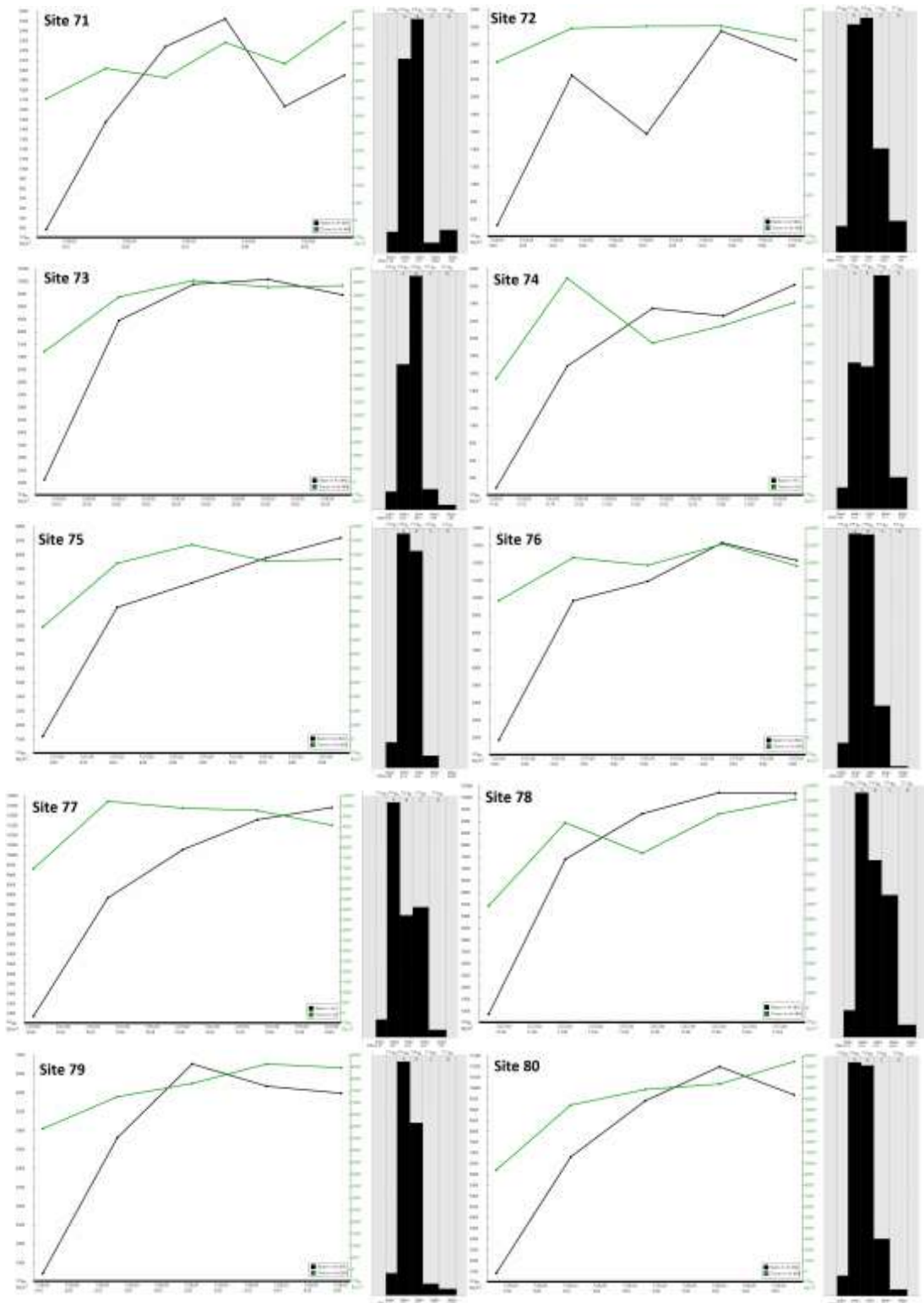


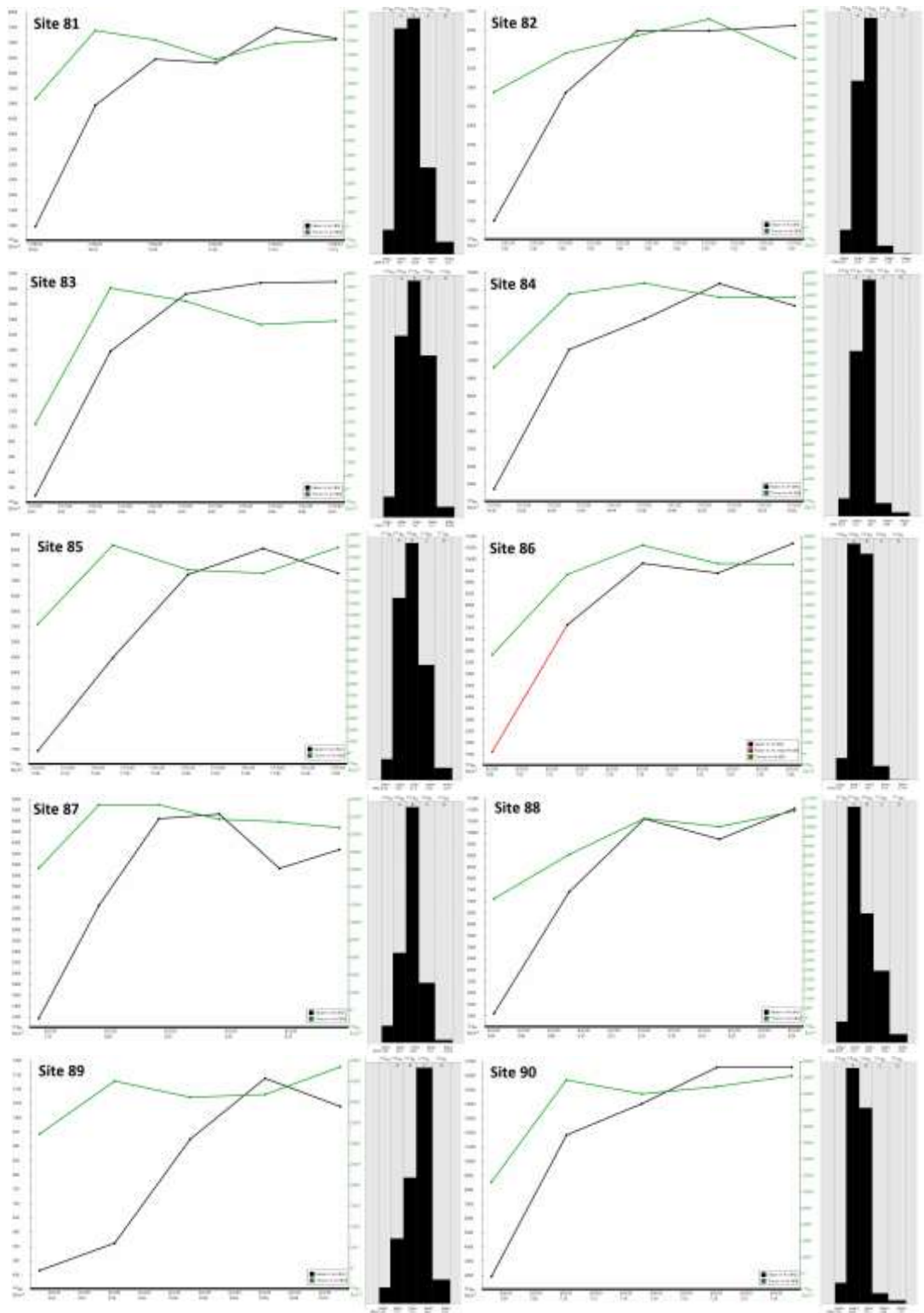


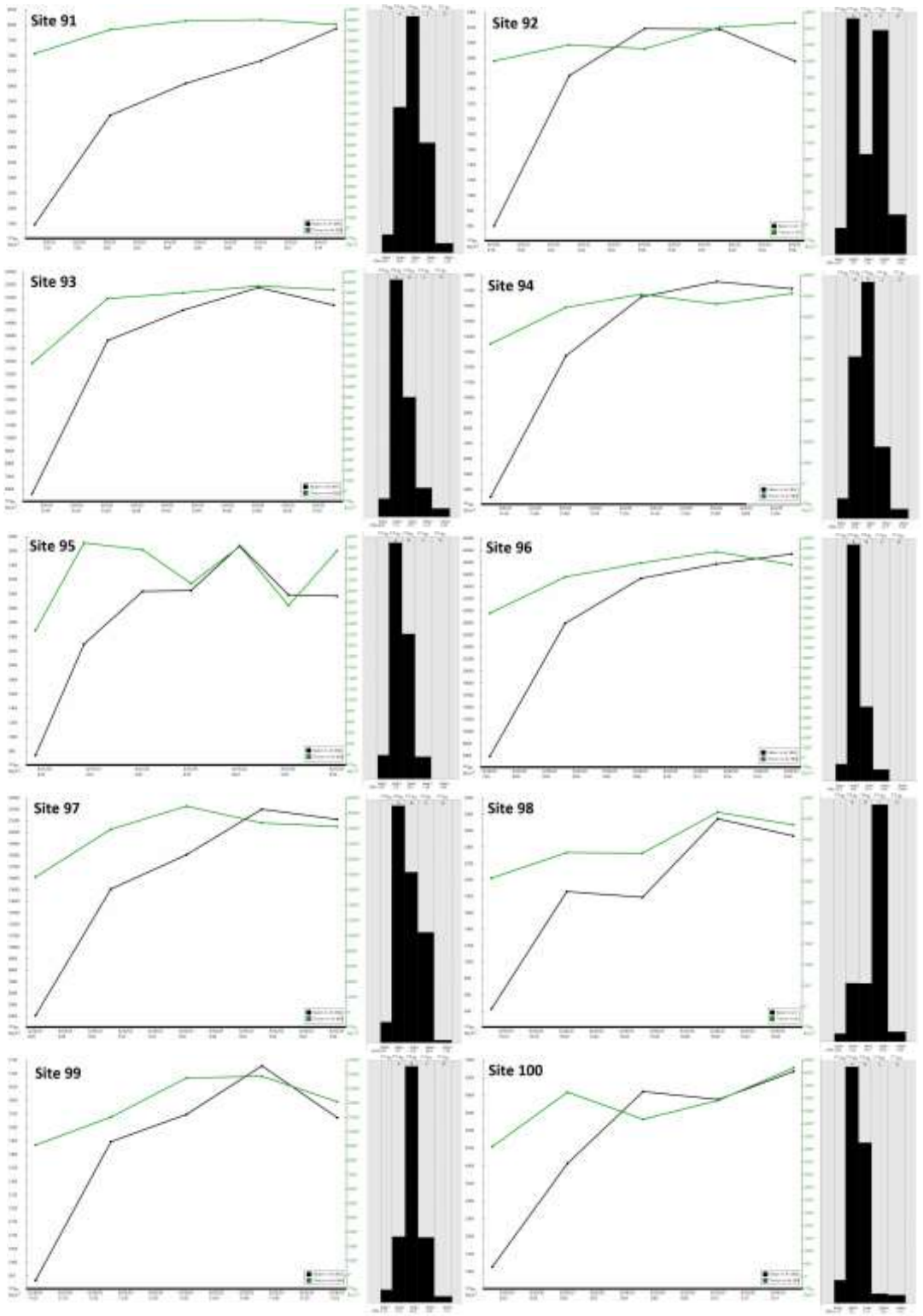


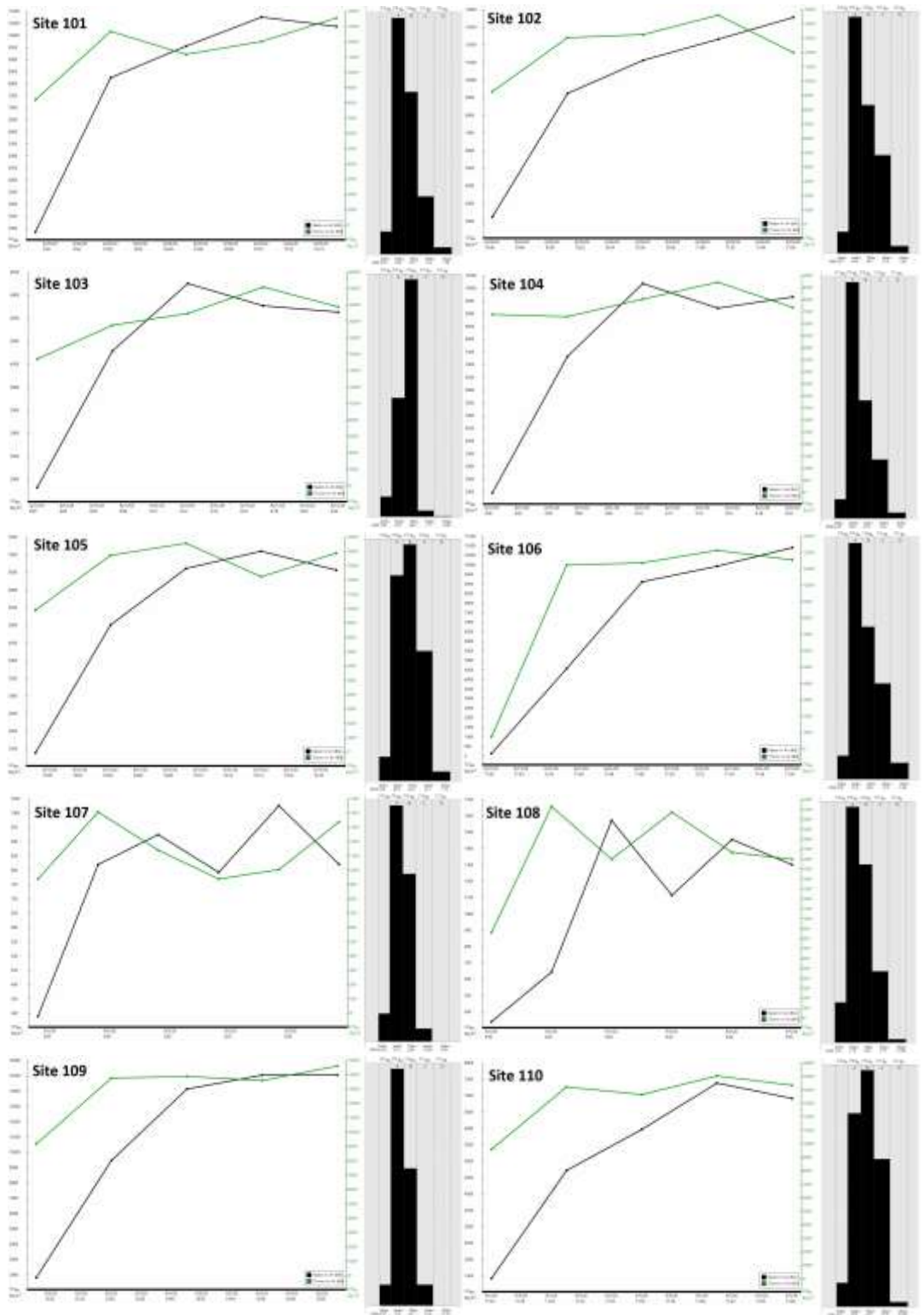


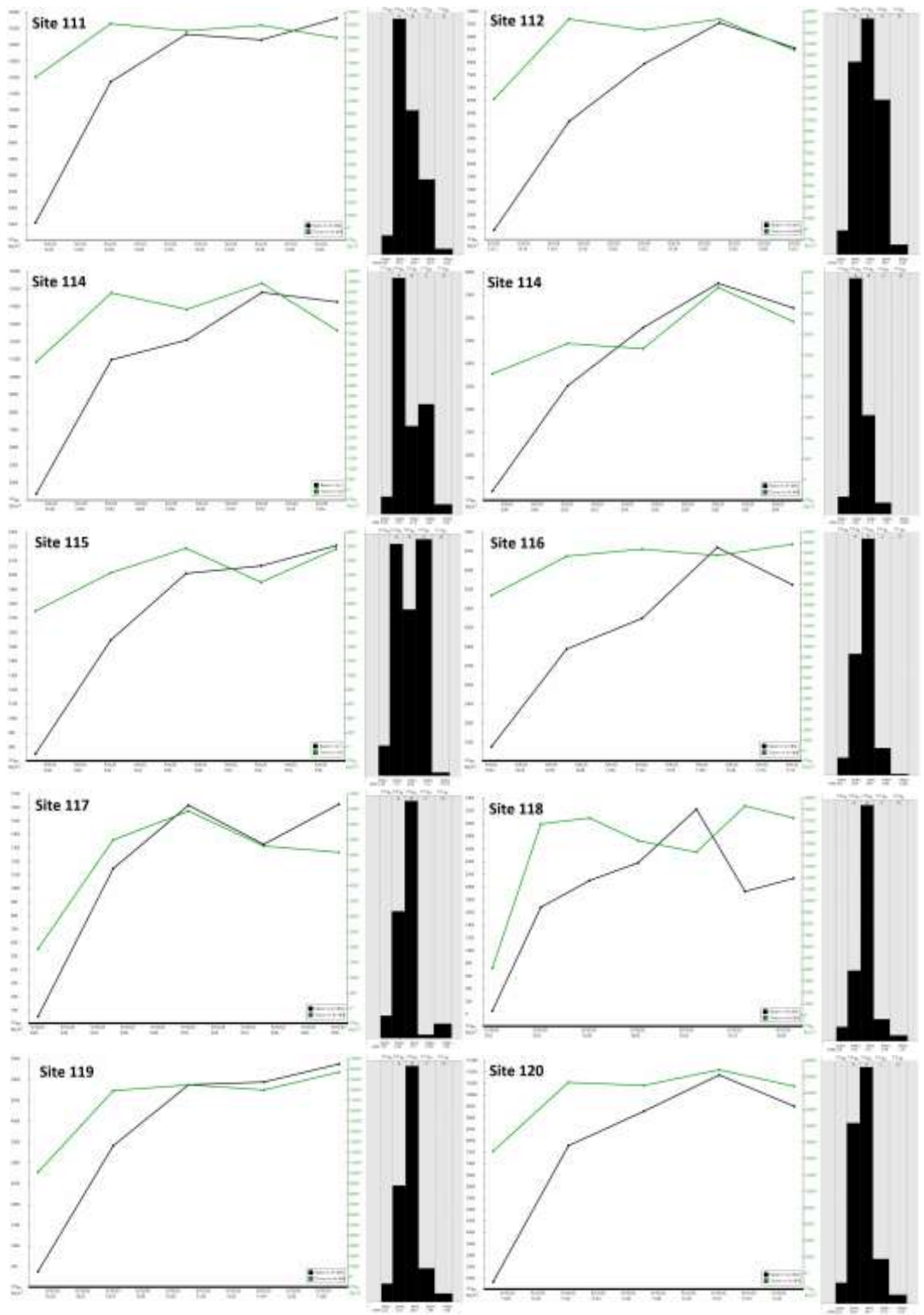


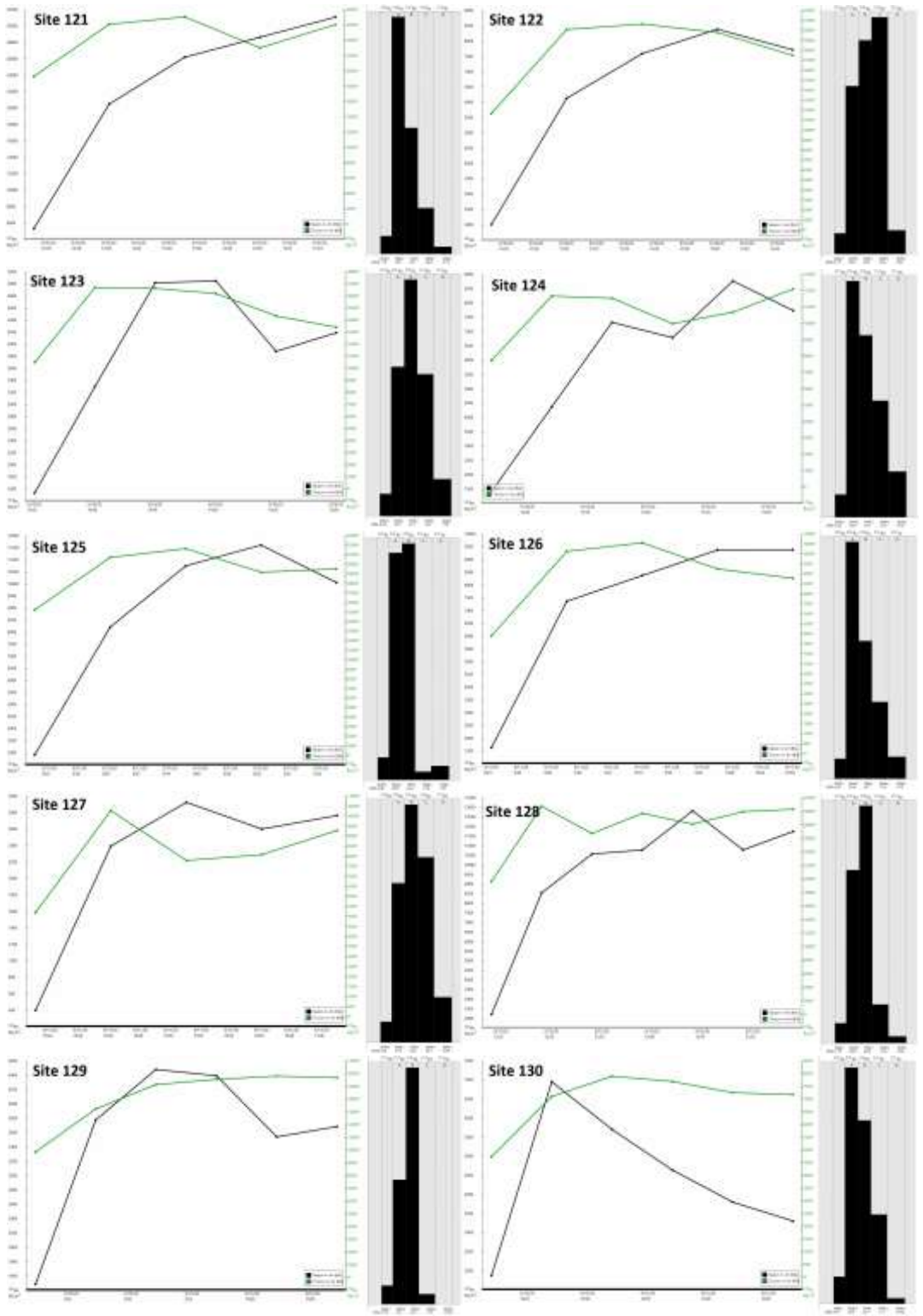


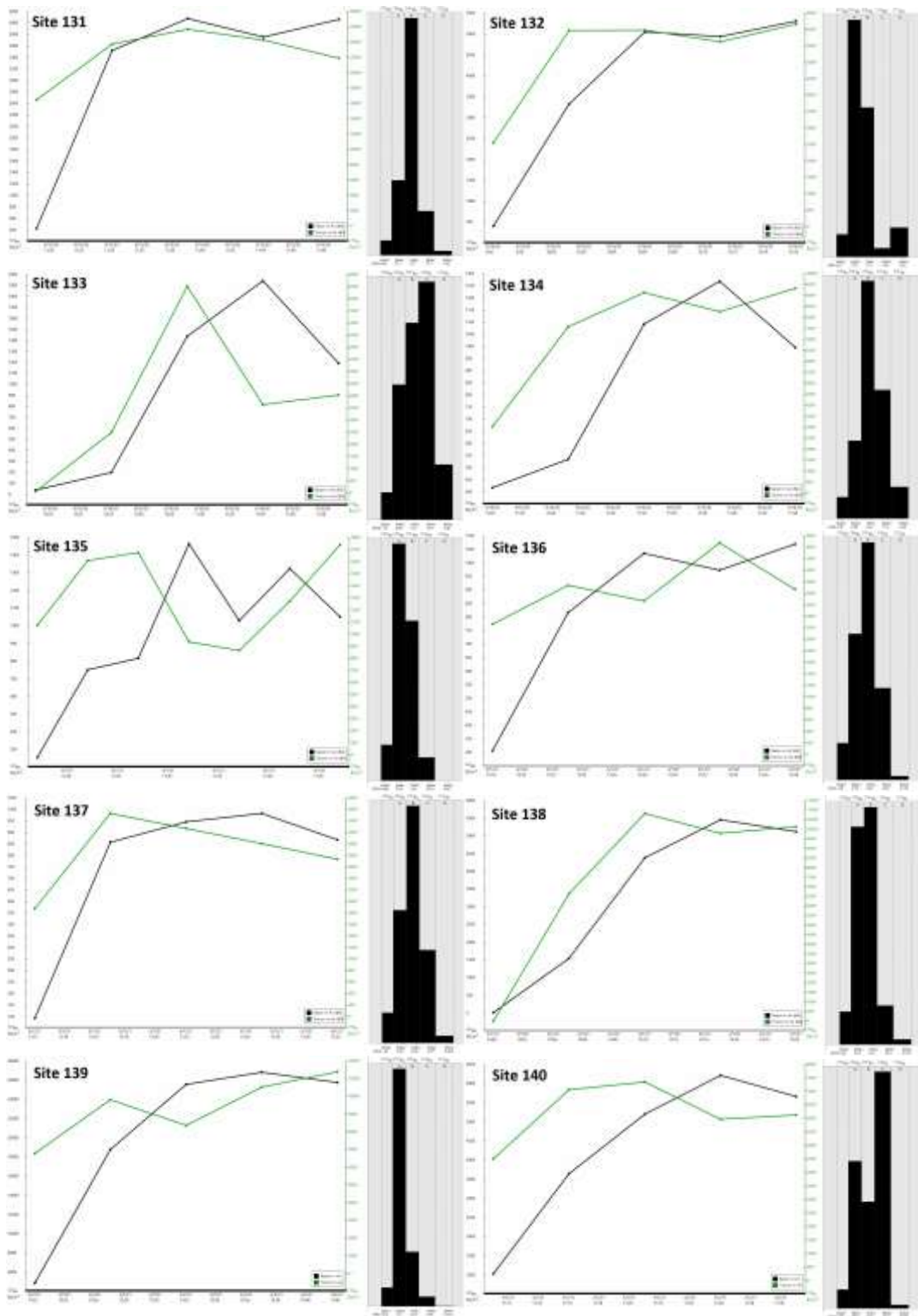


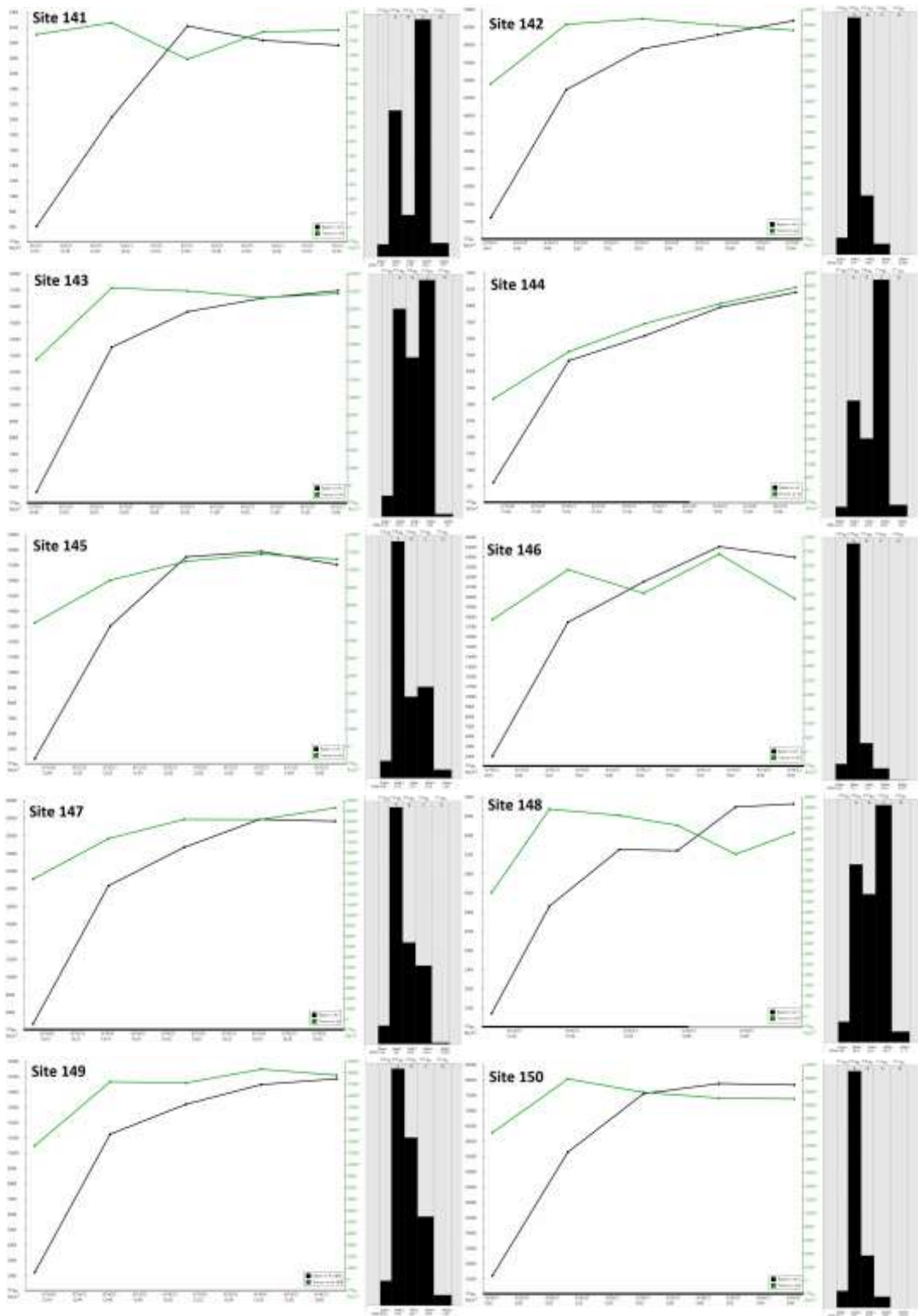


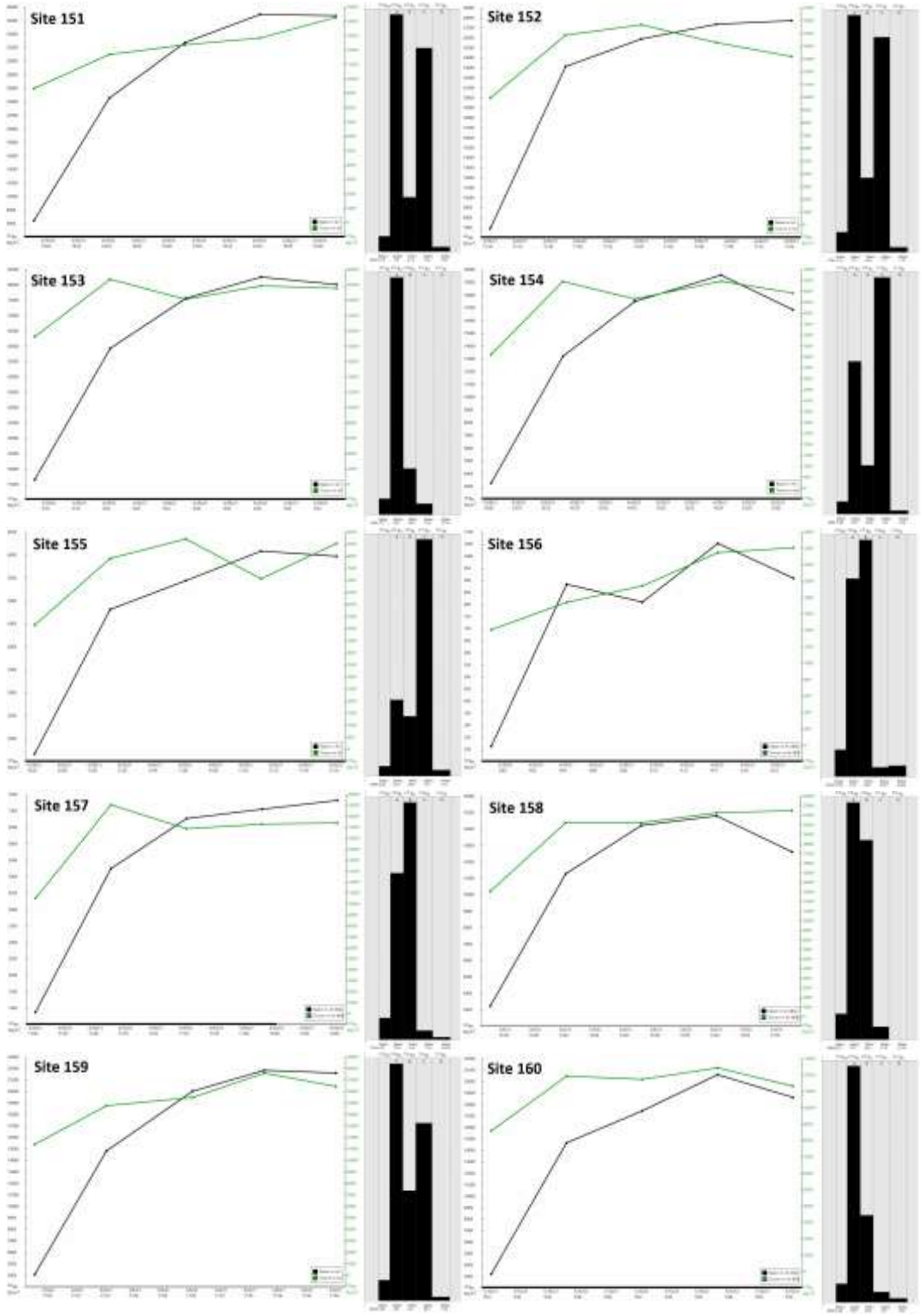


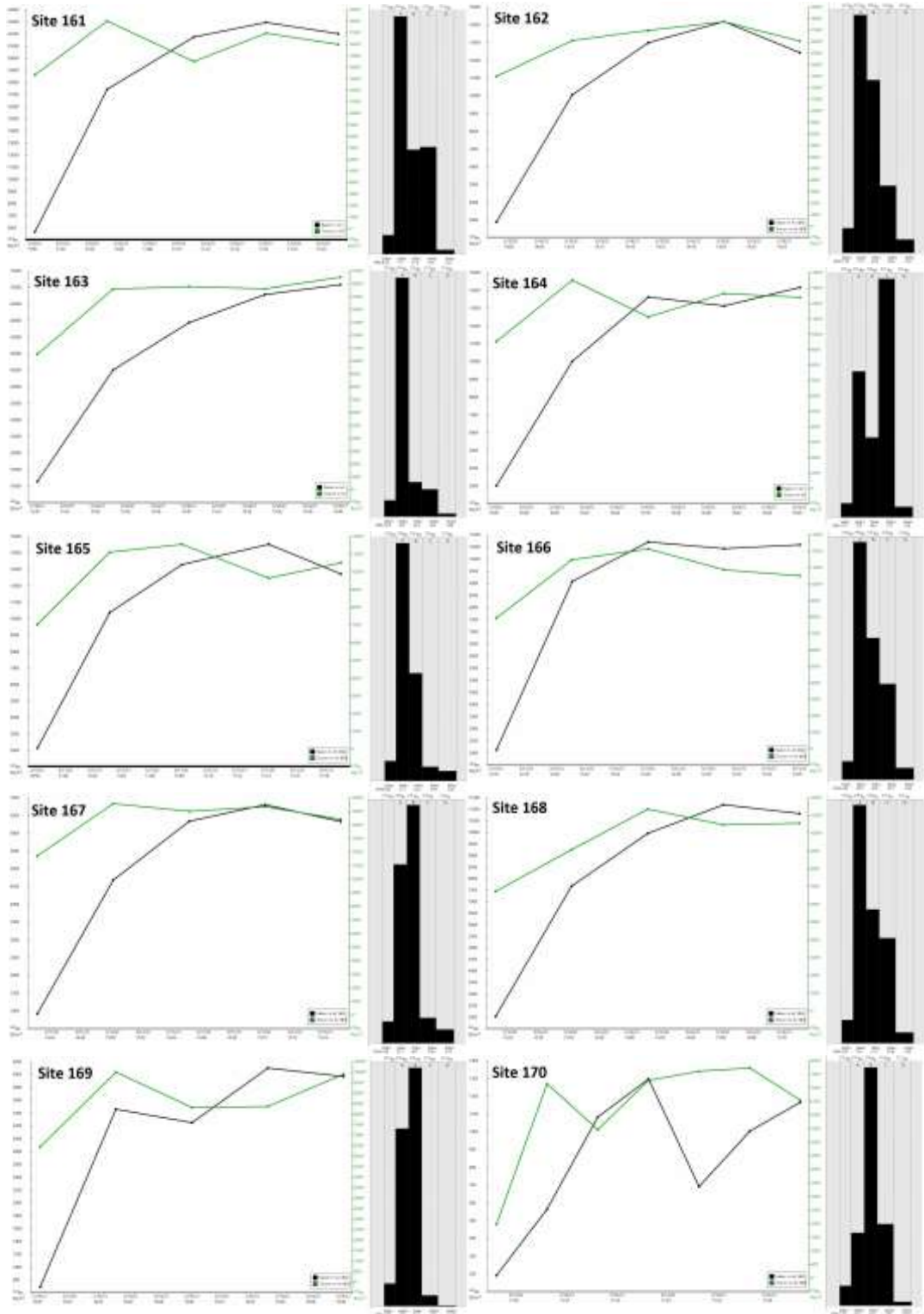


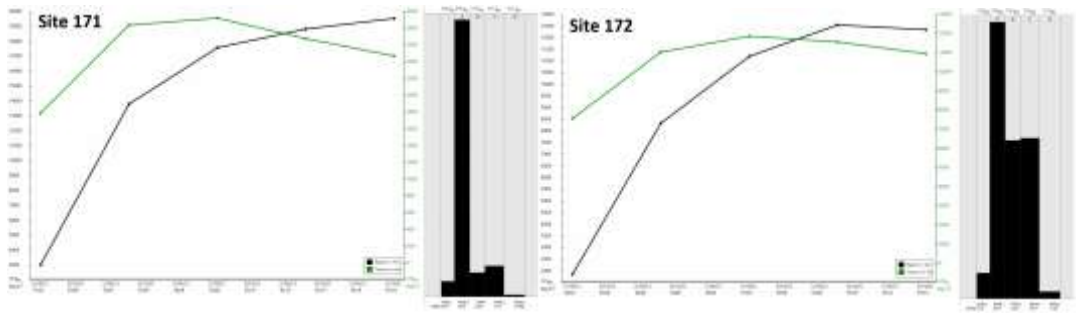












Appendix 2 - Groundwater-Rn spectra

